Orbital Entanglement and Correlation in Many-Electron Systems

Lexin Ding

München 2024

Orbital Entanglement and Correlation in Many-Electron Systems

Lexin Ding

Dissertation
an der Fakultät für Physik
der Ludwig–Maximilians–Universität
München

vorgelegt von
Lexin Ding
aus Guangzhou, China

München, den 31 Juli 2024

Erstgutachter: Dr. Christian Schilling
Zweitgutachter: Prof. Ali Alavi
Tag der mündlichen Prüfung: 13 September 2024

Contents

Zusammenfassung

Das Grundzustandsproblem von Vielelektronensystems stellt eine der wichtigsten Herausforderungen in vielfältigen Bereichen der Physik und Chemie dar. Die exponentielle Zunahme der Dimension des Lösungsraums und die steigende Komplexität des Grundzustands in stark korrelierten Systemen machen es schwierig, eine genaue und gleichzeitig effiziente Lösung zu finden. Aufgrund begrenzter Rechenressourcen ist es notwendig, spezifische Eigenschaften der Verschränkungsstrukturen von Systemen mit vielen Elektronen auszunutzen, indem man sich auf die Bereiche des Hibertraums konzentriert, in denen die Lösungen des Grundzustandproblems liegen. Ein nützlicher Freiheitsgrad ist die Wahlfreiheit bei der Einteilchenbasis (Orbitale), die verwendet wird um die Wellenfunktion des Vielelektronensystems zu parametrisieren. Zunächst werden präzise Werkzeuge aus der Quanteninformationstheorie bereitgestellt, um neben verschiedenen Eigenschaften und der Quantifizierung von Korrelationen und Verschränkungen auch die Herausforderungen zu berücksichtigen, die sich aus der Ununterscheidbarkeit der Elektronen ergeben. Diese Werkzeuge ermöglichen eine systematische Untersuchung der Abhängigkeit von Orbitalverschränkung von der gewählten Basis, die dann zur Anpassung der Orbitalverschränkung des Grundzustands in zwei entgegengesetzte Richtungen genutzt wird: (i) Durch die Reduzierung der Orbitalverschränkung gemäß entsprechend gestalteter Kostenfunktionen, der quanteninformationsunterstützte vollständige aktive Raum (QICAS) identifiziert direkt die energetisch optimalen aktiven Orbitale, ohne dass dabei das Grundzustandsproblem wiederholt gelöst werden muss, wie es beim herkömmlichen Ansatz des kompletten aktiven Raums mit selbstkonsistentem Feld (CASSCF) der Fall ist. (ii) Wird der Grundzustand jedoch durch die Anzahl der maximal verschränkten Atomorbitale (MEAO) dargestellt, erhält man ein äußerst intuitives Bild der Bindungsstruktur eines Moleküls. Jede kovalente Zweizentrenbindung entspricht einem Paar maximal (und monogam) verschränkter Orbitale. Dieser Zusammenhäng lässt sich sogar auf Multizentrenbindungen erweitern, indem man die sogenannte echte multipartite Verschränkung (GME) betrachtet. Die MEAO-Basis fungiert als einzigartiges Werkzeug um natürliche chemische Konzepte aus immer komplexeren Wellenfunktionslösungen abzurufen. Diese Ergebnisse betonen die Flexibilität und universelle Relevanz der Konzepte von Orbitalverschränkung und können wertvolle Einblicke in anspruchsvolle Probleme der Quantenphysik und -chemie bieten, die über das Grundzustandsproblem hinausgehen.

Abstract

The many-electron ground state problem is a ubiquitous challenge faced in a wide range of subfields of physics and chemistry. The exponential scaling of the dimension of the solution space, and the growing complexity of the ground state in strongly correlated systems, pose immense difficulties in obtaining the ground state solution with both accuracy and efficiency. That being said, exploiting the specific features of the entanglement structures of many-electron systems may allow one to target specific corners of the Hilbert space where the solutions to our problems lie. A useful degree of freedom in the problem is the choice of the single-particle basis (orbitals) in which we represent the many-electron system and parametrize wavefunction ansätze. In this thesis, we will investigate the consequences of the choice of the orbital basis in solving many-electron problems, through the lens of orbital entanglement and correlation. We will first provide precise tools from quantum information theory, for addressing and quantifying various aspects of correlation and entanglement, while taking into account complications due to the indistinguishability of electrons. With these tools, we are able to systematically explore the basis choice dependence of orbital entanglement and correlation, which we use as a steering wheel for tuning the orbital entanglement of the ground state in two opposite directions: (i) By reducing the orbital entanglement according to appropriately designed cost functions, we developed the quantum information-assisted complete active space (QICAS) method, which identifies the energetically optimal active orbitals, without having to solve the ground state problem many times as in the conventional complete active space self-consistent field (CASSCF) approach. (ii) In contrast, if we express the ground state in terms of the set of maximally entangled atomic orbitals (MEAO), we arrive at a highly intuitive picture of the bonding structure of the molecule. Every two-center covalent bond corresponds to a pair of maximally (and monogamously) entangled orbitals. This correspondence can even be extended to multi-center bonds, by invoking the so-called genuine multipartite entanglement (GME). The MEAO basis serves as a unique medium for retrieving natural chemical concepts, from ever more complex wavefunction solutions. Our results highlight the flexibility and universal relevance of the concepts of orbital entanglement and correlation, and may shed lights on challenging problems in quantum physics and chemistry beyond the ground state problem.

Publications

This thesis is based on and contains textual overlap with the following publications:

- **L. Ding**, S. Knecht, Z. Zimborás, C. Schilling, "Quantum Correlations in Molecules: from Quantum Resourcing to Chemical Bonding", *Quantum Sci. Technol.* **8** 015015 (2022)

- **L. Ding**, G. Dunnweber, C. Schilling, "Physical Entanglement between Localized Orbitals", *Quantum Sci. Technol.* **9** 015005 (2023)

- **L. Ding**, S. Knecht, C. Schilling, "Quantum Information-Assisted Complete Active Space Optimization (QICAS)", *J. Phys. Chem. Lett.*, **14**, 49, 11022–11029 (2023)

- K. Liao, **L. Ding**, C. Schilling, "Quantum Information Orbitals (QIO): Unveiling Intrinsic Many-Body Complexity by Compressing Single-Body Triviality", *J. Phys. Chem. Lett.*, **15**, 26, 6782–6790 (2024)

Some results in this thesis are also a part of a forthcoming manuscript by the author:

- **L. Ding**, E. Matito, C. Schilling, "Dissecting Chemical Bonds with Maximally Entangled Atomic Orbitals (MEAO)", forthcoming (2024).

Additionally, the author contributed to the following preprints and publications while working on the above projects:

- **L. Ding**, J. Liebert, C. Schilling, "Comment on 'Self-Consistent-Field Method for Correlated Many-Electron Systems with an Entropic Cumulant Energy' ", arXiv:2202.05532 (2022)

- C.-L. Hong, L. Colmenarez, **L. Ding**, C. L. Benavides-Riveros, C. Schilling, "Quantum Parallelized Variational Quantum Eigensolvers for Excited States", arXiv:2306.11844 (2023).

- **L. Ding**, C.-L. Hong, C. Schilling, "Ground and Excited States from Ensemble Variational Principles", arXiv:2401.12104 (2024).

- D. Aliverti-Piuri, K. Chatterjee, **L. Ding**, K. Liao, J. Liebert, C. Schilling, "What can Quantum Information Theory Offer to Quantum Chemistry?", *Faraday Discuss.* (2024).

In the above projects, the author had contributed significantly to conceptualization, analytic derivations, numerical calculations, data acquisition and presentation, manuscript writing and revision.

Introduction

The notion of entanglement dates back to nearly 90 years ago, when Einstein, Podolsky, and Rosen observed the fundamental contradiction between local realism and quantum mechanics in entangled systems [1]. The puzzling fact that measuring one of two distant but entangled particles instantaneously "steers" the state of the other, led to the so-called EPR paradox. The nonlocal nature of entanglement is validated by Bell [2] in 1964. Indeed, some entangled states (also known as Bell states) contain uniquely quantum statistics that violates so-called the Bell inequalities, thus ruling out the possibility of local realism. Since the discovery of the Bell inequalities, for a long time entanglement and nonlocality were used as synonyms. It was only until much later that researchers understood that not all entangled states violate the Bell inequalities [3]. The formal definition of entanglement, or more precisely the lack thereof, was presented in 1989 by Werner in an operational fashion: Entangled states are those that can not be prepared with only local operations and classical communications (LOCC) between separate parties [3].

The foundational definition of entanglement by Werner had spawned into myriads of research directions, including in particular, detecting and quantifying entanglement for general mixed states [4]–[10] (realistic quantum systems inevitably suffer from decoherence which renders their states to be mixed [11]). These studies are certainly of great interests on their own, but they are also highly motivated by the fact that entanglement is a valuable resource for quantum information processing tasks [12], [13]. Since entangled states are not preparable by LOCC, from a resource theory perspective they are external resources that allows one to perform protocols that would be impossible with LOCC alone [13]. Prime examples of such tasks are quantum teleportation [14], superdense coding [15], and quantum key distribution [16], to name a few. In perfect realization of these processes, the entanglement is used as a resource that is irreversibly spent. Therefore, knowing precisely the amount of usable entanglement in a general mixed state is of extremely high relevance.

The rapid development of entanglement theory in quantum information soon fostered a ubiquitous presence of entanglement in many fields of physics, including high energy physics [17]–[19], cosmology [20], quantum optics [21], [22], and condensed matter physics [23]–[26]. In condensed matter physics, entanglement transitioned from the object of study, to a tool for revealing fundamental physics. The unique behavior of entanglement

in many-body systems signifies fascinating many-body phenomena such as quantum phase transitions [23], [24], topological orders [25], [26], many-body localization [27], [28]. At the same time, entanglement characterizes the structure and complexity of the ground state itself, and sheds light on how one should approach the ground state problem by numerical means [29]–[32]. Possibly the most prominent example along this line of research was the discovery of the area law of entanglement in systems governed by gapped local Hamiltonians [30]. In such systems, the entanglement between a region A and its complement measured by the von Neumann entropy $S(\rho_A) = -\mathrm{Tr}[\rho_A \log(\rho_A)]$ of the reduced state ρ_A is only proportional to the degrees of freedom on the boundary ∂A, rather than all degrees of freedom within A. In 1D systems, the area law implies that the entanglement is asymptotically constant, since the boundary of any connected region in one dimension is of length $|\partial A| = 2$. This key observation directly justifies the suitability of matrix product states [33] (MPS) for simulating 1D systems. The MPS ansatz bypasses the exponential scaling of the ground state problem by mimicking precisely the entanglement growth in 1D gapped local systems, and has become one of the most successful numerical ansätze in the past two decades. Generalizations to higher dimensional settings gave rise to more sophisticated tensor network states such as projected entangled pair states [34] (PEPS) and multi-scale entanglement renormalization ansatz [35] (MERA). The structure of the Hamiltonian, and hence the structure of the ground states, are effectively translated into the structure of the desirable ansätze through the lens of entanglement.

As powerful as entanglement is in characterizing the representational complexity of quantum states, entanglement is hardly an intrinsic property of the quantum states for systems of indistinguishable particles. This is because entanglement is a relative quantity. Its value can change drastically when the underlying one-particle basis (i.e., orbitals or sites) changes. Let us consider the simplest example of a system of one spinless fermion in two spatial sites (labelled 1 and 2), governed by a tight-binding Hamiltonian $\hat{H} = -t(f_1^\dagger f_2 + f_2^\dagger f_1)$, where $f_{1/2}^{(\dagger)}$ are the fermionic annihilation (creation) operators of the spatial sites. When $t > 0$, the ground state is simply $|\Psi_{\mathrm{gs}}\rangle = \frac{1}{\sqrt{2}}(f_1^\dagger - f_2^\dagger)|0\rangle$, where $|0\rangle$ is the vacuum state. The two spatial sites 1 and 2 are clearly entangled, since the fermion is in a superposition of either occupying site 1 or site 2. The measurement outcome of the occupation of one of the sites immediately informs us about the occupation on the other, much like in the entangled state in the EPR paradox, or in a Bell state. Can we then conclude that the system can never admit a simpler description than $|\Psi_{\mathrm{gs}}\rangle$? Is it necessary to invoke entanglement to characterize the system? The answer to both questions is clearly no. The system is non-interacting and translationally invariant. Therefore, it can be solved by a mean-field state after Fourier transforming the spatial representation to the momentum basis. In fact, by simply inspecting the ground state $|\Psi_{\mathrm{gs}}\rangle$ one can redefine $c_{1/2}^\dagger = \frac{1}{\sqrt{2}}(f_1^\dagger \mp f_2^\dagger)$, leading to a new and simpler form of the ground state $|\Psi_{\mathrm{gs}}\rangle = c_1^\dagger|0\rangle$. The two new (momentum) sites are unentangled, since $|\Psi_{\mathrm{gs}}\rangle$ is a product state in this basis.

The basis dependence of entanglement may not be of utmost importance in condensed

matter physics, since some bases (e.g. the spatial or momentum one) are naturally preferred due to their local structures, or the symmetries of the Hamiltonians. In contrast, in quantum chemistry (QC) the choice of single orbital basis is much more flexible, and does play a significant role in compactifying the representations of wavefunctions and improving numerical results [36]–[41]. Under the Born-Oppenheimer approximation where the nuclei are treated as stationary objects, the non-relativistic many-electron Hamiltonian contains a one-body (kinetic and nuclear potential) and two-body term (Coulomb interaction) in second quantization

$$\hat{H}_{\mathrm{QC}} = \sum_{\sigma=\uparrow,\downarrow} \sum_{i,j=1}^{D} h_{ij} f_{i\sigma}^{\dagger} f_{j\sigma} + \frac{1}{2} \sum_{\sigma,\tau=\uparrow,\downarrow} \sum_{i,j,k,l=1}^{D} V_{ijkl} f_{i\sigma}^{\dagger} f_{j\tau}^{\dagger} f_{l\tau} f_{k\sigma}, \tag{1}$$

where $f_{i\sigma}^{(\dagger)}$ are fermionic operators associated with a given spin-orbital basis $\mathcal{B} = \{\phi_i\}_{i=1}^{D}$, and the h_{ij} and V_{ijkl} are basis dependent coefficients. Notice that compared to typical local Hamiltonians in condensed matter physics, the matrix elements h_{ij} of the one-particle Hamiltonian are no longer restricted to neighbors (e.g., in the Hubbard model [42]), and the interaction term even involves up to four orbitals at a time (instead of one for on-site interaction, and two for nearest neighbor interaction). The complicated nature of the Hamiltonian, together with the exponential scaling of the Hilbert space, are the reasons why quantum chemistry remains one of the hardest problems in quantum science [43].

Knowing well that the exact solution of the ground state problem is out of reach, quantum chemists solve the ground state problem by a step-by-step game of capturing "electron correlation". Starting from the mean field solution (via Hartree-Fock or density functional theories), numerous methods are developed to recover the missing "correlation energy", i.e., the difference between the mean field energy and the exact one [44]. The choice of (combinations of) methods depends on the type of correlation the system possesses. Related to this is the conceptual separation of static and dynamical correlations. Static correlations refer to the correlation due to a small number of Slater determinants with large weights in the configuration interaction (CI) expansion of the ground state wavefunction. This is usually due to near degenerate one-particle states such as the case of molecular dissociation or strong interaction. Dynamical correlation contrarily refers to a long tail of many Slater determinants with vanishingly small weights. Although each weight is small, the sheer number of such Slater determinants makes their contribution to the ground state energy considerable. Dynamical correlations are mostly attributed to the Kato cusp condition [45] of the wavefunction (consequence of the singularity in the Coulomb interaction when two charged particles come together). The notions of static and dynamical correlations are convenient tools: They help classify electronic systems into groups in which one type of correlation is dominating, so that ground state methods specifically designed for targeting either static or dynamical correlations can be applied. Methods that treat static correlations well include complete active space methods and configuration interaction methods, whereas single reference perturbation theory [46] and coupled cluster theory [47], [48] (CCSD) are typically capable of capturing dynamical correlation in the absence of

strong static correlation. In the case where both types of correlations are significant, one resorts to hybrid methods that combine the strength of both type of methods [49]–[51].

That being said, the notions of static and dynamical correlation suffer from three conceptual flaws: First, they are ambiguous concepts. Despite countless efforts, there is no clear line that separates the effect of static and dynamical correlation in a quantum state. Second, there are no straightforward metrics for quantifying either static or dynamical correlation. Although from the coefficients of the Slater determinants (also known as configuration interaction (CI) coefficients) one can to some extent qualitatively infer the degree of static or dynamical correlation, it is neither precise nor practically feasible for large systems, since CI coefficients are highly many-body quantities. Third, static and dynamical correlation are basis dependent effects: The CI coefficients of the same quantum state can vary significantly from one single-particle basis representation to another. Therefore, they are hardly intrinsic properties of the wavefunction. The lack of computable metrics further hinders the exploration (and ideally exploitation) of the basis dependence of both static and dynamical correlation.

On top of these ambiguities, as the MPS ansatz or more generally tensor network states made their entrance into quantum chemistry [52], more refined notions of electron correlation than static/dynamical correlation are urgently needed. The reason is that the ground states of the QC Hamiltonian are *a priori* not expected to be simulatable by an MPS in the regime of large system sizes, due to the lack of apparent local structure in the Hamiltonian, and hence the lack of an area law of entanglement in the ground state. One faces a barrier of entanglement by trying to fit a highly nonlocal and complex wavefunction with a locally correlated ansatz. For this reason, when simulating the many-electron ground state, typically the required bond dimension of the MPS grows steeply with the number of orbitals involved. Yet, the molecular ground state is not entirely without structure. In a given orbital basis, there are orbitals that contribute more/less correlation effects than the others. Qualitatively speaking, strongly correlated orbitals should be placed closed to each other (and hence become more local) when mapped to an MPS, so that the correlation effect can be more easily captured by an MPS. This then begs the question: Can one quantitatively measure the extent of correlation of each orbital, or even exploit the correlation pattern of the orbitals to find the optimal orbital basis such that the entanglement barrier of the MPS representation is tamed, if not removed? Answering this question benefit not only the application of MPS to molecular systems, but also potentially many conventional basis-dependent wavefunction methods in quantum chemistry.

All these aspects eventually resulted in a surge of new interest in applying quantum information theory of entanglement and correlation to many-electron systems [39], [41], [53]–[77]. Quantum information theory in the context of fermions is by itself a broad direction. It includes (but is not limited to) understanding the fundamental quantum mechanical restriction on the fermionic states (e.g., generalized Pauli constraints [57]–[59], [61], [68]), understanding the relation between the total and reduced states (e.g.,

the N-representability problem [55], [78]) and potentially solving the Schrödinger equation with reduced quantities [56], [79], and the analysis of the representational complexity of many-electron states with orbital entanglement and correlation [41], [62]. Although subtleties may arise due to the indistinguishable nature of electrons [64], this general research direction of fermionic correlation is not only beneficial to many-body physics and quantum chemistry, but can also give rise to new forms of entanglement resources for quantum technologies[69], [70], [73], [75], [77].

Specifically in the context of quantum chemistry, the notion of orbital entanglement and correlation may hold the key to exploiting the degrees of freedom in choosing a single-particle basis. Orthogonal molecular orbitals, much like spatial or momentum sites in condensed matter physics, do act as distinct subsystems. And there exists a plethora of precise quantum information concepts ranging from quantum to classical correlation [8], [80]–[82], and from bipartite to multipartite scenarios [83]–[86], which one can use to precisely quantify the correlation among molecular orbitals. In any case, orbital entanglement and correlation are again explicitly basis dependent. Their values can change drastically from one basis to another. Although the correlation patterns of some common orbital bases such as the Hartree-Fock canonical orbitals or the natural orbitals have been studied [41], [62], [87], more general statements on the basis dependence of orbital correlation are yet to be made. For example, one important feature of a set of orbital basis is the degree of spatial localization. It is therefore natural to ask how does orbital localization affect the value of orbital entanglement and correlation.

The upshot of exploring the orbital entanglement and correlation pattern in different orbital bases is three-fold: (i) **Extracting the entanglement resource in atoms and molecules.** In light of the second quantum revolution, atoms and molecules will soon become viable platforms for executing quantum information processing tasks [88]–[90]. Given the pivotal role of entanglement as the key resource for such tasks, it is thus crucial to measure the maximal capacity of usable orbital entanglement resource in molecular systems. The term "usable" refers to taking into account also the fermionic nature of many-electron systems, and incorporating the important superselection rules in the quantification of orbital entanglement [64], [91], [92]. (ii) **Improving interpretability of high-level wavefunctions for chemical understanding.** Numerical methods have improved tremendously since the intuitive modelling of the hydrogen molecule by Heitler and London. Wavefunctions are represented by more and more abstract ansätze, in orbital basis with less and less interpretability. Recovering the chemical knowledge from high-level wavefunction and advance our understanding of molecular properties should be the ultimate goal of any wavefunction methods. By choosing the appropriate orbital basis based on entanglement and correlation analysis, we may be able to re-express the wavefunction in such a way that the chemistry (e.g., bonding patterns) is more readily extracted. (iii) **Expanding the limitation of numerical ansätze for the ground state problem (and beyond).** MPS being a unique example where the entanglement of the state is directly and quantitatively related to the computational cost [29], [30], was one of the first

ansätze to be combined with quantum information-based orbital optimization. Techniques of reordering, locally rotating, and even globally optimizing the underlying basis based on bipartite entanglement and pairwise orbital correlation have been shown to be hugely effective in reducing the required bond dimension of the MPS [39], [41], [93], [94]. Besides the MPS, there are many other orbital basis dependent ansätze in quantum chemistry. For example, in the complete active space (CAS) methods [95]–[98], the selection of the so-called active orbitals, which are allowed to correlate with each other. Identifying the active space is a highly nontrivial task. Additionally, optimizing these active orbitals involves expensive self-consistent cycles. These methods may not have the same quantum informatic origin like MPS, but they too mimic specific structures of the ground state, and these structures can be quantified by means of orbital entanglement and correlation. Finding the optimal orbital basis where the correlation structure of the true ground state is the closest to that of the ansatz, enables us to unlock the full potential of these methods.

This thesis is structured as follows: In Chapter 1 we first recap the relevant concepts of entanglement and correlation in quantum information. We then explain how these concepts can be adapted for systems of many-electrons, taking their indistinguishability into consideration. In Chapter 2 we calculated analytically the orbital-orbital entanglement in 1D tight-binding systems, and derived its asymptotic properties. We then explore the connection between orbital entanglement and orbital localization in Chapter 3, which leads to the development an entanglement-based framework for analyzing the bonding structures of molecules from *ab initio* calculations. In Chapter 4 we establish a connection between orbital entanglement and the complexity of wavefunctions, and present a quantum information-assisted orbital optimization scheme for efficient optimization of active space orbitals.

Chapter 1

Fermionic Entanglement and Correlation

In the first section of this chapter, we introduce the relevant concepts from quantum information theory. These include the notions of correlation and entanglement between distinguishable parties, the separation of quantum and classical part of the total correlation, and last but not least how these various types of correlation are quantified consistently. For any correlation type, the most crucial ingredients are the notion of subsystems and correspondingly local operations. In the simplest bipartite setting, system A and B (e.g. two distant laboratories) are associated to two separate Hilbert spaces $\mathcal{H}_A$ and $\mathcal{H}_B$. Together they form a tensor product structure $\mathcal{H} = \mathcal{H}_A \otimes \mathcal{H}_B$ associated to the total system. Moreover, local operations of the type $\hat{O}_A \otimes \mathbb{1}_B$ on one subsystem have no effect on the other. The only common element of the two algebras of local operations $\{\hat{O}_A \otimes \mathbb{1}_B\}$ and $\{\mathbb{1}_A \otimes \hat{O}_B\}$ is the identity $\mathbb{1} = \mathbb{1}_A \otimes \mathbb{1}_B$ (corresponding to no operation at all) [99]. The tensor product structure of the Hilbert space together with the separation of local operations, provides a solid foundation for defining entanglement and correlation.

In the second section, we will explain how the well-established theory of entanglement (as well as other types of correlation) can be translated to systems consisting of indistinguishable particles, in our case, fermions. The most pressing question is: where can one find a tensor product structure in a fully-antisymmetrized N-particle Hilbert space? The short answer is that, within the N-particle Hilbert space, the usual notion of entanglement is ill-defined. Even the simplest two-fermion state $|\Psi\rangle$ with two modes ϕ and φ occupied is seemingly entangled (in first quantization)

$$|\Psi\rangle = \frac{|\phi, \varphi\rangle - |\varphi, \phi\rangle}{\sqrt{2}}. \tag{1.1}$$

This is due to the enforced antisymmetry of the Slater determinants, which are the building block of fermionic states. In other words, an unentangled pure product state does not exist

in the N-particle Hilbert space. One could abandon the usual definition of uncorrelated or unentangled states, and define from a "physical" perspective what fermionic states *should* be considered free of correlation, namely those corresponding to the eigen- and thermal states of non-interacting Hamiltonians. This leads to the formalism of *particle* correlation.

The alternative route to subsystems is perhaps the more familiar one to condensed matter theorists, namely the partitioning of sites or orbitals. Unlike fermions, the fermionic orbitals are themselves distinguishable. On one hand, if we embed the N-particle Hilbert space into the embedding total Fock space $\mathcal{F}$ consisting of all possible particle number sectors (including the vacuum), then $\mathcal{F}$ indeed factorizes into the tensor product of Fock spaces on each fermionic orbital. On the other hand, invoking the second quantization formalism means that the antisymmetry of the fermions is now encoded instead on the level of operators. The fact that creation and annihilation operators on different orbitals do not commute with each other (they by definition anticommute), implies that they can no longer be considered as *local* operations. We shall discuss in detail how this conundrum is resolved, by incorporating the important superselection rules.

1.1 Hierarchy of correlation types

1.1.1 Geometry of quantum states

In order to set the stage for what follows, it will be essential to first recall and discuss basic geometric aspects of the space of quantum states. This will allow us to quantify and compare on a unified basis the total, quantum and classical correlation, and entanglement.

Let us start by considering a complex finite-dimensional Hilbert space $\mathcal{H}$ of dimension d and denote the algebra of linear operators acting on $\mathcal{H}$ by $\mathcal{B}(\mathcal{H})$. The corresponding set $\mathcal{D}$ of density operators is given by all Hermitian operators ρ on $\mathcal{H}$ which are positive-semidefinite $\rho \geq 0$ (i.e., ρ has non-negative eigenvalues), and trace-normalized to unity,

$$\mathcal{D} = \{\rho \in \mathcal{B}(\mathcal{H}) \,|\, \rho^\dagger = \rho,\, \rho \geq 0,\, \mathrm{Tr}[\rho] = 1\}\,. \tag{1.2}$$

For the sake of completeness, we recall that for complex finite-dimensional Hilbert spaces, the Hermiticity of an operator is a direct mathematical consequence of its positive semidefiniteness and we could therefore have skipped the requirement $\rho^\dagger = \rho$ in Eq. (1.2). As it is illustrated in Figure 1.1, the set $\mathcal{D}$ is convex since the convex combination $p\rho + (1-p)\tilde{\rho}$ of any two density operators $\rho, \tilde{\rho} \in \mathcal{D}$ and any $0 \leq p \leq 1$ is again a density operator. Moreover, $\mathcal{D}$ is compact, i.e., it is bounded and closed as a subset of the Hermitian operators. In order to develop a better intuition for $\mathcal{D}$, we observe that a density operator ρ lies on the boundary of $\mathcal{D}$ if it is not strictly positive, that is, at least one of its eigenvalues

vanishes. A particularly important subset of boundary points is given by the extremal points of $\mathcal{D}$. These are per definition those "points" $\rho \in \mathcal{D}$ which cannot be written as convex combinations of other points in $\mathcal{D}$. One easily verifies that a density operator ρ is extremal if and only if it is a pure state

$$\rho \equiv |\Psi\rangle\langle\Psi| \quad \text{with } |\Psi\rangle \in \mathcal{H} \,, \tag{1.3}$$

or, equivalently, if ρ has eigenvalues $\{1, 0, \ldots, 0\}$. For Hilbert spaces of dimension larger than two, the extremal points define a proper subset of the boundary points and only in case of a two-dimensional $\mathcal{H}$ ("qubit") they would coincide.

Since the space $\mathcal{D}$ of density operators is a subset of the Euclidean vector space of linear operators on $\mathcal{H}$ (or equivalently just $\mathbb{C}^{d\times d}$) we can introduce a notion of distances and angles in a straightforward manner. To this end, we introduce the Hilbert-Schmidt inner product on $\mathcal{B}(\mathcal{H})$,

$$\langle \hat{A}, \hat{B} \rangle \equiv \mathrm{Tr}[\hat{A}^\dagger \hat{B}] \tag{1.4}$$

where $\hat{A}, \hat{B} \in \mathcal{B}(\mathcal{H})$ are linear operators. By employing either the induced norm, any other metric or a generalized distance function we can then quantify the similarity of quantum states. The huge advantage of this approach lies in the universality of its predictions: Whenever two density operators are close to each other, the same follows as a mathematical consequence for their expectation values for *any* choice of observable. A prominent generalized distance function is given by the quantum relative entropy [4], [100]

$$S(\rho||\sigma) \equiv \mathrm{Tr}[\rho(\ln\rho - \ln\sigma)] \,. \tag{1.5}$$

In a strict mathematical sense the quantum relative entropy does not define a distance function. For instance, $S(\rho||\sigma) \neq S(\sigma||\rho)$ is not symmetric, and it does not obey the triangle inequality. However, its relevance for quantum sciences and in particular our work originates from its distinctive information-theoretical meaning. It describes by concise means *"how difficult it is to distinguish the state ρ from the state σ"* [101] (see also Ref. [102]).

1.1.2 Correlation and entanglement

The quantum information theoretical concepts of correlation and entanglement refer to a notion of subsystems [3], [10], [103]. In order to discuss them in the context of *bipartite* systems, we assume that our total system comprises two *distinguishable* subsystems A and B. The corresponding Hilbert space then takes the form

$$\mathcal{H} = \mathcal{H}_A \otimes \mathcal{H}_B \tag{1.6}$$

and likewise for the algebra of observables,

$$\mathcal{B}(\mathcal{H}) = \mathcal{B}(\mathcal{H}_A) \otimes \mathcal{B}(\mathcal{H}_B) \,. \tag{1.7}$$

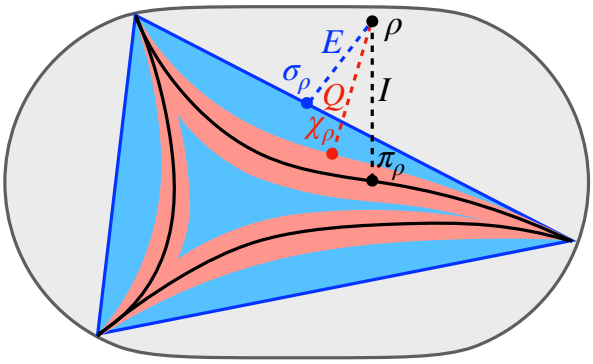

Figure 1.1: Schematic illustration of the state space $\mathcal{D}$. The subsets of uncorrelated ($\mathcal{D}_0$), classically correlated ($\mathcal{D}_{\text{cl}}$) and separable states ($\mathcal{D}_{\text{sep}}$) are shown in black, red and blue, respectively. The corresponding measures of total correlation I, quantum correlation Q and entanglement E are given by the quantum relative entropy (1.5) of ρ minimized with respect to those sets, with corresponding minimizers π_ρ, χ_ρ and σ_ρ.

To motivate the concept of total correlation let us consider two local measurements, with corresponding observables $\hat{A} \in \mathcal{B}(\mathcal{H}_A)$ of subsystem A and $\hat{B} \in \mathcal{B}(\mathcal{H}_B)$ of subsystem B. The correlation between these two measurements is described by the correlation function

$$\begin{aligned} \mathcal{C}(\hat{A},\hat{B}) &\equiv \langle \hat{A}\otimes\hat{B}\rangle_\rho - \langle \hat{A}\otimes \mathbb{1}_B\rangle_\rho \langle \mathbb{1}_A\otimes\hat{B}\rangle_\rho \\ &\equiv \langle \hat{A}\otimes\hat{B}\rangle_\rho - \langle \hat{A}\rangle_{\rho_A}\langle \hat{B}\rangle_{\rho_B}\,, \end{aligned} \tag{1.8}$$

where $\rho_{A/B} \equiv \text{Tr}_{B/A}[\rho_{AB}]$ denotes the reduced density operator of ρ for subsystem A/B and $\mathbb{1}_{A/B}$ the identity operator on $\mathcal{H}_{A/B}$. The crucial observation is now that a vanishing correlation function, $\mathcal{C}(\hat{A},\hat{B}) = 0$, does not necessarily imply the same for any other pair of local observables $\hat{A}', \hat{B}'$. This in turn strongly suggests the notion of uncorrelated states: A density operator ρ is called uncorrelated if and only if its correlation function (1.8) vanishes for *all* pairs of local observables $\hat{A}, \hat{B}$. As long as the algebra $\mathcal{A}_{A/B}$ of physical observables of system A/B includes all linear operators on $\mathcal{H}_{A/B}$, this is equivalent to the factorization of ρ into its reduced states, $\rho = \rho_A \otimes \rho_B$. The corresponding set

$$\mathcal{D}_0 \equiv \{\rho = \rho_A \otimes \rho_B\} \tag{1.9}$$

of all uncorrelated states is schematically illustrated in Figure 1.1. By referring to this geometric picture, a straightforward definition of the *total* correlation $I(\rho)$ contained in a quantum state ρ follows. It is given as the minimal "distance" of ρ to the set $\mathcal{D}_0$,

$$I(\rho) \equiv \min_{\pi\in\mathcal{D}_0} S(\rho||\pi) = S(\rho_A) + S(\rho_B) - S(\rho)\,,$$

measured in terms of the quantum relative entropy $S(\cdot||\cdot)$, where $S(\rho) \equiv -\text{Tr}[\rho\ln\rho]$ denotes the von Neumann entropy. Remarkably, the minimization in (1.10) can be executed analytically, leading to the mutual information (second line) where the closest uncorrelated

state follows as $\pi_\rho = \rho_A \otimes \rho_B$ [8]. Coming back to our motivation, we present an important relation between the total correlation and correlation functions which follows directly from results presented in [104], [105] (see Ref. [106] for a detailed derivation),

$$\frac{|\mathcal{C}(\hat{A},\hat{B})|}{\|\hat{A}\|_{\mathrm{op}}\,\|\hat{B}\|_{\mathrm{op}}} \leq \sqrt{2}\,\sqrt{I(\rho)}\,. \tag{1.10}$$

Here, $\|\hat{A}\|_{\mathrm{op}}$ denotes the operator norm of $\hat{A}$, i.e., the largest absolute value of its eigenvalues. Relation (1.10) confirms in quantitative terms that whenever a quantum state is close to the set $\mathcal{D}_0$ of uncorrelated states then its correlation function is small for *any* choice of local observables $\hat{A}, \hat{B}$. This highlights again the strength of quantum information theoretical concepts which is based on the universal character of their predictions.

Due to the information theoretical meaning of the quantum relative entropy (1.5), the total correlation (1.10) quantifies the additional information content in the state ρ beyond the information content in $\rho_A \otimes \rho_B$ (local information). The term "total" emphasizes here that $I(\rho)$ includes both classical and quantum correlations. In order to explore and conclusively understand the significance of either correlation part in chemical bonding and quantum chemistry in general, concise definitions of quantum correlation and classical correlations are needed as well. We first start, however, with the most prominent type of quantum correlation, the entanglement.

Separable or unentangled states are precisely those states that can be prepared by distant laboratories using local operations and classical communication (LOCC) only [3]. With local operations, two distant parties can prepare any uncorrelated state $\rho_A \otimes \rho_B$. In combination with classical communication arbitrary mixtures of uncorrelated states can be realized. Hence, the convex set of separable states is given by

$$\mathcal{D}_{\mathrm{sep}} \equiv \left\{ \sigma = \sum_i p_i \sigma_A^{(i)} \otimes \sigma_B^{(i)}, p_i > 0, \sum_i p_i = 1 \right\}. \tag{1.11}$$

As it is illustrated in Figure 1.1, this set is indeed nothing else than the convex hull of $\mathcal{D}_0$. Any state ρ that is not separable is called entangled.

For a pure state $|\Psi\rangle$, it is rather easy to check whether it is in the set $\mathcal{D}_0$. The only possible way in which $|\Psi\rangle\langle\Psi| \in \mathcal{D}_0$ is that $|\Psi\rangle = |\Psi_A\rangle \otimes |\Psi_B\rangle$ is a product state. That is equivalent to say, the reduced states on both systems must be pure. Therefore, it suffices to check the mixedness of either of the reduced states to tell whether $|\Psi\rangle \in \mathcal{D}_0$ is true. One possible quantity that reveals the mixedness of the reduced states is the von Neumann entropy $S(\rho) = -\mathrm{Tr}[\rho \log(\rho)]$.

For a mixed total state, however, one can not tell whether the mixedness of the reduced states originate from entanglement or simply the mixedness of the total state. For this reason, the von Neumann entropy of the reduced state is not a good indicator for

entanglement, and one must construct a new measure. In complete analogy to the quantification of total correlation, the entanglement of a general mixed state ρ can be quantified through the geometric picture [4]

$$E(\rho) \equiv \min_{\sigma \in \mathcal{D}_{\text{sep}}} S(\rho||\sigma) = S(\rho||\sigma_\rho)\,. \tag{1.12}$$

For general mixed states, no closed expression exists for this *relative entropy of entanglement*, except for highly symmetric states [107]. This unpleasant fact is due to the involved structure of the set (1.11) of separable states and the resulting complexity of its boundary. Although the set $\mathcal{D}_{\text{sep}}$ is convex, the form of its boundary is still unknown for Hilbert space dimension greater than 2×3 [108], [109], which makes the minimization (1.12) much more costly than common convex optimization problems. For pure states $\rho \equiv |\Psi\rangle\langle\Psi|$, however, (1.12) simplifies to the closed expression for pure state entanglement [4]

$$E(|\Psi\rangle\langle\Psi|) = S(\rho_A) = S(\rho_B). \tag{1.13}$$

As a consistency check, we recall that the spectra (and hence the von Neumann entropy) of the reduced states ρ_A and ρ_B are indeed identical, as it is guaranteed by the Schmidt decomposition [110] of $|\Psi\rangle$.

1.1.3 Quantum vs classical correlation

Entanglement is certainly a key concept of quantum physics [25], [30], [111] and its broad significance as a resource for realizing quantum information processing tasks is well established [12], [14], [112], [113]. Yet, there also exist quantum correlations *beyond* entanglement. In order to explain this crucial aspect of our work, and in analogy to the definition of total correlation and entanglement, we first characterize the family of states with zero quantum correlation [8], [81], [82] (illustrated as pink region in Figure 1.1):

$$\mathcal{D}_{\text{cl}} \equiv \Big\{ \chi = \sum_{i,j} p_{ij} |i\rangle\langle i| \otimes |j\rangle\langle j| \Big\}. \tag{1.14}$$

On the right-hand side, $\{|i\rangle\}$ and $\{|j\rangle\}$ could be *any* sets of orthonormal states in the Hilbert spaces of subsystems A and B, respectively, and $p_{ij} > 0$, $\sum_{ij} p_{ij} = 1$. The states in (1.14) are indeed *classical* in the following sense. There exists a joint local measurement $\{P_A^{(i)} \otimes P_B^{(j)}\}$ which leaves the state ρ unchanged, namely the measurement defined by the projectors $P_{A/B}^{(i)}$ projecting onto the local bases $\{|i\rangle\}$ and $\{|j\rangle\}$ of ρ. Therefore, the correlation encoded in the resulting joint probability distribution $\{p_{ij}\}$ has to be purely classical [82]. Any state not in $\mathcal{D}_{\text{cl}}$ then contains quantum correlation.

By referring again to the geometric picture of quantum states, the quantum correlation in ρ is quantified as its minimized quantum relative entropy with respect to the set of

classically correlated states [8] (with the minimizer denoted by χ_ρ),

$$Q(\rho) \equiv \min_{\chi \in \mathcal{D}_{\text{cl}}} S(\rho||\chi) \equiv S(\rho||\chi_\rho). \tag{1.15}$$

Note that $\mathcal{D}_0 \subseteq \mathcal{D}_{\text{cl}}$ since every uncorrelated state

$$\rho_A \otimes \rho_B \equiv \left(\sum_i p_A^{(i)} |i\rangle\langle i| \right) \otimes \left(\sum_j p_B^{(j)} |j\rangle\langle j| \right) \tag{1.16}$$

can be written as in (1.14), namely with $p_{ij} = p_A^{(i)} p_B^{(j)}$. On the other hand, the set $\mathcal{D}_{\text{sep}}$ in (1.11) is strictly larger than $\mathcal{D}_{\text{cl}}$. This is due to the fact that in the former (1.11), $\{\sigma_{A/B}^i\}$ are not necessarily simultaneously diagonalizable for all i. Comparing (1.10), (1.12) and (1.15) we then get the following instructive inclusion relations

$$\mathcal{D}_0 \subset \mathcal{D}_{\text{cl}} \subset \mathcal{D}_{\text{sep}}. \tag{1.17}$$

Thanks to the underlying geometric picture — which provides a unified basis for quantifying the different correlation types — this can directly be translated into relations between the respective measures

$$I(\rho) \geq Q(\rho) \geq E(\rho). \tag{1.18}$$

Finally, we present the classical counterpart of (1.15), the classical correlation. To motivate its measure we first rewrite (1.15) as [82]

$$Q(\rho) = \min_{\{P_A^{(i)}\},\{P_B^{(j)}\}} S\left(\rho \middle\| \sum_{ij} P_A^{(i)} \otimes P_B^{(j)} \rho P_A^{(i)} \otimes P_B^{(j)} \right) \tag{1.19}$$

where $\{P_A^{(i)}\}$ and $\{P_B^{(j)}\}$ are two projective measurements consisting of rank-1 projectors, satisfying $\sum_i P_{A/B}^{(i)} = \mathbb{1}_{A/B}$. The closest classical state χ_ρ is then the state resulting from ρ after the optimal projective measurements has been performed. Accordingly, the total correlation in χ_ρ is then nothing else than the classical correlation in ρ [8]

$$C(\rho) \equiv I(\chi_\rho). \tag{1.20}$$

Since quantum states cannot be dissected into classical and quantum parts in a strict mathematical sense, it is not surprising that our measures do typically not obey the relation $I = Q + C$. However, this exact additive relation is valid whenever the closest classical state χ_ρ and the closest uncorrelated state π_ρ have the same eigenstates. For a proof of this statement see Appendix A.

The set of classically correlated states (1.14) has a complicated and highly non-convex structure, which makes an optimization over it a formidable task. Fortunately, Ref. [8] provides a suitable theorem that connects the spectrum of the closest classical state χ_ρ to

Algorithm 1: Calculating Quantum Correlation

INPUT: bipartite quantum state ρ
OUTPUT: $Q(\rho)$ and the closest classical state χ_ρ to ρ
COMPUTATION:
SET initial local bases $\{|i^{(0)}\rangle_A\}$ and $\{|j^{(0)}\rangle_B\}$;
SET $n = 0$ and $U_A^{(0)} = U_B^{(0)} = \mathbb{1}$;
COMPUTE $\chi_\rho^{(0)} = \sum_{ij} |i^{(0)}\rangle\langle i^{(0)}| \otimes |j^{(0)}\rangle\langle j^{(0)}| \rho |i^{(0)}\rangle\langle i^{(0)}| \otimes |j^{(0)}\rangle\langle j^{(0)}|$;
COMPUTE $Q(\rho)^{(0)} = S(\rho||\chi_\rho^{(0)})$;
WHILE $n < N_{\text{step}}$ **DO**:
  SAMPLE random unitary matrices $V_{A,B}$;
  COMPUTE $V_{A,B} \leftarrow V_{A,B}^{\frac{1}{M}}$;
  UPDATE $U_{A,B}^{(n+1)} \leftarrow V_{A,B} U_{A,B}^{(n)}$;
  COMPUTE new local bases
    $U_A^{(n+1)}|i^{(n)}\rangle \mapsto |i^{(n+1)}\rangle$, $U_B^{(n+1)}|j^{(n)}\rangle \mapsto |j^{(n+1)}\rangle$
  COMPUTE new classical state
    $\chi_\rho^{(n+1)} = \sum_{ij} |i\rangle\langle i| \otimes |j\rangle\langle j| \rho |i\rangle\langle i| \otimes |j\rangle\langle j|$;
  COMPUTE $Q^{(n+1)} = S(\rho||\chi^{(n+1)})$;
  IF $Q^{(n+1)} < Q^{(n)}$:
    UPDATE $Q(\rho) \leftarrow Q^{(n)}(\rho)$;
    UPDATE $\chi_\rho \leftarrow \chi_\rho^{(n)}$;
    UPDATE $n \leftarrow n + 1$;
END

the diagonal entries of ρ in the eigenbasis of χ_ρ. More precisely, if $\chi_\rho = \sum_{ij} \lambda_{ij} |i\rangle\langle i| \otimes |j\rangle\langle j|$ is the closest classical state to ρ, then its spectrum is given by

$$\lambda_{ij} = \langle i| \otimes \langle j| \, \rho \, |i\rangle \otimes |j\rangle. \tag{1.21}$$

In other words, the closest classical state to ρ is of the form

$$\chi_\rho = \sum_{ij} \left(|i\rangle\langle i| \otimes |j\rangle\langle j| \right) \rho \left(|i\rangle\langle i| \otimes |j\rangle\langle j| \right). \tag{1.22}$$

This finding represents the starting point for our quest to search for the optimal local bases $\{|i\rangle\}$ and $\{|j\rangle\}$ of two subsystems A and B, respectively, recovering the minimizer of (1.15). Given that any two bases can be connected by a unique unitary operator $U|i\rangle \mapsto |i'\rangle$, provided that we fix the local computational bases, this search is then equivalent to finding the optimal unitary operators U_A and U_B for the respective subsystems. In the following we present a random walk algorithm assisted by probabilistic rejection, in search for the optimal local unitary operators U_A and U_B within the manifolds of local unitaries $\mathcal{U}_A$ and $\mathcal{U}_B$, respectively.

The computational scheme outlined in Algorithm 1 consists of the following steps: One first initializes a pair of local bases sets $\{|i^{(0)}\rangle\}$ and $\{|j^{(0)}\rangle\}$ for the two subsystems as well as the two local unitary operators as $U_{A,B}^{(0)} = \mathbb{1}$. The initial bases determine a candidate for the closest classical state $\chi_\rho^{(0)}$ according to (1.22) and the distance $Q^{(0)} = S(\rho||\chi_\rho^{(0)})$. The unitary operators live on the connected manifolds $\mathcal{U}_{A,B} \ni U_{A,B}$ which allows us to make use of a random walk algorithm to find the optimal set of unitary operators. We start by performing a small step in $\mathcal{U}_{A,B}$ by multiplying $U_{A,B}^{(0)}$ with a "small" unitary operator $V_{A,B}$ close to the identity, arriving at $U_{A,B}^{(1)}$, which, in turn, determines a pair of local bases $U_A^{(1)}|i^{(0)}\rangle \equiv |i^{(1)}\rangle$, $U_B^{(1)}|j^{(0)}\rangle \equiv |j^{(1)}\rangle$. If these new bases define a closer classical state according to (1.22), then this step is accepted, and otherwise rejected. This procedure is repeated until (i) a desired accuracy or (ii) a predefined number of steps is reached. To compensate for the stochastic nature of Algorithm 1, 10 initial local bases sets are chosen and the closest resulting classical state is taken as the optimal one. As a default in the subsequent chapters, the step size parameter M is chosen to be 10^3, and the number of steps $N_{\text{step}} = 10^4$.

1.2 Particle vs orbital correlation for fermions

In this section, we will discuss how the previously defined quantum information concepts are adapted to systems of fermions. For this, we need to establish first a notion of subsystems. As pointed out before, a proper notion of subsystems requires a tensor product structure in both the Hilbert space and the algebra of observables. To this end, we will consider two routes, namely regarding particles as subsystems, and regarding orbitals as subsystems. Both routes have their own practical merits as well as theoretical caveats, and should not be considered as competing perspectives of fermionic correlation, but rather complementing.

To set the stage, we consider a system of N fermions, each residing in a D-dimensional single-particle Hilbert space $\mathcal{H}^{(1)}$. To represent $\mathcal{H}^{(1)}$ we can choose a basis of single-particle wavefunctions (spin-orbitals) $\{\phi_i\}_{i=1}^D$. Note that i can be a compound index consisting of both spatial and spin indices, for spinful fermions. $f_{\phi_i}^{(\dagger)}$ denotes the annihilation (creation) operator associated to the spin-orbital ϕ_i. They satisfy the fermionic anti-commutation relations

$$\{f_{\phi_i}^{(\dagger)}, f_{\phi_j}^{(\dagger)}\} = 0, \quad \{f_{\phi_i}^\dagger, f_{\phi_j}\} = \delta_{i,j}\mathbb{1}, \tag{1.23}$$

with $\{A, B\} \equiv AB + BA$.

1.2.1 Particles as subsystems

Fermions themselves as indistinguishable particles can not be considered in the conventional sense subsystems. The antisymmetry of the fermionic wavefunction fundamentally forbids any product state with respect to the partition of particles, since they do not acquire a minus sign upon the exchange of any two particles:

$$\begin{aligned} &|\phi_1\rangle_1 \otimes \cdots |\phi_i\rangle_i \otimes \cdots |\phi_j\rangle_j \otimes \cdots \otimes |\phi_N\rangle_N \\ \neq &-|\phi_1\rangle_1 \otimes \cdots |\phi_j\rangle_i \otimes \cdots |\phi_i\rangle_j \otimes \cdots \otimes |\phi_N\rangle_N, \end{aligned} \tag{1.24}$$

where $|\phi_i\rangle_j$ denotes the single particle state where particle j is occupying the orbital (mode) ϕ_i. The building block of N-fermion states are instead fully-antisymmetrized Slater determinants

$$\begin{aligned} &\mathcal{A}(|\phi_1\rangle_1 \otimes \cdots |\phi_i\rangle_i \otimes \cdots |\phi_j\rangle_j \otimes \cdots \otimes |\phi_N\rangle_N) \\ \equiv &\sum_{\pi \in P_N} \mathrm{sign}(\pi) |\phi_{\pi(1)}\rangle_1 \otimes \cdots |\phi_{\pi(1)}\rangle_i \otimes \cdots |\phi_{\pi(j)}\rangle_j \otimes \cdots \otimes |\phi_{\pi(N)}\rangle_N \end{aligned} \tag{1.25}$$

where $\mathcal{A}$ is the antisymmetrization operator, the permutation π is an element of the N-order permutation group P_N, and $\mathrm{sign}(\pi) = 1$ ($\mathrm{sign}(\pi) = -1$) for even (odd) permutation. Although (1.25) formally looks "entangled", this entanglement is merely due to the artificial labelling that we put on the fermions. In fact, Slater determinants are ground states of systems of N non-interacting fermions, and should be considered as part of the uncorrelated states. Then what should be the proper definition of fermionic paricle correlation?

Recall that a two-qubit state is correlated if and only if there exists information on the two-qubit level which is inaccessible by single-qubit measurements. Such inaccessibility is signified by a pair of observables $\hat{O}_A$ and $\hat{O}_B$ on the two qubits A and B, whose joint measurement expectation can not be factorized

$$\mathcal{C}(\hat{O}_A, \hat{O}_B) = \langle \hat{O}_A \otimes \hat{O}_B \rangle - \langle \hat{O}_A \rangle \langle \hat{O}_B \rangle \neq 0. \tag{1.26}$$

According to (1.10), it necessarily implies that the total correlation between the two qubits measured by the mutual information is non-zero. For systems of two fermions, the analogous "local" and "global" observables are instead the single-particle and two-particle operators, which are monomials of $f_i^\dagger f_j$ and $f_i^\dagger f_j^\dagger f_l f_k$, respectively. By analogy, a two-fermion state should be considered correlated only when not all two-particle measurement outcomes can be inferred from single particle measurements. Fermionic states for which the expectation values of all N-particle observables can be decomposed into single-particle components are said to obey the Wick's Theorem, and they are called the *free* states. Formally, the set of free states defined on a collection of D orbitals is the closure of the set of thermal states of all possible non-interacting (single-particle) Hamiltonians

$$\mathcal{D}_{\text{free}} = \overline{\left\{ \frac{e^{-\hat{h}}}{\mathrm{Tr}[e^{-\hat{h}}]} \;\middle|\; \hat{h} = \sum_{i,j=1}^{D} h_{ij} f_i^\dagger f_j \right\}}, \tag{1.27}$$

where h_{ij}'s are elements of a Hermitian matrix $\mathbf{h}$. In general, free states are mixed, and can be convex combinations of states of different particle numbers. Therefore, $\mathcal{D}_{\text{free}}$ is no longer part of the N-fermion Hilbert space. The closure makes sure that N-particle Slater determinants are also included in the set. They are realized by Hamiltonians $\hat{h}$ with the highest N eigenvalues set at infinity.

At first sight it seems rather difficult to tell if a general fermionic state ρ belongs to $\mathcal{D}_{\text{free}}$. Even when given a pure state, one in principle should check whether it admits the form of a single Slater determinant in all possible orbital/mode basis. However, such an exhaustive check is not necessary. The set $\mathcal{D}_{\text{free}}$ is in fact invariant under orbital/mode basis transformation, which hints the possibility of checking the freeness of a general state by the property of a basis-independent object. This object turns out to be the spectrum of the one-particle reduced density matrix (1RDM) γ

$$\gamma_{ij} = \mathrm{Tr}[\rho f_i^\dagger f_j]. \tag{1.28}$$

The elements of the 1RDM can be evaluated in any basis associated with $\{f_i^\dagger\}$, and the spectrum would remain the same. The eigenbasis of γ is commonly referred to as the natural orbitals, and the eigenvalues are called the natural occupations. The diagonal elements of the 1RDM in any basis are constraint to be between 0 and 1, by Pauli's exclusion principle. If $|\Psi\rangle$ is a single Slater determinant, then it takes the form $|\Psi\rangle = c_1^\dagger c_2^\dagger \cdots c_N^\dagger |\Omega\rangle$ in some orbital basis with the associated creation operators $c_i^\dagger$. Then in this basis, the 1RDM is diagonal, with $\gamma_{ij} = \mathrm{Tr}[\rho c_i^\dagger c_j] = n_i \delta_{ij}$ where n_i is the occupation number of the i-th natural orbital, which is either 1 or 0. Matrices with eigenvalues 1's and 0's are called idempotent matrices, as they satisfy

$$\gamma^2 = \gamma. \tag{1.29}$$

Therefore, to check whether a pure state $|\Psi\rangle$ is a single Slater determinant, it suffices to calculate the 1RDM γ in any feasible orbital basis, and then check the eigenvalues of γ. If the eigenvalues are all 1's and 0's, then $|\Psi\rangle$ must be a single Slater determinant. Equivalently, one can check if the von Neumann entropy of the 1RDM $S(\gamma)$ vanishes.

For mixed states, we again need to inspect the spectral property of the corresponding 1RDM to decide whether it belongs to the set $\mathcal{D}_{\text{free}}$ of free states. A nice property of the free states $\rho \propto e^{-\hat{h}}$, as pointed out by Peschel [114], is that $\mathbf{h}$ and the 1RDM γ of ρ are diagonalized by the same orbital basis. To see this, we re-express ρ by inserting the

eigenbasis of $\mathbf{h}$ (with corresponding creation operators $f_i^\dagger$)

$$\begin{aligned}\rho &= \frac{1}{Z} e^{-\sum_{i=1}^{D} \eta_i f_i^\dagger f_i} \\ &= \frac{1}{Z} \bigotimes_{i=1}^{D} (|0\rangle_i\langle 0|_i + e^{-\eta_i} |1\rangle_l\langle 1|_i) \\ &= \bigotimes_{i=1}^{D} \frac{|0\rangle_i\langle 0|_i + e^{-\eta_l} |1\rangle_i\langle 1|_i}{1+e^{-\eta_i}} \\ &\equiv \bigotimes_{i=1}^{D} \rho_i.\end{aligned} \tag{1.30}$$

In other words, in the eigenbasis of $\hat{h}$, ρ is a product state consisting of local density matrices ρ_i. Then by the property of the von Neumann entropy, $S(\rho)$ is decomposed into the following sum

$$S(\rho) = S\left(\bigotimes_i \rho_i\right) = \sum_i S(\rho_i). \tag{1.31}$$

The natural orbital reduced states ρ_i's are diagonal, and their eigenvalues are given by

$$\mathrm{spec}(\rho_i) = \left\{ \frac{1}{1+e^{-\eta_i}}, \frac{e^{-\eta_i}}{1+e^{-\eta_i}} \right\}. \tag{1.32}$$

Now we compute the 1RDM in the diagonal basis of $\hat{h}$. This can be done element-wise as

$$\gamma_{ij} = \langle \Psi | f_i^\dagger f_j | \Psi \rangle = \mathrm{Tr}[\rho f_i^\dagger f_j] = \mathrm{Tr}[(\rho_i \otimes \rho_j) f_i^\dagger f_j] = \delta_{ij} \frac{e^{-\eta_i}}{1+e^{-\eta_i}} \equiv \delta_{ij} \lambda_i. \tag{1.33}$$

Inserting the natural occupations λ_i into the spectrum of ρ_i we find that it becomes

$$\mathrm{spec}(\rho_i) = \{\lambda_i, 1-\lambda_i\}. \tag{1.34}$$

Therefore the entropy of the total state ρ and the entropy of the one-particle (hole) RDM γ ($\mathbb{1} - \gamma$) are succinctly related as

$$\begin{aligned}S(\rho) &= \sum_i S(\rho_i) = \sum_i [-\lambda_i \log(\lambda_i) - (1-\lambda_i)\log(\lambda_i)] \\ &= \sum_i [-\lambda_i \log(\lambda_i)] + \sum_i [-(1-\lambda_i)\log(\lambda_i)] \\ &= S(\gamma) + S(\mathbb{1} - \gamma)\end{aligned} \tag{1.35}$$

One can check that for a single Slater determinant ρ, both the left and right-hand side vanishes. Therefore, (1.35) is the exact criterion for checking whether a general fermionic

state ρ is free. Any state violating the above criterion is considered to possess particle correlation, with respect to which not all the many-body information can be recovered from the single-particle level.

The form of the criterion (1.35) suggests that one can propose the following quantity as a measure for any deviation from the set of free states

$$\mathcal{N}(\rho) = S(\gamma) + S(\mathbb{1} - \gamma) - S(\rho). \tag{1.36}$$

This measure enjoy many appealing properties. First, it vanishes if and only if ρ is free. Indeed, $\mathcal{N}(\rho)$ is a non-negative number for any state ρ, and is refered to as the *nonfreeness* of the state ρ. Second, it is determined only by the spectrum of ρ and γ, and not the single-particle basis one chooses to represent the system in. $\mathcal{N}(\rho)$ is thus explicitly invariant under arbitrary orbital rotations. Third, and perhaps most remarkably, $\mathcal{N}(\rho)$ can be understood in a similar geometric picture as the bipartite total correlation: It is the minimum distance from the state ρ to the set of free states $\mathcal{D}_{\text{free}}$ measured by the quantum relative entropy [115], [116]

$$\mathcal{N}(\rho) = \min_{\sigma \in \mathcal{D}_{\text{free}}} S(\rho \| \sigma). \tag{1.37}$$

1.2.2 Orbitals as subsystems

Recovering a tensor product structure

In contrast to fermions, orbitals which the fermions occupy are in fact distinguishable. But to define the tensor product structure with respect to orbital partitions, we have to again lift the fully-antisymmetrized N-fermion Hilbert space to the total Fock space

$$\mathcal{F}(\mathcal{H}^{(1)}) = \bigoplus_{n=0}^{D} \mathcal{H}^{(n)}, \quad \mathcal{H}^{(n)} = \wedge^n \mathcal{H}^{(1)}. \tag{1.38}$$

The corresponding Fock space $\mathcal{F}[\mathcal{H}^{(1)}]$ is then spanned by the configuration states in a given single particle basis $\{\phi_i\}_{i=1}^D$

$$|n_{1\uparrow}, n_{1\downarrow}, \ldots, n_{D\downarrow}\rangle \equiv \prod_{i=1}^{D} \left(f_{\phi_i}^\dagger\right)^{n_i} |0\rangle \,. \tag{1.39}$$

Here, $|0\rangle$ is the vacuum state. With respect to the ordered basis $\{\phi_i\}_{i=1}^D$, we now establish the notion of subsystems. When considering the partitioning of orbitals $\{\phi_i\}_{i=1}^D$ into two subsets A and B, $\mathcal{H}^{(1)}$ is effectively divided into two complementary subspaces

of dimensions $D_{A/B}$, $\mathcal{H}^{(1)} = \mathcal{H}_A^{(1)} \oplus \mathcal{H}_B^{(1)}$. This splitting in turn induces a tensor-product decomposition on the Fock space,

$$\mathcal{F}[\mathcal{H}_A^{(1)} \oplus \mathcal{H}_B^{(1)}] \cong \mathcal{F}[\mathcal{H}_A^{(1)}] \otimes \mathcal{F}[\mathcal{H}_B^{(1)}], \tag{1.40}$$

through the map

$$\begin{aligned} &|n_{1\uparrow}, n_{1\downarrow}, \ldots, n_{D_A\downarrow}, n_{D_{A+1}\uparrow}, \ldots, n_{D\downarrow}\rangle \mapsto \\ &\quad |n_{1\uparrow}, n_{1\downarrow}, \ldots, n_{D_A\downarrow}\rangle \otimes |n_{D_{A+1}\uparrow}, , \ldots, n_{D\downarrow}\rangle. \end{aligned} \tag{1.41}$$

In fact, the corresponding tensor product structure can be generalized to arbitrary partitioning of the orbitals, including multipartite scenarios. In this thesis, we focus mainly on the partitioning of the spatial orbitals. That is, for spinful fermions, the smallest subsystem we consider is the composite Fock space generated by the two spin-orbitals $\phi_{i\uparrow}$ and $\phi_{i\downarrow}$.

Finally, we introduce the primary objects of interest, namely the one- and two-*orbital* reduced density matrices (RDMs). Formally, the one- and two-orbital RDMs of a pure state $|\Psi\rangle$ are defined via the following requirements

$$\rho_i : \mathrm{Tr}[\rho_i \hat{\mathcal{O}}] = \langle \Psi | \hat{\mathcal{O}} | \Psi \rangle, \quad \forall \hat{\mathcal{O}} \in \mathcal{A}_i \tag{1.42a}$$

$$\rho_{ij} : \mathrm{Tr}[\rho_{ij} \hat{O}] = \langle \Psi | \hat{\mathcal{O}} | \Psi \rangle, \quad \forall \hat{\mathcal{O}} \in \mathcal{A}_{ij}. \tag{1.42b}$$

In practice, they are computed from partial two- and four-*particle* RDMs [117], respectively. Exploiting the symmetry of the overall quantum state reduces further the computational cost [62]. For example, it is common to restrict the calculation of the molecular ground state to a predefined, fixed particle number N and spin magnetization m_S (for a given spin state $2S+1$). Consequently, the one- and two-orbital RDM can only be mixtures of fixed electron-number and magnetization states. In other words, the one-orbital RDM is diagonal in the fixed particle number and magnetization basis

$$\rho_i = \begin{pmatrix} \langle \mathbb{1} - \hat{n}_{i\uparrow} - \hat{n}_{i\downarrow} + \hat{n}_{i\uparrow}\hat{n}_{i\downarrow} \rangle & 0 & 0 & 0 \\ 0 & \langle \hat{n}_{i\uparrow} - \hat{n}_{i\uparrow}\hat{n}_{i\downarrow} \rangle & 0 & 0 \\ 0 & 0 & \langle \hat{n}_{i\downarrow} - \hat{n}_{i\uparrow}\hat{n}_{i\downarrow} \rangle & 0 \\ 0 & 0 & 0 & \langle \hat{n}_{i\uparrow}\hat{n}_{i\downarrow} \rangle \end{pmatrix}. \tag{1.43}$$

And the two-orbital RDM $\rho_{ij} = \mathrm{Tr}_{\setminus\{i,j\}}[|\Psi\rangle\langle\Psi|]$ is block diagonal in the tensor product basis [62], labelled by also the total particle number $N = N_i + N_j$ and magnetization $S^z = S_i^z + S_j^z$. We list below the non-zero matrix elements (omitting terms related by Hermiticity)

- $N = 0, S^z = 0$:

$$\langle 0,0|\rho_{ij}|0,0\rangle = \langle (\mathbb{1} - \hat{n}_{i\uparrow})(\mathbb{1} - \hat{n}_{i\downarrow})(\mathbb{1} - \hat{n}_{j\uparrow})(\mathbb{1} - \hat{n}_{j\downarrow}) \rangle \tag{1.44}$$

- $N = 1, S^z = 1/2$:

$$\begin{aligned}
\langle\uparrow, 0|\rho_{ij}|\uparrow, 0\rangle &= \langle\hat{n}_{i\uparrow}(\mathbb{1} - \hat{n}_{i\downarrow})(\mathbb{1} - \hat{n}_{j\uparrow})(\mathbb{1} - \hat{n}_{j\downarrow})\rangle, \\
\langle 0, \uparrow|\rho_{ij}|0, \uparrow\rangle &= \langle(\mathbb{1} - \hat{n}_{i\uparrow})(\mathbb{1} - \hat{n}_{i\downarrow})\hat{n}_{j\uparrow}(\mathbb{1} - \hat{n}_{j\downarrow})\rangle, \\
\langle\uparrow, 0|\rho_{ij}|0, \uparrow\rangle &= \langle f^\dagger_{i\uparrow} f_{j\uparrow}(\mathbb{1} - \hat{n}_{i\downarrow})(\mathbb{1} - \hat{n}_{j\downarrow})\rangle,
\end{aligned} \tag{1.45}$$

- $N = 1, S^z = -1/2$:

$$\begin{aligned}
\langle\downarrow, 0|\rho_{ij}|\downarrow, 0\rangle &= \langle(\mathbb{1} - \hat{n}_{i\uparrow})\hat{n}_{i\downarrow}(\mathbb{1} - \hat{n}_{j\uparrow})(\mathbb{1} - \hat{n}_{j\downarrow})\rangle, \\
\langle 0, \downarrow|\rho_{ij}|0, \downarrow\rangle &= \langle(\mathbb{1} - \hat{n}_{i\uparrow})(1 - \hat{n}_{i\downarrow})(\mathbb{1} - \hat{n}_{j\uparrow})\hat{n}_{j\downarrow}\rangle, \\
\langle\downarrow, 0|\rho_{ij}|0, \downarrow\rangle &= \langle f^\dagger_{i\downarrow} f_{j\downarrow}(\mathbb{1} - \hat{n}_{i\uparrow})(\mathbb{1} - \hat{n}_{j\uparrow})\rangle,
\end{aligned} \tag{1.46}$$

- $N = 2, S^z = 1$:

$$\langle\uparrow, \uparrow|\rho_{ij}|\uparrow, \uparrow\rangle = \langle\hat{n}_{i\uparrow}(\mathbb{1} - \hat{n}_{i\downarrow})\hat{n}_{j\uparrow}(\mathbb{1} - \hat{n}_{j\downarrow})\rangle, \tag{1.47}$$

- $N = 2, S^z = -1$:

$$\langle\uparrow, \uparrow|\rho_{ij}|\uparrow, \uparrow\rangle = \langle(\mathbb{1} - \hat{n}_{i\uparrow})\hat{n}_{i\downarrow}(\mathbb{1} - \hat{n}_{j\uparrow})\hat{n}_{j\downarrow}\rangle, \tag{1.48}$$

- $N = 2, S^z = 0$:

$$\begin{aligned}
\langle 0, \uparrow\downarrow|\rho_{ij}|0, \uparrow\downarrow\rangle &= \langle(\mathbb{1} - \hat{n}_{i\uparrow})(\mathbb{1} - \hat{n}_{i\downarrow})\hat{n}_{j\uparrow}\hat{n}_{j\downarrow}\rangle \\
\langle\uparrow\downarrow, 0|\rho_{ij}|\uparrow\downarrow, 0\rangle &= \langle\hat{n}_{i\uparrow}\hat{n}_{i\downarrow}(\mathbb{1} - \hat{n}_{j\uparrow})(\mathbb{1} - \hat{n}_{j\downarrow})\rangle \\
\langle\uparrow, \downarrow|\rho_{ij}|\uparrow, \downarrow\rangle &= \langle\hat{n}_{i\uparrow}(\mathbb{1} - \hat{n}_{i\downarrow})(\mathbb{1} - \hat{n}_{j\uparrow})\hat{n}_{j\downarrow}\rangle \\
\langle\downarrow, \uparrow|\rho_{ij}|\downarrow, \uparrow\rangle &= \langle(\mathbb{1} - \hat{n}_{i\uparrow})\hat{n}_{i\downarrow}\hat{n}_{j\uparrow}(\mathbb{1} - \hat{n}_{j\downarrow})\rangle \\
\langle 0, \uparrow\downarrow|\rho_{ij}|\uparrow\downarrow, 0\rangle &= \langle f^\dagger_{j\uparrow} f^\dagger_{j\downarrow} f_{i\downarrow} f_{i\uparrow}\rangle, \\
\langle 0, \uparrow\downarrow|\rho_{ij}|\uparrow, \downarrow\rangle &= \langle f^\dagger_{j\uparrow} f_{i\uparrow}(\mathbb{1} - \hat{n}_{i\downarrow})\hat{n}_{j\downarrow}\rangle, \\
\langle 0, \uparrow\downarrow|\rho_{ij}|\downarrow, \uparrow\rangle &= \langle f_{i\downarrow} f^\dagger_{j\downarrow}(\mathbb{1} - \hat{n}_{i\uparrow})\hat{n}_{j\uparrow}\rangle, \\
\langle\uparrow\downarrow, 0|\rho_{ij}|\uparrow, \downarrow\rangle &= f^\dagger_{j\downarrow} f_{i\downarrow}\hat{n}_{i\uparrow}(\mathbb{1} - \hat{n}_{j\uparrow}), \\
\langle\uparrow\downarrow, 0|\rho_{ij}|\downarrow, \uparrow\rangle &= f_{i\uparrow} f^\dagger_{j\uparrow}\hat{n}_{i\downarrow}(\mathbb{1} - \hat{n}_{j\downarrow}), \\
\langle\uparrow, \downarrow|\rho_{ij}|\downarrow, \uparrow\rangle &= \langle f^\dagger_{j\downarrow} f^\dagger_{i\uparrow} f_{j\uparrow} f_{i\downarrow}\rangle,
\end{aligned} \tag{1.49}$$

- $N = 3, S^z = 1/2$:

$$\begin{aligned}
\langle\uparrow, \uparrow\downarrow|\rho_{ij}|\uparrow, \uparrow\downarrow\rangle &= \langle\hat{n}_{i\uparrow}(\mathbb{1} - \hat{n}_{i\downarrow})\hat{n}_{j\uparrow}\hat{n}_{j\downarrow}\rangle, \\
\langle\uparrow\downarrow, \uparrow|\rho_{ij}|\uparrow\downarrow, \uparrow\rangle &= \langle\hat{n}_{i\uparrow}\hat{n}_{i\downarrow}\hat{n}_{j\uparrow}(\mathbb{1} - \hat{n}_{j\downarrow})\rangle, \\
\langle\uparrow, \uparrow\downarrow|\rho_{ij}|\uparrow\downarrow, \uparrow\rangle &= f_{i\downarrow} f^\dagger_{j\downarrow}\hat{n}_{i\uparrow}\hat{n}_{j\uparrow},
\end{aligned} \tag{1.50}$$

- $N = 3, S^z = -1/2$:

$$\begin{aligned}\langle\downarrow,\uparrow\downarrow|\rho_{ij}|\downarrow,\uparrow\downarrow\rangle &= \langle(\mathbb{1}-\hat{n}_{i\uparrow})\hat{n}_{i\downarrow}\hat{n}_{j\downarrow}\hat{n}_{j\uparrow}\rangle,\\ \langle\uparrow\downarrow,\downarrow|\rho_{ij}|\uparrow\downarrow,\downarrow\rangle &= \langle\hat{n}_{i\uparrow}\hat{n}_{i\downarrow}(\mathbb{1}-\hat{n}_{j\uparrow})\rangle\hat{n}_{j\downarrow},\\ \langle\downarrow,\uparrow\downarrow|\rho_{ij}|\uparrow\downarrow,\downarrow\rangle &= f_{i\uparrow}f^{\dagger}_{j\uparrow}\hat{n}_{i\downarrow}\hat{n}_{j\downarrow},\end{aligned} \tag{1.51}$$

- $N = 4, S^z = 0$:

$$\langle\uparrow\downarrow,\uparrow\downarrow|\rho_{ij}|\uparrow\downarrow,\uparrow\downarrow\rangle = \langle\hat{n}_{i\uparrow}\hat{n}_{i\downarrow}\hat{n}_{j\uparrow}\hat{n}_{j\downarrow}\rangle. \tag{1.52}$$

Superselection rules

With the tensor product structure of the total Fock space recovered, it would seem that we are already back to the setting of distinguishable subsystems in Section 1.1. It is important to note, however, that such a tensor-product decomposition does not hold on the level of fermionic operators that are defined within the respective subsystems. This is clear from the observation that the creation and annihilation operators associated with spin-orbitals in subsystem A and B do not commute with each other, and, as a result, cannot be considered local observable operators. The immediate consequences is the violation of special relativity, exemplified by the possibility of superluminal signaling [118], [119]. We resolve this by invoking the fermionic parity superselection rule [120], [121] (P-SSR). The P-SSR excludes observables that do not commute with the local particle number parity operator $\hat{\Pi}^{(A/B)} = \hat{P}^{(A/B)}_{\text{even}} - \hat{P}^{(A/B)}_{\text{odd}}$, where $\hat{P}^{A/B}_{\tau}$ is the projection onto the $\tau \in \{\text{even,odd}\}$ parity subspace acting on subsystem A/B. As a result, the accessible correlation and entanglement in a bipartite state ρ_{AB} is reduced to those in the superselected state formed by the projection $\mathcal{G}_{\Pi_{A/B}}$ onto the local subspaces compatible with P-SSR [91], [119]

$$\rho^{\text{P}}_{AB} \equiv \mathcal{G}_{\Pi_A} \otimes \mathcal{G}_{\Pi_B}[\rho_{AB}] = \sum_{\tau,\tau'=\text{even, odd}} \hat{P}^{(A)}_{\tau} \otimes \hat{P}^{(B)}_{\tau'} \rho_{AB} \hat{P}^{(A)}_{\tau} \otimes \hat{P}^{(B)}_{\tau'}, \tag{1.53}$$

since, from an operational point of view, ρ_{AB} and ρ^{P}_{AB} are equivalent. To summarize, the correlation quantities $X = I, C, Q, E$ defined in Section 1.1 under P-SSR can be calculated as

$$X^{\text{P}}(\rho_{AB}) = X(\rho^{\text{P}}_{AB}). \tag{1.54}$$

When the creation or annihilation of *pairs* of particles is also not possible, this results in an even more restrictive particle number superselection rules [120], [122] (N-SSR). In this case we simply replace ρ^{P}_{AB} in (1.54) with the N-SSR superselected state

$$\rho^{\text{N}}_{AB} = \sum_{m=0}^{2D_A}\sum_{n=0}^{2D_B} \hat{P}^{(A)}_{m} \otimes \hat{P}^{(B)}_{n} \rho_{AB} \hat{P}^{(A)}_{m} \otimes \hat{P}^{(B)}_{n}, \tag{1.55}$$

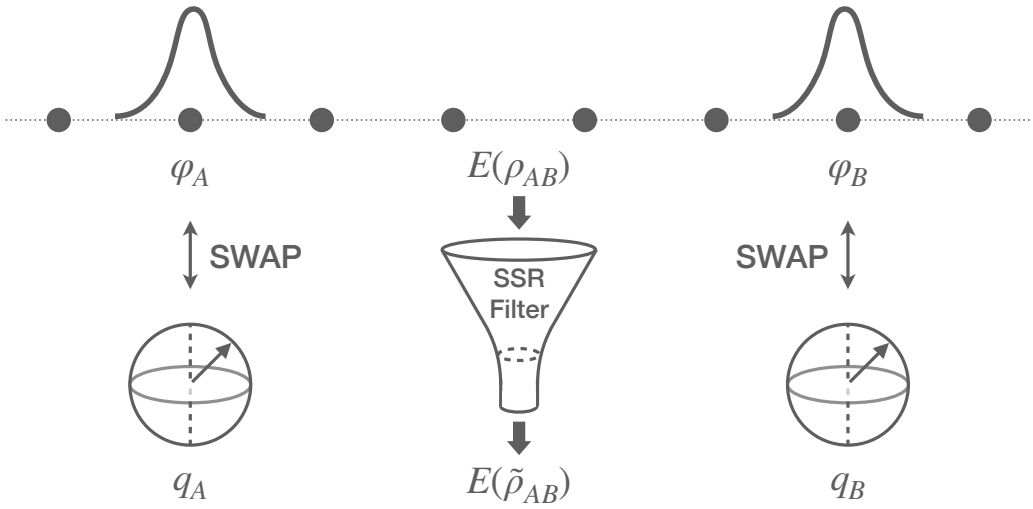

Figure 1.2: Entanglement swapping protocol under SSR between the two electronic orbitals φ_A and φ_B, and the two qubit registers q_A and q_B. See text for more details.

where $\hat{P}_m^{(A/B)}$ is the projection onto the m-particle subspace acting on subsystem A/B.

We remark that if one is only interested in the numerical structure of the quantum state, it is possible to quantify correlation and entanglement without superselection rules, simply by mapping the fermionic state to that of a spin system via the respective Jordan-Wigner transformation. By contrast, if the orbital entanglement in the molecules is to be accessed or utilized, e.g. through an entanglement swapping protocol from molecule to quantum registers, the inclusion of superselection rules is operationally crucial. Accessing orbital entanglement requires measurement or more generally operations to be performed on the orbitals, which are limited precisely by the superselection rules. Although at the moment, perfect control over every element within a molecule or arbitrary operations on orbitals is not yet possible, this status may greatly improve in the near future [123]. If superselection rules are ignored, one would overestimate the accessible correlation and entanglement.

Nature's restriction on the implementable local observables has a profound implication on the entanglement in fermionic states. From the perspective of state tomography, coherent terms between different local parity states can never be observed under P-SSR, for the observable needed for such measurement is simply not available by the laws of physics. Therefore, the entanglement arising from SSR-violating coherence, sometime referred to as the "fluffy bunny entanglement" [92], is not accessible. This reduction of entanglement due to SSR is proven rigorously in Ref. [91] on an abstract mathematical level. Here we demonstrate it in concrete terms with a swapping protocol.

In Figure 1.2 we depict schematically an entanglement swapping protocol between two fermionic orbitals (φ_A, φ_B) in the state ρ_{AB}, and two qubits (q_A, q_B) in the state $|00\rangle$, both

shared by Alice and Bob. We shall denote the orbital Fock spaces as $\mathcal{F}_{\varphi_{A/B}}$ and the qubit Hilbert spaces as $\mathcal{H}_{q_{A/B}}$. For both the Fock spaces and the qubit Hilbert spaces, we denote the local basis as $\mathcal{B} = \{|0\rangle, |1\rangle\}$. One should keep in mind that for the qubit space $\mathcal{B}$ is the computational basis, while for the Fock space, $\mathcal{B}$ refers to the occupational basis. The protocol in Figure 1.2 extracts the entanglement between the fermionic modes onto the qubit registers, on which this entanglement could be used to perform more flexible quantum information protocols.

The protocol consists of Alice swapping the two states on φ_A and q_A, and Bob doing the same on φ_B and q_B. Specifically, the SWAP channel $\mathcal{S}$ on a bipartite system is defined element-wise as

$$\mathcal{S}\colon\ |i\rangle\langle j| \otimes |k\rangle\langle l| \mapsto |k\rangle\langle l| \otimes |i\rangle\langle j|, \tag{1.56}$$

for all $i, j, k, l \in \{0, 1\}$. In a world without SSR, after the SWAP operation, the final state of the two qubits would be exactly ρ_{AB}, and it would accordingly contain exactly the same amount of entanglement as the original two-orbital state. However, the SWAP operation clearly does not preserve the local parities, and hence cannot be realized with physical fermionic operators. Instead, Alice/Bob can only perform the superselected channel

$$\tilde{\mathcal{S}}_{A/B} = \mathcal{G}_{\Pi_{A/B}} \circ \mathcal{S}_{A/B} \circ \mathcal{G}_{\Pi_{A/B}}. \tag{1.57}$$

To see the difference between $\mathcal{S}_{A/B}$ and $\tilde{\mathcal{S}}_{A/B}$, let us first observe the action of the SWAP channel on a pure state $|\psi_A\rangle = |+\rangle \otimes |+\rangle \in \mathcal{F}_{\varphi_A} \otimes \mathcal{H}_{q_A}$ where $|+\rangle = \frac{1}{\sqrt{2}}(|0\rangle + |1\rangle)$, which clearly violates the P-SSR. In a world free of SSR, $|\psi_A\rangle$ would be invariant under the SWAP channel. Under the P-SSR, however, the action of the physically implementable $\tilde{\mathcal{S}}_A$ consists of three steps: (1) $\mathcal{G}_{\Pi_A}$ turns $|\psi_A\rangle$ into a mixed state $\mathcal{G}_{\Pi_A}[\rho_A] = \frac{\mathbb{1}}{2} \otimes |+\rangle\langle+|$. Namely, the coherent terms between different fermionic parities are erased. (2) $\mathcal{S}_A$ swaps the two states to $\mathcal{S}_A \circ \mathcal{G}_{\Pi_A}[\rho_A] = |+\rangle\langle+| \otimes \frac{\mathbb{1}}{2}$, which again contains P-SSR violating terms. (3) $\mathcal{G}_{\Pi_A}$ then eliminates said terms and the final state is $\mathcal{G}_{\Pi_A} \circ \mathcal{S}_A \circ \mathcal{G}_{\Pi_A}[\rho_A] = \frac{\mathbb{1}}{2} \otimes \frac{\mathbb{1}}{2}$. In this example we see evidently that SWAP does not leave $|\psi_A\rangle$ invariant. Instead, P-SSR filters out any coherence between different parity sectors, and only the superselected state $\tilde{\rho}_A^{\mathrm{P}} \equiv \mathcal{G}_{\Pi_A}[|\psi_A\rangle\langle\psi_A|]$ can be transferred onto the qubit register. Moreover, the final state on the fermionic mode φ_A is also the superselected variant of the original qubit state.

Now that we understand the action of (1.57), we can proceed to write down the action of the protocol $\tilde{\mathcal{S}} \equiv \tilde{\mathcal{S}}_A \otimes \tilde{\mathcal{S}}_B$ on the composite Hilbert space $\mathcal{F}_{\varphi_A} \otimes \mathcal{H}_{q_A} \otimes \mathcal{F}_{\varphi_B} \otimes \mathcal{H}_{q_B}$: for any states ρ_{AB} on $\mathcal{F}_{\varphi_A} \otimes \mathcal{F}_{\varphi_B}$ and σ_{AB} on $\mathcal{H}_{q_A} \otimes \mathcal{H}_{q_B}$, we have

$$\tilde{\mathcal{S}}[\rho_{AB} \otimes \sigma_{AB}] = \tilde{\sigma}_{AB}^{\mathrm{P}} \otimes \tilde{\rho}_{AB}^{\mathrm{P}}, \tag{1.58}$$

where

$$\begin{aligned} \tilde{\rho}_{AB}^{\mathrm{P}} &\equiv \mathcal{G}_{\Pi_A} \otimes \mathcal{G}_{\Pi_B}[\rho_{AB}] \\ &= \sum_{\tau,\tau'=\text{even,odd}} \hat{P}_{\tau}^{(A)} \otimes \hat{P}_{\tau'}^{(B)} \rho_{AB} \hat{P}_{\tau}^{(A)} \otimes \hat{P}_{\tau'}^{(B)} \end{aligned} \tag{1.59}$$

and the same for $\tilde{\sigma}^{\mathrm{P}}_{AB}$. The final state $\tilde{\rho}^{\mathrm{P}}_{AB}$ on the qubit registers contains the same information as the original two-orbital state ρ_{AB}, except it is rid of the coherence between the different local parity sectors, which does not contribute to the physical entanglement. The decohering map $\mathcal{G}_{\Pi_A} \otimes \mathcal{G}_{\Pi_B}$ thus acts as an entanglement filter as depicted in Figure 1.2, and effectively reduces the available entanglement in the fermionic state. Only the entanglement within each local parity sector can be extracted for operational purposes.

We remark that so far we have restricted ourselves to the scenario where only one copy of the system is available. When multiple copies of the system are available, forming a bipartition $A_1A_2\cdots A_n|B_1B_2\cdots B_n$, SSR-violating operations on one of the components A_i are possible, as long as SSR is satisfied on the subsystem $A_1A_2\cdots A_n$. In this case, the accessible entanglement of the state $\rho_{A_iB_i}$ with respect to the partition $A_i|B_i$ would be higher than what we have calculated above.

Connection to particle correlation

Before ending this chapter, we would like to point out that the two seemingly orthogonal pictures of fermionic correlation (particle versus orbital) are on some level elegantly connected. The particle correlation measured by the nonfreeness $\mathcal{N}$ is invariant under any unitary transformation of the single particle basis, whereas the orbital correlation is explicitly basis dependent. To draw a connection, we need to find a way to remove the basis dependence of the latter.

To this end, let us consider the smallest subsystem in the orbital picture, the spin-orbitals. The Fock space of a single spin-orbital labelled by the composite index i with both spatial and spin information, is only two-dimensional, isomorphic to $\mathbb{C}^2$. A spin-orbital reduced state of an N-particle wavefucntion $|\Psi\rangle$ is a simple diagonal matrix

$$\rho_i = \mathrm{Tr}\left[|\Psi\rangle\langle\Psi|\right] = \begin{pmatrix} \langle \mathbb{1} - \hat{n}_i\rangle & 0 \\ 0 & \langle \hat{n}_i\rangle \end{pmatrix}, \tag{1.60}$$

where $\hat{n}_i = f_i^\dagger f_i = \gamma_{ii}$ is the particle number operator defined on the spin-orbital i. It is necessary to refer to the smallest subsystem since ρ_i can be expressed with the elements of the 1RDM γ alone, just as in the case of the nonfreeness for pure states.

For any N-particle wavefucntion $|\Psi\rangle$, the following statement holds true: The sum of all single spin-orbital entropy is bounded from below by the nonfreeness

$$\sum_i S(\rho_i) \geq \mathcal{N}\left(|\Psi\rangle\langle\Psi|\right). \tag{1.61}$$

In particular, the minimum of the left-hand side is obtained, if the spin-orbital basis is the eigenbasis of γ. To prove this statement, we first consider the following inequality

$$-\sum_i \gamma_{ii}\log(\gamma_{ii}) \geq -\sum_i \lambda_i \log(\lambda_i) = S(\gamma), \tag{1.62}$$

where λ_i's are the eigenvalues of the 1RDM γ. The entropy of the diagonal vector of γ is no less than the entropy of the spectrum of γ, which is guaranteed by the Hardy-Littlewood-Pólya theorem [124], and the Schur concavity of the von Neumann entropy. The same applies to the single-hole RDM $\mathbb{1} - \gamma$

$$-\sum_i (1-\gamma_{ii}) \log(1-\gamma_{ii}) \geq -\sum_i (1-\lambda_i) \log(1-\lambda_i) = S(\mathbb{1}-\gamma). \tag{1.63}$$

Combining the two inequalities we arrive at

$$\begin{aligned} \sum_i S(\rho_i) &= -\sum_i \gamma_{ii} \log(\gamma_{ii}) - \sum_i (1-\gamma_{ii}) \log(1-\gamma_{ii}) \\ &\geq -\sum_i \lambda_i \log(\lambda_i) - \sum_i (1-\lambda_i) \log(1-\lambda_i) \\ &= \sum_i S(\rho_i^{\mathrm{NO}}) = \mathcal{N}\left(|\Psi\rangle\langle\Psi|\right). \end{aligned} \tag{1.64}$$

Here, we use the superscript NO to distinguish the spin-orbital RDM in the natural basis (eigenbasis of γ). In other words, the particle correlation measured by the nonfreeness, is the same as the orbital correlation measured by the sum of spin-orbital entropy, minimized over all possible spin-orbital basis. And the minimizer is always the natural basis, namely the eigenbasis of the 1RDM γ. This profound connection (see also Ref. [60]) suggests that a part of the correlation in the ground state is only due to a suboptimal orbital representation, whereas the nonfreeness represent the intrinsic correlation of the quantum state. A similarly exact statement has not been proven yet on the level of orbital entropy rather than spin-orbital entropy, to the best of the author's knowledge. And therefore we do not expect the natural orbitals to be the most simplifying reference basis for every problem. However, this elegant connection between the particle and orbital pictures of correlation continues to motivate the exploration of orbital optimization guided by quantum information concepts, for the rest of this thesis.

Chapter Summary

In this chapter, we provided a comprehensive toolbox for correlation analysis, by recalling first the concepts of entanglement and correlation in the setting of distinguishable subsystems. This includes the formal definitions and operational meanings of entanglement and correlation, and the dissection of the total correlation into quantum and classical parts. We then explained various subtleties that arise when these concepts are translated into the context of indistinguishable electrons, and how these subtleties can be resolved. Two main approaches emerged as viable ways of quantifying electron correlation in a theoretically sound manner. First, the particle correlation measured by the nonfreeness quantifies the deviation of a quantum state from the set of free states, namely the ground and thermal states of particle number conserving single-particle Hamiltonians. Second, with orbitals considered as distinguishable subsystems, their entanglement and correlation are addressed

in the same as in the conventional qubit setting, with the caveat that one needs to incorporate the pertinent superselection rules. Both approaches offer unique perspectives into the problem of electron correlation, and can be in fact unified elegantly: The minimized sum of spin-orbital entropy is equal to the particle correlation measured by the nonfreeness.

Chapter 2

Orbital Entanglement in a Lattice

In the previous chapter, we mentioned that entanglement for mixed states is in general very expensive to calculate. It requires the optimization for the closest separable state from the set $\mathcal{D}_0$. However, when the system displays a high level of symmetry, one can exploit the symmetry of the ground state to simplify the task of finding the closest separable state [107], [125], even to a point that analytic expression for the entanglement is available. In Ref. [107] the author of the thesis and coworkers derived the first analytic formula for the superselected bipartite relative entropy of entanglement for two spatial orbitals (as a subsystem of a potentially much larger system equipped with several common symmetries). If the system is also exactly solvable, then the entanglement can be fully derived from the parameters of the Hamiltonian, and becomes a powerful tool for extracting analytic insights from the ground state, as has been the case of block entropy in integrable systems [114], [126], [127]. In this chapter we seize this rare opportunity, and apply the orbital-orbital entanglement formula to the system of free fermions in a tight-binding model. We then compare the results we obtained to the entanglement structure in the Hydrogen ring (H_{16}), to investigate if the behavior of the orbital-orbital entanglement is robust against electron-electron interaction.

Previously, we concluded that the true *physical* entanglement in a bipartite fermionic state ρ_{AB} in the presence of P-SSR, is precisely the entanglement in its superselected variant $\tilde{\rho}^{\mathrm{P}}_{AB} = \mathcal{G}_{\Pi_A} \otimes \mathcal{G}_{\Pi_B}[\rho_{AB}]$ quantified in the usual manner without P-SSR. In this section, we will briefly summarize the analytic formula for physical entanglement between two spatial orbitals in electronic systems, derived in Ref. [107]. We consider two orbitals A and B with internal spin-$\frac{1}{2}$ degrees of freedom. This system is described by a state ρ_{AB} acting on the Fock space $\mathcal{F}_A \otimes \mathcal{F}_B$, spanned by $\{|\alpha\rangle_A \otimes |\beta\rangle_B\}$, where $\alpha, \beta \in \{0, \uparrow, \downarrow, \uparrow\downarrow\}$. The mixedness of ρ_{AB} accounts for the physically relevant scenario where A and B are in contact with other orbitals. A key step in quantifying the entanglement $E(\tilde{\rho}^{\mathrm{P}}_{AB})$ is understanding its restriction to several smaller subspaces of the total Fock space, after

imposing several common symmetries exhibited by *realistic* condensed matter and quantum chemical systems.

The relevant systems in our case, the tight-binding model and the hydrogen ring, enjoy many symmetries, including (1) particle number, (2) magnetization, and (3) reflection symmetry between orbitals A and B (e.g. two orthogonalized 1s orbitals in a hydrogen ring). Under these symmetries, there are only four entangled pure states compatible with local P-SSR:

$$\begin{aligned} |\Phi_\pm\rangle &= \frac{|0\rangle_A \otimes |\uparrow\downarrow\rangle_B \pm |\uparrow\downarrow\rangle_A \otimes |0\rangle_B}{\sqrt{2}}, \\ |\Psi_\pm\rangle &= \frac{|\uparrow\rangle_A \otimes |\downarrow\rangle_B \pm |\downarrow\rangle_A \otimes |\uparrow\rangle_B}{\sqrt{2}}. \end{aligned} \tag{2.1}$$

Naturally, if $\tilde{\rho}^{\mathrm{P}}_{AB}$ enjoys the symmetries (1), (2), and (3), then $|\Phi_\pm\rangle$ and $|\Psi_\pm\rangle$ are eigenstates of $\tilde{\rho}^{\mathrm{P}}_{AB}$, with eigenvalues $p_\pm$ and $q_\pm$, respectively. Even so, the exact P-SSR orbital-orbital entanglement, though entirely analytic, has a heavily involved form, which can be found in the Appendix of Ref. [107]. Instead, we highlight another related entanglement formula from Ref. [107] in the case where the particle number superselection rule (N-SSR) applies. In this setting, no superposition between different local particle number states is possible and therefore even $|\Phi_\pm\rangle$ are forbidden. The N-SSR-compatible two-orbital state is obtained with the same reasoning via the superselection map

$$\tilde{\rho}^{\mathrm{N}}_{AB} \equiv \mathcal{G}_{N_A} \otimes \mathcal{G}_{N_B}[\rho_{AB}] = \sum_{n_A,n_B=0}^{2} \hat{P}_{n_A,n_B} \rho_{AB} \hat{P}_{n_A,n_B}, \tag{2.2}$$

where $\hat{P}_{n_A,n_B} = \hat{P}_{n_A} \otimes \hat{P}_{n_B}$ and $\hat{P}_{n_{A/B}}$ is the projection onto the sector of local particle number $n_{A/B}$ on subsystem A/B. The N-SSR entanglement of $\tilde{\rho}^{\mathrm{N}}_{AB}$ can then be derived, after considerable efforts, to be

$$E(\tilde{\rho}^{\mathrm{N}}_{AB}) = \begin{cases} r \log\left(\frac{2r}{r+t}\right) + t \log\left(\frac{2t}{r+t}\right), & r < t, \\ 0, & r \geq t, \end{cases} \tag{2.3}$$

where

$$t \equiv \max\{q_\pm\}, \quad r \equiv \mathrm{Tr}[\hat{P}_{1,1}\rho_{AB}] - t. \tag{2.4}$$

Note that $r < t$, or explicitly

$$\mathrm{Tr}[\hat{P}_{1,1}\rho_{AB}] < 2\max\{q_\pm\}, \tag{2.5}$$

is the exact entanglement criterion. Later, we will see that the P- and N-SSR orbital-orbital long-distance entanglement on a localized orbital chain are virtually indistinguishable. The simple form of the latter thus allows us to derive *analytically* asymptotic properties of the physical entanglement between orbitals for both P- and N-SSR.

2.1 Free Fermions

2.1.1 Reduced states in free fermions systems

In the second quantized formalism, a general particle number conserving non-interacting fermionic Hamiltonian $\hat{H}$ defined on a set of L orbitals (characterized by an algebra of associating creation and annihilation operators $\{f_i^\dagger\}_{i=1}^L$ and $\{f_i\}_{i=1}^L$, respectively) can be written as a sum of one-body operators whose coefficients form a Hermitian matrix $\mathbf{h}$

$$\hat{H}_{\text{free}} = \sum_{i,j=1}^{L} h_{ij} f_i^\dagger f_j, \quad h_{ij} = h_{ji}^*. \tag{2.6}$$

The spectrum of H_{free} can be analytically solved by applying to the Hamiltonian a unitary transformation U such that the transformed matrix $\mathbf{d} = \mathbf{UhU}^\dagger$ is diagonal. The unitary U transform the operators $\{f_i^\dagger\}_{i=1}^L$ to a new basis, where the Hamiltonian is rewritten as

$$\hat{H}_{\text{free}} = \sum_{i=1}^{L} d_{ii} c_i^\dagger c_i \equiv \sum_{i=1}^{L} d_{ii} \hat{n}_i, \quad c_i^\dagger = \sum_{j=1}^{L} U_{ij} f_j^\dagger. \tag{2.7}$$

Notice that in the new basis, the orbital degrees of freedom are completely decoupled, and each term (local particle number operator $\hat{n}_i = c_i^\dagger c_i$) in the Hamiltonian commutes with all other terms. Eigenstates of $\hat{H}_{\text{free}}$ are simply tensor product states consisting of eigenstates ($|0\rangle_i$ and $|1\rangle_i \equiv c_i^\dagger |0\rangle_i$) of the local particle number operators (also known as Slater determinant)

$$|n_1, \ldots, n_i, \ldots, n_L\rangle = \prod_{i=1}^{L} \left(c_i^\dagger\right)^{n_i} |0\rangle, \quad |0\rangle \equiv \bigotimes_{i=1}^{L} |0\rangle_i. \tag{2.8}$$

If we further assume that the spectrum d_{ii} is ordered increasingly (which can always be achieved by relabelling the orbitals), then

$$|\Psi_N\rangle = c_1^\dagger c_2^\dagger \cdots c_N^\dagger |0\rangle, \tag{2.9}$$

is a (possibly degenerate) ground state of the Hamiltonian $\hat{H}$.

In order to calculate the entanglement of the state $|\Psi_N\rangle$ (and in the same fashion any eigenstates or Gibbs state of $\hat{H}$) with respect to a partitioning of the orbitals (in any basis), we must be able to compute first the reduced density matrix

$$\rho_A = \text{Tr}_{\setminus A}[|\Psi_N\rangle\langle\Psi_N|] \tag{2.10}$$

of the ground state defined on a sub-lattice A. The entanglement between the subsystem A and its complement is simply given by the von Neumann entropy

$$S(\rho_A) = -\text{Tr}[\rho_A \log \rho_A]. \tag{2.11}$$

At first glance, one might consider the reduced state ρ_A to be trivial. If A is a sub-lattice being associated with the subalgebra $\{c_i\}_{i\in A}$, then the reduced state is simply given by discarding the tensor product states of the complement lattice

$$\rho_A = \bigotimes_{i\in A} |n_i\rangle\langle n_i|. \tag{2.12}$$

Since ρ_A is always pure, its entropy is by definition 0. Consequently, the entanglement between the sub-lattice A and its complement is always 0, for any A defined by $\{c_i\}_{i\in A}$. The problem is entirely trivial.

However, the crucial point is that the partitioning of the sub-lattice A and its complement that we are interested in may not be realizable in the basis where $\mathbf{h}$ is diagonalized. For example, a translationally invariant free hopping Hamiltonian is diagonalized in the momentum lattice, but one might be interested in the entanglement between the left and the right half of the spatial lattice, which is likely to be non-trivial. Let A be defined by the subalgebra $\{f_i^\dagger\}_{i\in A}$ where $f_i^\dagger$'s are related to the natural basis $c_i^\dagger$ by $c_i^\dagger = \sum_j V_{ij} f_j^\dagger$. The most direct way of computing ρ_A is to first transform the state $|\Psi_N\rangle$ to the new basis

$$|\Psi_N\rangle = \prod_{i=1}^{N} \left(\sum_{j=1}^{L} V_{ij} f_j^\dagger \right) |0\rangle, \tag{2.13}$$

and then perform the partial trace on the complementary lattice. This way of calculating the reduced state is, however, extremely cumbersome.

Remarkably, Peschel put forward a shortcut, which allows us to compute $S(\rho_A)$ with much less effort [128]. From an information point of view, one realizes that in the virtue of Wick's theorem, the expectation value of any observable of the non-interacting state $|\Psi_N\rangle$ is a function of the two-point correlator $\langle\Psi_N| f_i^\dagger f_j |\Psi_N\rangle \equiv \gamma_{ji}$. The latter defines the one-particle reduced density matrix (1-RDM) γ of the ground state. As ρ_A is uniquely defined via the expectations of all physical observables on the subsystem A [64], one can then, in principle, express any functions (including the von-Neumann entropy) of ρ_A using only information contained in γ.

2.1.2 Tight-binding model

We consider the following tight-binding Hamiltonian on a periodic chain with L lattice sites

$$\hat{H}_{\mathrm{tb}} = -\frac{1}{2} \sum_{\sigma=\uparrow,\downarrow} \sum_{l=1}^{L} f_{l\sigma}^\dagger f_{l+1,\sigma} + h.c. \tag{2.14}$$

with periodic boundary conditions imposed. Here, $f_{l\sigma}^{(\dagger)}$ annihilates(creates) an electron with spin σ at the Wannier orbital/lattice site labeled by l. Each Wannier orbital can host

up to two electrons with different spin. The discrete translation invariance of the system allows us to diagonalize the Hamiltonian via a Fourier transform

$$c_{k\sigma}^{\dagger} = \frac{1}{\sqrt{L}} \sum_{l=1}^{L} e^{-\frac{2\pi i}{L} kl} f_{l\sigma}^{\dagger}. \tag{2.15}$$

In this basis, the Hamiltonian (2.14) is diagonal, and the one-electron spectrum is given by the dispersion relation

$$E_k = -\cos\left(\frac{2\pi k}{L}\right), \quad k = 0, \pm 1, \ldots, \pm\frac{L-1}{2}. \tag{2.16}$$

As the system is non-interacting, the N-electron ground state is the configuration where the N lowest energy levels are filled. For simplicity, we shall assume from now on that the number of electrons is either $N = 0$, or $N = 4k_{\max} + 2$ where $k_{\max} \geq 0$ denotes the highest occupied momentum. In the former case, the ground state is simply the vacuum. In the latter, the N-particle ground state $|\Psi_N\rangle$ is uniquely characterized by the Fermi level

$$\langle \Psi_N | c_{k\sigma}^{\dagger} c_{k'\sigma'} | \Psi_N \rangle = \delta_{kk'} \delta_{\sigma\sigma'} \Theta(k_{\max} - |k|), \tag{2.17}$$

where Θ is the Heaviside step function. With (2.15) and (2.17) at hand, we are ready to compute the matrix elements of the 1RDM in the spatial basis as

$$\langle \Psi_N | f_{l\sigma}^{\dagger} f_{l'\sigma'} | \Psi_N \rangle = \frac{1}{L} \delta_{\sigma,\sigma'} \sum_{k=-k_{\max}}^{k_{\max}} e^{\frac{2\pi i (l-l')k}{L}}. \tag{2.18}$$

When $l = l'$, all summands in (2.18) become 1, and thus we obtain

$$\begin{aligned} \langle \Psi_N | f_{l\sigma}^{\dagger} f_{l\sigma'} | \Psi_N \rangle &= \delta_{\sigma\sigma'} \frac{2k_{\max} + 1}{L} \\ &= \delta_{\sigma\sigma'} \frac{N}{2L} \equiv \delta_{\sigma\sigma'} \eta, \end{aligned} \tag{2.19}$$

where $\eta = N/(2L)$ is the particle filling fraction. This agrees with the physical intuition that the electrons travel freely along the chain and appear at every site with uniform probability. When $l \neq l'$, by introducing $\omega \equiv \frac{2\pi(l-l')}{L}$, we arrive at

$$\begin{aligned} \langle \Psi_N | f_{l\sigma}^{\dagger} f_{l'\sigma'} | \Psi_N \rangle &= \frac{1}{L} \delta_{\sigma\sigma'} \frac{e^{i\omega k_{\max}} - e^{-i\omega k_{\max}}}{1 - e^{iw}} \\ &= \frac{1}{L} \delta_{\sigma\sigma'} \frac{\sin\left[\omega\left(k_{\max} + \frac{1}{2}\right)\right]}{\sin\left(\frac{\omega}{2}\right)} \\ &= \frac{1}{L} \delta_{\sigma\sigma'} \frac{\sin\left(\frac{\omega N}{4}\right)}{\sin\left(\frac{\omega}{2}\right)}. \end{aligned} \tag{2.20}$$

In the thermodynamic limit where $N, L \to \infty$ while $\eta = N/(2L)$ is kept fixed, the off-diagonal elements of the 1RDM become

$$\lim_{L\to\infty} \langle \Psi_N | f^\dagger_{l\sigma} f_{l'\sigma} | \Psi_N \rangle = \frac{\sin(\pi d\eta)}{\pi d} \equiv W(d,\eta), \tag{2.21}$$

where $d{=}|l-l'|$ is the orbital separation distance.

Next, we use Wick's theorem to calculate the quantities needed for the entanglement between the orbitals l and l' from the elements of the 1RDM derived above. The relevant operators for calculating r and t in the analytic formula (2.3) are the orthogonal projection $\hat{P}^{ll'}_{--}$ onto the local odd parity subspace, and the orthogonal projections $\hat{P}^{ll'}_{\Psi_\pm}$ onto $|\Psi_\pm\rangle$, all defined on the orbitals l and l'

$$\begin{aligned} \hat{P}^{ll'}_{--} &= \sum_{i,j=l,l'} \sum_{\sigma\tau} \hat{n}_{i\sigma}\hat{n}_{j\tau}(1-\hat{n}_{i\bar{\sigma}})(1-\hat{n}_{j\bar{\tau}}) \\ \hat{P}^{ll'}_{\Psi_\pm} &= |\Psi^{ll'}_\pm\rangle\langle\Psi^{ll'}_\pm| \\ &= \hat{n}_{l\uparrow}\hat{n}_{l'\downarrow}(1{-}\hat{n}_{l\downarrow})(1{-}\hat{n}_{l'\uparrow}) \pm f^\dagger_{l\uparrow} f^\dagger_{l'\downarrow} f_{l'\uparrow} f_{l\downarrow}. \end{aligned} \tag{2.22}$$

Here, $\hat{n}_{l\sigma} = f^\dagger_{l\sigma} f_{l\sigma}$ denotes the spin-σ particle number operator on orbital l, and $\bar{\sigma}$ denotes the opposite spin of σ. After some straightforward but lengthy calculations, we obtain the following expressions for the parameters r and t, required in Eq. (2.3),

$$\begin{aligned} t &= \max\{\langle\Psi_N|\hat{P}^{ll'}_{\Psi_\pm}|\Psi_N\rangle\} = A + B, \\ r &= \langle\Psi_N|\hat{P}^{ll'}_{--}|\Psi_N\rangle - t = 3A - 3B, \end{aligned} \tag{2.23}$$

where

$$A \equiv \left[\eta^2 - \eta - W(d,\eta)^2\right]^2, \quad B \equiv W(d,\eta)^2. \tag{2.24}$$

With this, the N-SSR entanglement can be neatly expressed as

$$E(\tilde{\rho}^{\mathrm{N}}_{ll'}) = (A+B)\log\left(\frac{A+B}{2A-B}\right) + (3A-3B)\log\left(\frac{3A-3B}{2A-B}\right) \tag{2.25}$$

provided the entanglement criteria (2.5) (here it translates to $A < 2B$) is met, and otherwise 0. We present in Figure 2.1 the orbital-orbital entanglement as a function of the filling fraction η, at various orbital separations d, together with the entanglement when only P-SSR is assumed, also obtained analytically.

Figure 2.1 reveals the rich entanglement structure of the Slater determinant ground state. At different particle filling fraction η, the orbital-orbital entanglement behaves in qualitatively distinct ways, which we will now account for in detail. First, we notice that the curve of orbital-orbital entanglement is symmetric around the half-filling point $\eta{=}1/2$. This is due to the unbroken particle-hole symmetry of the Hamiltonian (2.14) in the ground states. Moreover, observing (2.25), we notice that the entanglement as a function of η is

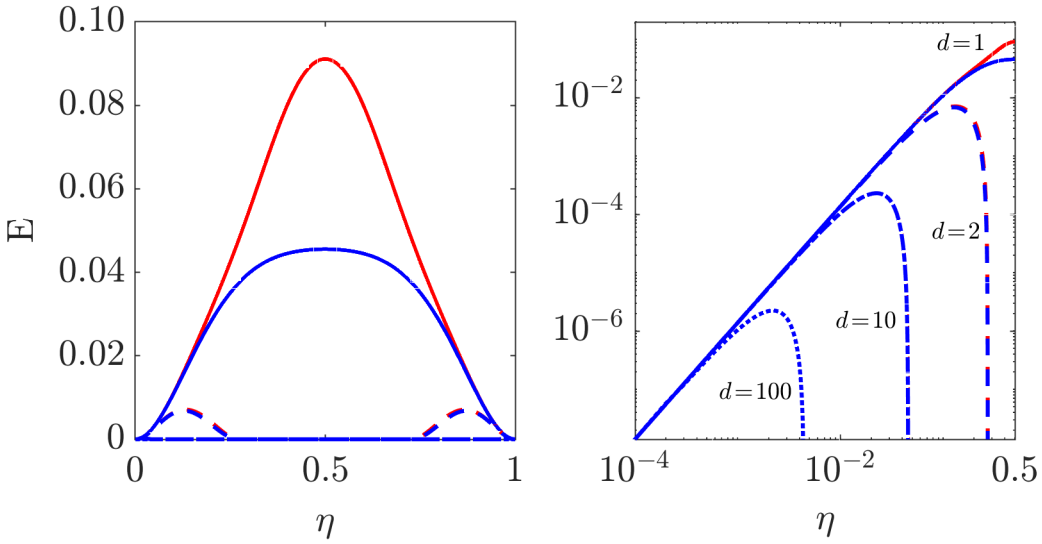

Figure 2.1: Entanglement between the spatial orbitals separated by inter-orbital distance 1 (solid), 2 (dashed), 10 (dashed-dotted), and 100 (dotted), under P-SSR (red) and N-SSR (blue) in the ground state of the tight-binding Hamiltonian (2.14) as a function of the particle/hole density η. In the left panel, the dashed-dotted and dotted curves look essentially flat. They can be seen more clearly in the log-log plot in the right panel.

symmetric about $\eta=1/2$. Because of this, it suffices to consider only $0\leq\eta\leq1/2$, and treat it as a particle or hole filling fraction. For this η-region, we present the entanglement and filling fraction both in log-scale in the right panel of Figure 2.1 for more details.

Second, the analytic properties of the orbital-orbital entanglement highly depend on the combination of orbital separation d and the filling fraction η. The common feature here is the vanishing of orbital-orbital entanglement at both $\eta=0$ and $\eta=1$. In these two cases the ground state is invariant under any orbital rotation and contains zero correlation in any orbital basis. For two neighboring orbitals ($d=1$), the entanglement between them is maximized exactly when the chain is half filled ($\eta=1/2$), for both P- and N-SSR entanglement. Around half-filling, the P-SSR entanglement is significantly higher than the N-SSR one. This is not surprising, as N-SSR imposes a stronger restriction on the accessible entanglement. Yet, at small particle or hole filling fractions, the two become essentially the same. For $d\geq2$, the P- and N-SSR entanglement is practically indistinguishable. This is because at small particle (hole) filling, the chances of finding a doubly occupied (empty) orbital is very low, which suppresses the possible amount of entanglement arising from the even-even parity sector. This observation allows us to restrict the investigation of analytic properties to the latter by referring to (2.25) for all practical purposes here, and also in the following section. In this case, two maxima occur which appear symmetrically on the η-axis about $\eta=1/2$ (see the left panel of Figure 2.1) due to the particle-hole symmetry of (2.25). At a lower η, more and farther separated orbital pairs become entangled, though

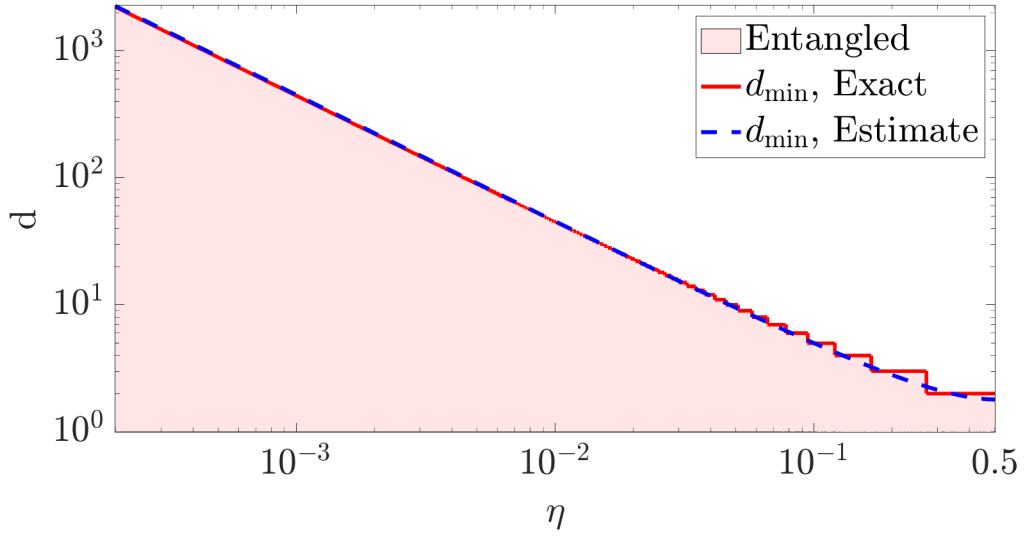

Figure 2.2: Minimal disentangling distance $d_{\min}$ as a function of particle/hole density η.

this entanglement grows vanishingly small with the filling fraction.

Third, we find that entanglement across extremely long distances can be engineered by tuning the filling fraction to be infinitesimally small. In the right panel of Figure 2.1, we see more clearly in the log-log scale that for each separation d, there exists a critical η, below which the two orbitals are always entangled. At the same time, for any filling fraction η, there is a minimal disentangling distance $d_{\min}(\eta)$, beyond which all orbital pairs are in a separable state. This phenomenon of completely vanishing entanglement is called the sudden death of entanglement [129]. Geometrically, it means nothing else than that the two-orbital reduced quantum state evolves along a trajectory which at some point enters the convex set of separable states. We shall explore this phenomenon in more details in the next section.

Previously, we observed that interesting phenomena such as long-distance entanglement and sudden death of entanglement occur when the particle filling η or hole filling $1-\eta$ is small. Moreover, the P- and N-SSR entanglement in this region are practically identical. Therefore, we can focus on the latter in our analysis.

For a fixed orbital separation d, when $\eta \ll d^{-1}$, we Taylor expand (2.21) as $W(d,\eta) = \eta + \mathcal{O}(\eta^3)$. The N-SSR entanglement between two orbitals separated by d becomes

$$E(\tilde{\rho}_{ij}^{\mathrm{N}}) = 2\log(2)\eta^2 + \mathcal{O}(\eta^5), \quad \eta \ll d^{-1}, \tag{2.26}$$

i.e., the N-SSR orbital-orbital entanglement is quadratic in η for small η. In log-log scale this relation becomes linear

$$\log(E(\tilde{\rho}_{ij}^{\mathrm{N}})) = 2\log(\eta) + \mathcal{O}(1), \quad \eta \ll d^{-1}. \tag{2.27}$$

For the sake of completeness, we also verify that the P-SSR entanglement indeed reduces to the N-SSR one, i.e.

$$\log(E(\tilde{\rho}_{ij}^{\mathrm{P}})) = 2\log(\eta) + \mathcal{O}(1), \quad \eta \ll d^{-1}. \tag{2.28}$$

Eqs. (2.27) and (2.28) then explain the asymptotic linear behavior of both the P-SSR (red) and N-SSR (blue) entanglement in the log-log scale, with the same slope and for any separation d, in Figure 2.1 (right panel). This relation is more robust for small separation d, as we can see that for large separation the orbital-orbital entanglement quickly deviates from the linear asymptote and plunges into sudden death as η increases. On the other hand, for small η and $d < d_{\min}(\eta)$, the orbital-orbital entanglement is only a function of η, but not of d. All orbital pairs below the critical separation are equally entangled with one another. Due to the particle-hole symmetry, the orbital-orbital entanglement at small hole fraction $1-\eta \ll d^{-1}$ is also quadratic in $1-\eta$.

Beyond the critical separation $d_{\min}(\eta)$, all orbital pairs are disentangled. Based on Figure 2.2, $d_{\min}(\eta)$ seems to diverge as η approaches 0. To understand the asymptotic behavior of $d_{\min}(\eta)$ at small η, we analyze the entanglement criteria (2.5). Recall from the previous section that the two orbitals are in a separable state if A and B in (2.24) satisfy the relation $A \geq 2B$, which in explicit terms reads

$$\eta^2 - \eta \leq W(d,\eta)^2 - \sqrt{2}|W(d,\eta)|. \tag{2.29}$$

Although (2.29) cannot be solved analytically, in the limit of large d using the expansion $W(d,\eta) \approx (\pi d)^{-1}$ we can derive an analytic estimation for the minimal disentangling separation $d_{\min}(\eta)$

$$d_{\min}(\eta) = \frac{\sqrt{2}}{\pi}\frac{1}{\eta(1-\eta)} + \mathcal{O}(1). \tag{2.30}$$

In log-log scale, this relation becomes linear

$$\log(d_{\min}(\eta)) = \begin{cases} -\frac{\sqrt{2}}{\pi}\log(\eta) + \mathcal{O}(\eta), & \eta \ll 1, \\ -\frac{\sqrt{2}}{\pi}\log(1-\eta) + \mathcal{O}(1-\eta), & 1-\eta \ll 1. \end{cases} \tag{2.31}$$

In Figure 2.2, we plot the exact minimal disentangling distance obtained by numerically locating the sudden death of entanglement using (2.29), together with the analytic estimation (2.30). We can see the agreement is excellent, even up to the order 10^{-1} in η.

2.2 Hydrogen ring

In the previous section, we thoroughly explored the orbital-orbital entanglement of the tight-binding model (2.14), using the analytic tools provided in Ref. [107]. In this section,

we upgrade the tight-binding model to the hydrogen ring H_{16}, while fashioning an orbital localization scheme that produces Wannier type orbitals similar to the tight-binding model. The hydrogen ring (or open chain) is a common system for benchmarking ground state methods due to its strongly correlated character [130]–[133]. This system shares many similarities with the tight-binding chain: a localized orbital basis can be established, and there is a local hopping generated by the overlapping atomic orbitals. As a molecular system, however, it additionally contains a periodic nuclear potential and the Coulomb interaction between the electrons, which is the source of computational complexity. It is thus of considerable interest to ask, to what extent the entanglement effects in the hydrogen ring can be explained by the insights we gained from the tight-binding model (2.14) of non-interacting electrons in the previous section.

2.2.1 Model and Hamiltonian

We consider a finite periodic hydrogen ring, defined by the uniform nearest internuclear distance R, with the minimal STO-3G basis set. This basis contains one 1s orbital at each atomic center, and it is the minimal setting for describing the dissociation of hydrogen molecules.

The electronic Hamiltonian contains three terms: the nuclear potential, the kinetic energy, and the Coulomb interaction. In the second quantization formalism, they can be conveniently packed into the one- and two-electron Hamiltonians $\hat{h}$ and $\hat{V}$, which comprise the total electronic Hamiltonian

$$\hat{H} = \hat{h} + \hat{V} = \sum_{ij}\sum_{\sigma} h_{ij} f^\dagger_{i\sigma} f_{j\sigma} + \frac{1}{2}\sum_{ijkl}\sum_{\sigma\sigma'} V_{ijkl} f^\dagger_{i\sigma} f^\dagger_{j\sigma'} f_{l\sigma'} f_{k\sigma}, \tag{2.32}$$

where

$$\begin{aligned} h_{ij} &= \int \mathrm{d}x^3 \phi^*_i(x) \left(-\frac{\hbar}{2m_e}\nabla^2 + \sum_{m=0}^{M-1} \frac{Z_m}{|\hat{x} - \mathbf{X}_m|} \right) \phi_j(x), \\ V_{ijkl} &= \int \mathrm{d}x^3 \mathrm{d}x'^3 \phi^*_i(x)\phi^*_j(x') \frac{1}{|\hat{x} - \hat{x}'|} \phi_l(x')\phi_k(x). \end{aligned} \tag{2.33}$$

Here, ϕ_i's are orthonormal molecular orbitals which form a complete basis of the one-particle Hilbert space spanned by the non-orthogonal atomic orbitals. M is the total number of nuclear centers with charges Z_m. In the case of H_{16}, $Z_m = 1$ for all $m = 1, 2, \ldots, 16$ and $\mathbf{X}_m$ are defined as

$$\mathbf{X}_m = \frac{R}{2\sin\left(\frac{\theta}{2}\right)} (\cos(m\theta), \sin(m\theta), 0), \quad \theta = \frac{2\pi}{16}, \tag{2.34}$$

so that the 16 hydrogen atoms are arranged evenly on a ring, with the straight-line distance between two nearest neighbor atoms equal to R. From here on, we shall use atomic units

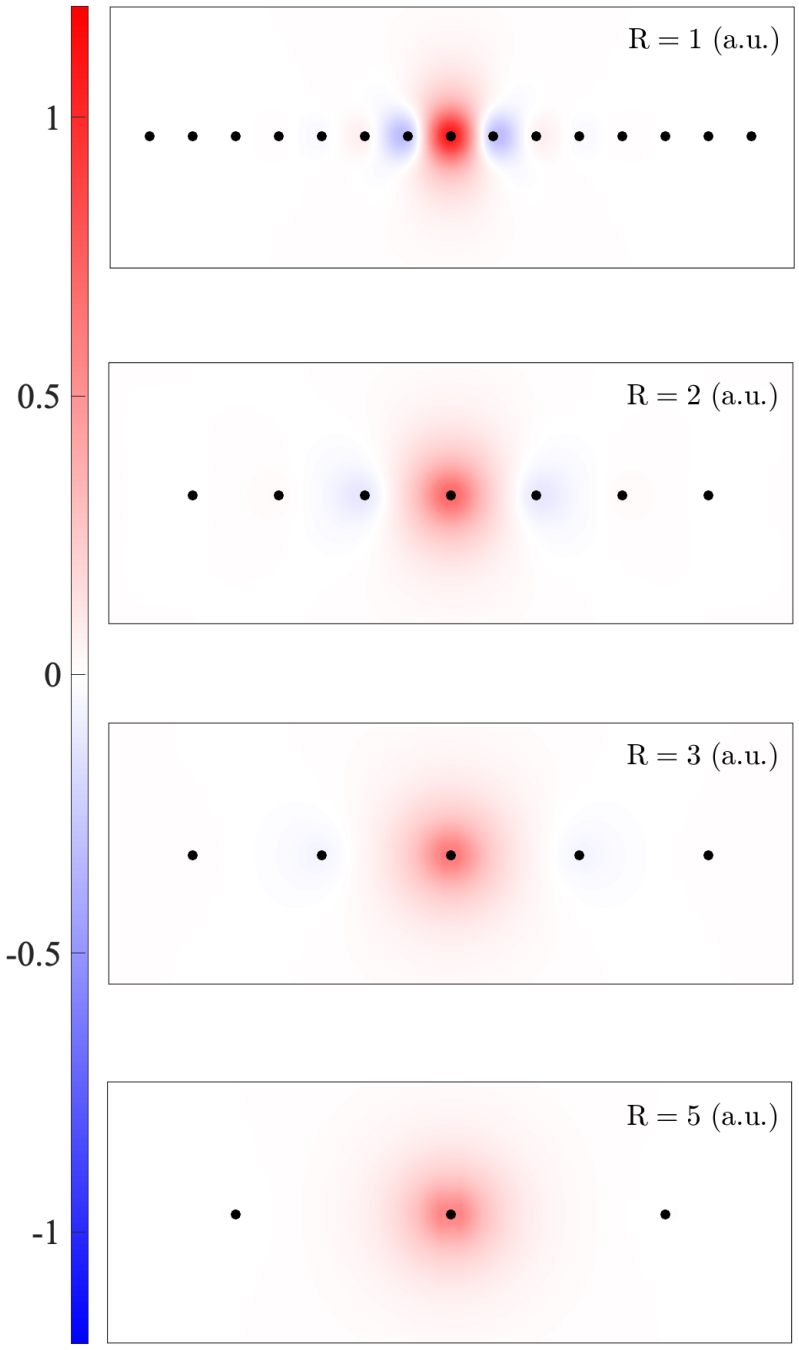

Figure 2.3: Wavefunction values of the localized orbitals in H_{16} in the STO-3G basis, for various nearest neighbor distances R (a.u.). Nuclear centers are represented as black dots. The horizontal range is 16 a.u., and the vertical range 6 a.u..

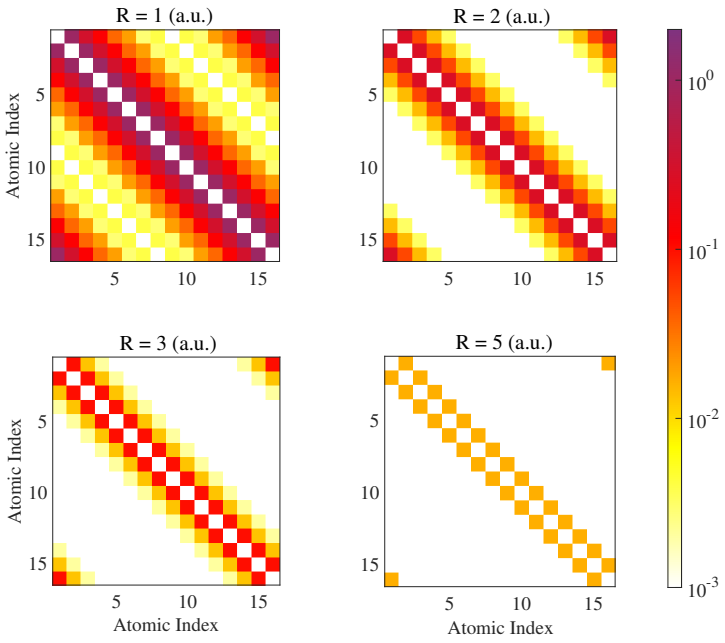

Figure 2.4: Absolute values of matrix elements of the one-electron Hamiltonian $|(h_1)_{ij}|$ (a.u.) with $i \neq j$, for nearest neighbor separation $R = 1, 2, 3, 5$ (a.u.). Periodic boundary conditions are imposed by the ring geometry.

(denoted by a.u.) for both distance and energy, which correspond to Bohr and Hartree, respectively.

The matrix elements of the one- and two-electron Hamiltonians are explicitly orbital basis dependent. The set of localized orthonormal orbitals is obtained by symmetrically orthogonalizing [134] the local 1s atomic orbitals. In Figure 2.3, we plot these localized orbitals for different nearest neighbor distances R. Locally they resemble the atomic orbitals, but they necessarily have finite contributions from atomic orbitals on other nuclear centers to ensure orthogonality. At $R=1$, each localized orbital at the corresponding atomic center still contains significant weight of the atomic orbitals on the nearest neighbors, while for $R \geq 3$, the localized orbitals are virtually single-centered.

Do these localized orbitals exhibit a local interaction structure similar to the tight-binding chain? To answer this question, we plot the hopping terms h_{ij} for $i \neq j$ in Figure 2.4. Recall that the hydrogen atoms are arranged on a ring, and therefore orbital 1 and 16 are in fact nearest neighbors, despite appearing on the opposite ends of the axes in Figure 2.4. At small separation, e.g. $R = 1$ (a.u.), hopping between distant localized orbitals is possible, but the hopping strength decays exponentially as internuclear distance increases. As we stretch the hydrogen ring, the hopping strength decays faster with the orbital separation. Finally at $R=5$ (a.u.), the hopping is strictly between nearest neighbors,

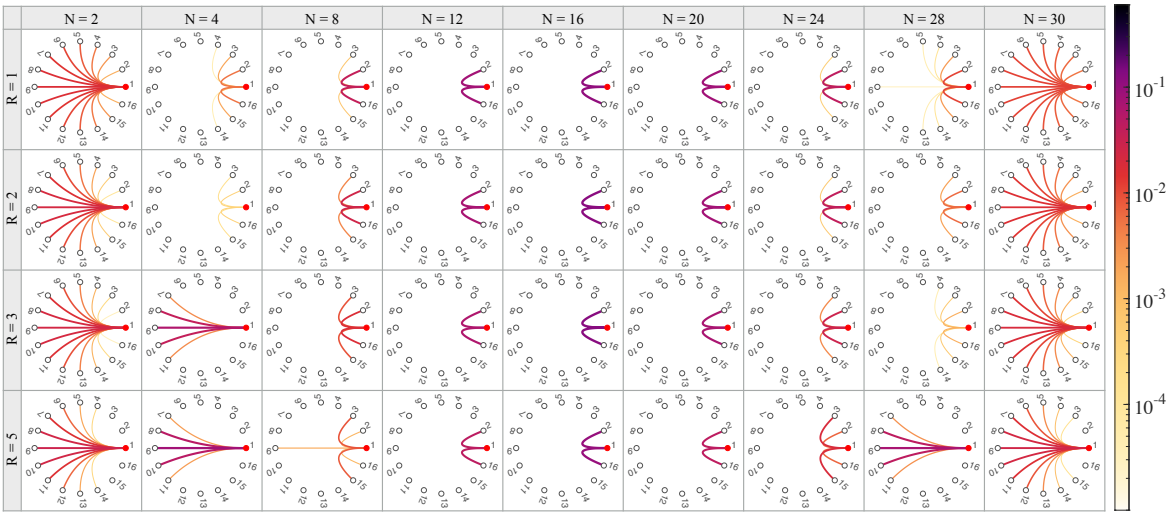

Figure 2.5: P-SSR entanglement between localized orbitals in H_{16} in STO-3G basis, for various numbers N of electrons and nearest neighbor distances R (a.u.). Since all orbitals are identical up to relabeling, only entangled pairs involving orbital 1 (filled red circle) are shown.

just as in the tight-binding model (2.14).

The calculation of the ground state of the hydrogen ring is done in three steps: (1) using the atomic wavefunction overlap matrix provided by MOLPRO [135]–[137], we symmetrically orthogonalize [134] the atomic orbitals into the localized orbitals, for nearest neighbor separation $R = 1, 2, 3, 5$ (a.u.). (2) With a preceding Hartree-Fock calculation, we then transform the Hartree-Fock canonical orbitals into the localized orbitals as a post Hartree-Fock step, and compute the matrix elements of the one- and two-electron Hamiltonians followed by outputting them in `FCIDUMP` [138] file format, all within the framework of MOLPRO. (3) With the `FCIDUMP` file, quantum chemistry density matrix renormalization group (QC-DMRG) calculations are performed to solve for the ground states, using the SYTEN [139], [140] package, originally created by Claudius Hubig. The calculations are carried out for various electron numbers, initialized with random configuration states. The DMRG convergence is particularly challenging, because of both the strong intrinsic correlation in the system and the additional entanglement due to the localized orbital basis representation. For the data we use, the maximal bond dimension is set at $m = 1000$. The final energies are chemically accurate, verified by the energy improvement below the order 10^{-3} (a.u.) in the DMRG calculations performed with bond dimension 2000.

2.2.2 Entanglement between orthogonal atomic orbitals in H_{16}

In this section, we present our main findings on the entanglement structure of the hydrogen ring H_{16}. We tabulate in Figure 2.5 the P-SSR entanglement between two localized orbitals for various nearest neighbor separations R and different numbers of electrons N in the ground state. For readability, we exploit the rotational symmetry of the system and only plot the entanglement associated to the localized orbital labeled 1 (represented as filled red circle). Entanglement involving other localized orbitals can be understood by relabeling them. The exact values of the P- and N-SSR entanglement can be found in Table D.1 and Table D.2 in Appendix D, respectively. With these data, we observe three consequential features of the orbital-orbital entanglement between the localized orbitals in H_{16}.

First, we observe that at half-filling ($N = 16$), the orbital-orbital entanglement is in complete agreement with the tight-binding model (2.14), namely only neighboring localized orbitals are entangled. In fact, this agreement extends beyond half-filling, as there is a region of filling fraction around $1/2$ where all orbital pairs separated by more than one lattice constant are disentangled, exactly as in Figure 2.1. This is particularly surprising for systems with small nearest neighbor distance R, since there the hopping strength beyond nearest neighbors is rather considerable.

Second, at low or high filling, the hydrogen ring also displays long-distance entanglement similar to the tight-binding model. This phenomenon here differs from the latter, however, by preferring to entangle localized orbitals that are farther apart. Recall that in the tight-binding model, the orbital-orbital entanglement is uniform when long-distance entanglement is realized. This departure from the non-interacting scenario is best exemplified by the $N=2$ column in Figure 2.5. In the ground state, due to the strong Coulomb repulsion, the two electrons would like to situate themselves as far apart as possible, forming singlet pairs at distant localized orbitals. Singlet states of such type, usually observed in a dissociated molecule, contain significant amount of entanglement. Singlet states realized on orbitals located closer to each other are of course possible, but they contribute to the total ground state with smaller weights. These two observations put together qualitatively explain the system's preference for long-distance entanglement at low particle filling. Furthermore, we notice that despite the lack of particle-hole symmetry in the system, the orbital entanglement in the $N=30$ column in Figure 2.5 displays a similar behavior as in $N=2$.

Third, the long-distance entanglement in the hydrogen ring is far more potent than that in the tight-binding model. In Eq. (2.26), we see that the long-distance entanglement in the tight-binding chain is quadratic in η for small η, which is obviously not the case here. This is best demonstrated by the entanglement between orbitals 1 and 9, which form the farthest separated pair, at $N=2$. The entanglement between them is of the order 10^{-2}, which is the same order as the nearest neighbor entanglement. In the tight-binding model, the available entanglement at this filling fraction would yield at the order 10^{-3}. This

yet again validates that interacting electronic systems contain significant entanglement that naturally distributed across distant spatial regions, making them ideal platforms for realizing quantum information protocols.

Chapter Summary

To summarize, in Section 2.1 we built upon Ref. [107] and derived analytic expressions for the entanglement between any two spatial orbitals in the tight-binding model (2.14), as a function of both inter-orbital separation d and particle filling fraction η. In particular, Eq. (2.3) revealed the existence of long-distance entanglement when the filling fraction is close to 0 or 1. Moreover, our asymptotic analyses for small particle (hole) filling fraction revealed that the entanglement between two orbitals is almost independent of their distance d, and quadratic in the particle (hole) filling fraction. For a fixed filling η, the entangling range is still finite, evident by the sudden death of entanglement when the two orbitals are separated beyond a critical distance. The leading order of the minimal disentangling distance $d_{\min}$ is proven to be diverging as η^{-1} when η is small, and $(1-\eta)^{-1}$ when η is close to 1.

In Section 2.2 we then upgraded the tight-binding model to the hydrogen ring, and analyzed the orbital-orbital entanglement therein. We discovered that the entanglement between the localized orbitals on the hydrogen ring can to a large degree be rationalized using the much simpler tight-binding model: close to half-filling only nearest neighbor orbitals can be entangled, but away from half-filling, long-distance entanglement appears. Yet, in contrast to the vanishingly weak long-distance entanglement in the tight-binding model, the entanglement between two localized orbitals sitting on far-separated nuclei is much more potent, at an order comparable to the nearest neighbor entanglement at half-filling. This surprising feature, conjectured to be a result of Coulomb interaction, suggests that chain-like molecules can potentially be considered as reservoirs of entanglement, and platforms for quantum information processing tasks.

Chapter 3

Orbital Entanglement in Covalent Bonds

Covalent bonding is a fundamentally quantum effect that binds atoms together as molecules. In 1916, Lewis first proposed the "octate rule" which defines the Lewis structure of bonding molecules [141] that every chemistry undergraduate student nowadays learns. The overlap between atomic orbitals from different atoms promotes the sharing of electron, and thus lowers the energy when the system is at equilibrium geometry. The idea of electron sharing from the Lewis theory still lies in the heart of modern theories of covalent bonding, and gave birth to many quantifiers that measures the order of a bond [142]. Examples include the covariance of atomic populations [143], electron delocalization index [144], Wiberg's index [145], to name a few. Most of these quantifiers can recover quite well the bonding picture in the Lewis paradigm.

However, there are many more systems that lie beyond the standard Lewis structures, and their bonds involve more than two atomic centers at a time. To characterize them, several multi-center bonding indices (MCI) were developed in attempt to prolong the success of the idea of electron sharing [146]–[151], but they suffer from several conceptual limitations. First, they generally require the pre-determined knowledge of the number of centers involved in the bond. Second, in the regime of large basis set, MCI can be rather difficult to calculate. Third, with or without additional normalization of such indices, it is conceptually delicate to compare the MCI values in bonds that involve different numbers of centers. Due to these limitations, so far there is no universally accepted post-Lewis bond order measure that is able to consistently and automatically extract the multi-center bonding structures from *ab initio* calculations with improvable accuracy.

Taking a step back, one realizes that electron sharing between two spatial regions is essentially reflected by the correlation function of electron density of the two regions,

much like a two-site correlator serving as the order parameter of a phase in a lattice model [152], [153]. Similar to the idea of using entanglement as an indicator of phase transition rather than resorting to one specific order parameter for each phase [23], [24], quantifying the all-inclusive entanglement between (among) the atomic regions, may finally resolve the above ambiguities related to electron sharing [154], [155]. Moreover, extenstive theories from quantum information on the quantification of bipartite [4]–[6], [156] and even multipartite entanglement [83]–[86] could facilitate a new bonding measure that assesses the large variety of bonding mechanisms under a unified framework.

To this end, there are a few conceptual questions we need to answer. First, how are the atomic regions defined? Establishing the notion of an atom in the molecule is the necessary first step of any bonding theory. Currently, there are two main approaches: One is the partitioning of the real space, leading to Bader's quantum theory of atoms in molecules (QTAIM) [157] and theories of "fuzzy atoms" [158]. While the real space approach is intuitive and is relatively insensitive to the choice of atomic basis sets, integrating (many-)electron density over the real space comes with demanding computational cost and is prone to numerical errors [159]. The other approach is the partitioning of the single-particle Hilbert space based on various orbital localization schemes [160]–[163], which is the approach we follow. But they introduce an additional degree of arbitrariness in the way that the orbitals are localized. This then brings us to the second question, namely, how does orbital localization affect orbital entanglement? To answer this, we must compare the orbital entanglement patterns at different degrees of orbital localization (delocalized, partially localized, and fully localized). The third question is, given the variety of different correlation measures discussed in Section 1.1, which one is more relevant for the description of a chemical bond? Or more precisely, should it be the total correlation, quantum correlation, or entanglement between the orbitals? And lastly, keeping in mind the ongoing second quantum revolution, we are also interested in the amount of useful entanglement between the atomic regions. This would mean to also take into account different superselection rules when quantifying orbital entanglement.

This chapter is organized as follows: In Section 3.1 we will thoroughly explore the effect of orbital localization together with P- and N-SSR, on various correlation quantities including the pivotal entanglement. We will demonstrate these effects in terms of both toy model examples for gaining analytic insights on the connection between orbital entanglement and chemical bonds, and *ab initio* ground state calculations for validating these insights in the presence of electron interaction. In Section 3.2 we turned what we learned in Section 3.1 into a fully automated construction of maximally entangled atomic orbitals (MEAO). Under this framework, we will define a unified measure for two- and multi-center bonds using genuine multipartite entanglement (GME).

3.1 Basis dependence of orbital entanglement

3.1.1 Analytic examples

In this subsection we demonstrate with two analytic examples (i) the strong influence of superselection rules on the accessible correlation and entanglement, (ii) the drastic difference of orbital correlation and entanglement between delocalized and localized orbital basis representation, and (iii) the subtle connection between entanglement and chemical bonding.

Single electron state

We consider a single polarized electron within the space of two orbitals A and B. The state of the electron is then simply a superposition of the form

$$|\Psi(\theta,\varphi)\rangle = \cos(\theta)|1_A,0_B\rangle + e^{i\varphi}\sin(\theta)|0_A,1_B\rangle, \tag{3.1}$$

where $|n_A,n_B\rangle \equiv (f_A^\dagger)^{n_A}(f_B^\dagger)^{n_B}|0\rangle$ are local occupation number eigenstates, and $\theta \in [0,\pi)$, $\varphi \in [0,2\pi)$. Such a state belongs to the one-particle Hilbert space $\mathcal{H}^{(1)}$ isomorphic to that of a single qubit, which is a subspace of the four-dimensional total Fock space $\mathcal{F}[\mathcal{H}^{(1)}]$. Referring to the tensor product between the two local Fock spaces $\mathcal{F}[\mathcal{H}^{(1)}] = \mathcal{F}[\mathcal{H}_A^{(1)}]\otimes \mathcal{F}[\mathcal{H}_B^{(1)}]$, the density operator $\rho(\theta,\varphi)$ is given in the basis $|0_A,0_B\rangle, |1_A,0_B\rangle, |0_A,1_B\rangle, |1_A,1_B\rangle$ by,

$$\rho(\theta,\varphi) = |\Psi(\theta,\varphi)\rangle\langle\Psi(\theta,\varphi)| = \begin{pmatrix} 0 & 0 & 0 & 0 \\ 0 & \cos^2(\theta) & \frac{e^{i\varphi}}{2}\sin(2\theta) & 0 \\ 0 & \frac{e^{-i\varphi}}{2}\sin(2\theta) & \sin^2(\theta) & 0 \\ 0 & 0 & 0 & 0 \end{pmatrix}. \tag{3.2}$$

Since $\rho(\theta,\varphi)$ is pure (cf. Eq. (1.3)), the associated entanglement E and quantum correlation Q are the same, and so are the closest separable χ_ρ and classical states σ_ρ, respectively. The closest product state π_ρ as well as the classical and separable states (in this case they coincide) χ_ρ to $\rho(\theta,\varphi)$ is diagonal in the same basis with

$$\begin{aligned} \mathrm{diag}(\pi_\rho) &= (\cos^4(\theta), \frac{1}{4}\sin^4(2\theta), \frac{1}{4}\sin^4(2\theta), \sin^4(\theta)), \\ \mathrm{diag}(\chi_\rho) &= (0, \cos^2(\theta), \sin^2(\theta), 0). \end{aligned} \tag{3.3}$$

Moreover, the total correlation I, quantum correlation Q, classical correlation C, and entanglement E of $\rho(\theta,\varphi)$ are given by

$$\begin{aligned} \frac{1}{2}I(\rho) &= Q(\rho) = C(\rho) = E(\rho) \\ &= -[\cos^2(\theta)\log(\cos^2(\theta)) + \sin^2(\theta)\log(\sin^2(\theta))] \\ &\equiv P(\theta). \end{aligned} \tag{3.4}$$

	I	C	Q	E
No SSR	$2P(\theta)$	$P(\theta)$	$P(\theta)$	$P(\theta)$
P/N-SSR	$P(\theta)$	$P(\theta)$	0	0

Table 3.1: Total correlation I, classical correlation C, quantum correlation Q, and entanglement E between the two orbitals A and B in the single electron state (3.1), for the case without SSR and with P/N-SSR.

In the presence of a superselection rule, the superselected state $\rho^{\mathrm{P}}(\theta,\varphi)$ ($\rho^{\mathrm{N}}(\theta,\varphi)$) loses all coherence between different local parity (particle number) sectors

$$\rho^{\mathrm{P,\,N}}(\theta,\varphi) = \cos^2(\theta)|1_A,0_B\rangle\langle 1_A,0_B| + \sin^2(\theta)|0_A,1_B\rangle\langle 0_A,1_B| \ . \tag{3.5}$$

As can be easily seen from its form in Eq. (3.5), the superselected state $\rho^{\mathrm{P,\,N}}(\theta,\varphi)$ is separable, since it can be written as a simple mixture of product states. Furthermore, it is also classical since it is diagonal in a product basis. From this it follows, that all correlation in (3.5) between the two orbitals are classical. Therefore a single electron state of the form (3.1) does not contain any useful entanglement or quantum correlation resource. We summarize all correlation quantities with and without SSRs in Table 3.1.

Single covalent bond

In the second analytic example, we apply the same quantum information concepts as in the previous section now to a pair of bonding electrons in a symmetric diatomic molecule, described by the state

$$|\Psi\rangle = f^\dagger_{\phi\uparrow} f^\dagger_{\phi\downarrow}|0\rangle \ . \tag{3.6}$$

Here, ϕ is the bonding orbital, formed by superimposing two $1s$-like orbitals on the two nuclear centers L (left) and R (right)

$$\phi = \frac{\varphi_L + \varphi_R}{\sqrt{2(1+\langle\varphi_L|\varphi_R\rangle)}}. \tag{3.7}$$

Before we are able to proceed with a calculation of the correlation in $|\Psi\rangle$, being it quantum or classical, we first have to decide on a choice of orbital splitting. An obvious choice would be to consider the correlation between the bonding orbital ϕ and the corresponding antibonding orbital

$$\bar{\phi} = \frac{\varphi_L - \varphi_R}{\sqrt{2(1-\langle\varphi_L|\varphi_R\rangle)}}. \tag{3.8}$$

Together ϕ and $\bar{\phi}$ form a minimal active space, within which we will perform all our entanglement analysis. Referring to the splitting between ϕ and $\overline{\phi}$, $|\Psi\rangle$ is clearly a product

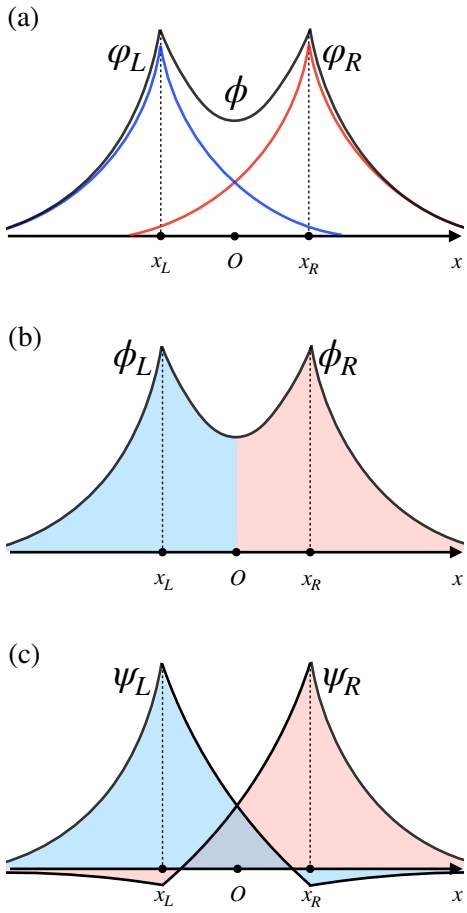

Figure 3.1: (a) Formation of the (up to normalization) bonding orbital ϕ with two local atomic $1s$-type orbitals φ_L and φ_R with nuclear centers at $x_{L,R}$. (b) Projection of the bonding orbital onto the left and right half space. (c) Rotated bonding and antibonding orbitals ψ_L and ψ_R.

state. As a result, it has zero correlation and entanglement. While this finding seems odd at first sight, as one would expect a considerable amount of entanglement to be "stored" in a chemical bond, let us next consider a different, seemingly less intuitive alternate choice of the splitting.

In the top panel of Figure 3.1, we illustrate the formation of the bonding orbital ϕ from the two local $1s$-type orbitals φ_L and φ_R, respectively. We then make a cut at the center of the molecule dividing the space into left and right half, and project the bonding orbital onto the two half-spaces (central panel), denoted as ϕ_L and ϕ_R. After normalization, the resulting two-electron wave function (3.6) can be written as

$$\begin{aligned} |\Psi\rangle &= \frac{1}{2}(f^\dagger_{\phi_L\uparrow} + f^\dagger_{\phi_R\uparrow})(f^\dagger_{\phi_L\downarrow} + f^\dagger_{\phi_R\downarrow})|0\rangle \\ &= \frac{1}{2}(f^\dagger_{\phi_L\uparrow}f^\dagger_{\phi_L\downarrow} + f^\dagger_{\phi_R\uparrow}f^\dagger_{\phi_R\downarrow} + f^\dagger_{\phi_L\uparrow}f^\dagger_{\phi_R\downarrow} - f^\dagger_{\phi_L\downarrow}f^\dagger_{\phi_R\uparrow})|0\rangle. \end{aligned} \tag{3.9}$$

Hence, with respect to a splitting between the left and right projected orbitals ϕ_L and ϕ_R, simple calculations lead to a set of entirely different values of correlation quantities of $\rho = |\Psi\rangle\langle\Psi|$

$$\frac{1}{2}I(\rho) = Q(\rho) = C(\rho) = E(\rho) = 2\log 2. \tag{3.10}$$

When superselection rules are considered, P-SSR and N-SSR eliminate coherent terms between different local parity and particle number sectors, respectively, leading to superselected states of the form

$$\begin{aligned} \rho^{\mathrm{P}} &= \frac{1}{2}|\Psi_{\mathrm{even}}\rangle\langle\Psi_{\mathrm{even}}| + \frac{1}{2}|\Psi_{\mathrm{odd}}\rangle\langle\Psi_{\mathrm{odd}}| \\ \rho^{\mathrm{N}} &= \frac{1}{4}|\Psi_{2,0}\rangle\langle\Psi_{2,0}| + \frac{1}{4}|\Psi_{0,2}\rangle\langle\Psi_{0,2}| + \frac{1}{2}|\Psi_{1,1}\rangle\langle\Psi_{1,1}|, \end{aligned} \tag{3.11}$$

where

$$\begin{aligned} |\Psi_{\mathrm{odd}}\rangle &= |\Psi_{1,1}\rangle = \frac{1}{\sqrt{2}}(f^\dagger_{\phi_L\uparrow}f^\dagger_{\phi_R\downarrow} - f^\dagger_{\phi_L\downarrow}f^\dagger_{\phi_R\uparrow})|0\rangle, \\ |\Psi_{\mathrm{even}}\rangle &= \frac{1}{\sqrt{2}}(f^\dagger_{\phi_L\uparrow}f^\dagger_{\phi_L\downarrow} + f^\dagger_{\phi_R\uparrow}f^\dagger_{\phi_R\downarrow})|0\rangle \\ |\Psi_{2,0}\rangle &= f^\dagger_{\phi_L\uparrow}f^\dagger_{\phi_L\downarrow}|0\rangle, \\ |\Psi_{0,2}\rangle &= f^\dagger_{\phi_R\uparrow}f^\dagger_{\phi_R\downarrow}|0\rangle. \end{aligned} \tag{3.12}$$

In this case both P- and N-SSR reduce quantum correlation as well as entanglement by 50% and 75%, respectively, while at the same time having no effect on the classical correlation. Consequently, the total correlation is lowered by the same amount of decrease in the quantum correlation, as the relation $I = C + Q$ holds in this case. We summarize the correlation quantities with and without SSRs in Table 3.2.

$\phi, \overline{\phi}$	I	C	Q	E
No SSR	0	0	0	0
P, N-SSR	0	0	0	0
ϕ_L, ϕ_R	I	C	Q	E
No SSR	$4\log 2$	$2\log 2$	$2\log 2$	$2\log 2$
P-SSR	$3\log 2$	$2\log 2$	$\log 2$	$\log 2$
N-SSR	$\frac{5}{2}\log 2$	$2\log 2$	$\frac{1}{2}\log 2$	$\frac{1}{2}\log 2$

Table 3.2: Total correlation, classical correlation, quantum correlation, and entanglement between the bonding and antibonding orbitals in single bond state $|\Psi\rangle$ in (3.6) (top panel), and between the two projected orbitals in the same state $|\Psi\rangle$ re-expressed in (3.9) (bottom panel), for the case without SSR, with P- and N-SSR.

This example already illustrates that, by referring to a suitable orbital splitting that allows to capture a certain degree of spatial locality, one can recover strong correlation as one would expect in a chemical bond. Although the above choice of splitting seems from a quantum information perspective to be reasonable in terms of recovering correlation effects, it requires an artificial cut of the bonding orbital into two halves. Moreover, from the resulting orbitals ϕ_L and ϕ_R, one cannot recover the antibonding orbital $\overline{\phi} \propto \varphi_L - \varphi_R$. As a matter of fact, $\{\phi_L, \phi_R\}$ do not span the same Hilbert space as the two local atomic orbitals $\{\varphi_L, \varphi_R\}$. Therefore, the optimal approach must include in addition the antibonding orbital $\overline{\phi}$ into the total Hilbert space. To explore all possible choices of orbital bases, we unitarily (assuming for simplicity but without loss of generality real coefficients) transform the orbitals ϕ, $\overline{\phi}$

$$\begin{aligned} \psi_L &= \cos(\theta)\phi + \sin(\theta)\overline{\phi}, \\ \psi_R &= -\sin(\theta)\phi + \cos(\theta)\overline{\phi}. \end{aligned} \tag{3.13}$$

After this unitary basis rotation, we can rewrite the state $|\Psi\rangle$ in Eq. (3.6) as

$$|\Psi\rangle = [\cos^2(\theta) f^\dagger_{\psi_L\uparrow} f^\dagger_{\psi_L\downarrow} + \sin^2(\theta) f^\dagger_{\psi_R\uparrow} f^\dagger_{\psi_R\downarrow} + \cos(\theta)\sin(\theta)(f^\dagger_{\psi_L\uparrow} f^\dagger_{\psi_R\downarrow} - f^\dagger_{\psi_L\downarrow} f^\dagger_{\psi_R\uparrow})]|0\rangle. \tag{3.14}$$

The spectrum of the orbital reduced state ρ_L can be read off from the above expansion

$$\mathrm{Spec}(\rho_L) = \{\cos^4(\theta), \sin^4(\theta), \cos^2(\theta)\sin^2(\theta), \cos^2(\theta)\sin^2(\theta)\}. \tag{3.15}$$

The entanglement of $\rho = |\Psi\rangle\langle\Psi|$ is simply the von Neumman entropy of ρ_L

$$\begin{aligned} E(\rho) &= S(\rho_L) \\ &= -\cos^4(\theta)\log(\cos^4(\theta)) - \sin^4(\theta)\log(\sin^4(\theta)) \\ &\quad - 2\cos^2(\theta)\sin^2(\theta)\log(\cos^2(\theta)\sin^2(\theta)) \\ &= -2\cos^2(\theta)\log(\cos^2(\theta)) - 2\sin^2(\theta)\log(\sin^2(\theta)) \\ &= 2P(\theta). \end{aligned} \tag{3.16}$$

From Eq. (3.16) it follows that maximal entanglement is realized by a rotation with angle $\theta = \frac{\pi}{4}$. As can be seen from Table 3.2, in the latter basis the resulting $E(\rho)$ reaches also $2\log 2$, in perfect agreement with the case of the artificial half-splitting discussed previously. Moreover, assuming a rotation of $\theta = \frac{\pi}{4}$, the transformed orbitals ψ_L and ψ_R, illustrated in the bottom panel (c) of Figure 3.1, are simply equal superpositions of the initial bonding ϕ and antibonding $\overline{\phi}$ orbitals, with plus and minus signs respectively. As a matter of fact, the final expression for the state in Eq. (3.14), expressed in the basis $\{\psi_L, \psi_R\}$, takes the same form as its counterpart in Eq. (3.9), with the replacement $\psi_{L,R} \to \phi_{L,R}$. Therefore, in the particular choice of $\theta = \frac{\pi}{4}$, we find that all correlation quantities (with or without SSRs) of the state given by Eq. (3.14) coincide with those of the state in Eq. (3.9). Thus, we can interpret the rotation angle $\theta = \frac{\pi}{4}$ as the point where maximal orbital localization effect is achieved, while still keeping the orbitals orthogonal and without dissecting them.

To explore more comprehensively the connection between orbital entanglement and chemical bonding, let us consider the cases of maximal and minimal entanglement in some prototypical states of definite bond order. In molecular orbital (MO) theory, the bond order of a state is defined as the difference in the occupation number between the bonding orbital ϕ and its antibonding orbital partner $\overline{\phi}$ divided by 2 [164], [165]

$$\text{bond order} = \frac{1}{2}(N_{\text{bond}} - N_{\text{antibond}}). \tag{3.17}$$

To illustrate the concept of a bond order we consider the following four states

$$\begin{aligned}
|\Psi_1\rangle &= f^\dagger_{\phi\uparrow}|0\rangle, \\
|\Psi_2\rangle &= f^\dagger_{\phi\uparrow} f^\dagger_{\phi\downarrow}|0\rangle, \\
|\Psi_3\rangle &= f^\dagger_{\phi\uparrow} f^\dagger_{\phi\uparrow} f^\dagger_{\overline{\phi}\uparrow}|0\rangle, \\
|\Psi_4\rangle &= f^\dagger_{\phi\uparrow} f^\dagger_{\phi\downarrow} f^\dagger_{\overline{\phi}\uparrow} f^\dagger_{\overline{\phi}\downarrow}|0\rangle,
\end{aligned} \tag{3.18}$$

which have a bond order of $\frac{1}{2}$, 1, $\frac{1}{2}$, and 0, respectively, according to (3.17). We can easily find the minimal entanglement of all four states to be zero, with respect to the orbital partition between ϕ and $\overline{\phi}$, that is, the bonding and antibonding orbitals. Under an arbitrary orbital rotation of angle θ

$$\begin{aligned}
f^\dagger_{\psi_L\sigma} &= \cos(\theta) f^\dagger_{\phi\sigma} + \sin(\theta) f^\dagger_{\overline{\phi}\sigma}, \\
f^\dagger_{\psi_R\sigma} &= \sin(\theta) f^\dagger_{\phi\sigma} - \cos(\theta) f^\dagger_{\overline{\phi}\sigma},
\end{aligned} \tag{3.19}$$

the four states transform to

$$\begin{aligned}
|\Psi_1\rangle &= \cos(\theta) f^\dagger_{\psi_L\uparrow}|0\rangle + \sin(\theta) f^\dagger_{\psi_R\uparrow}|0\rangle, \\
|\Psi_2\rangle &= \cos^2(\theta) f^\dagger_{\psi_L\uparrow} f^\dagger_{\psi_L\downarrow}|0\rangle + \sin^2(\theta) f^\dagger_{\psi_R\downarrow} f^\dagger_{\psi_R\downarrow}|0\rangle + \cos(\theta)\sin(\theta)(f^\dagger_{\psi_L\uparrow} f^\dagger_{\psi_R\downarrow} - f^\dagger_{\psi_L\downarrow} f^\dagger_{\psi_R\uparrow})|0\rangle, \\
|\Psi_3\rangle &= f^\dagger_{\psi_L\uparrow}(\cos(\theta) f^\dagger_{\psi_L\downarrow} f^\dagger_{\psi_R\uparrow} - \sin(\theta) f^\dagger_{\psi_R\uparrow} f^\dagger_{\psi_R\downarrow})|0\rangle, \\
|\Psi_4\rangle &= f^\dagger_{\psi_L\uparrow} f^\dagger_{\psi_L\downarrow} f^\dagger_{\psi_R\uparrow} f^\dagger_{\psi_R\downarrow}|0\rangle.
\end{aligned} \tag{3.20}$$

$\overline{\phi}$	—	—	$\uparrow$	$\uparrow\downarrow$
ϕ	$\uparrow$	$\uparrow\downarrow$	$\uparrow\downarrow$	$\uparrow\downarrow$
	$\|\Psi_1\rangle$	$\|\Psi_2\rangle$	$\|\Psi_3\rangle$	$\|\Psi_4\rangle$
Bond Order	$\frac{1}{2}$	1	$\frac{1}{2}$	0
$E_{\max}$	$\log 2$	$2\log 2$	$\log 2$	0
$E_{\min}$	0	0	0	0

Table 3.3: Bond order, maximal and minimal entanglement of the four states given in Eq. (3.18).

The latter shows that the resulting entanglement E with respect to the partition between ψ_L and ψ_R of $|\Psi_{1,2,3}\rangle$ is maximized for $\theta = \frac{\pi}{4}$, whereas the entanglement of $|\Psi_4\rangle$ remains invariant under orbital transformation. To summarize these findings we compile in Table 3.3 the maximal and minimal entanglement of these four states as a function of the bond order. Remarkably, we find that the maximal entanglement, realized between the maximally localized orbitals, is *indeed* proportional to the bond order (3.17) of each state. A single bond of bond order 1 thus corresponds to the entanglement value $E = 2\log 2$ between the fully-localized atomic-like orbitals. Intriguingly, this value exceeds by an order of magnitude the numbers reported in previous studies [62], [155], [166]–[172]. In turn, this clearly demonstrates that quantum information tools applied to delocalized orbitals describe primarily the validity of the independent electron-pair picture rather than the bonding structure of molecular systems.

Lastly, we remark that the insights we gained from the single covalent bond states extends beyond bonds of order 1. Namely, for a prototypical K-fold bond state $|\Psi_K\rangle = \prod_{k=1}^{K} f^\dagger_{\phi_k\uparrow} f^\dagger_{\phi_k\downarrow}|0\rangle$, rotating pairs of bonding and antibonding orbitals ϕ_k and $\bar{\phi}_k$ by $\pi/4$ leads to K pairs of maximally entangled rotated orbitals, amounting to $K(2\log 2)$ of total orbital-orbital entanglement.

3.1.2 Numerical examples: ethylene, polyene, and benzene

In the previous section we identify in the simple molecular orbital (MO) picture that a single covalent bond correspond to a pair of maximally entangled localized atomic-like orbitals. Now, we would like to extend this identification (i) to cases of interacting electrons in molecules, (ii) cases of more than two atomic centers, and (iii) cases without a clear Lewis structure. To still maintain a tight connection to the analytic examples above, we consider only the out-of-plane π-orbitals of ethylene (C_2H_4), polyenes (CH_2-$(CH)_n$-CH_2), and bezene C_6H_6, so that only one atomic orbital per atomic center is taken into consideration. The π-orbitals of each molecule form a complete active space (CAS), within which

we solve the electronic interaction problem to near exact accuracy using a matrix product state (MPS) ansatz optimized by density matrix renormalization group (DMRG) software QCMaquis [173]–[175]. The remaining orbitals associated to the σ-bonds are treated in a mean-field manner. All calculations were carried out in C_1 point group symmetry as well as with correlation-consistent Dunning-type basis sets [176] of double-ζ quality (cc-pVDZ).

In order to critically assess the correlation contributions introduced in Section 1.1 within the π-space of our molecular systems, we considered three distinct set of MOs that are related to each other by suitable orbital rotations. We first performed self-consistent field (SCF) Hartree-Fock (HF) calculations for the spin-singlet ($S = 0$) ground state of each molecule, yielding a set of *canonical* HF MOs for the respective molecular systems. In a following step, we then applied a Pipek-Mezey (PM) [161] localization procedure which gives a second set of *partially* localized MOs (dubbed as "PM-localized" in the following) while retaining the σ- and π-character of the initial canonical MOs, respectively. It should be emphasized that, although it is possible to perform the PM-localization on the entire set of canonical MOs [154], in this work the PM-localization is implemented separately within the bonding (occupied) and antibonding (virtual) orbital subspaces, as it is common practice in the quantum chemistry community. The final set of *atomic-like* orbitals was obtained by means of a (sequence of) 2×2 Jacobi-rotation(s) by an angle θ within the π-space, and setting out from either the PM-localized MO basis (ethylene and polyenes) or the canonical MO basis (benzene). In the former, a single rotation by $\theta = \frac{\pi}{4}$ within a pair of bonding π and its antibonding partner π^* suffices to yield the desired atomic-like molecular basis. In contrast to the remaining molecules studied in this work, obtaining an atomic-like orbital basis for benzene requires in general six-orbital unitary transformations, which can be decomposed into three consecutive sets of pairwise rotations (see Appendix B).

Ethylene

We first study one of the simplest molecules containing a prototypical π-bond, namely ethylene (C_2H_4). Since the π-bond comprises only two carbon centers, the resulting CAS contains only $n_e = n_o = 2$ or for short CAS(2,2), that is the bonding and antibonding orbitals π and π^*, which are constructive and destructive superposition of two out-of-plane p_z-orbitals on the two carbon atoms, respectively. For non-interacting electrons, both electrons would occupy the energetically more favorable π-orbital, forming a product state with respect to partitioning of the bonding and antibonding orbitals, as in (3.6), whereas electron interaction lifts the occupancy of the π^*-orbital to around 0.03 electron pair, thus introducing a small deviation from the aforementioned product state. From this simple observation, we should expect a low correlation and entanglement between the π- and π^*-orbital, and this is indeed what we conclude from our analysis in Figure 3.2 for the common, *canonical* case. However, more correlation and entanglement will be recovered as we *fully* localize these two orbitals.

C_2H_4					
Canonical	I	C	Q	E	
No SSR	0.2819	0.1410	0.1410	0.1410	
P-SSR	0.2819	0.1410	0.1410	0.1410	
N-SSR	0.1410	0.1410	0.0000	0.0000	
PM-localized	I	C	Q	E	
No SSR	0.2819	0.1410	0.1410	0.1410	
P-SSR	0.2819	0.1410	0.1410	0.1410	
N-SSR	0.1410	0.1410	0.0000	0.0000	
Atomic-like	I	C	Q	E	
No SSR	2.6468	1.3234	1.3234	1.3234	
P-SSR	2.0165	1.3234	0.6931	0.6931	
N-SSR	1.7916	1.3234	0.4682	0.4682	

Figure 3.2: Total correlation I, classical correlation C, quantum correlation Q, and entanglement E between two canonical, PM-localized, and atomic-like orbitals used for constructing the ground state of C_2H_4, for the case without SSR, with P-SSR, and with N-SSR. For each choice of orbital pair, contour plots (with an isosurface value of 0.05) of the orbitals are shown on the right most column.

In Figure 3.2 we listed the total correlation I, classical correlation C, quantum correlation Q, and entanglement E between the two orbitals based on canonical, PM-localized, and atomic-like orbitals. In addition, for each correlation quantity, the effect of P-SSR and N-SSR are taken into account in our analysis. Since the active space comprises in all three cases only two orbitals, it follows that single orbital correlation and entanglement (those between one orbital and the rest of the system) will coincide with the orbital-orbital ones.

Starting with the canonical case (upper panel of Figure 3.2), all correlation quantities are low, as anticipated above. In the case without SSRs and recalling that in this particular example the two-orbital reduced state is pure, the total correlation I is simply twice the amount of the classical C and quantum parts Q such that there is no distinction between quantum correlation Q and entanglement E. Interestingly, P-SSR does not show any diminishing effect in any of the correlation quantities. We can explain this somewhat surprising fact with the observation that the electronic ground state does not contain contributions from singly-excited configurations, and thus can solely be written as a superposition of doubly-occupied and empty configurations, respectively. Moreover, this is also the reason why no quantum correlation or entanglement survive in the presence of N-SSR: the ground state contains only a superposition of configurations with different local particle numbers.

Hence, in order to recover strong correlation and entanglement in the π-bond, we applied two different localization schemes to the canonical orbitals as detailed at the start of this section. In this particular case, the PM-localization scheme yields *localized* π-MOs matching the original canonical π-orbitals, since the system comprises only σ- and π-type orbitals and the PM-localization scheme preserves the σ- and π-character of the MOs. As a result, we see no difference in their respective correlation quantities with respect to the canonical case and the data for the PM case coincide in all three rows (see second panel in Figure 3.2) with their respective counterpart in the upper panel of the canonical case. In passing we note that these findings will not hold when the canonical MOs span over several bonding regions, as we shall see in the following sections. Our second localization scheme sets out from the PM-localized MOs (in this case equivalently the canonical MOs) where we apply in an ensuing step a 2×2 Jacobi rotation between the two PM-localized orbitals by an angle $\theta = \frac{\pi}{4}$. This unitary rotation leads to two atomic-like orbitals

$$\begin{aligned} \psi_L &= \frac{1}{\sqrt{2}}\pi_{\mathrm{PM}} + \frac{1}{\sqrt{2}}\pi^*_{\mathrm{PM}}, \\ \psi_R &= \frac{1}{\sqrt{2}}\pi_{\mathrm{PM}} - \frac{1}{\sqrt{2}}\pi^*_{\mathrm{PM}}, \end{aligned} \tag{3.21}$$

where $\pi^{(*)}_{\mathrm{PM}}$ are the PM-localized $\pi^{(*)}$-orbitals. As illustrated in the third panel of Figure 3.2 (atomic-like), the resulting $\psi_{1,2}$ are indeed fully localized around one carbon center in stark contrast to the localized molecular orbitals obtained from the PM localization scheme. Moreover, these atomic-like orthogonal orbitals act identically as the original atomic orbitals, in a sense that the same linear combination of the former as the latter give rise to the bonding and antibonding orbitals (up to overall normalization)

$$\begin{aligned} \pi_{PM} &= \frac{1}{\sqrt{2}}\psi_L + \frac{1}{\sqrt{2}}\psi_R, \\ \pi^*_{PM} &= \frac{1}{\sqrt{2}}\psi_L - \frac{1}{\sqrt{2}}\psi_R, \end{aligned} \tag{3.22}$$

thus preserving the information of the bond construction. And most importantly, we now recover strong correlation and entanglement in the π-bond. Without SSRs, the entanglement E between ψ_1 and ψ_2 reaches 95% of its maximum value of $2\log 2$, in excellent agreement with the degree of entanglement that we observed for a prototypical bond in the analytic example discussed in Section 3.1.1. Moreover, the effect of SSRs is qualitatively different in case of the atomic-like orbitals. P-SSR cancels around half of the entanglement, whereas around a third of the entanglement is still accessible under the restriction of N-SSR. The latter is rooted in the complexity of the ground state wave function which, in contrast to the much simpler form within the canonical and PM-localized orbitals bases, is now composed of several configurations of comparable weights, including those with single local occupations.

It is worth noting that the fully localized orbitals are only 95% maximally entangled. This deviation from the perfect single bond in Section III B is not an artifact of an imper-

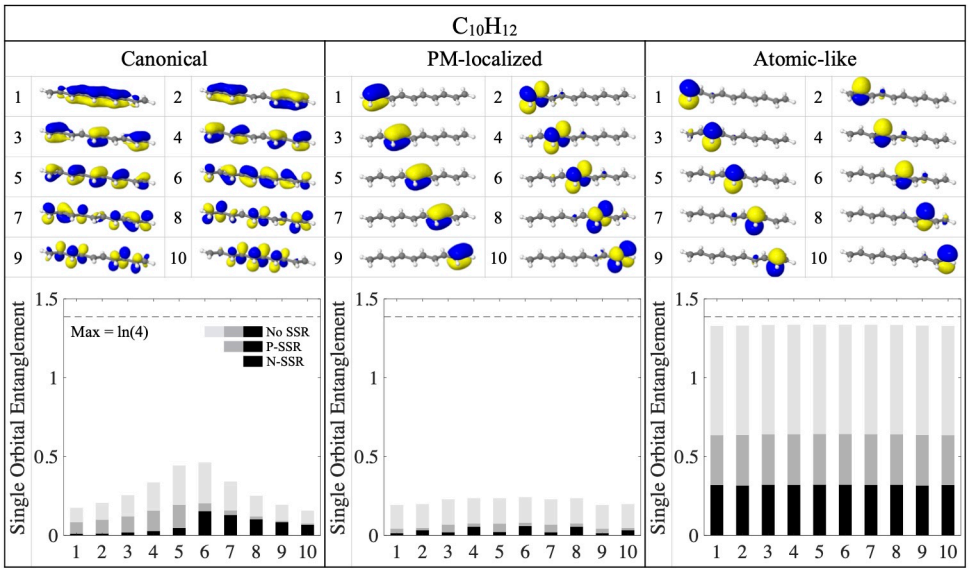

Figure 3.3: Single orbital entanglement in the CAS(10,10)-optimized electronic ground state of $C_{10}H_{12}$. The orbital numbering on the x-axis in the lower panel follows the one given for the canonical, PM-localized, and atomic-like orbitals in the upper panel (plotted with an isosurface value of 0.05). The color code for the single orbital entanglement data is as follows: no SSR (all color), P-SSR (black and dark grey), and N-SSR (dark grey).

fect choice of orbitals, but rather an inevitable consequence of electron interaction. The latter namely introduces a multireference character to the ground state, and excites finite occupation in the antibonding orbital. In other words, the maximal entanglement $2\log 2$ in a perfect single bond state $f^\dagger_{\phi\uparrow} f^\dagger_{\phi\downarrow}|0\rangle$ can never be realized in an interacting molecule.

To summarize the main conclusions from this seemingly simple example, enforcing *atomic-like* locality in the MO basis for the π-orbital space leads to two distinct features of the π-bond in comparison to the commonly considered canonical case: (i) the ground state electronic wave function markedly changes character from single- to strongly multi-configurational and, more importantly, (ii) the actual entanglement E between the valence $\pi^{(*)}$-orbitals without SSR increases drastically from 5% to 95% of its maximum value of $2\log 2$ which was established by means of an analytical model for a chemical bond in Section 3.1.1.

Polyene

Having analyzed in the previous section the conceptually most simple "mono"-ene, we will focus in the following on all-*trans* polyenes CH_2-$(CH)_n$-CH_2, a family of extended, prototypical, π-conjugated molecular systems. More specifically, we consider two exemplary

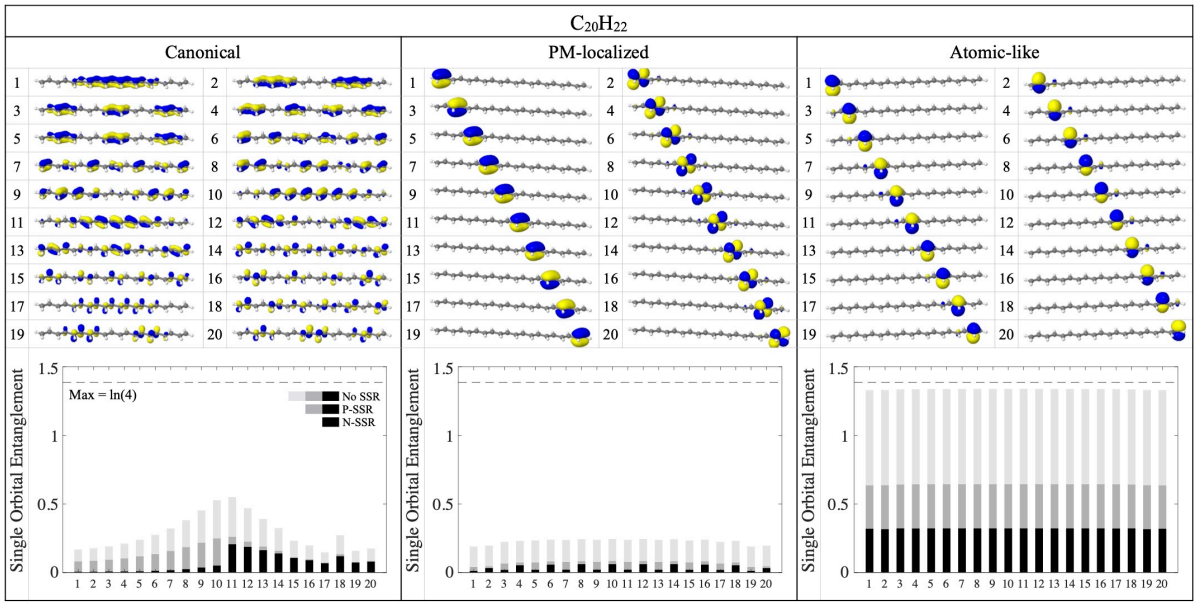

Figure 3.4: Single orbital entanglement in the CAS(20,20)-optimized electronic ground state of $C_{20}H_{22}$. The orbital numbering on the x-axis in the lower panel follows the one given for the canonical, PM-localized, and atomic-like orbitals in the upper panel (plotted with an isosurface value of 0.05). The color code for the single orbital entanglement data is as follows: no SSR (all color), P-SSR (black and dark grey), and N-SSR (dark grey).

systems with $n = 8$ (decapentaene, $C_{10}H_{12}$) and $n = 18$ (eicosadecaene, $C_{20}H_{22}$). To unambiguously study the individual correlation contributions within the valence $\pi^{(*)}$-space requires for those molecular systems active orbital spaces of CAS(10,10) and CAS(20,20), respectively. Given the size of these CAS spaces, single-orbital and orbital-orbital correlations will no longer coincide, and need to be addressed separately. With $n_o > 2$, the single orbital correlation quantifies the correlation between one orbital and all other orbitals, including multipartite correlations, much beyond any orbital-orbital correlations. As in the case of ethylene in the previous section, we will consider for our analysis three distinct choices of MO basis, namely canonical, PM-localized, and atomic-like orbitals.

As we are dealing with a pure ground state, single orbital correlation can be related to the single orbital entanglement via simple linear relations [119], and the latter is equivalent with the single-orbital quantum correlation. To this end, it suffices to focus in this paragraph solely on single-orbital entanglement data.

In Figure 3.3 and Figure 3.4, respectively, we present the canonical, PM-localized, and atomic-like orbitals for $C_{10}H_{12}$ and $C_{20}H_{22}$ (upper panels) along with the single orbital entanglement of each orbital (lower panels of Figures 3.3 and 3.4), namely the entanglement between one orbital and the remaining orbitals comprised in the active space. Before embarking on an in-depth discussion of the entanglement data, we first emphasize two obvious key differences between the MOs of the polyenes shown in the upper panels of Figure 3.3 and Figure 3.4, respectively, and those of ethylene: (i) the canonical MOs for both extended systems are highly delocalized across the entire carbon-carbon chain; (ii) the PM-localized MOs no longer coincide with the canonical ones, and are localized only around two carbon centers involved in a $\pi^{(*)}$-bond. Hence, the PM-localization scheme succeeds in *partially* localizing the canonical MOs. Finally, as was the case for ethylene, to obtain atomic-like orbitals requires a further rotation of each corresponding pair of PM-localized $\pi^{(*)}$-MOs by $\theta = \frac{\pi}{4}$.

Considering next the single orbital entanglement shown in the lower panels of the respective Figures 3.3 and 3.4, the three choices of MO basis reveal drastically different behaviors. For both molecules, the canonical MOs display a large variation in their single orbital entanglement. The most entangled orbital #6 (#11 in $C_{20}H_{22}$) corresponds to the lowest unoccupied molecular orbital (LUMO) in either case and contains almost three times the amount of the least entangled ones. The difference between the two SSRs manifests itself as follows: while the superselected entanglement (allowed by either P- or N-SSR) of the first half of the canonical π-MOs is mostly forbidden by N-SSR, that of the second half of the orbitals — corresponding to the π^*-subspace — is mostly N-SSR compatible. The fact that we still find single orbital entanglement for the π-orbitals is therefore a clear indication of their departure from a double occupancy (as would be expected in an uncorrelated mean-field model) in the CAS-optimized ground-state wave function due to the presence of electron-electron correlation which is most dominant for the highest occupied molecular orbital (HOMO) and the one directly below (HOMO-1). Likewise, a

similar explanation holds for P- and N-SSR single orbital entanglement data within the π^*-subspace where the discernible deviations between the two SSR schemes are a result of the departure from zero occupancy of the π^*-MOs, predominantly of the LUMO and LUMO+1.

Naively, one would expect that the single orbital entanglement of the PM-localized and atomic-like orbitals should qualitatively show the same kind of deviation from that of the canonical MOs, with the latter being stronger for the atomic-like orbitals. However, this is clearly not the case here. The single orbital entanglement of the PM-localized MOs is much more uniformly distributed than that of the canonical ones, and overall visibly lower. On the one hand, the uniformity of the entanglement originates from the near translation invariance of the PM-localized MOs. Moreover, the entanglement differs only slightly from uniformity when the MO is located at the edge of the carbon-carbon chain, where a boundary effect comes into play. On the other hand, the lower value of entanglement of the PM-localized MOs is rooted in their shapes. Each MO is centered around two carbon atoms involved in a chemical π-bond, effectively masking the entanglement of the bond within the subspace of local bonding and antibonding orbitals. Interestingly, from the orbital plots shown in the upper panels of Figures 3.3 and 3.4, we conclude that the PM-localized MOs can still be identified as either bonding π- or antibonding π^*-MOs. This classification remains also apparent in the superselected entanglement values. The bonding π-orbitals (with odd indices) contain mostly N-SSR forbidden entanglement whereas in the antibonding π^* ones (even indices) most superselected entanglement is N-SSR compatible, similar to the situation encountered within the canonical MO basis.

By contrast, the single orbital entanglement of the atomic-like orbitals is almost equally distributed, with or without superselection rules. This finding is perhaps not surprising as the atomic-like orbitals are almost identical up to translation and a possible phase change. Furthermore, the even distribution of entanglement after applying either the P- or N-SSR for the single orbital entanglement is a clear indication that there are no favored orbitals in terms of parity or occupation number. In stark contrast to the PM-localized orbitals, the degree of entanglement becomes substantially higher than that of the canonical MOs, reaching 96% of the theoretical maximum of $2 \log 2$. To explain this finding, we recall that the atomic-like orbitals are, by construction, a superposition of bonding and antibonding PM-localized orbitals. Such a rotation between matching π-π^*-MOs entails a release of the entanglement tucked away within the PM-localized orbitals, and becomes manifest in an entanglement between the atomic-like orbitals . As we shall see later, each atomic-like orbitals centered on one carbon atom has a pairwise entanglement with exactly only one other atomic-like orbital, localized around the second carbon center that is contributing to the same chemical bond.

We now analyze the orbital-orbital correlations (classical, quantum, entanglement) in the ground states of $C_{10}H_{12}$ and $C_{20}H_{22}$. We consider the two-orbital reduced density states as the "overall" state, which are typically mixed. They serve as our point of departure

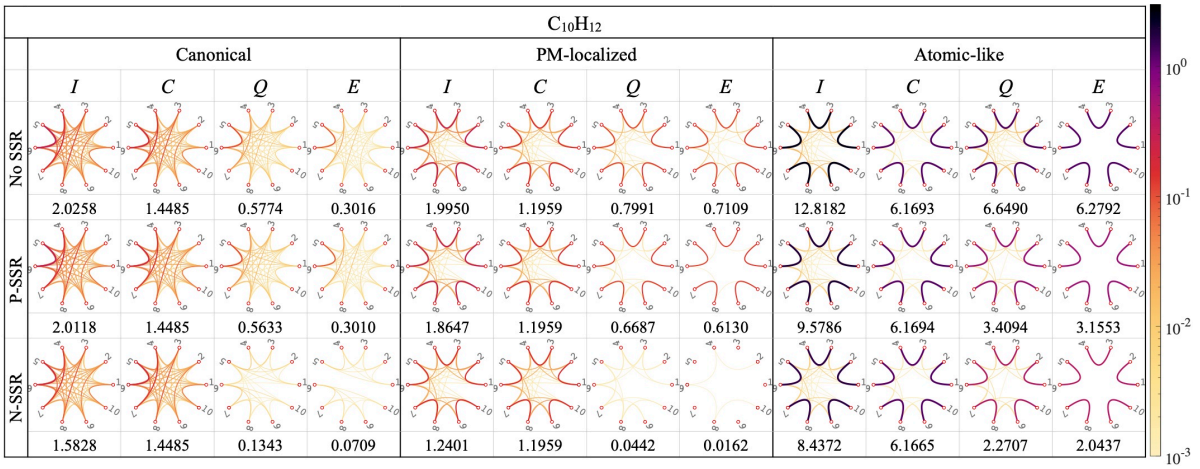

Figure 3.5: Pairwise orbital total correlation I, classical correlation C, quantum correlation Q, and entanglement E in the CAS(10,10)-optimized electronic ground state of $C_{10}H_{12}$ in case of no SSR, P-SSR, and N-SSR. The orbital numbering follows the one given for the canonical, PM-localized, and atomic-like orbitals in the upper panel of Figure 3.3. The corresponding pairwise correlation sum (see Eq. (3.23)) is given below each plot.

to study the correlation between any two orbitals (within our CAS). In this scenario, the total correlation I is no longer linearly related to the entanglement E, and the latter is always smaller or equal to the quantum correlation Q. In order to enable an unambiguous comparison of correlation strengths throughout our various choices of MO bases, we define the following quantities as the pairwise total correlation sum I_{sum}, pairwise classical correlation sum C_{sum}, pairwise quantum correlation sum Q_{sum}, and pairwise entanglement sum E_{sum},

$$X_{\text{sum}}^{(\text{P, N})}(\{\phi_l\}, |\Psi\rangle) = \sum_{i<j} X(\rho_{ij}^{(\text{P, N})}) \qquad X = I, C, Q, E \tag{3.23}$$

where $\rho_{ij}^{(\text{P, N})}$ is the (P, N-SSR compatible) reduced state of $|\Psi\rangle$ on the orbital ϕ_i and ϕ_j of the specified basis set $\{\phi_l\}$.

In Figure 3.5 and 3.6 we highlight the orbital-orbital total correlation I, classical correlation C, quantum correlation Q, and entanglement E between the canonical, PM-localized, and atomic-like orbitals in the ground states of $C_{10}H_{12}$ and $C_{20}H_{22}$, respectively. Moreover, the corresponding pairwise correlation sum is shown below each plot. We discuss in the following three major conclusions that can be drawn from the orbital-orbital correlation data. We first observe a primarily low total correlation I between either canonical or PM-localized MOs, whereas the degree of correlation between the atomic-like orbitals is strikingly higher, exhibiting a six-fold increase in going from the PM-localized to the atomic-like orbitals basis. Simultaneously, the pairwise entanglement E reaches up to 91%

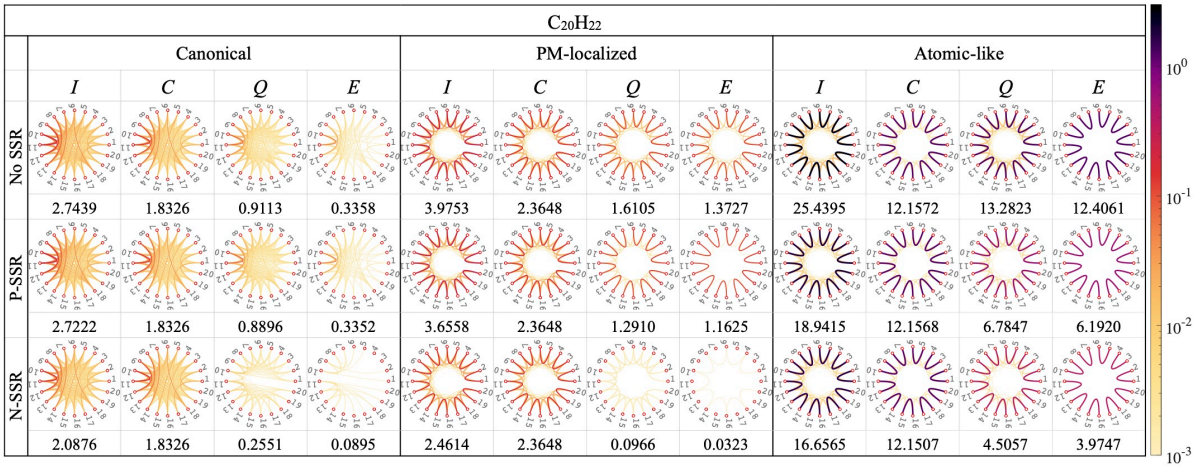

Figure 3.6: Pairwise orbital total correlation I, classical correlation C, quantum correlation Q, and entanglement E in the CAS(20,20)-optimized electronic ground state of $C_{20}H_{22}$ in case of no SSR, P-SSR, and N-SSR. The orbital numbering follows the one given for the canonical, PM-localized, and atomic-like orbitals in the upper panel of Figure 3.4. The corresponding pairwise correlation sum (see Eq. (3.23)) is given below each plot.

of $2\log 2$ for both $C_{10}H_{12}$ and $C_{20}H_{22}$. Moreover, in the atomic-like orbitals basis, we find that the pairwise quantum correlation Q can be as large as 94% of $2\log 2$. We already saw in the case of C_2H_4 that 100% of maximal entanglement can never occur in an interacting molecule. Here however, the entanglement is further lowered due to the presence of orbital coupling. To see this we first notice that the two-orbital reduced states are now mixed, as a result of interaction between the two orbitals and the rest of the system. This degree of mixedness indicates that the two orbital system is also entangled with other orbitals, and hence reduces the maximally achievable entanglement between them.

In addition to a comparison of absolute correlation data, it is instructive to consider the relative contributions of quantum and classical correlation to the total correlation, focusing first on the case without SSRs. In the canonical MO basis, a larger portion of the total correlation is classical rather than quantum in nature. For example, the pairwise quantum correlation sum Q_{sum} in the ground state of $C_{10}H_{12}$ is only 29% of the pairwise total correlation sum I_{sum}, and, similarly, 33% for $C_{20}H_{22}$. As we move to the PM-localized MO basis, though the overall total correlation does not increase, the relative contribution of quantum correlation Q rises to 40% and 41% for $C_{10}H_{12}$ and $C_{20}H_{22}$ respectively. This effect becomes even more apparent in the atomic-like orbitals basis, where the fraction of quantum correlation ($> 52\%$) surpasses that of the classical correlation for both molecules. Furthermore, in passing from a canonical as well as PM-localized to an atomic-like orbitals basis, we not only observe an increase of the percentage of quantum correlation comprised in the total correlation, but also encounter a significant increase of the share of entanglement E in the quantum correlation. The latter increases from 37% and 85% to up to 93% for $C_{20}H_{22}$, as

the orbitals are becoming more and more localized. *Secondly*, besides the effects on the importance of quantum correlation and entanglement, (almost fully) localizing the MOs introduces a distinct pairing structure. Among the canonical MOs, we do not find any obvious pairing structure except for those MOs located around the Fermi level (HOMO–LUMO, HOMO-1–LUMO-1) which also exhibit the largest pairwise correlations. Moving to the PM-localized MOs, a clear pairing structure emerges with pairs of MOs grouped together by relatively strong (total) pairwise correlation and entanglement. Nonetheless, such a pairwise correlation is still too weak to fully describe a chemical bond, compared to the maximal entanglement we found in Subsection 3.1.1. The pattern observed in this case stems from the fact that the two pairing MOs are the respective bonding π- and antibonding π^*-orbitals located primarily on the same two carbon atoms, an effect similar to the correlation between the canonical and PM-localized MOs in C_2H_4 in Section 3.1.2. In a mean-field picture, all the local bonding orbitals are doubly occupied while the antibonding ones remain empty. By contrast, in a correlated picture electron-electron interaction introduces a finite occupation in the latter while simultaneously reducing the double-occupancy occupation of the former, thus creating a *weak* pairwise correlation between the local bonding and antibonding orbitals. Considering next the atomic-like orbitals basis, the overall picture changes strikingly. The pronounced pairing structure of the correlation and entanglement data between MOs located on neighboring carbon atoms is an order of magnitude stronger than that of the PM-localized MOs. The pairwise entanglement E becomes even so strong that a so-called monogamy effect results, namely each atomic-like orbitals is *only* entangled to one other MO with which a bond is formed, in sharp contrast to the weak correlation background (yellow connecting lines) in the quantum correlation plots where MOs from different pairs are still correlated. This clear distinction indicates that (pairwise) entanglement may be a more appropriate quantity to describe chemical bonds than quantum correlation would be.

Finally, we would like to highlight the effect of SSRs and their implication on the resulting complexity of the ground state wave function. For the canonical and PM-localized MO basis, P-SSR hardly changes the pairwise entanglement, whereas N-SSR suppresses almost all of it. This suggests that the dominating configurations in the total wave function are those with double or zero occupancy on the respective orbitals. In particular, the leading configurations are those where the bonding π-orbitals are doubly occupied rather than the antibonding π^* ones, giving rise to a weak pairing structure that could not survive in the presence of N-SSR. In other words, within the two-electron Hilbert space of two pairing orbitals (one bonding π_i and antibonding π_j^*), the leading configuration is simply $|\uparrow\downarrow\rangle_{\pi_i} \otimes |0\rangle_{\pi_j^*}$. Turning instead to atomic-like orbitals ϕ_i and ϕ_j that form a chemical bond, a far more complicated structure of the ground state emerges in this basis. For a given pair i, j of strongly entangled orbitals, none of the four configurations with fixed local occupation numbers

$$\begin{aligned} &|\uparrow\downarrow\rangle_{\phi_i} \otimes |0\rangle_{\phi_j}, \quad |0\rangle_{\phi_i} \otimes |\uparrow\downarrow\rangle_{\phi_j}, \\ &|\uparrow\rangle_{\phi_i} \otimes |\downarrow\rangle_{\phi_j}, \quad |\downarrow\rangle_{\phi_i} \otimes |\uparrow\rangle_{\phi_j}, \end{aligned} \tag{3.24}$$

in the two-electron Hilbert space is particularly dominating, as the entanglement is nearly at its maximum (if we only consider the two-electron subspace). This is also the reason why we encounter a strong P-SSR and N-SSR entanglement between the atomic-like orbitals. The drastically increased number of configurations with appreciable non-zero weight in the total wave function leads to a strongly, and *statically* correlated ground state description. Hence, even though the atomic-like orbital basis is the most suitable for an intuitive description of chemical bonds, this basis compared to the canonical and PM-localized counterparts introduces a strong correlation structure in the electronic molecular ground state wave function.

Benzene

Having discussed the linear, π-conjugated systems, we will in this section focus on the correlation pattern of the ground state of *the* prototypical, cyclic, π-conjugated aromatic molecule, namely benzene (C_6H_6).

To ease comparison, we perform the same correlation analysis as in Section 3.1.2, by making use of the same three distinct sets of MO bases: canonical, PM-localized, and atomic-like orbitals , whose isosurfaces are shown in Figure 3.7. Before embarking on the correlation analysis, a comment is in order on how the atomic-like orbitals basis can be obtained for benzene. Compared to the other π-conjugated molecular systems, an atomic-like orbitals basis for benzene requires a generalized localization scheme. To explain this fact, we first point out that, for the polyenes, the PM-localized orbitals already indicated how atomic-like orbitals can be obtained. As we can see in Figure 3.3 and 3.4, the PM-localized orbitals of $C_{10}H_{12}$ and $C_{20}H_{22}$ are of bonding and antibonding π-type, respectively, stretching primarily across two carbon centers. Making then use of the insight from our analytic example in Section 3.1.1, it is straightforward to see that the respective atomic-like orbitals result from a unitary rotation with angle θ of the bonding and antibonding orbital pairs located on the same carbon centers by $\theta = \frac{\pi}{4}$. By contrast, such a pairing structure no longer emerges for the PM-localized basis in case of benzene. First, the PM-localized orbitals span over more than two carbon centers, due to the absence of a fixed local bonding region. Second, there is no obvious way of rotating any two orbitals which could give rise to atomic-like ones, solely based on geometrical considerations. Hence, we propose in the following a systematic way that leads to an atomic-like orbitals basis starting from the canonical rather than the PM-localized MO basis.

The canonical π-MOs of benzene (denoted as ϕ_i's) are linear combinations of atomic orbitals (LCAO)

$$\tilde{\phi}_i = \sum_j \mathbf{U}_{ij}\alpha_j. \tag{3.25}$$

where α_i's are the atomic orbitals and $\mathbf{U}$ a unitary matrix. Because the atomic orbitals

have finite overlap with each other, the LCAO's need to be further normalized

$$\phi_i = \mathbf{\Lambda}_{ij}\tilde{\phi}_j = (\mathbf{\Lambda U})_{ij}\alpha_j = \frac{\tilde{\phi}_i}{\|\tilde{\phi}_i\|}. \tag{3.26}$$

This last normalization transformation $\mathbf{\Lambda}$ makes the mapping $\mathbf{\Lambda U}$ from the atomic orbitals to the canonical orbitals non-unitary. Hence, we may ask ourselves what would happen if we transform the canonical orbitals by $\mathbf{U}^{-1}$? The resulting orbitals are still orthogonal of course, since $\mathbf{U}^{-1}$ is unitary. To assess the locality of these orbitals, we first consider an extreme example. Suppose that we have a molecule with internuclear distances such that all of its atomic orbitals (at different atomic centers) have vanishingly small overlap with each other. This entails that the LCAO's in Eq. (3.25) are already normalized ($\mathbf{\Lambda} = \mathbb{1}$). Then the inverse transform

$$\tilde{\alpha}_i = \sum_j (\mathbf{U}^{-1})_{ij}\phi_j = \sum_j (\mathbf{U}^{-1}\mathbf{\Lambda U})_{ij}\alpha_j \tag{3.27}$$

would only give back the original atomic orbitals $\tilde{\alpha}_i = \sum_j (\mathbf{U}^{-1}\mathbf{U})_{ij}\alpha_j = \alpha_i$. When the atomic overlap is finite, $\mathbf{\Lambda}$ then deviates from the identity map, and so does $\mathbf{U}^{-1}\mathbf{\Lambda U}$. However, as long as the atomic overlap is not exceedingly large[1], $\mathbf{\Lambda}$ is close to an identity map, and each orbital $\overline{\alpha}_i$ will have a dominating contribution from the atomic orbital α_i and, simultaneously only small weights from the remaining ones, thus making the new *molecular* orbitals $\tilde{\alpha}_i$ atomic-like. We applied for benzene the above localization scheme starting out from the canonical MO basis. As can be seen from Figure 3.7, each atomic-like orbitals has a large contribution from a p_z-shaped *atomic* orbital on one carbon center, and only small weights from the remaining p_z-shaped orbitals on the other carbon centers. Moreover, all atomic-like orbitals are identical up to translations by an integer multiple of the lattice constant along the benzene ring. The localization scheme therefore successfully preserves the original shape of the atomic orbitals, while maintaining the orthogonality of the canonical ones.

In Figures 3.7 and 3.8, respectively, we present the single-orbital and orbital-orbital correlation results for all three sets of MO bases. The correlation patterns within the canonical and PM-localized MO basis mainly resemble those of the linear polyenes discussed in the previous subsection. In more detail, we first observe an overall low single orbital and orbital-orbital entanglement. Secondly, in the case without SSR most of the orbital-orbital correlation is again classical in nature with a share of 76% and 71%, respectively, of the orbital-orbital total correlation for the two MO bases. Thirdly, the distribution pattern of the superselected single orbital entanglement is also in alignment with previous findings. The bonding π-orbitals (odd indices in Figure 3.7) have an occupancy close to the mean-field value of 2.0 and, consequently, only exhibit a small amount of N-SSR entanglement,

[1]For example, straightforward calculation would show for the case of two identical atomic orbitals with overlap of 0.75, each resulting atomic-like orbital is still dominated by one atomic orbital with 69% relative weight.

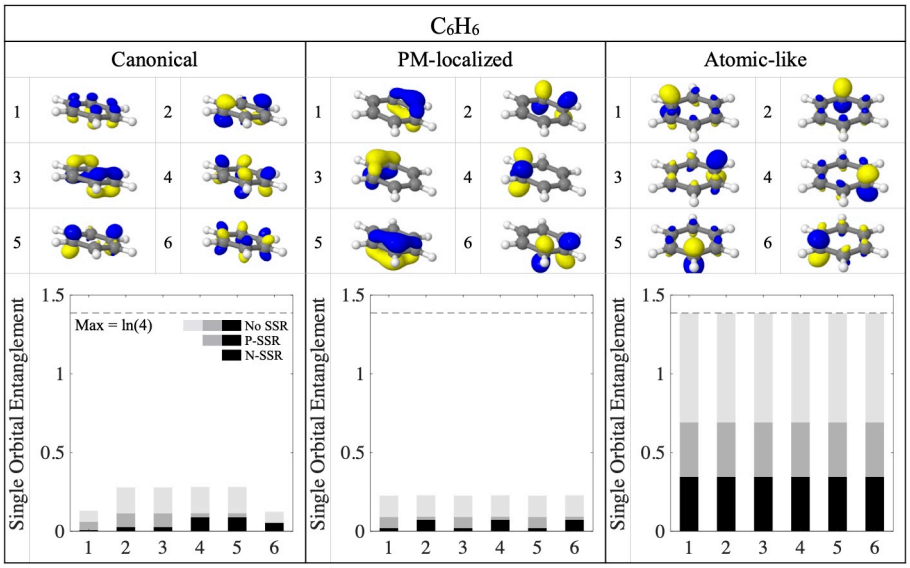

Figure 3.7: Single orbital entanglement in the CAS(6,6)-optimized electronic ground state of benzene. The orbital numbering on the x-axis in the lower panel follows the one given for the canonical, PM-localized, and atomic-like orbitals in the upper panel (plotted with an isosurface value of 0.05 for the canonical and PM-localized MOs, and 0.1 for the atomic-like orbitals). The color code for the single orbital entanglement data is as follows: no SSR (all color), P-SSR (black and dark gray), and N-SSR (dark gray).

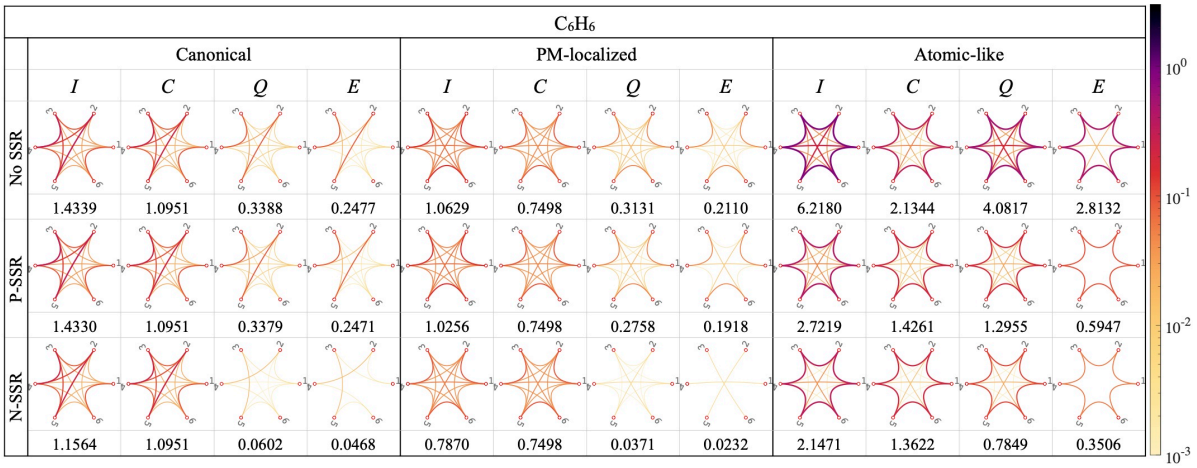

Figure 3.8: Pairwise orbital total correlation I, classical correlation C, quantum correlation Q, and entanglement E in the CAS(6,6)-optimized electronic ground state of benzene in case of no SSR, P-SSR, and N-SSR. The orbital numbering follows the one given for the canonical, PM-localized, and atomic-like orbitals in the upper panel of Figure 3.7. The corresponding pairwise correlation sum (see Eq. (3.23)) is given below each plot.

whereas the occupancy in the antibonding π^*-MOs (even indices in Figure 3.7) departs from its mean-field value of zero such that their superselected single orbital entanglement becomes N-SSR compatible.

Similar to the situation encountered for polyene systems, the correlation structure in the atomic-like orbitals basis becomes much richer. Considering first the single-orbital entanglement without SSR, we find that every atomic-like orbitals is maximally entangled (with value $2\log 2$) with the rest of the system, as can be seen from Figure 3.7. This strong entanglement is missing at the orbital-orbital level, though. A closer inspection of Figure 3.8 reveals that the maximal pairwise entanglement E is considerably weaker than the one between the atomic-like orbitals in the polyenes. Compared to 92% of $2\log 2$ for the latter, the maximum value of E in benzene amounts to merely 33% of $2\log 2$. The origin of this discrepancy can be explained as follows. In sharp contrast to the pairing structure of the entanglement between the atomic-like orbitals in the polyenes, each atomic-like orbital on the benzene ring is equally entangled to *both* of its neighbors. This "left-right pairing" is rooted in the underlying symmetry of the molecular Hamiltonian and closely resembles the simplified "left-right overlap" model of the Hückel Hamiltonian for benzene [177]. Hence, the unique electronic ground state within our minimal π-π^* CAS(6,6) active orbital space enjoys the same symmetry as the molecule itself, and is invariant under six-fold rotation and reflection about the mirror planes. A simplified, polyene-like pairing structure which would gives rise to a π-type bond involving only two neighboring carbon centers is therefore suppressed by the molecular symmetry. Although, even if we are to sum up the orbital-orbital entanglement between one orbital and both of its neighbors, 33% of the single orbital entanglement would not be accounted for from this partially summed *bipartite* orbital-orbital entanglement sum. As a result, we ascribe the missing part of the entanglement in this π-conjugated, aromatic molecule to genuine *multipartite* entanglement.

3.2 Maximally Entangled Atomic Orbitals (MEAO)

Previously we established that a single covalent bond can be identified as the maximal entanglement between two atomic-like orbitals, which is observed on the π-orbital level for several conjugated molecules with well pronounced π-bonds. Moreover, compared to other correlation quantities (quantum or classical), entanglement was found to be specially suitable for describing chemical bonding, due to its monogamy effect. Our scheme of localizing said atomic-like orbitals however has the following limitations. First, so far we have studied the case where only one atomic-like orbital was considered per atomic center. Second, we relied on the existence of localized bonding and antibonding orbitals from the PM method, as well as manual orbital rotations to localize the orbitals further. Third, although we demonstrated that going from PM-localized orbitals to atomic-like orbitals the pairwise entanglement is enhanced, there is still a conceptual gap between orbital localization

(referring to the geometry of the orbitals) and orbital-orbital entanglement maximization (referring to the entanglement properties of the ground state). Mixing localized orbitals assigned to the same atomic center should not change the locality of the orbitals, but could lead to completely different entanglement patterns than the dimerized Lewis structure we observed above. In this section, we will resolve these issues by implementing an orbital optimization scheme that directly maximizes the entanglement between pairs of orbitals localized on different atomic centers.

3.2.1 Dissecting chemical bonds with MEAO

In order to assign localized orbitals to atoms, we start by defining the notion of atom in molecules (AIM), which is given by the intrinsic atomic orbitals [163] (IAO). The IAO are free atomic orbitals polarized by the molecular environment through a mean-field singlet wavefunction $|\Psi_{\mathrm{MF}}\rangle = \prod_{i=1}^{N/2} f_{i\uparrow}^{\dagger} f_{i\downarrow}^{\dagger}|0\rangle$. The mean-field orbitals form a large molecular orbital basis $\mathcal{B}_1 = \{|i\rangle\}$, with the first $N/2$ orbitals being doubly occupied. Now let us consider a potentially much smaller basis set $\mathcal{B}_2 = \{|\alpha\rangle\}$ consisting of the minimal free atomic orbitals (AO) on all atoms (e.g., $1s$+$2s$+$2p_{x,y,z}$ for the first row elements). These free AOs are well understood in terms of their geometries and can facilitate chemical interpretation. However, the fact that $\mathcal{B}_2$ is much smaller than $\mathcal{B}_1$ means that the overlaps between the mean-field MOs $|i\rangle$ and the basis $\mathcal{B}_2$ can be also quite small. In the original language of Knizia, the set $\mathcal{B}_2$ lacks polarization from the molecular environment [178], and hence the mean-field wavefunction $|\Psi\rangle$ can not be reconstructed with MOs expanded in terms of orbitals in $\mathcal{B}_2$ only.

To build a new basis set the size of $\mathcal{B}_2$ that is capable of representing the HF MOs, while maintaining its atomic character, Knizia performed the following procedure. He first decomposed the HF MOs into the part $|\tilde{i}\rangle$ within the span of $\mathcal{B}_2$ and their orthogonal counterparts

$$|i\rangle = |\tilde{i}\rangle + |\tilde{i}^{\perp}\rangle. \tag{3.28}$$

The vector $|\tilde{i}\rangle$'s are what Knizia called depolarized MOs and can be entirely expressed in terms of free atomic AOs in $\mathcal{B}_2$. Then we identify the occupied subspaces in both basis $\{|i\rangle\}$ (polarized MOs) and $\{|\tilde{i}\rangle\}$ (depolarized MOs) using the projectors

$$\begin{aligned} P &= \sum_{i \leq \frac{N}{2}} |i\rangle\langle i|, \\ \tilde{P} &= \sum_{i,j \leq \frac{N}{2}} \left(\boldsymbol{S}^{-1}\right)_{ij} |\tilde{i}\rangle\langle\tilde{j}|, \end{aligned} \tag{3.29}$$

where $S_{ij} = \langle\tilde{i}|\tilde{j}\rangle$ is the overlap matrix of the depolarized basis. The pre-orthogonal IAO $|\tilde{\alpha}\rangle$ is then constructed from the free AOs $|\alpha\rangle$ as

$$|\tilde{\alpha}\rangle = \left[P\tilde{P} + (1-P)(1-\tilde{P})\right]|\alpha\rangle. \tag{3.30}$$

To see that the span of $\{|\tilde{\alpha}\rangle\}$ indeed contains the span of the occupied MOs $\{|i\rangle\}_{i=1}^{N/2}$, we simply check the span of the projected orbitals $\{P|\tilde{\alpha}\rangle\}$ on the subspace of occupied MOs

$$P|\tilde{\alpha}\rangle = P\tilde{P}|\alpha\rangle, \tag{3.31}$$

and conclude that they are indeed $N/2$ linearly independent vectors. One might suggest that simply using $\{P|\alpha\rangle\}$ one can also span $\{|i\rangle\}_{i=1}^{N/2}$ just by simple dimension counting. But $\{P|\alpha\rangle\}$ becomes entirely of MO character instead of AO. As a minimal example, we can consider the single covalent bond in H_2 with a minimal basis set. Since there is only one bonding orbital, the two orbitals in $\{P|\alpha\rangle\}$ with $|\alpha\rangle$ being the left and the right $1s$ orbital are then proportional to the bonding orbital, and in this case also identical. Therefore, the non-zero support on the unoccupied subspace is crucial for maintaining localization. If the projector $1-P$ is used but the $\tilde{P}$ and $1-\tilde{P}$ projectors are dropped, then $|\tilde{\alpha}\rangle$ reduces back to the free AOs, which are ignorant of the molecular environment. Therefore, the inclusion of the second set of projectors $(1-P)(1-\tilde{P})$ is also important.

After symmetric orthogonalization [134], the IAOs form an orthonormal basis set of a low-dimension subspace of the single-particle Hilbert space. Given their well-defined atomic character, IAO can be used for computing atomic properties (e.g., partial charges), and are shown to be insensitive to the choice of basis set [163]. The span of all IAO on one atomic center A is a subspace $\mathcal{H}_1^{(A)}$ of the one-particle Hilbert space $\mathcal{H}_1$ which defines the atom A in the molecule. Based on this definition of AIM, any linear combinations of IAO in $\mathcal{H}_1^{(A)}$ can be considered as an orbital localized on atom A. Although the IAOs correctly account for the polarization of the atomic orbitals due to the molecular environment, they are constructed as pre-hybridized atomic orbitals. Because of this, IAOs from two different atomic centers cannot form maximally entangled orbital pairs that resemble the Lewis structure of a prototypical bond as in (3.9). In fact, the entanglement between IAOs are far from the maximum of $2\log(2)$. Since the IAO are already fully localized, and the atomic partition is fixed, the only degrees of freedom left to optimize are the internal orbital rotation within the atomic centers. The basis $\mathcal{B}_{\mathrm{MEAO}}$ of maximally entangled atomic orbitals is defined through the following maximization problem

$$\mathcal{B}_{\mathrm{MEAO}} = \arg\max_{\mathcal{B}\in\mathcal{S}_{\mathrm{local}}} \sum_{(i,j)} E(\mathcal{B})_{ij}, \tag{3.32}$$

where (i,j) runs over all pairs of inter-center orbitals, and $E(\mathcal{B})_{ij}$ is the entanglement between orbital i and j in basis $\mathcal{B}$. The set $\mathcal{S}_{\mathrm{local}}$ collects all orbital bases that are related to the IAO basis $\mathcal{B}_{\mathrm{IAO}}$ by local unitary transformations, which leave the AIM defined by the IAOs invariant.

The entanglement $E(\mathcal{B})_{ij}$ between two orbitals is in general very costly to compute. It refers to the mixed state $\rho_{ij} = \mathrm{Tr}_{\setminus\{i,j\}}[|\Psi\rangle\langle\Psi|]$, whose entanglement is only properly defined by yet another optimization problem

$$E(\mathcal{B})_{ij} = E(\rho_{ij}) = \min_{\sigma\in\mathcal{D}_{\mathrm{sep}}} S(\rho_{ij}\|\sigma), \tag{3.33}$$

where the minimization is over all separable states σ that can be written as sums of product states (recall Eq. (1.11) in Section 1.1), and $S(\rho\|\sigma) = \mathrm{Tr}[\rho(\log\rho - \log\sigma)]$ is the quantum relative entropy. This entanglement measure is also known as the relative entropy of entanglement, which has many favorable properties. Unfortunately (3.33) is not analytically computable except for highly symmetric states in low dimensions [4], [107]. Although we can calculate (3.33) using techniques from semidefinite programming [179], (3.33) is still too expensive as a cost function. Moreover, to calculate the full two-orbital RDM one needs the information from up to four-particle RDMs (since two orbitals can be at most occupied by four electrons), which poses a tremendous challenge in computational storage and tensor manipulations. To make the maximization problem (3.32) feasible, we need a computable substitute for the entanglement. In Ref. [107] (see also Section 2.1), it was observed that two coherent terms in ρ_{ij} play an important role in the value of entanglement

$$\begin{aligned}\Gamma^{i\uparrow,i\downarrow}_{j\uparrow,j\downarrow}(\mathcal{B}) &= \langle 0,\uparrow\downarrow|\rho_{ij}|\uparrow\downarrow,0\rangle,\\ \Gamma^{i\uparrow,j\downarrow}_{j\uparrow,i\downarrow}(\mathcal{B}) &= \langle\uparrow,\downarrow|\rho_{ij}|\downarrow,\uparrow\rangle\end{aligned} \tag{3.34}$$

which are elements of the two-particle reduced density matrix $\mathbf{\Gamma}$ (2RDM)

$$\Gamma^{i\sigma,j\tau}_{k\sigma,l\tau}(\mathcal{B}) = \langle\Psi|f^\dagger_{i\sigma}f^\dagger_{j\tau}f_{l\tau}f_{k\sigma}|\Psi\rangle. \tag{3.35}$$

The pivotal role of the two coherence terms in (3.34) can also be seen in the prototypical bonding state (3.9): They are precisely the coherence between the two even-occupancy states, and that between the two odd-occupancy states. The magnitudes of both terms in this case are simultaneously maximized to 1/4. We therefore propose to use the sum of magnitudes of the two coherence terms as a substitute for $E(\mathcal{B})_{ij}$ in the orbital optimization problem (3.32). To reiterate, the MEAOs based on a mean-field wavefucntion are obtained as

$$\begin{aligned}\mathcal{B}_{\mathrm{MEAO}} &= \arg\max_{\mathcal{B}\in\mathcal{S}_{\mathrm{local}}} F_{\mathrm{MEAO}}(\mathcal{B}),\\ F_{\mathrm{MEAO}}(\mathcal{B}) &\equiv \sum_{(i,j)}\left|\Gamma^{i\uparrow,i\downarrow}_{j\uparrow,j\downarrow}(\mathcal{B})\right|^2 + \left|\Gamma^{i\uparrow,j\downarrow}_{j\uparrow,i\downarrow}(\mathcal{B})\right|^2.\end{aligned} \tag{3.36}$$

The 2RDM can be calculated from any level of theory, ranging from SCF to exact diagonalization. If the trial wavefunction $|\Psi\rangle$ is a mean-field one, similar to the trial wavefunction for constructing the IAOs, then the 2RDM elements can be expressed fully in terms of the one-particle reduced density matrix $\gamma^{i\sigma}_{j\sigma} = \langle\Psi|f^\dagger_{i\sigma}f_{j\sigma}|\Psi\rangle$ in the virtue of Wick's theorem as

$$\Gamma^{i\uparrow,i\downarrow}_{j\uparrow,j\downarrow}(\mathcal{B}) = \Gamma^{i\uparrow,j\downarrow}_{j\uparrow,i\downarrow}(\mathcal{B}) = \gamma^{i\uparrow}_{j\uparrow}(\mathcal{B})\gamma^{i\downarrow}_{j\downarrow}(\mathcal{B}). \tag{3.37}$$

The optimization for the basis $\mathcal{B}_{\mathrm{MEAO}}$ can be performed efficiently with a gradient-based method. We reserve the explicit expressions of the gradients of the relevant 2RDM elements for Appendix C.

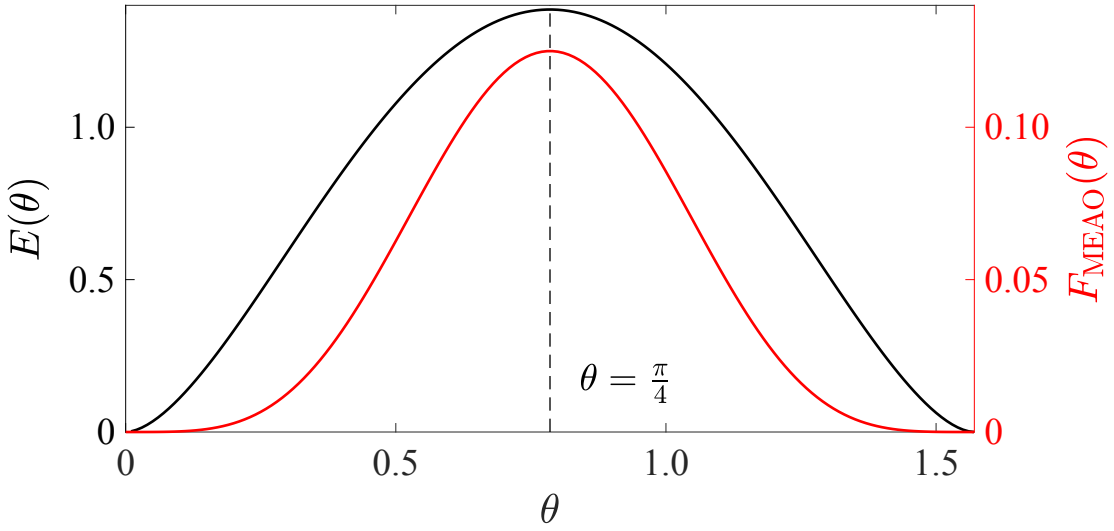

Figure 3.9: Entanglement between ψ_L and ψ_R in Eq. (3.40) (left axis, black) and the cost function F_{MEAO} in Eq. (3.36) (right axis, red) as functions of the orbital rotational parameter θ.

Before we proceed, we provide an additional justification for the cost function F_{MEAO} in (3.36), by revisiting the example of the perfect covalent bond in the active space of two electrons and two orbitals

$$|\Psi_{\mathrm{bond}}\rangle = |\uparrow\downarrow\rangle_{\phi} \otimes |0\rangle_{\bar{\phi}}, \tag{3.38}$$

where ϕ and $\bar{\phi}$ are the bonding and antibonding orbitals, respectively. The entanglement between the two orbitals is zero. But when we perform the following orbital transformation

$$\begin{aligned} \psi_L &= \cos(\theta)\phi + \sin(\theta)\overline{\phi}, \\ \psi_R &= -\sin(\theta)\phi + \cos(\theta)\overline{\phi}, \end{aligned} \tag{3.39}$$

the state $|\Psi_{\mathrm{bond}}\rangle$ is re-expressed as

$$\begin{aligned} |\Psi_{\mathrm{bond}}\rangle = \cos^2(\theta)|\uparrow\downarrow\rangle_{\psi_L} \otimes |0\rangle_{\psi_R} + \sin^2(\theta)|0\rangle_{\psi_L} \otimes |\uparrow\downarrow\rangle_{\psi_R} \\ + \cos(\theta)\sin(\theta)|\uparrow\rangle_{\psi_L} \otimes |\downarrow\rangle_{\psi_R} - \cos(\theta)\sin(\theta)|\downarrow\rangle_{\psi_L} \otimes |\uparrow\rangle_{\psi_R}. \end{aligned} \tag{3.40}$$

Then the entanglement between the transformed orbitals ψ_L and ψ_R is a function of θ (see Eq. (3.16) for a derivation)

$$E(\theta) = -2\cos^2\theta\log(\cos^2\theta) - 2\sin^2\theta\log(\sin^2\theta), \tag{3.41}$$

Correspondingly, in the transformed bases, the cost function $F_{\mathrm{MEAO}}(\theta)$ is also θ-dependent, and can be written as

$$F_{\mathrm{MEAO}}(\theta) = 2\cos^4\theta\sin^4\theta. \tag{3.42}$$

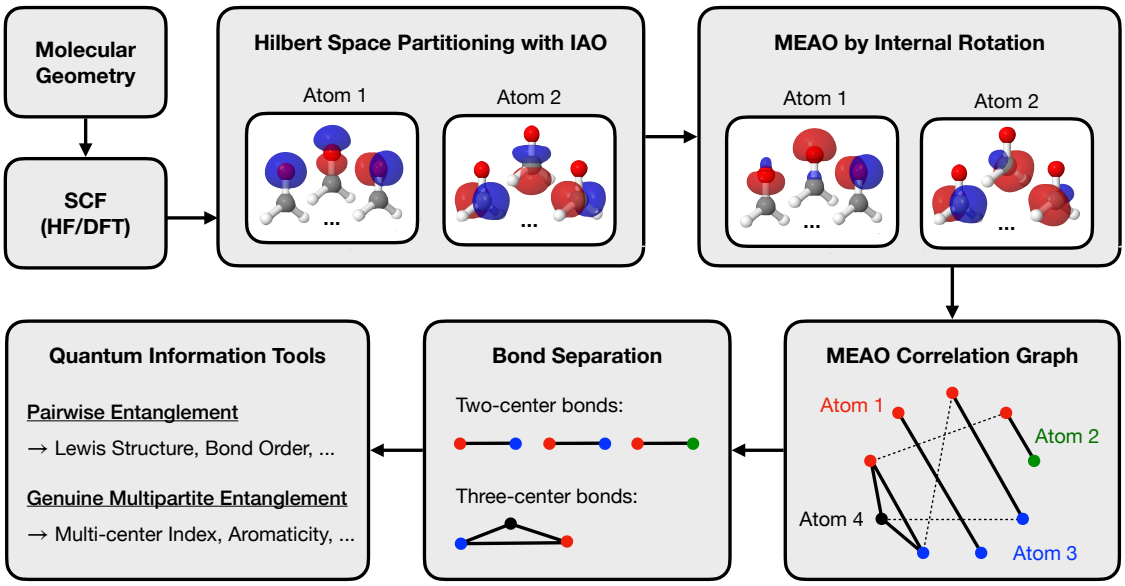

Figure 3.10: *Ab initio* procedure for determining the bonding structures of molecules with maximally entangled atomic orbitals (MEAO).

Remarkably, $E(\theta)$ and $F_{\mathrm{MEAO}}(\theta)$ are maximized at the same θ value of $\frac{\pi}{4}$. Therefore, in this example, $F_{\mathrm{MEAO}}(\theta)$ is indeed a viable cost function for maximizing the exact entanglement.

Once we obtained the set of MEAOs, we can extract from them the bonding structure of the molecule. This consists of three extra steps. First, we calculate the total correlation (mutual information) between any two orbitals residing on different atomic centers. This is an approximation step where high level of accuracy is unnecessary. We therefore calculate the pairwise total correlation instead of the expensive entanglement, and the wavefunction we used for this can be as inexpensive as a mean-field one for most systems. Second, the inter-center orbital-orbital mutual information is used to form a weighted adjacency matrix $\boldsymbol{I}$, where only the values of the mutual information above 10% of its maximal value $4\log(2)$ is taken into account. The weighted adjacency matrix $\boldsymbol{I}$ allows us to separate the orbitals into bonds. This can be performed either by reading off the non-zero blocks in $\boldsymbol{I}$, or by the support of the eigenvectors of $\boldsymbol{I}$ which correspond to the inseparable clusters. We remark that in all cases we studied in this section, the bond separation step is insensitive to the choice of wavefunction ansatz, and we have chosen the HF solution for this purpose. To obtain the two-orbital RDMs from the HF one-particle RDM γ, we recall Eq. (1.44) to (1.52), and invoke Wick's theorem. In the last step, we calculate exactly the entanglement within the clusters, using accurate wavefunction methods. The value of bipartite (multipartite) orbital entanglement is then interpreted as the order of the two-center (multi-center) bond. We summarize this scheme in Figure 3.10.

3.2.2 Restoring the Lewis structures from accurate wavefucntions

We now demonstrate the power of the MEAO formalism in restoring the Lewis structures in molecules with two-center bonds. First, we compare the shapes of the IAOs and the MEAOs. In Figure 3.11 we present the isosurface plots of IAO and MEAO of the organic molecules CH_4, C_2H_6, C_2H_4, and C_2H_2 in the cc-pVDZ basis set. The IAOs are constructed from the set of minimal atomic orbitals. These molecules are prototypical for hosting single, double, and triple bonds, with well understood mechanisms of bonding in terms of atomic orbital hybridization. While both orbital sets are fully localized by construction, the key difference lies in the hybridization of the orbitals. The IAOs retain most of the free atomic orbital features, with clear separation between s- and p-orbitals in all three spatial directions. In contrast, the MEAOs are combinations of the $s-$ and $p-$ orbitals with the right degree of hybridization. For CH_4 the carbon MEAOs are sp^3-hybrids (hybridization of one $2s$ orbital and three $2p$ orbitals) pointing towards the vertices of the tetrahedron where the hydrogen atoms are located. They then form covalent bonds with the hydrogen MEAOs. The Carbon MEAOs in C_2H_6 share the same shape as the ones in CH_4, while two of them points towards each other to form a C-C σ-bond. For C_2H_4 the σ-type MEAOs are instead sp^2-hybrids (hybridization of one $2s$ orbital and two $2p$ orbitals), and the out-of-plane p_z-orbitals are correctly preserved in the orbital transformation, forming a π-bond between the two carbon atoms. For C_2H_2 only the $2p$-orbital along the molecule is mixed with the s-orbitals forming sp-hybridiztation, and now two p-orbitals on each carbon atom are left invariant during the transformation from the IAOs to the MEAOs.

The drastic differences between the IAOs and the MEAOs in terms of orbital shapes lead to also distinct pairwise correlation patterns. We recall again from Section 1.1 the simplest orbital correlation/entanglement quantities, namely the single orbital entropy [62], [87], [119], [180], [181]

$$S_i = S(\rho_i) = -\mathrm{Tr}[\rho_i \log(\rho_i)], \tag{3.43}$$

which quantifies the entanglement between orbital i and the rest of the system, and the pairwise mutual information [8], [62], [87], [119], [180]–[183]

$$I_{ij} = S_i + S_j - S_{ij}, \tag{3.44}$$

which measures the correlation (both quantum and classical), between the two orbitals i and j only. In the "perfect" single covalent bond (3.9), the single orbital entropy is $S_1 = S_2 = 2\log(2)$, whereas the mutual information between the two orbitals is $I_{12} = 4\log(2)$. We therefore normalize S_i to $2\log(2)$, and I_{ij} to $4\log(2)$.

The orbital reduced density matrices used for calculating S_i and I_{ij} are from a matrix product state (MPS) ansatz parametrized with up to 1500 bond dimension, whose energy we have converged to sub-μ Hartree accuracy. For the systems we studied, the ground state

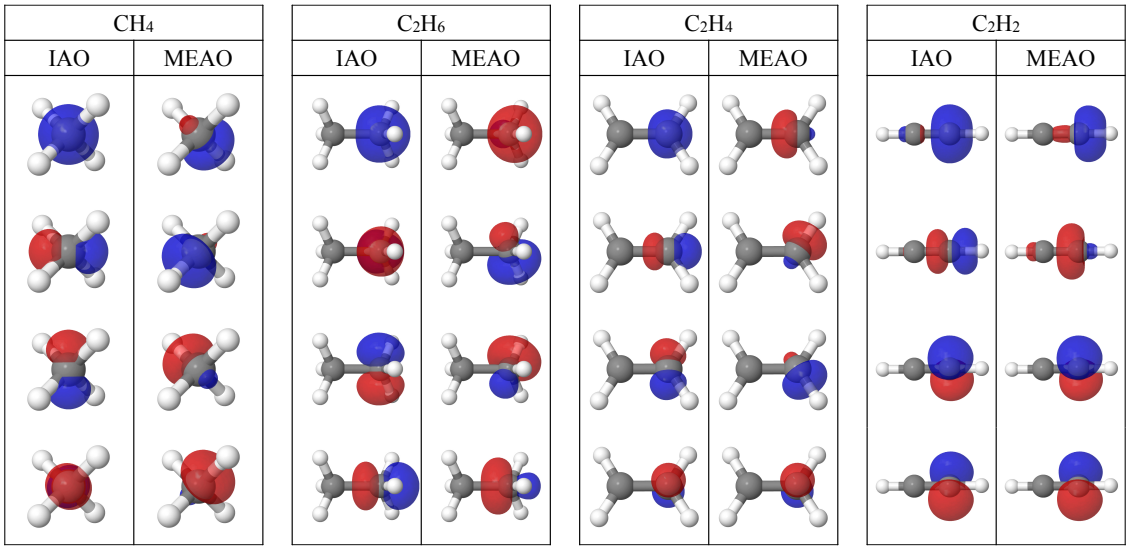

Figure 3.11: The carbon IAOs and MEAOs (excluding $1s$) of CH_4, C_2H_6, C_2H_4, and C_2H_2 in the cc-pVDZ basis. For obtaining both bases the Hartree-Fock wavefunction is used. The isosurface value is 0.2 for CH_4 and 0.1 for the rest.

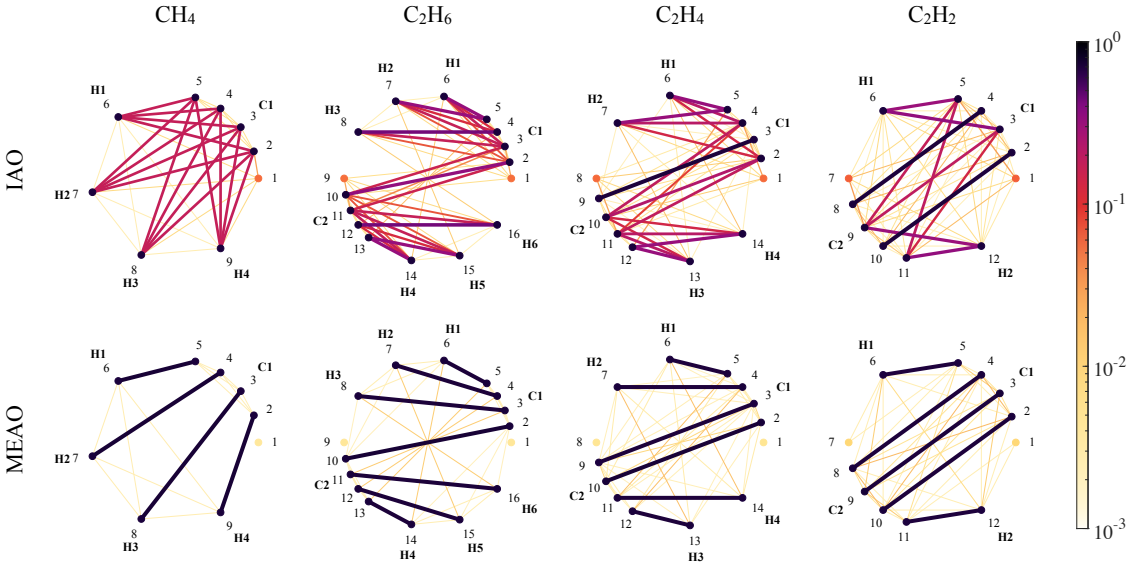

Figure 3.12: Single orbital entropy S_i (vertices) and Correlation I_{ij} (edges) between the IAOs and MEAOs of CH_4, C_2H_6, C_2H_4, and C_2H_2 in the cc-pVDZ basis. For obtaining both bases the Hartree-Fock wavefunction is used. Single orbital entropy is normalized to $2\log(2)$ and correlation is normalized to $4\log(2)$.

MPS can be considered exact. The discrepancy between the IAO-DMRG and MEAO-DMRG energies are also less than 10^{-6} Ha, so that we can safely claim that the correlation patterns of in the IAO basis and those in the MEAO basis stem from the same ground state wavefunctions. A very important step for converging the energy in DMRG with highly localized orbitals is the ordering of the orbitals. Since the orbital entanglement is very strong, if two highly entangled orbitals are placed far from each other, the required bond dimension of the MPS would be much higher and the energy minimization would become much more difficult. To resolve this, one can use methods such as the Fiedler ordering [39]. In our case we simply place after orbital i the corresponding orbital $\bar{i}$ with which orbital i is the most correlated, in terms of the estimation of the pairwise orbital correlation given by the HF wavefunction.

In Figure 3.12 we present a direct comparison of the correlation structures in the IAO basis and the MEAO basis of the ground states of all four molecules. The orbitals are grouped according to the atomic assignment. The orbitals are represented as vertices whose color encodes the value of single orbital entropy (normalized to $2\log(2)$), whereas the pairwise orbital correlation (normalized to $4\log(2)$) are color coded as connecting edges. We use X_i where $\mathrm{X} = \mathrm{C}, \mathrm{H}, \ldots$, and $i = 1, 2, \ldots$, to distinguish identical elements. We notice first that for every set of carbon IAO, there is one extremely weakly correlated orbital. These are the $1s$-orbitals which are almost fully occupied. Second, we observe that the correlation between the IAO correctly identified the connectivity graph of the molecule. That is, from the IAO correlation plot we can tell which carbon atom is bonding with which hydrogen atom, based on the correlation edges connecting the two centers. However, the internal structure of the correlation between any two centers is entirely scrambled due to the lack of hybridization of the IAO. For example, in CH_4, the $2s$- and $2p_{x,y,z}$ IAO on the carbon are evenly correlated with every $1s$ IAO on the hydrogens. Third, while the pairwise correlation not maximal, the single orbital entropy S_i of the carbon IAO is very close to 1 (excluding the $1s$-orbitals). This means each IAO is maximally entangled with its environment, but this entanglement is distributed to several orbitals on other atomic centers.

The MEAO bases on the other hand display much clearer correlation patterns. The MEAO bases still reveal the connectivity graphs between atomic centers, but they do so distinctly with separated, maximally correlated (closed to 1) orbital pairs. All other pairwise correlation is of the order 10^{-3}. Interestingly, even correlation involving the $1s$-IAO can be transformed into the correlation of the frontier MEAOs, rendering the $1s$-MEAO much less correlated in terms of the single orbital entropy. In the above examples, each frontier MEAO is highly correlated to only one other, and together they are identified as a two-center bond. In that sense, the MEAO basis representation of the ground state wavefunctions is a perfect reconstruction of the Lewis picture. If we trim away the edges corresponding to weak correlation, we are left with a perfect dissection of the single-particle Hilbert space into orbital groups, each corresponding to a covalent bond.

	bond	I_{ij}	E_{ij}	E_{ij}^{u}
CH_4	C-H	0.957	0.954	0.782
C_2H_6	C-H	0.928	0.930	0.678
	C-C(σ)	0.955	0.947	0.732
C_2H_4	C-H	0.914	0.917	0.644
	C-C(σ)	0.944	0.933	0.687
	C-C(π)	0.918	0.895	0.738
C_2H_2	C-H	0.906	0.911	0.642
	C-C(σ)	0.915	0.909	0.658
	C-C(π)	0.915	0.875	0.693

Table 3.4: Pairwise correlation I_{ij}, entanglement E_{ij}, and unextendible entanglement E_{ij}^{u} between the bonding MEAOs. Correlation is normalized to $4\log(2)$ and (unextendible) entanglement is normalized to $2\log(2)$.

We present the entanglement (normalized to $2\log(2)$) and correlation (normalized to $4\log(2)$) between every pair of bonding MEAOs in Table 3.4. The entanglement is calculated via semidefinite programming [179] with the CVX package [184], [185]. The entanglement values between the bonding MEAO are also very close to 1, just like their correlation values. Notice that some entanglement values in Table 3.4 is even higher than the total correlation. This is, however, not a contradiction, since their normalization factors differ by a factor of 2. There is also no need to calculate the entanglement values between two MEAOs that are not bonding, since they are necessarily of the order 10^{-3} or less based on the correlation values (recall from Section 1.1 that the entanglement is always bounded from above by the total correlation). This is again reminiscent of the monogamy effect of entanglement. If two orbitals i and j in a system are exactly maximally entangled, then the corresponding reduced state ρ_{ij} is necessarily a pure state. Therefore, the subsystem formed by orbital i and j can not be entangled to any other orbitals. Of course in our calculations the entanglement is not exactly maximal, because the two orbital reduced state ρ_{ij} is mixed. Therefore, in theory each highly entangled orbital can still share some entanglement with an orbital other than its monogamous partner. The only question is, how much entanglement can it actually share?

One can quantify the lack of "sharability" of the entanglement in the following way. For a given bipartite state ρ_{AB} we define a set of state on system A and C (which is a copy of B) such that they can be reduced from a same state on the joint system tripartite

system ABC [186], namely

$$\mathcal{D}_{\rho_{AB}} = \{\sigma_{AC} \,|\, \exists\, \omega_{ABC},\ \text{s.t. } \mathrm{Tr}_B[\omega_{ABC}] = \sigma_{AB} \text{ and } \mathrm{Tr}_C[\omega_{ABC}] = \rho_{AB}\}. \tag{3.45}$$

If ρ_{AB} is entangled and $\rho_{AB} \in \mathcal{D}_{\rho_{AB}}$, then the entanglement between system A and B can be simultaneously held between also A and C (of the same dimension as B) for a given state ω_{ABC}. If $\rho_{AB} \notin\in \mathcal{D}_{\rho_{AB}}$, then the entanglement is not entirely sharable. The extent to which the entanglement is unsharable or unextendible, is quantified by the distance from ρ_{AB} to the set $\mathcal{D}_{\rho_{AB}}$

$$E^{\mathrm{u}}(\rho_{AB}) = \frac{1}{2} \min_{\sigma \in \mathcal{D}_{\rho_{AB}}} S(\rho_{AB} \| \sigma_{AB}). \tag{3.46}$$

This is called the generalized unextendible entanglement [186]. The prefactor $1/2$ is for it to have the same maximal value as the standard bipartite entanglement. For pure states one can check that (3.46) reduces to the relative entropy of entanglement (3.33). E^{u} can be calculated efficiently via semidefinite programming, since the set $\mathcal{D}_{\rho_{AB}}$ is convex and its constraints can be neatly summarized by a set of linear matrix inequalities. We again performed the semidefinite programming using the CVX package [184], [185]. We present the values of E^{u} (normalized to $2\log(2)$) for the relevant orbital pairs in Table 3.4. We see that approximately 70% to 80% of the entanglement between two bonding MEAOs is not extendible for σ-bonds, and this ratio is closer to 80% for π-bonds.

The values of E^{u} in Table 3.4 seems to show that the entanglement between two bonding MEAOs are not as "monogamous" as we thought. However, simply because the unextendible entanglement E^{u} is not extremely close to the entanglement E, does not mean in the ground state wavefunction of these molecules (CH_4 to C_2H_2) each MEAO is significantly entangled to more than two orbitals. Again, we know for a fact that the total correlation between two non-bonding MEAOs are of the order $10^{-3} \times 4\log(2)$, which bounds the exact value of entanglement from above in the virtue of the unified geometric picture of different correlation types outlined in Section 1.1. The discrepancy between the theoretical value of unextendible entanglement, and the almost perfectly monogamous entanglement structure we observed in the above examples, is indeed puzzling. We try to ascribe the discrepancy to the fact that in the definition of $\mathcal{D}_{\rho_{AB}}$ there is no constraint regarding the symmetry of the three-orbital RDM ω_{ABC}. Since ω_{ABC} is the reduced state of the ground state with well-defined particle number and magnetization, ω_{ABC} should also enjoy these symmetries, and admit a block diagonal form where each block correspond to a fixed particle number and magnetization sector. Implementing this constraint would effectively reduce the set $\mathcal{D}_{\rho_{AB}}$, and increases the value of the unextendible entanglement E^{u}. However, after implementing these constraints, we only found an insignificant increase in the unextendible entanglement. Although this discrepancy does not affect the excellent efficacy of the MEAO framework in restoring the Lewis structure of various molecules, it would be an interesting question to explore in the future.

3.2.3 Genuine multipartite entanglement in multi-center bonds

Multi-center bonds are bonding effects beyond the standard Lewis paradigm. Such bonds cannot be described by bonding orbitals localized to two atomic centers, or localized orbitals from two separate centers alone. Instead, several electrons are shared among several centers, and the number of electrons and number of centers involved may not match. Much unlike the two-center bonds, where we know exactly how the maximally bipartite entangled state (3.9) looks like, in the multipartite scenario there is no single maximally entangled state (up to local unitary transformations). Instead, one is presented with many classes of multipartite entangled state. For example, in the tripartite scenario, where our subsystems are qubits for simplicity's sake, the Greenberger–Horne–Zeilinger (GHZ) state [187], [188] and the W-state [189]

$$\begin{aligned} |\mathrm{GHZ}\rangle &= \frac{1}{\sqrt{2}}(|000\rangle + |111\rangle), \\ |\mathrm{W}\rangle &= \frac{1}{\sqrt{3}}(|100\rangle + |010\rangle + |001\rangle), \end{aligned} \tag{3.47}$$

are both "maximally entangled" in their own rights, but they belong to different multipartite entanglement classes as they are not related by any local transformations [189]. And most strikingly, simple calculations reveal that while for $|\mathrm{W}\rangle$ every two qubits are entangled with each other, no qubit pairs are entangled in $|\mathrm{GHZ}\rangle$. Instead, the three qubits are collectively entangled in $|\mathrm{GHZ}\rangle$ (also see the illustration in Figure 3.13). Therefore, the goal is not to design a prototypical three- or four-center bond, in analogy to $|\Psi_{\mathrm{bond}}\rangle$, but to find a tool that can detect and measure the entanglement truly shared among several orbitals.

Let us first recall some concepts in multipartite entanglement theory. A k-partite pure state $|\Psi\rangle$ is k-separable if it has a k-partite tensor product form $|\Psi\rangle = |\psi_1\rangle \otimes |\psi_2\rangle \otimes \cdots \otimes |\psi_k\rangle$ [8], [10]. Any pure state not of that form then contains k-partite entanglement. But note that not all k-partite entanglement truly involves all k parties. For example, the state $|\Psi\rangle = |\psi_{123}\rangle \otimes |\psi_{45\ldots k}\rangle$ where $|\psi_{123}\rangle$ and $|\psi_{45\ldots k}\rangle$ are entangled states, does contain k-partite entanglement. But the tensor product reveals that the first three qubits are not entangled with the last $k-3$ qubits. A k-partite pure state $|\Psi\rangle$ is said to contain genuine multipartite entanglement (GME) if there is no bipartition under which $|\Psi\rangle$ is a product state [84]. The set of biseparable mixed states is however much more complicated

$$\mathcal{D}_{\mathrm{bisep}} = \left\{ \rho = \sum_i p_i |\psi_i\rangle\langle\psi_i| \;\middle|\; \psi_i \text{ is biseparable, } p_i \geq 0, \sum_i p_i = 1 \right\}. \tag{3.48}$$

Note that the states $|\psi_i\rangle$ in the convex combination might be biseparable under different bipartitions [84]. Similar to the bipartite setting, we can define the genuine multipartite entanglement (GME) as the minimal distance to the set of all biseparable states

$$\mathrm{GME}(\rho) = \min_{\sigma \in \mathcal{D}_{\mathrm{bisep}}} S(\rho \| \sigma). \tag{3.49}$$

$$|\mathrm{W}\rangle = \frac{1}{\sqrt{3}}(|100\rangle + |010\rangle + |001\rangle) \qquad |\mathrm{GHZ}\rangle = \frac{1}{\sqrt{2}}(|000\rangle + |111\rangle)$$

Figure 3.13: Illustration of the entanglement structure of the tripartite entangled states $|\mathrm{W}\rangle$ and $|\mathrm{GHZ}\rangle$.

Note that in the bipartite setting, $\mathrm{GME}(\rho)$ reduces to the usual relative entropy of entanglement.

Both detecting and measuring GME for mixed states are generally extremely difficult tasks [7]. For pure states however, at least the detection of GME becomes much simpler, and one simply needs to check whether the entropy of all possible subsystems is non-zero. Based on this observation, the following measure for pure state GME was introduced [85], [190]

$$\mathrm{GME}(|\Psi\rangle) = \min_A S(\rho_A), \tag{3.50}$$

where A runs over all possible subsystems. We have replaced the linear entropy in Ref. [85] with the von Neumann entropy to be consistent with our chosen bipartite entanglement measure. The pure state GME measure (3.50) enjoys the following easy-to-check properties:

1. $\mathrm{GME}(|\Psi\rangle)$ is 0 if and only if $|\Psi\rangle$ is biseparable. This is fulfilled by construction, since $\mathrm{GME}(|\Psi\rangle) = 0$ implies there exists a subsystem A such that ρ_A is pure, and therefore $|\Psi\rangle$ is biseparable. The other direction is obviously true.

2. $\mathrm{GME}(|\Psi\rangle)$ is invariant under any k-partite local unitary transformation $U = U_1 \otimes U_2 \otimes \cdots \otimes U_k$ applied to $|\Psi\rangle$. This is fulfilled by the unitary invariance of the von Neumann entropy of the reduced states of all subsystems.

3. When $k = 2$, $\mathrm{GME}(\Psi\rangle)$ reduces to the standard bipartite entanglement measure for pure states, namely the von Neumann entropy of one of the reduced states.

As demonstrations, in Figure 3.14 we presented the MEAO correlation plot of three typical molecules with multi-center bonds: $C_3H_5^-$ (3-center with 4-electron, $(3c, 4e)$), B_2H_6 $((3c, 2e))$, and C_6H_6 $(6c, 6e)$. We first obtained the mutual information plot from a mean-field HF wavefunction. Using the bond separation scheme outlined in the previous sections,

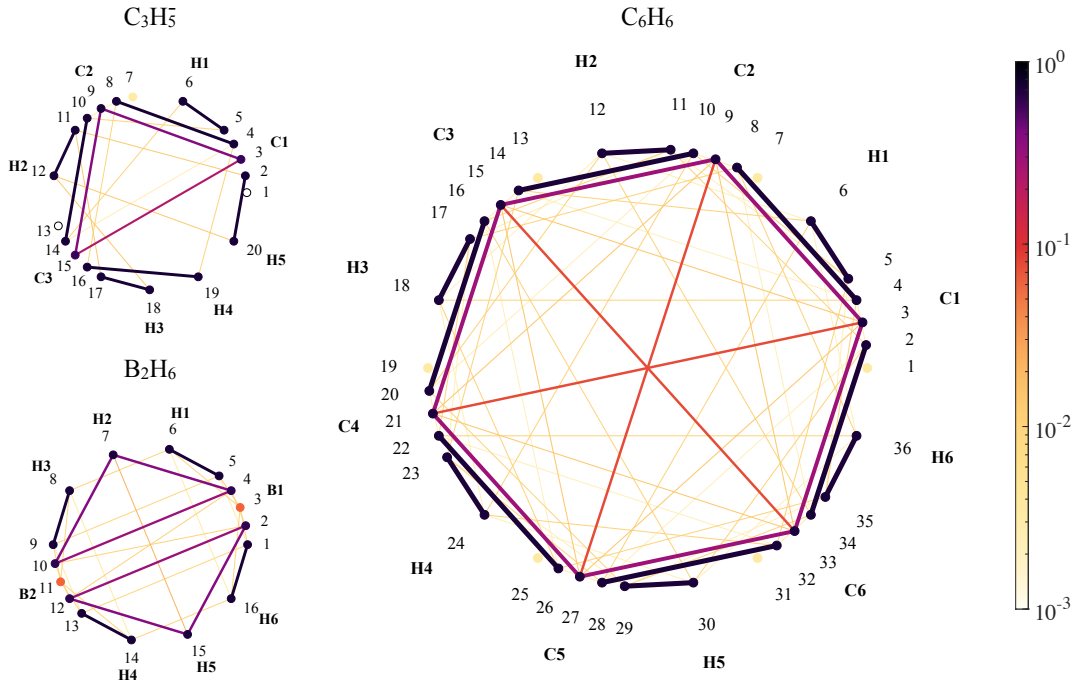

Figure 3.14: Single orbital entropy S_i (vertices) and Correlation I_{ij} (edges) between the MEAO of $C_3H_5^-$, B_2H_6, and C_6H_6 in cc-pVDZ basis. Single orbital entropy is normalized to $2\log(2)$ and correlation is normalized to $4\log(2)$.

	bond type	CAS	GME
$C_3H_5^-$	$(3c, 4e)$	$(3c, 4e)$	0.772
B_2H_6	$(3c, 2e)$	$(6o, 4e)$ $(3o, 2e)$	0.130 0.852
C_6H_6	$(6c, 6e)$	$(6o, 6e)$	0.970
$C_{10}H_8$	$(10c, 10e)$	$(10o, 10e)$	0.968
$C_5H_5^-$	$(5c, 6e)$	$(5o, 6e)$	0.954
C_4H_5N	$(5c, 6e)$	$(5o, 6e)$	0.720
C_4H_4O	$(5c, 6e)$	$(5o, 6e)$	0.560
C_4H_4S	$(5c, 6e)$	$(5o, 6e)$	0.557

Table 3.5: GME (normalized to $2\log(2)$) of various multi-center bonds with cc-pVDZ basis set. The bond type describes the numbers of centers and electrons involved in the bond, and CAS denotes the number of active orbitals and electrons we used to solve for the MPS ground state.

we are able to isolate inseparable orbital clusters of sizes larger than 2. These clusters are signatures of GME: no matter how we partition the cluster, we always separate a pair of entangled orbitals. In the next step, we then group the MEAOs into two collections, the active set $\mathcal{A}$ consisting of orbitals from the multi-center clusters, and the non-active orbitals $\mathcal{N}$ containing all other orbitals. Then the natural orbitals of the 1RDM restricted to $\mathcal{N}$ are taken as core and virtual orbitals, depending on the corresponding natural occupation numbers. The orbitals involved in the multi-center clusters form complete active spaces (CAS), where the number of active electrons are automatically determined by the number of core orbitals. The active spaces are then solved exactly with MPS ansätze using the Block2 [191] DMRG package. The corresponding values of GME (normalized to $2\log(2)$) are presented in Table 3.5.

First, we notice in Figure 3.14 that the two-center bonds (C-C σ, C-H σ, and B-H σ) are clearly separated from the multi-center bonds. The two-center bonds are again represented by the near maximal and monogamous entanglement between two MEAOs, whereas the multi-center bonds are represented by an inseparable cluster of orbitals. Second, we observe in Table 3.5 that all GME values are less than its normalization $2\log(2)$. This is always

guaranteed by the definition (3.49), since

$$\min_A S(\rho_A) \leq S(\rho_i) \leq 2\log(2). \tag{3.51}$$

But this does not necessarily mean that the minimum is obtained in the bipartition of one orbital versus the rest. The entropy of two orbitals, for example, could in some cases be smaller. Third, among the three molecules $C_3H_5^-$, B_2H_6, and C_6H_6, the benzene ring contains the highest amount of GME. We explain this via the argument of symmetry: the six-π-orbital cluster of the benzene ring has the highest level of point group symmetry, including six mirror axes, and a six-fold rotational symmetry. In contrast, the three-center bonds in $C_3H_5^-$ and B_2H_6 are only symmetric about one mirror axis. The other symmetry the benzene uniquely enjoy among all three is the particle hole symmetry in the π-orbital ring. Without any electron deficiency or over-abundance, the CAS state on the π-orbital ring lives in the half-filled subspace of the Hilbert space, which has the highest dimensionality, and therefore more degrees of freedom for hosting entanglement. Both types of symmetry allow the π-electron of the benzene to be more evenly shared among all orbital centers, and enhance the value of GME. Lastly, we find that it is absolutely crucial to calculate the GME only for each multi-center bond separately. We have the unique opportunity in B_2H_6 to calculate the GME of the two electron-deficient bonds. Expectedly, the GME of the six-orbital cluster is rather low, at 0.130. This is because the two three-orbital clusters are only weakly correlated. But once we separate the two bonds, and we do so by including the MEAOs on one of the $(3c, 2e)$ bonds into the non-active space, we immediately observe a drastic increase of GME within a single three-orbital cluster, at the value of 0.852.

A direct comparison between the values of GME and the values other multi-center bonding indices can be rather arbitrary, since different indices have different origins and normalization [149], [159]. But we can already anticipate the potential advantage of GME within the MEAO framework over other multi-center indices, because we do not require any pre-existing knowlegde of the number of atomic centers involved within a bond, or the specific ordering of the atomic centers along the ring [149], [159]. The framework we propose is fully automatic after the input of molecular geometry.

We now check whether GME can stand the tests of expected chemical trends (see Table 3.5). First, we compare the GME of benzene and naphthalene ($C_{10}H_8$). The latter is essentially two benzene rings fused together. The second ring distorts the perfectly symmetric electron sharing in the original ring, and the multi-bonding character is weakened, as indicated by various multi-center bonding indices [192]. And indeed the distortion by the second ring reduces slightly the GME, as is shown in Table 3.5. Another test is the substitution of one of the carbon atom by another element, which is also expected to weaken the multi-center bond by breaking the point group symmetry. For this, we use a family of molecules with $(5c, 6e)$ bonds: cyclopentadienide ($C_5H_5^-$), pyrrole (C_4H_5N), furan (C_4H_4O), and thiophene (C_4H_4S). The distortions caused by the substitutions become stronger as the substituting atoms become heavier and heavier starting from C to S [193].

This trend is indeed confirmed by a visible decrease of GME in the correct order, from 0.954 for $C_5H_5^-$ to only 0.557 for C_4H_4S. Moreover, all the GME values for the $(5c, 6e)$ bonds are lower than that of benzene (which has a $(6c, 6e)$ bond), which again emphasizes the roles of particle-hole and point group symmetries in promoting the value of GME. All the above active space calculations are performed with an MPS ansatz, and the ground states are solved to sub-μ accuracy using the Block2 DMRG solver [191].

Chapter Summary

In this chapter, we thoroughly explored the resourcefulness of entanglement and quantum correlation in molecules. We investigated the potency of various types of correlation in the electronic ground state in several common orbital basis sets of different degrees of orbital localization. We also incorporated two important superselection rules to exactly quantify the potential resource in these systems for quantum information processing tasks. We found that partially localizing (via Pipek-Mezey) the canonical Hartree-Fock (HF) molecular orbitals (MO) further reduce the weak correlation among the HF MOs, while fully (but still manually) localizing the orbitals to a single atomic center reveals maximally entangled structures. Remarkably, the maximally entangled orbitals form monogamous pairs, each corresponding to a well-defined two-center covalent bond. We therefore put forward a conjecture that a single covalent bond can always be rationalized by the maximal entanglement between two fully localized atomic-like orbitals.

Based on this conjecture, we designed a systematic procedure for identifying these atomic-like orbitals for arbitrary molecules. Using the intrinsic atomic orbitals (IAO) as a starting point, we maximized the inter-center orbital-orbital entanglement, and arrived at the set of maximally entangled atomic orbitals (MEAO). The MEAOs are automatically equipped with the correct hybridization, and naturally reproduces the standard Lewis structures of simple molecules, again in the form of maximally and monogamously entangled orbital pairs. To characterize the more exotic multi-center bonds beyond the Lewis paradigm, we extended the bipartite entanglement to the genuine multipartite entanglement (GME). Our results showed that not only can the GME detect the existence of multi-center bonds, it can also serve as a multi-center bond order index which agrees well with expected chemical trends in families of multi-center bonding molecules. Our unifying scheme of analyzing the bonding structure of molecules requires no manual intervention, or expert knowledge of chemical bonding (e.g., the classification of bonding, antibonding and non-bonding orbitals). We therefore anticipate that after future works on fully testing the MEAO framework with large datasets of molecules, it can be a powerful tool for extracting chemical insights from ever more accurate *ab initio* wavefunction solutions.

Chapter 4

Quantum Information-Assisted Orbital Optimization

In the previous chapters, we have developed a comprehensive quantum information toolbox for electronic structure analysis. Especially, we have established both analytically and numerically that the level of orbital correlation can vary drastically from one orbital basis to another. At the same time, we also know that the choice of orbitals also affects significantly both the accuracy and the efficiency of various wavefunction methods. Let us again take the example of matrix product states (MPS). Mathematically speaking, at a fixed maximal bond dimension, different orbital bases give rise to different manifolds of MPS, and consequently different energetically minimal solutions. From a practical point of view, a poor choice of orbital basis can lead to a suboptimal convergence behavior, and requires a larger bond dimension to achieve the desired accuracy [41].

The MPS ansatz is somewhat a special case, as its tuning parameter for expressiveness and complexity — the bond dimension m — is directly connected to orbital entanglement. Specifically, m is the maximal Slater rank (number of positive Slater coefficients) of the Schmidt decomposition of the MPS with respect to the left-right partition at a given bond. The Shannon entropy of the corresponding squared Schmidt coefficients is then the entanglement between the left and right subset of the orbitals. It is therefore natural to reduce some measure of orbital entanglement via orbital transformation, in attempt to achieve an optimal MPS structure for the target ground state. Such a transformation can be discrete, i.e. in the form of orbital reordering based on the orbital-orbital mutual information [39], [93]. It can also be continuous orbital rotations which can be implemented on the fly during a DMRG sweep [41].

As for other common wavefunction ansätze, the connection between the orbital correlation/entanglement and the quality of the ansatz is yet to be precisely established.

Nonetheless, the quantum chemistry community has been guided by the notion of correlation for decades, regardless of the term they use for correlation: It is well established that Møller-Plesset perturbation theory and coupled cluster theory work well in the regime where the ground state is close to a single Slater determinant [194]. This is the regime where all orbitals have small entropy. It has also been proposed and tested that active orbitals should be those with strongly fractional occupation numbers in some description of the ground state beyond the restricted Hartree-Fock approach (e.g., unrestricted Hartree Fock [36], second-order Møller-Plesset perturbation theory [38], coupled clusters singles and doubles [38], etc.). This intuition is then later made more precise by Stein and Reiher, that active orbitals are those of high orbital entanglement [195]. The goal of this chapter is to harness the insights we gained in the previous chapters, and actively exploit quantum information tools to simplify electronic wavefunctions. Accordingly, such simplification leads to a novel way of active space optimization.

This chapter is organized as follows: In Section 4.1 we draw a quantitative connection between the notions of orbital correlation and the representational complexity of a quantum state. With this as the foundational motivation, we present in Section 4.2 a quantum information-assisted complete active space optimization (QICAS) method. We will show that our algorithm can bypass the expensive complete active space self-consistent field iterations.

4.1 Orbital correlation and representational complexity

In this section, we provide both analytic and numerical evidence that orbital correlation can indeed be used as a descriptor of the representational complexity of the wavefunction. The latter we define it to be the Shannon entropy of the configuration interaction (CI) coefficients

$$H_{\mathrm{CI}}^{(\mathcal{B})}(|\Psi\rangle) = -\sum_{n_1,n_2,\ldots,n_D} |c_{n_1,n_2,\ldots,n_D}^{(\mathcal{B})}|^2 \log(|c_{n_1,n_2,\ldots,n_D}^{(\mathcal{B})}|^2), \tag{4.1}$$

in the expansion of the wavefunction $|\Psi\rangle_{\mathcal{B}}$ in a single-particle basis $\mathcal{B} = \{\phi_i\}_{i=1}^{D}$

$$|\Psi\rangle = \sum_{n_1,n_2,\ldots,n_D} c_{n_1,n_2,\ldots,n_D}^{(\mathcal{B})} |n_1, n_2, \cdots, n_D\rangle_{\mathcal{B}}, \tag{4.2}$$

where

$$\sum_{n_1,n_2,\ldots,n_D} |c_{n_1,n_2,\ldots,n_D}^{(\mathcal{B})}|^2 = 1. \tag{4.3}$$

$H_{\mathrm{CI}}^{(\mathcal{B})}$ is clearly orbital basis dependent. Moreover, it vanishes for single Slater determinants in its natural basis, and positive if the quantum state always require more than one single

Slater determinant to represent, regardless of the single-particle basis. Although $H_{\mathrm{CI}}^{(\mathcal{B})}(|\Psi\rangle)$ is a straightforward measure for the multireference character or the representational complexity of a wavefunction $|\Psi\rangle$ expanded in a basis $\mathcal{B}$, it is in general very expensive to calculate as the number of configurations grows factorially with the number of electrons and the number of orbitals.

To circumvent the factorial scaling, we can use orbital entropy as an inexpensive alternative to $H_{\mathrm{CI}}^{(\mathcal{B})}(|\Psi\rangle)$. Calculating the orbital entropy only requires the expectation values of a handful of local observables, the number of which grows only linearly with the system size. Yet, the orbital entropy is closely related to the CI entropy. Let us first look at the example of a two-electron singlet state $|\Psi\rangle$ in two orbitals (1 and 2) associated with annihilation (creation) operators $f_{1/2\sigma}^{(\dagger)}$. Then the following form is general

$$|\Psi(\mathbf{p})\rangle = p_0|\Psi_0\rangle + p_1|\Psi_1\rangle + p_2|\Psi_2\rangle, \tag{4.4}$$

where

$$\begin{aligned} |\Psi_0\rangle &= f_{1\uparrow}^\dagger f_{1\downarrow}^\dagger|0\rangle, \\ |\Psi_1\rangle &= \frac{1}{\sqrt{2}}(f_{1\uparrow}^\dagger f_{2\downarrow}^\dagger - f_{1\downarrow}^\dagger f_{2\uparrow}^\dagger)|0\rangle, \\ |\Psi_2\rangle &= f_{2\uparrow}^\dagger f_{2\downarrow}^\dagger|0\rangle. \end{aligned} \tag{4.5}$$

Although the form of $|\Psi(\mathbf{p})\rangle$ is the most general, it is not the most concise in terms of its CI expansion. We calculate the CI entropy of $|\Psi(\mathbf{p})\rangle$ in the current basis as

$$H_{\mathrm{CI}}(|\Psi(\mathbf{p})\rangle) = -p_0^2\log(p_0^2) - p_1^2\log\left(\frac{p_1^2}{2}\right) - p_2^2\log(p_2). \tag{4.6}$$

In this very special case, the CI entropy precisely coincides with the entanglement between the two spatial orbitals, given by the von Neumann entropy

$$S(\rho) = -\mathrm{Tr}[\rho\log(\rho)] \tag{4.7}$$

of either one of the orbital reduced density matrix

$$\rho_{1/2}(\mathbf{p}) = \mathrm{Tr}_{2/1}[|\Psi(\mathbf{p})\rangle\langle\Psi(\mathbf{p})] = \begin{pmatrix} p_0^2 & 0 & 0 & 0 \\ 0 & p_1^2/2 & 0 & 0 \\ 0 & 0 & p_1^2/2 & 0 \\ 0 & 0 & 0 & p_2^2 \end{pmatrix}. \tag{4.8}$$

The sum of orbital entropy in this case is precisely the double of the CI entropy, in every orbital basis.

The relation between the two entropic quantities we observed in the above example in general does not hold. One would also not expect any exact and general relation to hold,

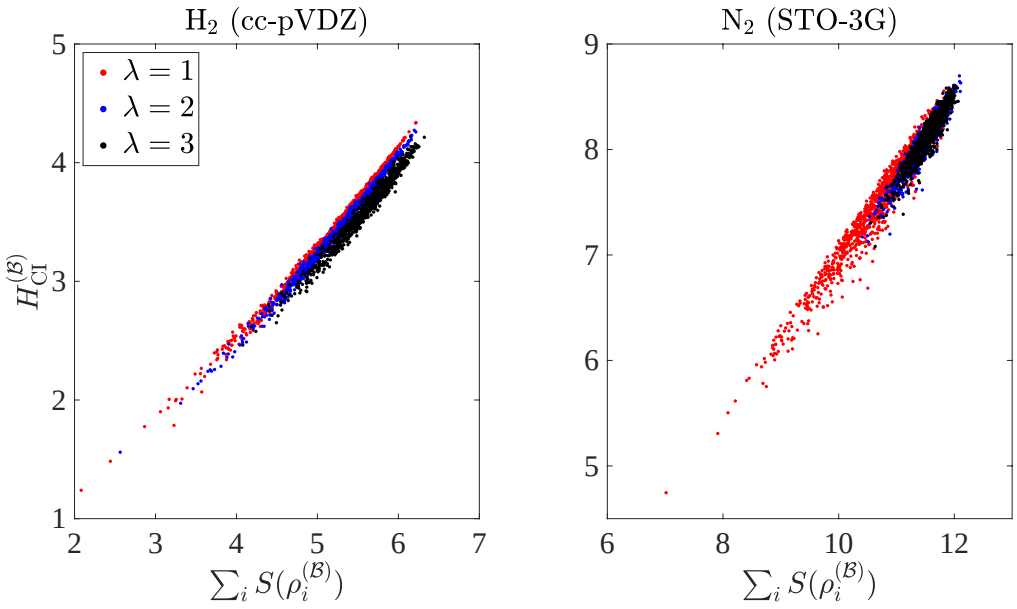

Figure 4.1: CI entropy ($H_{\mathrm{CI}}^{(\mathcal{B})}$) against the sum of orbital entropy ($\sum_i S(\rho_i^{(\mathcal{B})})$) for H_2 (in cc-pVDZ basis) and N_2 (in STO-3G basis) at $\lambda = 1, 2, 3$ times of the respective equilibrium bond length (0.74 Å for H_2 and 1.09 Å for N_2). For each geometry we collect data points corresponding to 1000 orbital bases, transformed from the Hatree Fock canonical basis by a random orthogonal matrix sampled uniformly from the orthogonal group.

as the CI expansion simply contains more information than the orbital reduced state. We therefore turn to a numerical approach to investigate the correlation between the sum of orbital entropy and the CI entropy. In Figure 4.1 we present results from full configuration interaction (FCI) calculation of the ground states of H_2 and N_2. The x- and y-axis show the values of the sum of orbital entropy and the CI entropy, respectively. We have studied for both molecules three molecular geometries at different multiples ($\lambda = 1, 2, 3$) of the equilibrium bond length. For each geometry, the ground state is expanded in 1000 orbital bases transformed from the Hartree-Fock canonical basis by orthogonal matrices sampled uniformly from the appropriate orthogonal group.

In Figure 4.1 we first observe that for both molecules, a rough linear relation between $\sum_i S(\rho_i^{(\mathcal{B})})$ and $H_{\mathrm{CI}}^{(\mathcal{B})}$ persists even beyond the setting of two electrons in two orbitals. Compared to H_2, the deviation from perfect linear behavior is stronger in the case of N_2. We see that the deviation is already quite considerable at equilibrium geometry. The second observation we make is that true multireference character can not be transformed away by orbital rotation. This can be seen when comparing across different internuclear distances. At equilibrium, the ground state is more of a single reference character. Interestingly, the ranges of both entropic quantities are wider at equilibrium. This means although in some basis the ground state might seem multiconfigurational, by choosing a suitable orbital basis this "fake" correlation can be transformed away. In contrast, at stretched

geometries where the ground state is genuinely multiconfigurational, the ranges of both entropic quantities are much smaller. This in turn implies that the true multireference character of the wavefunction can not be transformed away via orbital rotations.

4.2 Complete active space optimization

In strongly correlated systems, the ground states are not accurately represented by single Slater determinants, such as the ones obtained by solving the Hartree-Fock (HF) equation. Instead, multiple configurations are needed for a qualitatively correct description of the system. This type of correlation is commonly referred to as static correlation. Although a full configuration interaction (full CI, or FCI) approach is not realistic for systems consisting of more than a couple of dozens of orbitals at half-filling [196], it is possible to recover the electron correlation to a large degree, by restricting the interacting configurations to those that only differ in a small fraction of orbitals. This amounts to the so-called complete active space configuration interaction (CASCI) approach. If, in addition, the underlying molecular orbital basis is optimized in a self-consistent fashion, CASCI turns into the variationally superior complete active space self-consistent field (CASSCF) approach [95]–[98], [197], [198].

That being said, determining accurate active spaces in practice is a crucial challenge since the quality as well as the rate of convergence of a CASCI/CASSCF calculation are highly sensitive to the choice of (initial) active orbitals [199]. Moreover, the purpose of choosing an active space is to recover correlation effects sufficiently well such that the system is described adequately by a CAS model. To this end, chemical knowledge of the individual systems is often required [178], [200]–[202] for active space selection. However, such *a priori* knowledge of the system may not always be available, especially when the system is large, and its absence severely hinders the black-box applications of CAS methods. Nonetheless, there is hope that the electronic structure estimated by post-HF solutions can be exploited to remove this roadblock: Based on a correlated wavefunction, active orbitals may be selected by means of orbital "observables" (e.g. their occupation numbers) that provide an estimate of orbital correlation effects [36], [38], [203]–[206].

Consequently, diagnostic tools offered by quantum information (QI) which quantify the orbital correlations concisely [87], [119], [180], [195], [207], [208] may hold the key to effective black-box active space selection protocols. There is a caveat, though, as extracting orbital correlation inevitably requires a multireference description of the system. Such a description obviously should not be an exact, but rather an affordable approximation (otherwise the purpose of the general idea would be defeated). The latter is nowadays accessible at reasonable computational cost, thanks to the advent of the matrix product state (MPS) ansatz [33], [209] underlying the density matrix renormalization group (DMRG) approach [210], [211] in QC [52], [212]–[215].

To provide first evidence for the promising prospects of this QI-inspired paradigm, Stein and Reiher determined in [195] suitable active space sizes based on approximate ground states $|\Psi_0\rangle$ obtained from preceding DMRG calculations with low bond dimensions. To be more specific, it was their crucial observation that for a given system with orbitals $\{\phi_i\}$ the corresponding entanglement profile $\{S(\rho_i)\}$ of single-orbital entropy

$$\begin{aligned} S(\rho_i) &= -\mathrm{Tr}[\rho_i \log(\rho_i)], \\ \rho_i &\equiv \mathrm{Tr}_{\setminus\{\phi_i\}}[|\Psi_0\rangle\langle\Psi_0|], \end{aligned} \tag{4.9}$$

reveals a plateau structure, by which one can determine reasonable choices for the active space size. Despite the fruitful application of the single orbital entropy (4.9) in the context of fixed orbital bases, the full analytic potential of QI quantities such as $S(\rho_i)$ is yet to be exploited for active space optimization. In particular, it is still an open challenge to establish a correlation-based measure of the "goodness"/"badness" of an active space and the accompanying CASCI energy.

In this section, we provide this pivotal missing link by proposing a tailored measure that evaluates the quality of a given active space based on orbital entanglement entropy. This in turn then allows us to propose a quantum information-assisted complete active space optimization (QICAS) method with the following appealing features: QICAS (1) requires little system-dependent knowledge, (2) chooses active orbitals not from a fixed but a variable set of orbitals which is optimized based on our QI-motivated cost function, and (3) produces active spaces from which a subsequent CASSCF calculation is either practically converged or requires much fewer iterations.

4.2.1 Cost function based on orbital entropy

In Ref. [195] the authors proposed a novel scheme (AutoCAS) for selecting active orbitals from a set of orthonormal orbitals $\{\phi_i\}_{i=1}^{D}$ (e.g. Hartree Fock canonical orbitals) based on single orbital entropy. The scheme relies on the so-called entropy threshold diagrams (see Figure 4.10 for an example). Each orbital ϕ_i is associated with its single orbital entropy $S(\rho_i)$. For the purpose of a naive selection, any orbital with entropy value higher than a threshold T is deemed active. The number of active orbitals is a T-dependent integer D_T. The threshold diagram is then the plot T-D_T. If a subgroup of orbitals are significantly more correlated than the others, indicated by their higher values of entropy, then the threshold diagram should exhibit a plateau structure (a horizontal segment). Within the plateau, increasing the inclusion threshold T does not change the number of active orbitals. The larger the difference between the entropy of the active and non-active orbitals, the longer and more prominent the plateau. Through identifying the earliest prominent plateau in the threshold diagram, one can determine both the size of the active space, and the proposed active orbitals.

It is rather natural to notice that entropy threshold diagram, and specifically its plateau structure, is orbital basis dependent. Can one find a set of orthonormal orbitals such that the plateau structure is more prominent, and therefore leads to a more accurate active space? To optimize the orbitals we would need a well-motivated cost function F that suits our purpose. We are aiming at (i) an overall simplification of the representational complexity, and (ii) a maximally pronounced plateau structure in the threshold diagram. From the previous Section, we know that the minimizing the sum of orbital entropy can lead to (i). Therefore, a component of the cost function can be

$$F_1 = \sum_{i=1}^{D} S(\rho_i). \tag{4.10}$$

To achieve (ii), we can maximize the difference in entropy between the active and non-active orbitals

$$F_2 = \sum_{i \text{ active}} S(\rho_i) - \sum_{i \text{ non-active}} S(\rho_i). \tag{4.11}$$

Combining the two components, we then arrived at our QI-motivated cost function F_{QI} for active space optimization

$$F_{\text{QI}}(\mathcal{B}) \equiv \frac{1}{2}(F_1 - F_2) = \sum_{i \text{ non-active}} S(\rho_i). \tag{4.12}$$

Two remarks are in order here. First, one notices that to evaluate $F_{\text{QI}}(\mathcal{B})$ one must first decide on the size of the active space D_{CAS}. This can be resolved by a preceding AutoCAS calculation, or based on the threshold diagram in the orbital basis that minimizes F_1 which is agnostic of the target active space size. We shall revisit this point in Section 4.2.4. Second, given a set of orbitals, one needs to decide beforehand which orbitals are active and which orbitals are non-active. For the purpose of orbital optimization, this decision can be arbitrarily made (e.g., the first D_{CAS} orbitals are active). Since reordering is also an orbital rotation, the optimization process will take care of the assignment.

In the following, we provide both theoretical and numerical arguments that F_{QI} is indeed a suitable cost function for active space optimization. Let $\mathcal{B}$ be an ordered orbital basis, and let us consider a CAS problem defined by the tuple $(N_{\text{CAS}}, D_{\text{CAS}})$ of the number of active electrons N_{CAS} and the number of active orbitals D_{CAS}. A corresponding CASCI calculation leads to a $\mathcal{B}$-CASCI ground state energy $E_0^{\text{CASCI}}(\mathcal{B})$ with respect to an electronic Hamiltonian $\hat{H}$. When $E_0^{\text{CASCI}}(\mathcal{B})$ is minimized over all possible choice of orbital bases $\mathcal{B}$, we arrive at the CASSCF ground state energy E_0^{CASSCF}. When $D_{\text{CAS}} = D$, then any active space calculation is equivalent to exact diagonalization, and would result in the exact ground state energy E_0. This can be summarized as

$$E_0^{\text{CASCI}}(\mathcal{B}) \geq \min_{\mathcal{B}'} E_0^{\text{CASCI}}(\mathcal{B}') = E_0^{\text{CASSCF}} \geq E_0, \quad \forall \mathcal{B}. \tag{4.13}$$

The energy gap $\Delta E(\mathcal{B}) \equiv E_0^{\text{CASCI}}(\mathcal{B}) - E_0$ is the missing correlation energy from the $\mathcal{B}$-CAS scheme. $\Delta E(\mathcal{B})$ is the most direct measure of the accuracy of the active space. In the following Theorem, we prove that $\Delta E(\mathcal{B})$ is bounded from above by F_{QI}.

Theorem 1. *For any molecular system with electronic Hamiltonian $\hat{H}$ the following energy-correlation relation holds*

$$\Delta E(\mathcal{B}) \equiv E_0^{\mathrm{CASCI}}(\mathcal{B}) - E_0^{\mathrm{FCI}} \leq k(\hat{H}) F_{\mathrm{QI}}(\mathcal{B}), \tag{4.14}$$

for all orbital bases $\mathcal{B}$, where $k(\hat{H})$ is a constant independent of $\mathcal{B}$.

Proof. For a fixed orbital basis $\mathcal{B}$, and a CAS(N_{CAS}, D_{CAS}), the corresponding linear space of complete active space N-electron wavefunctions is given by

$$\begin{aligned} \mathcal{S}_{\mathrm{CAS}} \equiv \{|\Psi\rangle = |\mathbf{n}\rangle_{\mathcal{N}} \otimes |\psi\rangle_{\mathcal{A}}, \text{ with } \hat{N}|\Psi\rangle = N|\Psi\rangle, \\ \hat{N}|\psi\rangle_A = N_{\mathrm{CAS}}|\Psi\rangle\}. \end{aligned} \tag{4.15}$$

Here $|\mathbf{n}\rangle_{\mathcal{N}} = \bigotimes_{i\in\mathcal{N}} |n_i\rangle$ is the wavefunction in the non-active subspace (denoted by $\mathcal{N}$), where $n_i \in \{0, \uparrow\downarrow\}$ defines the occupation numbers of the non-active orbitals ϕ_i, $i \in \mathcal{N}$, $\hat{N}$ denotes the total particle number operator, and $|\psi\rangle_{\mathcal{A}}$ is an N_{CAS}-electron wavefunction defined within the active space (denoted by $\mathcal{A}$) of D_{CAS} active orbitals. The orthogonal projection operator onto the subspace $\mathcal{S}_{\mathrm{CAS}}$ shall be denoted by $\hat{P}$. In the following, we consider two states in $\mathcal{S}_{\mathrm{CAS}}$: The state $|\Psi'_{\mathrm{CAS}}\rangle$ which has maximal overlap with the full CI ground state $|\Psi_0\rangle$,

$$|\Psi'_{\mathrm{CAS}}\rangle = \arg\max_{|\Phi\rangle\in\mathcal{S}_{\mathrm{CAS}}} |\langle\Phi|\Psi_0\rangle|^2 = \frac{\hat{P}|\Psi_0\rangle}{\|\hat{P}|\Psi_0\rangle\|_2}, \tag{4.16}$$

and the $\mathcal{B}$-CASCI ground state $|\Psi_{\mathrm{CAS}}\rangle$ of the Hamiltonian $\hat{H}$,

$$|\Psi_{\mathrm{CAS}}\rangle = \arg\min_{|\Phi\rangle\in\mathcal{S}_{\mathrm{CAS}}} \langle\Phi|\hat{H}|\Phi\rangle. \tag{4.17}$$

Because of the Rayleigh-Ritz variational principle, the two states satisfy the inequality

$$\langle\Psi'_{\mathrm{CAS}}|\hat{H}|\Psi'_{\mathrm{CAS}}\rangle \geq \langle\Psi_{\mathrm{CAS}}|\hat{H}|\Psi_{\mathrm{CAS}}\rangle. \tag{4.18}$$

Using the spectral decomposition of the Hamiltonian $\hat{H} = \sum_{i\geq 0} E_i|\Psi_i\rangle\langle\Psi_i|$, we can split the expectation $\langle\Psi'_{\mathrm{CAS}}|\hat{H}|\Psi'_{\mathrm{CAS}}\rangle$ as

$$\begin{aligned} E' &\equiv \langle\Psi'_{\mathrm{CAS}}|\hat{H}|\Psi'_{\mathrm{CAS}}\rangle \\ &= E_0|\langle\Psi'_{\mathrm{CAS}}|\Psi_0\rangle|^2 + \sum_{i>0} E_i|\langle\Psi'_{\mathrm{CAS}}|\Psi_i\rangle|^2 \\ &\leq E_0|\langle\Psi'_{\mathrm{CAS}}|\Psi_0\rangle|^2 + \max_i E_i(1 - |\langle\Psi'_{\mathrm{CAS}}|\Psi_0\rangle|^2). \end{aligned} \tag{4.19}$$

By introducing $\epsilon \equiv 1 - |\langle\Psi'_{\mathrm{CAS}}|\Psi_0\rangle|^2$, we then obtain

$$\Delta E \leq \Delta E' \leq \Delta E_{\max}\epsilon, \tag{4.20}$$

where $\Delta E' \equiv E' - E_0$, and $\Delta E_{\max} \equiv \max_i E_i - E_0$.

By definition, the CAS state with the largest overlap with the exact ground state is $|\Psi'_{\mathrm{CAS}}\rangle = \hat{P}|\Psi_0\rangle/\sqrt{1-\epsilon}$. We can therefore decompose the exact ground state $|\Psi_0\rangle$ into the component in the CAS subspace $\mathcal{S}_{\mathrm{CAS}}$, and the component perpendicular to it

$$\begin{aligned} |\Psi_0\rangle &= \hat{P}|\Psi_0\rangle + (\mathbb{1}-\hat{P})|\Psi_0\rangle \\ &= \sqrt{1-\epsilon}|\Psi'_{\mathrm{CAS}}\rangle + \sqrt{\epsilon}\sum_{\mathbf{m}\neq\mathbf{n}} \lambda_{\mathbf{m}}|\mathbf{m}\rangle \otimes |\psi_{\mathbf{m}}\rangle, \end{aligned} \tag{4.21}$$

where $\sum_{\mathbf{m}\neq\mathbf{n}} |\lambda_{\mathbf{m}}|^2 = 1$ and $|\psi_{\mathbf{m}}\rangle = (\langle\mathbf{m}|\otimes\mathbb{1})(\mathbb{1}-\hat{P})|\Psi_0\rangle/(\sqrt{\epsilon}\lambda_{\mathbf{m}})$. The summation $\sum_{\mathbf{m}\neq\mathbf{n}}$ explicitly omits the occupation vector $\mathbf{n}$ in the non-active space, which can be justified by the following logic: If $|\Psi_0\rangle$ can be written as

$$|\Psi_0\rangle = \sqrt{1-\epsilon}|\Psi'_{\mathrm{CAS}}\rangle + \sqrt{\epsilon}\lambda_{\mathbf{n}}|\mathbf{n}\rangle \otimes |\psi_{\mathbf{n}}\rangle + \sqrt{\epsilon}\sum_{\mathbf{m}\neq\mathbf{n}} \lambda_{\mathbf{m}}|\mathbf{m}\rangle \otimes |\psi_{\mathbf{m}}\rangle, \tag{4.22}$$

then we can redefine

$$|\Psi''_{\mathrm{CAS}}\rangle = \frac{\sqrt{1-\epsilon}|\Psi'_{\mathrm{CAS}}\rangle + \sqrt{\epsilon}\lambda_{\mathbf{n}}|\mathbf{n}\rangle \otimes |\psi_{\mathbf{n}}\rangle}{\sqrt{1-(1-|\lambda_{\mathbf{n}}|^2)\epsilon}}, \tag{4.23}$$

which attains a larger overlap with the exact ground state $|\Psi_0\rangle$ than $|\Psi'_{\mathrm{CAS}}\rangle$. This then contradicts with the definition of the CAS state $|\Psi'_{\mathrm{CAS}}\rangle$ with the largest overlap with the exact ground state.

With the expansion of the ground state (4.21), we are now equipped to calculate the orbital reduced density matrices ρ_i where the index i belongs to the non-active subspace. We first notice that ρ_i is diagonal in the occupation number basis. This is because the particle number and the magnetization are well-defined symmetries of the Hamiltonian, and hence also of the ground state. Then all there is left to do is to calculate the diagonal elements of ρ_i based on the following expressions

$$\begin{aligned} (\rho_i)_{00} &= \langle 0|\rho_i|0\rangle = \mathrm{Tr}[\rho_i(1-\hat{n}_{i\uparrow}-\hat{n}_{i\downarrow}+\hat{n}_{i\uparrow}\hat{n}_{i\downarrow})], \\ (\rho_i)_{11} &= \langle\uparrow|\rho_i|\uparrow\rangle = \mathrm{Tr}[\rho_i(\hat{n}_{i\uparrow}-\hat{n}_{i\uparrow}\hat{n}_{i\downarrow})], \\ (\rho_i)_{22} &= \langle\downarrow|\rho_i|\downarrow\rangle = \mathrm{Tr}[\rho_i(\hat{n}_{i\downarrow}-\hat{n}_{i\uparrow}\hat{n}_{i\downarrow})], \\ (\rho_i)_{33} &= \langle\uparrow\downarrow|\rho_i|\uparrow\downarrow\rangle = \mathrm{Tr}[\rho_i\hat{n}_{i\uparrow}\hat{n}_{i\downarrow}]. \end{aligned} \tag{4.24}$$

Since in (4.21) the expansion is already in the occupational basis of the non-active orbitals, computing the above expectation values is rather straightforward. For instance, to compute $\langle\hat{n}_{i\uparrow}\rangle = \mathrm{Tr}[\rho\,\hat{n}_{i\uparrow}]$, one simply collects the configurations in (4.21) where the local state on the i-th orbital is $|\uparrow\rangle$, and sums over the collected squared amplitudes. For a virtual orbital

i, the diagonal elements of ρ_i are given by

$$\begin{aligned}
(\rho_i)_{00} &= 1-\epsilon+\epsilon \sum_{\mathbf{m}\neq\mathbf{n}:m_i=0} |\lambda_{\mathbf{m}}|^2 \equiv 1-\epsilon p_i, \\
(\rho_i)_{11} &= \epsilon \sum_{\mathbf{m}\neq\mathbf{n}:m_i=\uparrow} |\lambda_{\mathbf{m}}|^2 \equiv \epsilon q_i, \\
(\rho_i)_{22} &= \epsilon \sum_{\mathbf{m}\neq\mathbf{n}:m_i=\downarrow} |\lambda_{\mathbf{m}}|^2 \equiv \epsilon r_i, \\
(\rho_i)_{33} &= \epsilon \sum_{\mathbf{m}\neq\mathbf{n}:m_i=\uparrow\downarrow} |\lambda_{\mathbf{m}}|^2 \equiv \epsilon s_i,
\end{aligned} \tag{4.25}$$

where $p_i = \sum_{\mathbf{m}\neq\mathbf{n}:m_i\neq n_i} |\lambda_{\mathbf{m}}|^2$. For a core orbital i, the diagonal elements of ρ_i are instead given by

$$\begin{aligned}
(\rho_i)_{00} &= \epsilon \sum_{\mathbf{m}\neq\mathbf{n}:m_i=0} |\lambda_{\mathbf{m}}|^2 \equiv \epsilon s_i, \\
(\rho_i)_{11} &= \epsilon \sum_{\mathbf{m}\neq\mathbf{n}:m_i=\uparrow} |\lambda_{\mathbf{m}}|^2 \equiv \epsilon q_i, \\
(\rho_i)_{22} &= \epsilon \sum_{\mathbf{m}\neq\mathbf{n}:m_i=\downarrow} |\lambda_{\mathbf{m}}|^2 \equiv \epsilon r_i, \\
(\rho_i)_{33} &= 1-\epsilon+\epsilon \sum_{\mathbf{m}\neq\mathbf{n}:m_i=\uparrow\downarrow} |\lambda_{\mathbf{m}}|^2 \equiv 1-\epsilon p_i,
\end{aligned} \tag{4.26}$$

Note that s_i and p_i are defined differently depending on the core/virtual nature of the orbital, and the equality $p_i = q_i + r_i + s_i$ is satisfied in both cases. The von Neumann entropy $S(\rho_i)$ of ρ_i is then given by the Shannon entropy $H(\boldsymbol{x}_i)$

$$S(\rho_i) = H(\boldsymbol{x}_i) = -\sum_{k=0}^{3} (\boldsymbol{x}_i)_k \log((\boldsymbol{x}_i)_k), \tag{4.27}$$

of the spectrum of ρ_i which we denote as $\boldsymbol{x}_i \equiv \mathrm{spec}(\rho_i) = (1-\epsilon p_i, \epsilon q_i, \epsilon r_i, \epsilon s_i)$. We further define $\boldsymbol{y}_i \equiv (1-\epsilon p_i, \epsilon p_i, 0, 0)$, which satisfies $\boldsymbol{y}_i \succ \boldsymbol{x}_i$, where $\succ$ stands for vector majorization. For two probability vectors $\boldsymbol{a}$ and $\boldsymbol{b}$ of length L, the majorization condition reads

$$\boldsymbol{a} \succ \boldsymbol{b} \quad \Leftrightarrow \quad \sum_{k\leq K} a_k \geq \sum_{k\leq K} b_k, \ \forall K \leq L, \quad \text{and} \quad \sum_{k=1}^{L} a_k = \sum_{k=1}^{L} b_k = 1. \tag{4.28}$$

Because the Shannon entropy is Schur concave, and that $\boldsymbol{y}_i \succ \boldsymbol{x}_i$, the entropy of $\boldsymbol{x}_i$ and $\boldsymbol{y}_i$ then satisfy

$$H(\boldsymbol{x}) \geq H(\boldsymbol{y}) = B(\epsilon p_i). \tag{4.29}$$

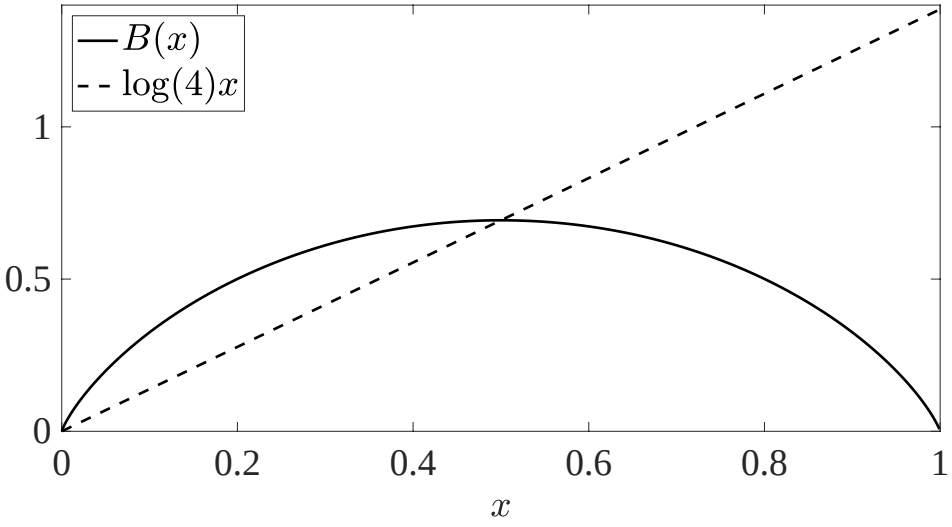

Figure 4.2: Concavity of the binary entropy $B(x)$, and illustration of $B(x) \geq \log(4)x$ when $0 \leq x \leq 1/2$.

Here, $B(x) \equiv -x\log(x) - (1-x)\log(1-x)$ is the so-called binary entropy. In other words, we arrived at

$$\sum_{i\in\mathcal{N}} S(\rho_i) \geq \sum_{i\in\mathcal{N}} B(\epsilon p_i). \tag{4.30}$$

The binary entropy $B(x)$ is a concave function, and symmetric about the vertical line defined by $x = 1/2$, where the function attains its maximal value $\log(2)$ (see Figure 4.2). Consequently, $B(x)$ is bounded from below by $\log(4)x$, in the region $0 \leq x \leq 1/2$. We now insert an additional but well motivated assumption to the theorem, namely $0 \leq \epsilon \leq 1/2$. This assumption states that the norm squared of the projection of the exact ground state $|\Psi_0\rangle$ onto the CAS subspace $\mathcal{S}$ should be at least $1/2$. This is a valid assumption, if we consider the active space method to be a sensible ansatz for the current problem. Finally, we conclude that

$$\sum_{i\in\mathcal{N}} S(\rho_i) \geq \log(4)\epsilon \sum_{i\in\mathcal{N}} p_i \geq \log(4)\epsilon, \tag{4.31}$$

where we have used the inequality $\sum_{i\in\mathcal{N}} p_i \geq 1$. To prove this inequality, recall that $p_i = \sum_{\mathbf{m}\neq\mathbf{n}:m_i\neq n_i} |\lambda_{\mathbf{m}}|^2$. Since $\mathbf{m} \neq \mathbf{n}$, there exists for every such $\mathbf{m}$ a non-active orbital index i such that $m_i \neq n_i$. Therefore

$$\sum_{i\in\mathcal{N}} p_i = \sum_{i\in\mathcal{N}} \sum_{\mathbf{m}\neq\mathbf{n}:m_i\neq n_i} |\lambda_{\mathbf{m}}|^2 \geq \sum_{\mathbf{m}\neq\mathbf{n}} |\lambda_{\mathbf{m}}|^2 = 1. \tag{4.32}$$

Inserting $\Delta E_{\max}\epsilon \geq \Delta E$, we then arrive at

$$\Delta E \leq \frac{\Delta E_{\max}}{\log(4)} \sum_{i \in \mathcal{N}} S(\rho_i) = \frac{\Delta E_{\max}}{\log(4)} F_{\mathrm{QI}}(\mathcal{B}), \tag{4.33}$$

which concludes the proof. □

Theorem 1 laid the foundation for using F_{QI} as a cost function for orbital optimization. The theorem ensures that when F_{QI} approaches 0, the missing correlation energy in the $\mathcal{B}$-CASCI calculation also approaches 0 at most linearly as F_{QI}. When $F_{\mathrm{QI}} = 0$, then the $\mathcal{B}$-CASCI result is the exact ground state solution. There is a serious issue, however, that the prefactor of this linear bound is almost unattainable: It involves the highest excitation gap of the Hamiltonian. This is because the CAS solution $|\Psi_{\mathrm{CAS}}\rangle$ is not an exact eigenstate of $\hat{H}$ but a superposition of all eigenstates, and *a priori* we have no mathematical knowledge about the weight of the highest eigenstate of the Hamiltonian in the CAS solution. In other words, we have taken into account the worst case scenario where $|\Psi_{\mathrm{CAS}}\rangle$ is a superposition of only the ground state and the highest excited state. If the prefactor is uncontrollably large, it could potentially render Theorem 1 irrelevant. That being said, physically we expect this worst case scenario to be highly unlikely, and that most of the significantly contributing eigenstates in the expansion of $|\Psi_{\mathrm{CAS}}\rangle$ to be only the low-lying ones. We therefore also expect that the prefactor $k(\hat{H})$ in Theorem 1 to be much smaller in practical scenarios, and therefore the theorem is still highly relevant.

To further explore the relation between the CASCI energy and the cost function F_{QI} in practice, we conduct the following numerical experiment. For this we choose the molecule C_2 at internuclear distance $R = 1.243$ Å in the cc-pVDZ basis set (12 electrons in 28 orbitals in total), and adopt a CAS(8,8) model (an active space of 8 electrons in 8 orbitals). We start by calculating the 28-orbital ground state with an MPS ansatz. The DMRG calculation is performed with a maximal bond dimension of 200 and 50 sweeps in total. From this we obtained the 1- and 2-particle reduced density matrices (1- and 2-RDM), γ and Γ, respectively, which allow us to compute the cost function $F_{\mathrm{QI}}(\mathcal{B})$ in any basis $\mathcal{B}$. We are able to find the optimal basis $\mathcal{B}^*$ (details presented in the next Section) which minimizes the cost function $F_{\mathrm{QI}}(\mathcal{B})$. We then sample 10^3 orbital bases randomly from the neighborhood of $\mathcal{B}^*$. The sampling is achieved by 10^3 orthogonal rotation $U = \exp(\alpha \mathbf{X})$ parametrized by 28-by-28 antisymmetric matrices $\mathbf{X}$ and angles α. The independent elements of $\mathbf{X}$ are drawn uniformly from $[-1, 1]$, and α is drawn uniformly from $[0, 0.05]$. For every sampled orbital basis $\mathcal{B}$, we compute the corresponding $\mathcal{B}$-CASCI(8,8) energy, treating the first 2 orbitals as core orbitals, and the last 18 orbitals as virtual. At the same time, the cost function $F_{\mathrm{QI}}(\mathcal{B})$ is also computed for every $\mathcal{B}$.

In Figure 4.3, we present the result of our numerical experiment. The x-axis represents the value of $F_{\mathrm{QI}}(\mathcal{B})$ whereas the y-axis marks the corresponding $\mathcal{B}$-CASCI(8,8) energy for each basis $\mathcal{B}$. The sampled orbital basis sets are presented as scattered red dots. The

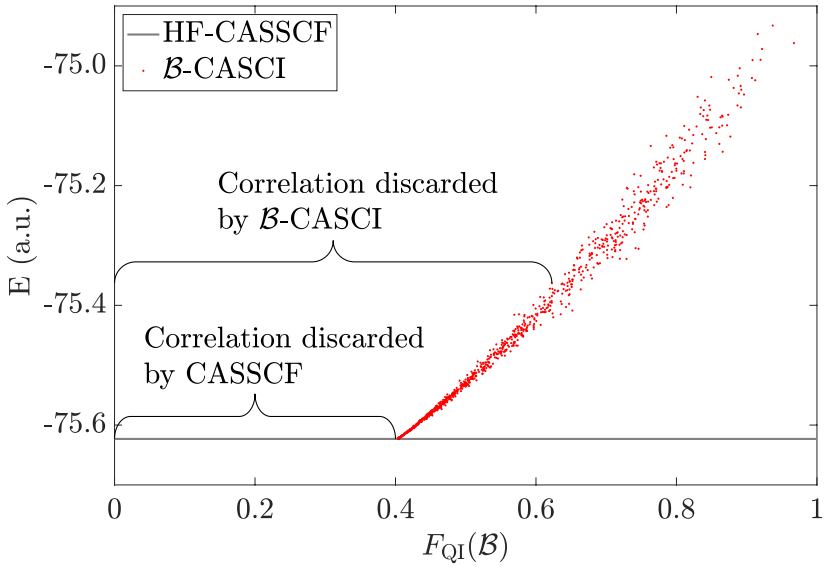

Figure 4.3: $\mathcal{B}$-CASCI(8,8) energy for C_2 at R = 1.243 Å in the cc-pVDZ basis set versus out-of-CAS correlation $F_{\mathrm{QI}}(\mathcal{B})$. 10^3 random orbital bases $\mathcal{B}$ (red dots) are sampled (see text for more details on the sampling scheme). The CASSCF(8,8) energy is plotted as a solid line for reference.

variationally optimal CASSCF(8,8) energy is also plotted as a reference. First, we notice that the correlation of the two quantities is strikingly strong. Recall that Theorem 1 only guaranteed a linear inequality, and by no means implies any quasi-linear relation that we observe in Figure 4.3 between the cost function $F_{\mathrm{QI}}(\mathbf{B})$ and the $\mathcal{B}$-CASCI energy. From left to right $F_{\mathrm{QI}}(\mathcal{B})$ increases, meaning more orbital correlation is discarded by the CAS ansatz when the $\mathcal{B}$-CASCI calculation is performed. Accordingly, the quality of the CAS deteriorates, leading to a larger error compared to the optimal CASSCF energy. Based on this observation, we can interpret $F_{\mathrm{QI}}(\mathcal{B})$ as the out-of-CAS correlation, which can serve as a measure for the quality of the current active space. Second, we notice that the quasi-linear relation is stronger when $\mathcal{B}$ is closer to the minimizer $\mathcal{B}^*$ of $F_{\mathrm{QI}}(\mathcal{B})$, and that dispersion starts to appear when $F_{\mathrm{QI}}(\mathcal{B})$ becomes large. Given that we are sampling only within a small neighborhood around $\mathcal{B}^*$, we expect the quasi-linear relation to break down beyond a certain distance from $\mathcal{B}$ (e.g., when α is of the order 1). Third, and perhaps most importantly, the $\mathcal{B}^*$-CASCI energy approximates extremely well the CASSCF energy. This indicates the two landscapes, $F_{\mathrm{QI}}(\mathcal{B})$ and the $\mathcal{B}$-CASCI energy, share a very similar minimizing orbital basis, despite the fact that they are conceptually distinct quantities. This instrumental observation strongly validates the approach of using $F_{\mathrm{QI}}(\mathcal{B})$ as a cost function for active space optimization.

To summarize, in this section we constructed a cost function $F_{\mathrm{QI}}(\mathcal{B})$ for active space optimization based on the intuition that orbitals with high entropy should be included in

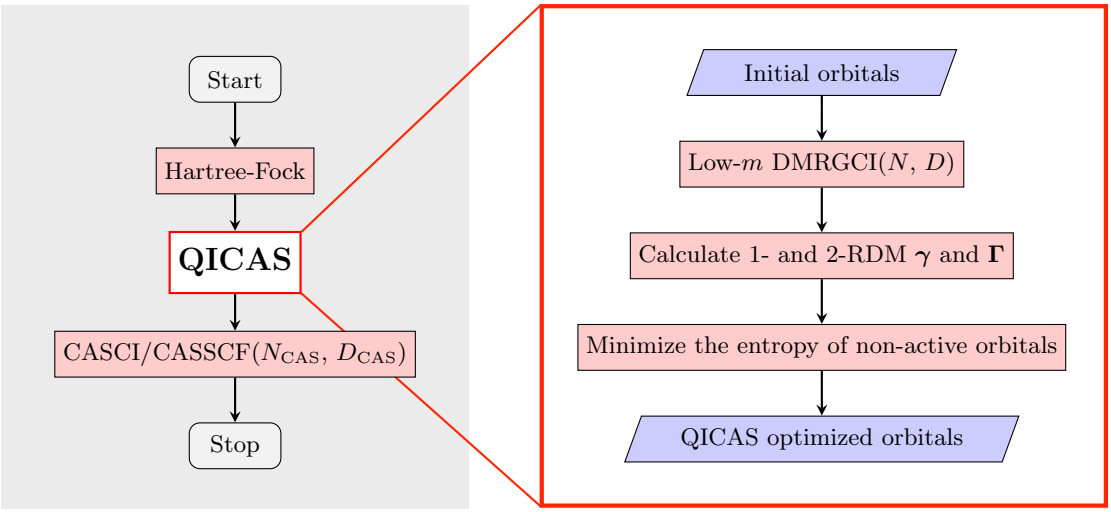

Figure 4.4: Flowchart of the QICAS subroutine and its applications as a post-HF treatment to prepare orbitals for CASCI/CASSCF calculations.

the active space. We provided further motivation and validation through the forms of an analytic theorem and a numerical experiment that $F_{\mathrm{QI}}(\mathcal{B})$ is indeed closely connected to the CASCI energy landscape. Most importantly, minimizing $F_{\mathrm{QI}}(\mathcal{B})$ results in an energetically optimal active space.

4.2.2 The QICAS algorithm

We now present the quantum information-assisted complete active space optimization (QICAS) algorithm. In Figure 4.4 we show QICAS as a subroutine as a post-HF treatment for the purpose of active space preparation. The QICAS block contains the following steps: (i) Taking into account all initial orbitals and all electrons, a low bond dimension MPS ground state is calculated using a partially converged DMRG run. (ii) From (i), the 1- and 2-RDM γ and Γ are computed. (iii) The entropy-based cost function $F_{\mathrm{QI}}(\mathcal{B})$ is minimized, and the minimizer is returned as the QICAS optimized orbitals. We shall elaborate on these three steps in more details below. After executing QICAS, the optimized orbitals then contain a proposed partition of active and non-active orbitals, which can be used for a direct CASCI calculation, or as a starting point for CASSCF.

Step (i) is the crucial step of estimating the out-of-CAS correlation, by explicitly correlating all orbitals on the same footing. Recall that the entropy of the reduced state ρ_i of non-active orbitals are by definition 0 for a CAS wavefunction, since $\rho_i = |0\rangle\langle 0|$ for virtual orbitals, and $\rho_i = |\uparrow\downarrow\rangle\langle\uparrow\downarrow|$ for core orbitals. To estimate the correlation loss due to the assumption of an active space, one necessarily has to go beyond the scope of CAS wavefunctions. Ideally the information regarding the correlation loss can be obtained via

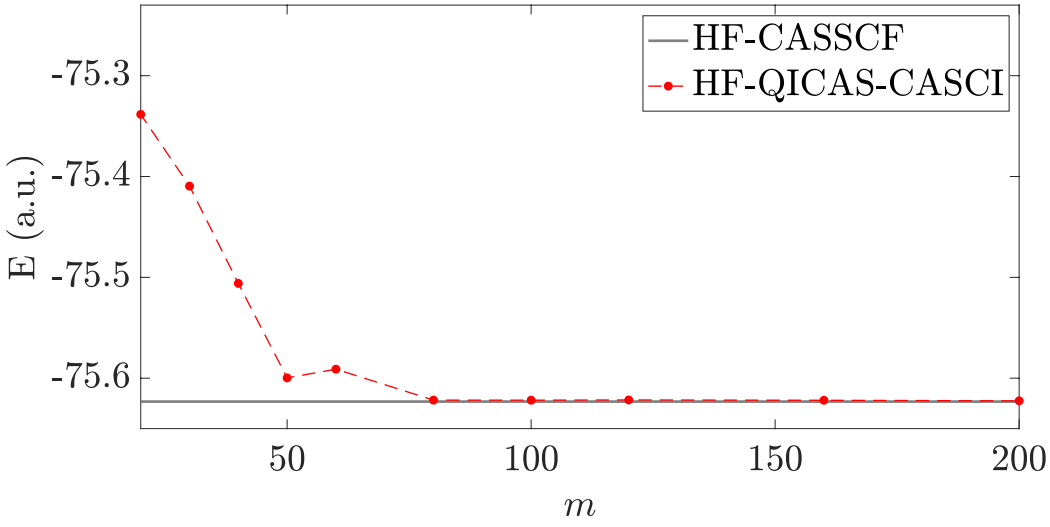

Figure 4.5: HF-QICAS-CASCI(8, 8) energy for C_2 in the cc-pVDZ basis at R = 1.243 Å versus the bond dimension m of the MPS ground state $|\Psi_0\rangle$. The HF-CASSCF energy is plotted as a reference.

a full CI wavefunction that contains the all orbital correlation. However, that would be computationally intractable, and would defeat the purpose of employing a CAS scheme for the problem at hand. What we need is an inexpensive estimate that democratically correlate all orbitals, in such a way that the accuracy of this estimation can be systematically tuned. For this purpose, we adopt a low bond dimension (m) MPS ansatz, similar to the AutoCAS scheme in Ref. [195]. The intuition is that the quantum state itself converges to a decent quality faster than the energy [216], thus provides a good estimation of the orbital correlation. We indeed verify that effective estimation of the orbital entropy for QICAS is possible using a low-m MPS. In Figure 4.5 we demonstrated the performance of QICAS evaluated by a subsequent CASCI calculation, as a function of the bond dimension m of the trial wavefunction. The data are computed for the C_2 molecule at R = 1.243Å in the cc-pVDZ basis set. On one hand, we see that with a higher bond dimension m, the performance of QICAS indeed improves, indicated by a lower CASCI energy based on the QICAS optimized orbitals. On the other hand, the QICAS-CASCI energy quickly approaches the lower bound, the CASSCF energy, for bond dimension beyond 80. At $m = 80$, the energy error of QICAS-CASCI compared to CASSCF is already around 1.4 mHa.

Step (ii) highlights the simplicity of the necessary ingredients for computing the QI based cost function $F_{\mathrm{QI}}(\mathcal{B})$. Since each orbital can be occupied by up to two electrons of opposite spins, only partial information from the 1- and 2-RDM, γ and Γ, is needed for computing single orbital reduced states. The elements of 1- and 2-RDM of the (approximate) ground state $|\Psi_0\rangle$ are defined as two-point and four-point correlation functions

respectively

$$\begin{aligned}
\gamma^i_j &= \langle\Psi_0|f^\dagger_{i\uparrow}f_{j\uparrow}|\Psi_0\rangle,\\
\gamma^{\bar{i}}_{\bar{j}} &= \langle\Psi_0|f^\dagger_{i\downarrow}f_{j\downarrow}|\Psi_0\rangle,\\
\Gamma^{ij}_{kl} &= \langle\Psi_0|f^\dagger_{i\uparrow}f^\dagger_{j\uparrow}f_{l\uparrow}f_{k\uparrow}|\Psi_0\rangle,\\
\Gamma^{i\bar{j}}_{k\bar{l}} &= \langle\Psi_0|f^\dagger_{i\uparrow}f^\dagger_{j\downarrow}f_{l\downarrow}f_{k\uparrow}|\Psi_0\rangle,\\
\Gamma^{\bar{i}j}_{\bar{k}l} &= \langle\Psi_0|f^\dagger_{i\downarrow}f^\dagger_{j\uparrow}f_{l\uparrow}f_{k\downarrow}|\Psi_0\rangle,\\
\Gamma^{\bar{i}\bar{j}}_{\bar{k}\bar{l}} &= \langle\Psi_0|f^\dagger_{i\downarrow}f^\dagger_{j\downarrow}f_{l\downarrow}f_{k\downarrow}|\Psi_0\rangle.
\end{aligned} \tag{4.34}$$

Note that the spin symmetry of the ground state requires the non-spin-preserving correlation functions to vanish. The eigenvalues of the orbital RDM ρ_i are related to the particle RDMs in the following way [62], [119]

$$\begin{aligned}
\rho_i\,|0\rangle_i &= (1-\gamma^i_i-\gamma^{\bar{i}}_{\bar{i}}+\Gamma^{i\bar{i}}_{i\bar{i}})\,|0\rangle_i \equiv \lambda^{(i)}_0|0\rangle_i,\\
\rho_i\,|\uparrow\rangle_i &= (\gamma^i_i-\Gamma^{i\bar{i}}_{i\bar{i}})\,|\uparrow\rangle_i \equiv \lambda^{(i)}_1|\uparrow\rangle_i,\\
\rho_i\,|\downarrow\rangle_i &= (\gamma^{\bar{i}}_{\bar{i}}-\Gamma^{i\bar{i}}_{i\bar{i}})\,|\downarrow\rangle_i \equiv \lambda^{(i)}_2|\downarrow\rangle_i,\\
\rho_i\,|\uparrow\downarrow\rangle_i &= \Gamma^{i\bar{i}}_{i\bar{i}}\,|\uparrow\downarrow\rangle_i \equiv \lambda^{(i)}_3|\uparrow\downarrow\rangle_i.
\end{aligned} \tag{4.35}$$

For the sake of readability, the orbital basis $\mathcal{B}$ dependence of ρ_i, γ and Γ is only implicitly assumed in the above equations. We now can rewrite the cost function $F_{\mathrm{QI}}(\mathcal{B})$ as

$$F_{\mathrm{QI}}(\mathcal{B}) = -\sum_{i\in\mathcal{N}}\sum_{k=0}^{3}\lambda^{(i)}_k\log(\lambda^{(i)}_k). \tag{4.36}$$

To compute $F_{\mathrm{QI}}(\mathcal{B}')$ for another orbital basis $\mathcal{B}'$, one simply rotates the 1- and 2-RDM γ and Γ to basis $\mathcal{B}'$, compute the eigenvalues of the orbital RDMs according to (4.35), and evaluates the cost function according to (4.36). In other words, the computation for the particle RDMs only needs to be performed once, in the initial orbital basis.

We now discuss step (iii), the minimization of $F_{\mathrm{QI}}(\mathcal{B})$. In this Section, we adopt a non-gradient optimization method, and all numerical results presented here are based on this optimization method. In Appendix C we devise a quasi-newton optimization scheme based on analytically calculated gradient and the diagonal of the Hessian of the cost function. Relevant python-based codes have been made public in [217].

We target the following minimization problem

$$\mathcal{B}^* = \min_{\mathcal{B}} F_{\mathrm{QI}}(\mathcal{B}). \tag{4.37}$$

We start by parametrizing the manifold of orbital bases by an orthogonal transformation $\mathbf{U}$ acting on the initial basis $\mathcal{B}^{(0)} = \{\phi_i\}$ according to

$$\tilde{\phi}_i = \sum_j U_{ij}\phi_j. \tag{4.38}$$

Then we established a one-to-one correspondence between the group of orthogonal matrices of order D, and the set of real orbital bases. The former can be parametrized as an exponential of antisymmetric matrices

$$\mathbf{U} \equiv \exp(\mathbf{X}) = \mathbb{1} + \mathbf{X} + \frac{1}{2}\mathbf{X}^2 + \cdots , \tag{4.39}$$

where $\mathbf{X}^{\mathrm{T}} = -\mathbf{X}$. Now the quest of solving (4.37) is reduced to optimizing the $D(D-1)/2$ independent parameters X_{ij}'s in $\mathbf{X}$.

A remark is in order here. Notice that the CASCI energy is invariant under the so-called redundant rotation within the core and virtual orbital subspace, separately. In contrast, $F_{\mathrm{QI}}(\mathcal{B})$ is explicitly not invariant under internal rotation within the non-active space. Therefore, there is an apparent mismatch between the two quantities. On one hand, there is a chance that redundant rotations are included in the process of minimizing $F_{\mathrm{QI}}(\mathcal{B})$. On the other hand, ignoring redundant rotations may prevent us from reaching the true minimum of $F_{\mathrm{QI}}(\mathcal{B})$, thus affecting the accuracy of the optimized active space. This is a cost-and-effect trade-off that many methods face. As a guide, we can follow two strategies: If QICAS is followed directly by a CASCI calculation and high level of accuracy of the active space is desired, then it is beneficial to consider all orbital rotations. This is suitable for a small system. If QICAS is used to prepare a starting point for a CASSCF calculation, then one can afford to consider only rotation between the non-redundant rotations (core-active, active-virtual, and core-virtual). This is suitable for the scenario where the underlying orbital space is significantly larger than the target active space.

We optimize the elements of the antisymmetric matrix X_{ij} sequentially. This effectively applies a two-orbital rotation (Jacobi rotation) $\mathbf{J}^{(ij)}(X_{ij})$ between the orbital i and j

$$\mathbf{J}^{(ij)}(X_{ij}) = \begin{pmatrix} 1 & & & & & & 0 \\ & \ddots & & & & & \\ & & \cos(X_{ij}) & \cdots & \sin(X_{ij}) & & \\ & & \vdots & & \vdots & & \\ & & -\sin(X_{ij}) & \cdots & \cos(X_{ij}) & & \\ & & & & & \ddots & \\ 0 & & & & & & 1 \end{pmatrix} \tag{4.40}$$

to the current orbital basis. After an element in $\mathbf{X}$ is optimized, the 1- and 2-RDM are updated and the history of two-orbital rotations is documented. The final orthogonal matrix $\mathbf{U}^*$ is the product of the documented Jacobi rotations

$$\mathbf{U}^* = \prod_{n=1}^{N_{\mathrm{cycle}}} \prod_{(i,j)} \mathbf{J}^{(ij)}(X_{ij}^{(n)})\mathbf{U}_0. \tag{4.41}$$

Here, N_{cycle} is the number of times the list of relevant parameters is repeated, and $\mathbf{U}_0$ is the initial orthogonal matrix which can either be the identity or randomized. The process of obtaining $\mathbf{U}^*$ can be summarized as follows:

1. Shuffle the orbital indices $L = \{1, 2, \ldots, D\}$ and denote it as $L' = \{d_1, d_2, \ldots, d_D\}$.

2. For $i, j \in L'$, if $i \in \mathcal{N}$ or $j \in \mathcal{N}$ (to ignore rotations within the non-active space, replace "or" with the "exclusive or"), do the next step.

3. For $X_{ij} \in [0, \pi]$ in step size 10^{-2}, evaluate $F_{\text{QI}}(\mathbf{J}^{(ij)}(X_{ij}))$ and find the minimizing X^*_{ij}. Then in the smaller interval $[X^*_{ij} - 10^{-2}, X^*_{ij} + 10^{-2}]$, in step size 10^{-4} sample again the minimum of $F_{\text{QI}}(\mathbf{J}^{(ij)}(X_{ij}))$. If the improvement $F_{\text{QI}}(\mathbf{0}) - F_{\text{QI}}(\mathbf{J}^{(ij)}(X_{ij})) > \epsilon_1$, rotate $\boldsymbol{\gamma}$ and $\boldsymbol{\Gamma}$ by $\mathbf{J}^{(ij)}(X_{ij})$, and update $\mathbf{U}$ with $\mathbf{J}^{(ij)}(X_{ij})\mathbf{U}$.

4. For N_{cycle} times, repeat the above procedures, or until the improvement in F_{QI} after the cycle is less than ϵ_2 compared to the end of the last cycle. When the algorithm terminates, the optimized orthogonal matrix is then $\mathbf{U}^* = \mathbf{U}$.

Before moving on to the demonstration of QICAS, we briefly discuss the scaling of the algorithm. The MPS calculation using DMRG scales polynomially with the number of sites/orbitals D, and the bond dimension m [218]. Moreover, since we do not fully converge the DMRG run, we expect further reduction in the computational cost (e.g. a lower prefactor in the scaling). For the orbital optimization step, if redundant orbital rotations are ignored, then the complexity is formally the same for CASSCF and QICAS. The exhaustive manner of minimizing $F_{\text{QI}}(\mathcal{B})$ presented above is a rather expensive implementation of QICAS. With the newton method in the next Section, the cost of orbital optimization in QICAS is comparable to CASSCF. The biggest cost comes from the exponentiation of the antisymmetric matrix into an orthogonal matrix, and the rotation of the 2-RDM Γ, which is a rank-4 tensor. In CASSCF, however, the tensor of Coulomb integrals (again a rank-4 tensor) also needs to be rotated. The potential major advantage of QICAS compared to CASSCF lies in the fact that the orbital optimization step does not require any calculation of the energy or its gradients. In CASSCF, the orbital rotation is guided by the energy gradient. After the orbital is rotated, the full CI problem needs to be solved again in the updated active space, which concludes a macro iteration. In QICAS, the orbital rotation is guided entirely by the orbital correlation provided by the 1- and 2-RDM. The full CI problem is solved only once, namely after the orbitals are completely optimized (in the case where QICAS is followed by a CASCI calculation). We therefore expect in the regime of large active spaces (which is solved by again basis-dependent ansätze such as MPS), QICAS should fair better than CASSCF.

Now that we are equipped to minimize $F_{\text{QI}}(\mathcal{B})$ and perform the QICAS algorithm, we propose and test two applications of QICAS as post-HF treatments (see also Figure 4.6):

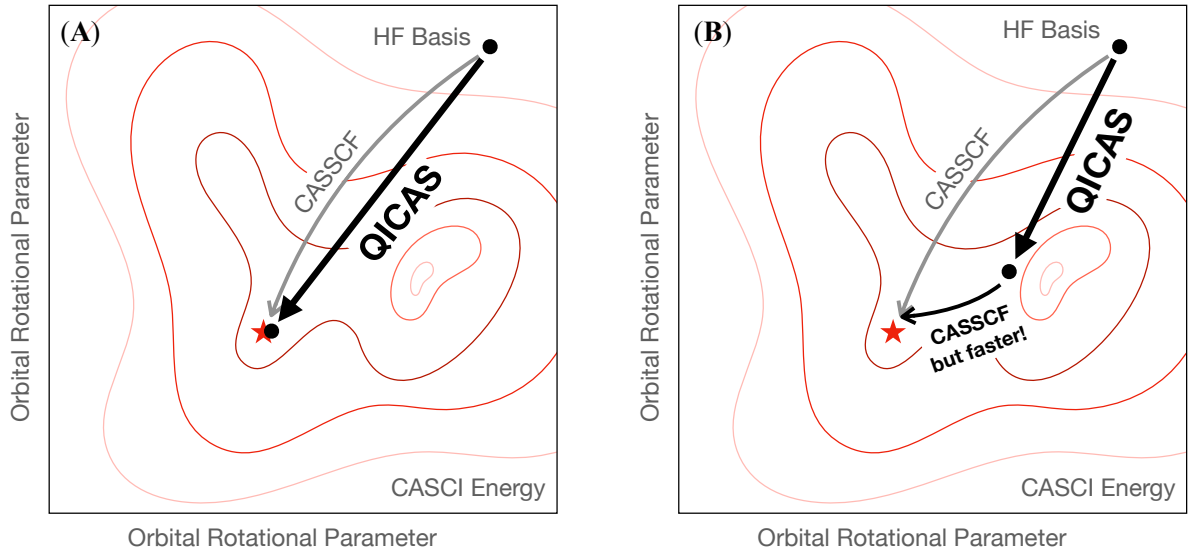

Figure 4.6: Illustration of two possible way of using QICAS. (**A**) QICAS is followed by a CASCI calculation. (**B**) QICAS is performed on a subset of orbitals to prepare a warm starting point for CASSCF.

(**A**) QICAS is followed by a CASCI calculation (HF-QICAS-CASCI),

(**B**) QICAS is performed on a subset $\mathcal{S}$ of orbitals ($D_{\text{CAS}} < |\mathcal{S}| \leq D$) to prepare a warm starting point for CASSCF (HF-QICAS-CASSCF).

4.2.3 Results on C_2 and Cr_2

First we revisit the example of C_2 at equilibrium geometry R = 1.243 Å, and examine the change in the orbital correlation pattern before and after the QICAS optimization. We use the HF canonical orbital as the starting basis, and an MPS with bond dimension $m = 200$ to estimate the orbital correlation. In the upper panel of Figure 4.7, we present the single orbital entropy of the HF (gray) and QICAS (red) optimized orbital basis. In both bases the active space consists of the orbitals indexed 3 to 10 (pink shaded region). We recall that the single orbital entropy of the inactive orbitals explicitly enter the cost function $F_{\text{QI}}(\mathcal{B})$. For the non-active orbitals, the entropy profile in the QICAS optimized basis is much lower than that in the HF basis, which is expected. Most of the reduction occurs for orbitals 14-17, which are considerably correlated in the HF basis. The out-of-CAS correlation $F_{\text{QI}}(\mathcal{B})$ reduces from 0.64 in the HF basis $\mathcal{B}_{\text{HF}}$ to 0.38 in the QICAS optimized basis $\mathcal{B}^*$. For the active orbitals, although the two profiles look rather similar up to some reordering, the sum of orbital entropy is actually slightly higher in the QICAS basis, namely 3.28 compared to 3.17 in the HF basis. This might seem counter-intuitive at first, but it in fact

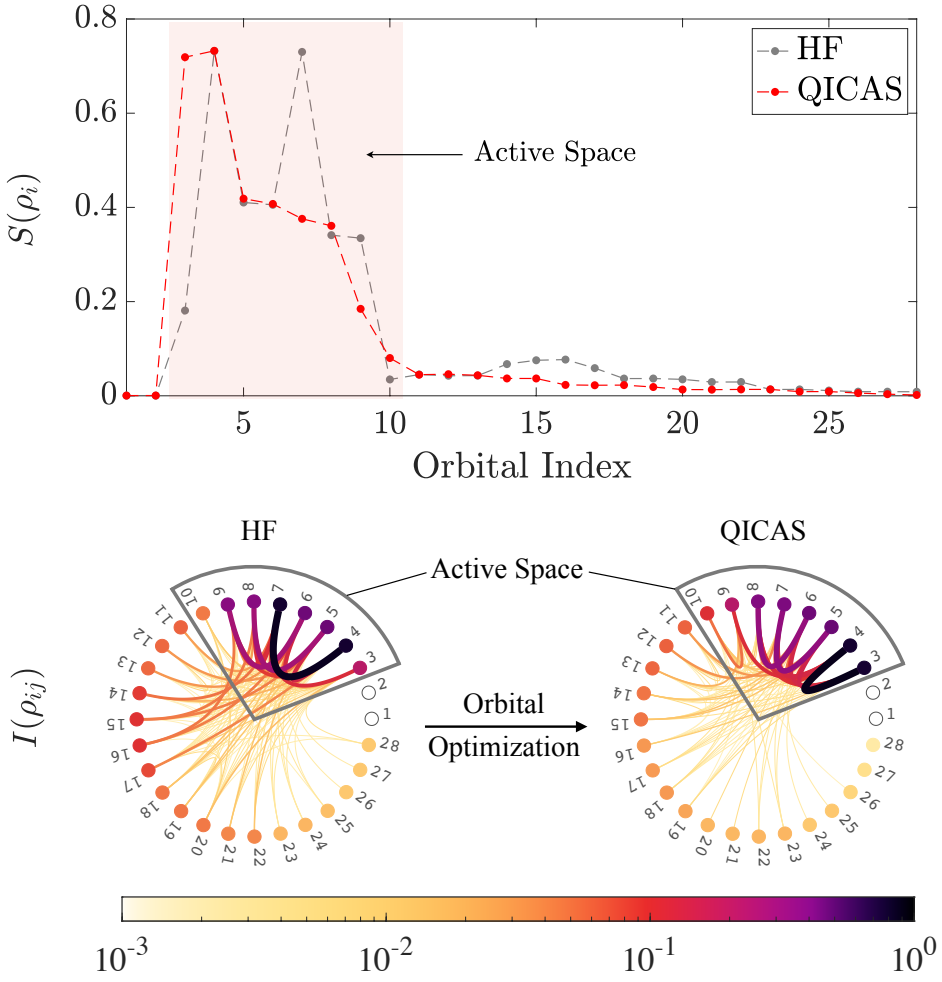

Figure 4.7: Single orbital entropy $S(\rho_i)$ (upper panel) and orbital-orbital correlation $I(\rho_{ij})$ (lower panel) of the Hartree-Fock orbitals (HF) and QICAS optimized orbitals (QICAS) for C_2 in the cc-pVDZ basis set, with internuclear distance at R = 1.243 Å.

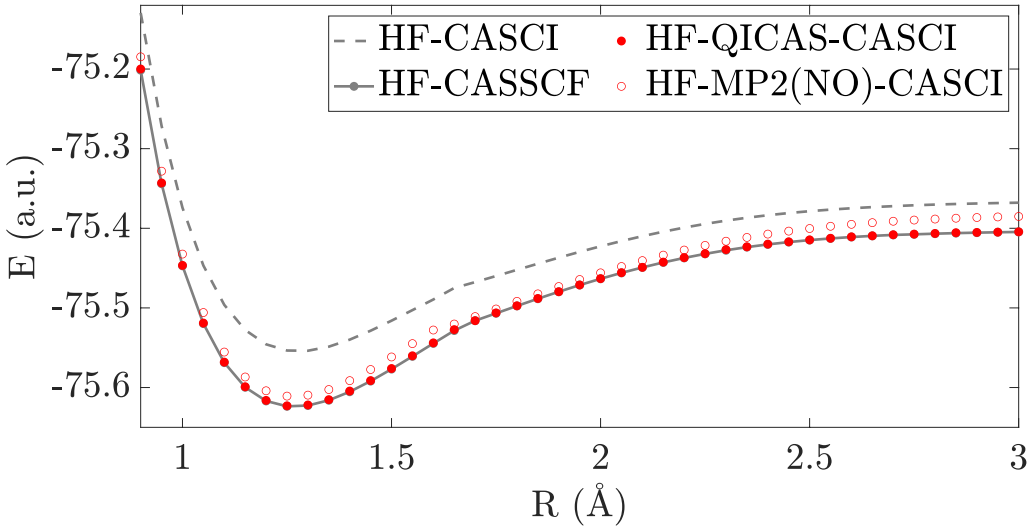

Figure 4.8: HF-CASCI(8, 8), HF-CASSCF(8, 8) and HF-QICAS-CASCI(8, 8) energy (a.u.) for C_2 with cc-pVDZ basis set as functions of internuclear distance R (Å).

aligns perfectly with the purpose of QICAS: It determines an active space that discards the *least* amount of correlation by reducing the correlation within the inactive space, while simultaneously shuffling some excess correlation into the active orbitals.

Besides the improvement in the single orbital entropy profile, the success of QICAS lies also in the consistent simplification of the correlation pattern *between* orbitals. To verify this on a quantitative level, we measure the correlation between every pair of orbitals i and j with the quantum mutual information [8], [62], [87], [119], [180]–[183]

$$I(\rho_{ij}) \equiv S(\rho_i) + S(\rho_j) - S(\rho_{ij}). \tag{4.42}$$

In our calculation, the two-orbital reduced density matrices ρ_{ij} are obtained by using the Syten toolkit [139], [140]. In the lower panel of Figure 4.7 we present $I(\rho_{ij})$ for both bases as colored curves connecting corresponding vertices i, j, with the single orbital entropy $S(\rho_i)$ color-coded on the respective vertices. Compared to the HF basis, the "correlation net" is indeed thinner for the QICAS optimized basis. In particular, the pairwise correlation associated with orbitals 14-17 is absorbed into the active space. Figure 4.7 unambiguously demonstrates the ability of QICAS to position most of the correlation effects into the active space, thus achieving a more compact active space structure and, by virtue of Theorem 1, an optimal CASCI energy.

The nearly perfect efficacy of QICAS indeed holds for all internuclear distances of C_2. In Figure 4.8 we present one of our key results: using the HF-QICAS-CASCI method we are able to reproduce the entire dissociation curve of C_2 in the cc-pVDZ basis with an error of up to only 2.3 mHa compared to the HF-CASSCF method. For the most part

of the dissociation curve (for 39 out of 41 evenly spaced data points), the error is within chemical accuracy (< 1.6 mHa), as evidenced by the fact that the HF-QICAS-CASCI data points (red dots) are virtually on top of the HF-CASSCF ones (grey dots on solid line). Tabulated data can be found in Appendix D obtained by performing QICAS based on MPS ground states with a maximal bond dimension $m = 100$ and 50 QC-DMRG sweeps. The HF-CASSCF energy at R = 1.65 Å is computed with the Molpro [135]–[137] package, and all other HF-CASCI/CASSCF energies with PySCF [219]. Here we again emphasize that the orbital optimization is based solely on the quantum information-inspired cost function $F_{\text{QI}}(\mathcal{B})$, which, despite not being directly connected to the complex CASCI energy landscape, leads to the correct minimum. The success of QICAS confirms that the underlying correlation structure of the approximate ground state $|\Psi_0\rangle$ can indeed be exploited for an accurate active space identification. Moreover, the useful part of the correlation is mostly static, evident by the fact that even when $|\Psi_0\rangle$ is approximated by an MPS with a small bond dimension $m = 100$, the correlation captured by the MPS is already sufficient for QICAS to identify a chemically accurate active space. Lastly, in Figure 4.8 we compared the CASCI energy obtained by using the QICAS orbitals, and the CASCI energy with the natural orbital (NO) basis of the second-order Møller-Plesset perturbation theory (MP2) solution. In this example, we find the QICAS orbitals to be consistently better. At the same time, QICAS does not suffer from the potential failure of MP2 when degeneracies arise.

For larger systems, performing a QC-DMRG calculation involving *all* orbitals can be rather expensive, if not unrealistic, even for moderate bond dimensions. To overcome this limitation, we propose to optimize just a subset $\mathcal{S}$ of $\tilde{D} = |\mathcal{S}|$ orbitals with QICAS, based on the MPS ground state on the chosen $\tilde{D}$ orbitals. Since not all orbitals in the basis are optimized, a gap would inevitably appear between the HF-QICAS-CASCI energy and the HF-CASSCF energy. Nonetheless, one would expect the former to still be much lower than the HF-CASCI energy, and that the convergence of CASSCF could be accelerated by starting with the optimized basis $\mathcal{B}^*$ instead of the HF orbitals.

To showcase exactly this second promising application (**B**) of QICAS, we study the notoriously strongly correlated Cr_2 at an internuclear distance R = 1.679 Å around the experimental equilibrium [220]. The cc-pV5Z-DK (306 orbitals) and aug-cc-pV5Z-DK (404 orbitals) basis sets [221] are used, together with the scalar-relativistic exact two-component (X2C) Hamiltonian [222], [223]. With such large basis sets, CASSCF starts to become costly, even with a small active space for which full CI is still feasible. We consider in the following two active space sizes, CAS(12, 12) and CAS(12, 14) and freeze the most inner 12 HF orbitals (the "Mg core"). We reduce the scope of QICAS to the subset of $\tilde{D} = 60$ lowest lying HF orbitals above the fixed Mg core, and correlate 24 electrons, such that sufficient correlation can be captured at a manageable cost. The bond dimension of the 60-orbital MPS is set at $m = 250$ and 50 DMRG sweeps are performed.

To compare the convergence of CASSCF starting from either the HF or QICAS opti-

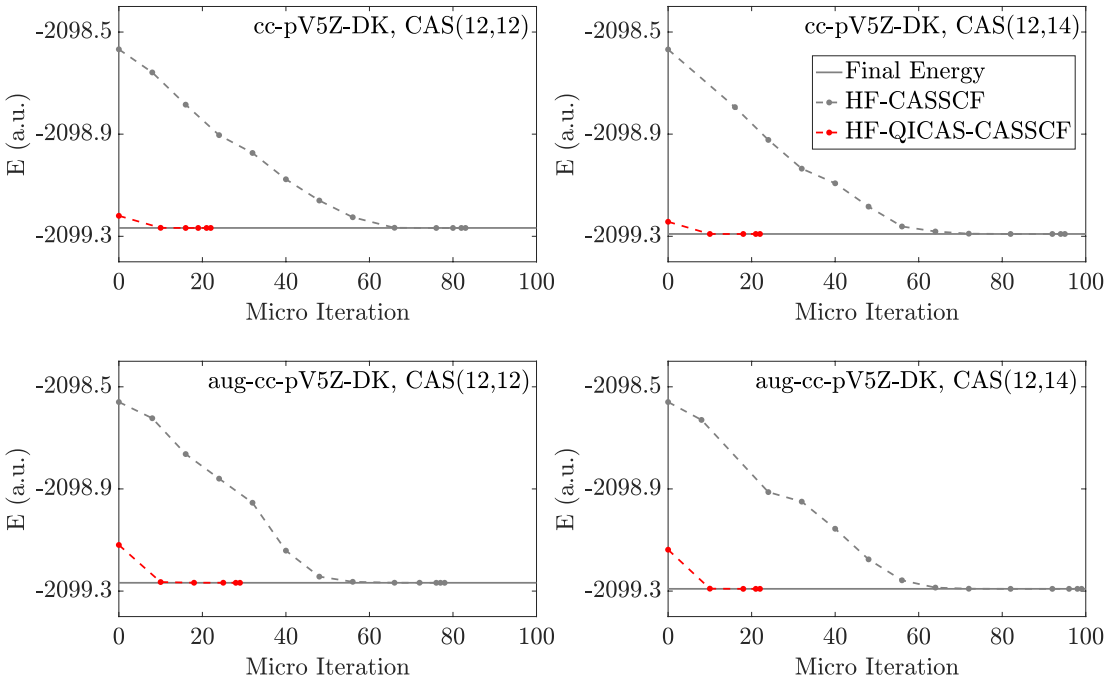

Figure 4.9: Energy evolution as the number of micro iterations in CASSCF(12,12) and CASSCF(12,14) for Cr_2 in the cc-pV5Z-DK and aug-cc-pV5Z-DK basis set at R = 1.679 Å, starting from HF-orbitals and from QICAS optimized orbitals. See text for more details.

Basis	D	Method(N_{CAS}, D_{CAS})	Energy (a.u.)	Post-HF Time (h)
V5Z	306	CASSCF(12, 12)	-2099.26725956	1.24
		QICAS-CASSCF(12, 12)	-2099.26725956	1.57 (1.25+0.32)
		CASSCF(12, 14)	-2099.29109845	8.24
		QICAS-CASSCF(12, 14)	-2099.29109856	3.18 (1.40+1.78)
aV5Z	404	CASSCF(12, 12)	-2099.26745743	2.93
		QICAS-CASSCF(12, 12)	-2099.26745742	1.99 (1.04+0.95)
		CASSCF(12, 14)	-2099.29130834	9.46
		QICAS-CASSCF(12, 14)	-2099.29130846	3.38 (1.13+2.25)

Table 4.1: Energy and runtime comparison of CASSCF(12,12) and CASSCF(12,14) for Cr_2 in the cc-pV5Z-DK (V5Z) and aug-cc-pV5Z-DK (aV5Z) basis set at R = 1.679 Å, between starting from HF-orbitals and from QICAS optimized orbitals. In particular, the post-HF time when QICAS is invoked is broken down into the run time of QICAS and that of the CASSCF calculation.

mized orbitals, we present in Figure 4.9 the respective energy evolution against the number of CASSCF micro iterations. The horizontal gap between two adjacent data points represents one macro iteration. In the case of CAS(12,14), for both basis sets the state drifted to a subspace of incorrect spin symmetry at one macro iteration during the HF-CASSCF calculation. Both macro iterations are omitted from the plot, but the exact values of the unphysical drifted energy can be found in the Appendix D. The spin symmetry remains unbroken in all other macro iterations, and is retained in all final CASSCF solutions. Other indicators of computational effort of CASSCF are displayed in Table 4.1, including the number of micro iteration and the post-HF run time (all calculations are performed on an Intel Xeon Platinum 8358 central processing unit). The results clearly reveal that QICAS provides a distinctly superior starting basis for CASSCF and can significantly accelerate convergence. For both basis sets, and for both active space sizes, the HF-QICAS-CASCI energy (at 0 iteration in the respective plots) is already much lower than the HF-CASCI energy, demonstrating a drastic improvement thanks to QICAS relative to the HF orbitals. Furthermore, starting from the optimized orbitals the correct CASSCF energy is practically reached after only 1 or 2 macro iterations. In contrast, starting from HF-orbitals CASSCF takes at least 8 macro iterations to reach chemical accuracy. Consequently, each post-QICAS CASSCF calculation requires much fewer computations of the two-electron integrals, and the run time is overall 3-4 times shorter than that of the corresponding post-HF CASSCF calculation.

Obtaining the QICAS optimized orbitals is certainly not for free. Yet, the effort invested in computing the MPS ground state and minimizing the out-of-CAS correlation $F_{\mathrm{QI}}(\mathcal{B})$ is well exceeded by the computational cost saved in a post-QICAS CASSCF. The majority of the QICAS run time is spent on the QC-DMRG calculation, whereas the minimization of $F_{\mathrm{QI}}(\mathcal{B})$ takes only a few minutes. In this sense, QICAS is at least as economic as other methods that are based as well on MPS ground state approximations with low bond dimension (e.g., Ref. [195]), while at the same time QICAS offers an advantageous starting point for CASSCF uniquely achieved by our QI-motivated orbital optimization.

4.2.4 Determining active space sizes with QICAS

An apparent requirement for implementing the orbital optimization for the minimization of the QI cost function $F_{\mathrm{QI}}(\mathcal{B})$ is the number of active/non-active orbitals. This feature is however not a drawback, as we readily have all the ingredients to calculate the entropy profile of the initial set of orbitals once the 1- and 2-RDMs are obtained, which can be used for active space *size* selection, also known as AutoCAS proposed by Stein and Reiher [195]. The main idea in Ref. [195] is that the set of orbitals with substantially higher orbital entropy than the others should constitute the active space. To be more concrete, Stein and Reiher utilized the so-called threshold diagrams, where they count the number of orbitals whose entropy exceeds a certain percentage of the maximal entropy among all

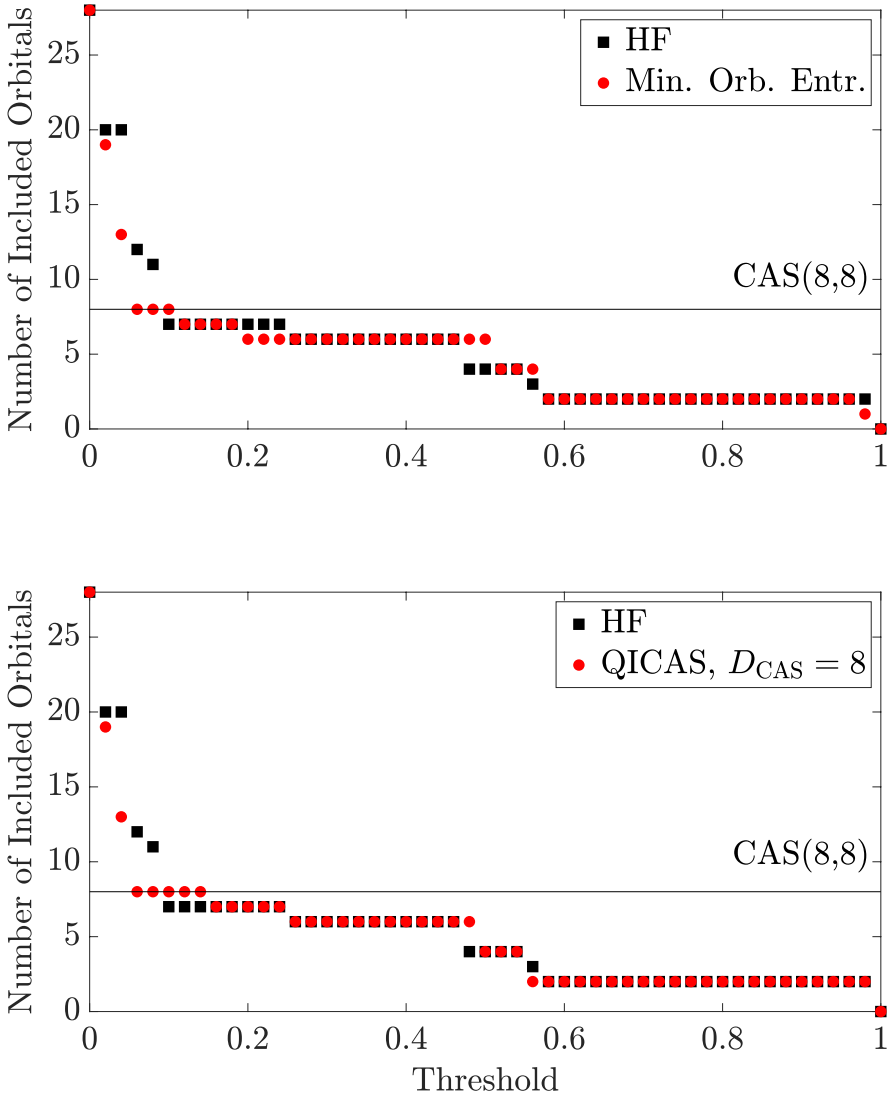

Figure 4.10: Threshold diagrams of the entropy of three orbital basis for the C_2 molecule at equilibrium geometry $R = 1.243$Å in cc-pVDZ basis set: the Hartree-Fock (HF) basis as the initial guess, the basis with minimal overall orbital entropy (Min. Orb. Entr.) which minimizes $F'_{\mathrm{QI}}(\mathcal{B})$, and the QICAS optimized basis with $D_{\mathrm{CAS}} = 8$.

orbitals. This diagram effects a top-down scanning of the entropy profile for identifying strong orbital correlation.

The success of AutoCAS relies on two assumptions: (i) the optimal active orbitals exhibit a high plateau in the orbital entropy profile, and (ii) the entropy profile of the current basis set based on which the prediction of the active space size is made, is similar to that of the optimal basis. Assumption (i) lies in the heart of almost all correlation-based active space selection methods. Instead of relying on high orbital entropy, active orbitals can also be distinguished by other indicators of strong orbital correlation, such as fractional occupation numbers. The second assumption, however, may not always hold. A poorly chosen set of initial guess orbitals could have a qualitatively different entropy profile than that of the optimal orbitals.

QICAS can lift the assumption (ii) by optimizing the orbital entropy profile. For this, we propose to generalize the QICAS cost function $F_{\mathrm{QI}}(\mathcal{B})$ to the following

$$F'_{\mathrm{QI}}(\mathcal{B}) = \sum_i S(\rho_i), \tag{4.43}$$

namely summing over all orbitals instead of just the non-active ones. This yields an unbiased optimization of the overall orbital entropy, based on which a threshold diagram can be produced. Once an active space size D_{CAS} is predicted, an ordinary QICAS routine can be run.

As an example, we present in Figure 4.10 the threshold diagrams of the entropy of three orbital bases for the C_2 molecule at the equilibrium geometry $R = 1.243$Å in the cc-pVDZ basis set: (a) the Hartree-Fock (HF) basis as the initial guess, (b) the basis with minimal overall orbital entropy (Min. Orb. Entr.) which minimizes $F'_{\mathrm{QI}}(\mathcal{B})$, and (c) the QICAS optimized basis with $D_{\mathrm{CAS}} = 8$. The y-axis represents the number of orbitals with entropy larger than [Threshold $\times$ $\max_i S(\rho_i)$]. The first identifiable plateau in the low threshold regime then predicts the size of the active space. First we focus on the HF orbitals. The earliest plateau in the HF basis predicts $D_{\mathrm{CAS}} = 7$, while at the optimal size $D_{\mathrm{CAS}} = 8$ the HF orbitals do not exhibit a plateau. In basis (b) where the overall entropy is minimized, the first plateau appears at D_{CAS}, albeit it is not very prominent. However, when we feed this predicted active space size into QICAS and obtain the corresponding optimized orbitals, the plateau at $D_{\mathrm{CAS}} = 8$ is further accentuated with a substantial extension, confirming that this is indeed the correct active space size.

Chapter Summary

In this chapter, we proposed an orbital optimization scheme QICAS which exploits the correlation structure of cheaper post-HF solutions to determine accurate active spaces. To this end, we utilized a preceding QC-DMRG calculation with a low bond dimension, and minimize the sum of orbital correlations $F_{\mathrm{QI}}(\mathcal{B})$ of the non-active orbitals in a basis

$\mathcal{B}$. According to Theorem 1, this choice of a cost function is very well-motivated: $F_{\mathrm{QI}}(\mathcal{B})$ bounds exactly that portion of the correlation energy which the corresponding active space fails to recover. In practical applications, QICAS demonstrated a remarkable potential. For C_2, we observed an excellent agreement between the CASCI energy of the QICAS optimized orbitals and the CASSCF energy along the entire dissociation curve. For the more challenging Cr_2, we found that optimizing a subset of orbitals using QICAS provided a warm starting point for CASSCF, and consistently reduced the number of iterations required for convergence.

We believe that the potential transformative impact of QI tools in theoretical and computational chemistry to simplify electronic structure is not limited to active space methods. Schemes and ideas related to QICAS may lead to advances in the development and application of any method where orbital optimization plays a prominent role. Prime examples would be quantum computing [224]–[227], where a poor choice of reference orbitals results in a large circuit depth, and the density matrix embedding theory [228]–[230], where the sought-after local fragment and bath orbitals form a structure similar to that of an active space [229].

Summary and Conclusions

Solving the ground state problem for strongly correlated electrons requires a deeper understanding of what exactly electron correlation means and how we can manipulate it to our advantage. In this thesis, we focused on a major aspect of electron correlation, namely the correlation of single-particle basis functions, or *orbitals*. The choice of orbital basis does not affect the *formal* complexity of the electronic Hamiltonian in a molecule (the interaction remains two-body), nor the energy of the exact ground state wavefunction. But it certainly has a huge impact on both the accuracy and efficiency of any imposed, non-exact ansätze, such as, complete active space configuration interaction (CASCI), coupled cluster singles and doubles (CCSD), or matrix product states (MPS) with limited bond dimensions. Moreover, the choice of the orbital basis also alters the representation of the ground state, which depending on the particular choice may facilitate or hinder the physical or chemical interpretation of the solution. All these aspects of orbital dependence are in fact quantifiable through the lens of orbital entanglement and correlation.

We started by thoroughly investigating the basis dependence of orbital entanglement and correlation in the ground states of molecular systems. The degree of orbital localization was found to have a drastic effect on the overall pattern of orbital entanglement. On one hand, we discovered that partially localizing the orbitals leads to a lower overall orbital entanglement profile, which confirms the expectation that there is still some level of locality in chemical systems despite the long-range Coulomb interaction. These orbitals are then particularly well-suited for any ansatz whose accuracy hugely hinges on a local structure, such as the MPS ansatz and parametrized quantum circuits. On the other hand, fully localized atomic-like orbitals exhibit almost maximal entanglement. While these orbitals are highly entangled among each other, this entanglement is again locally confined. And, for molecules with well-defined Lewis structure, these fully localized orbitals form dimerized entangled pairs, each representing a localized two-center covalent bond.

This observation eventually led to the development of maximally entangled atomic orbitals (MEAO), designed to reveal the bonding structure of a molecule from *ab initio* ground state calculations. These orbitals combine the appealing qualities of both the molecular orbital and valence bond picture of chemical bonding. Namely, they are fully localized and correctly hybridized, thus providing an intuitive chemical picture, and at the

same time orthonormal to each other, setting a solid base for a wide range of wavefunction methods. Most importantly, the entanglement structure of the MEAOs fully reflects the bonding structure of the molecule. Compared to other bonding analysis tools, our scheme is entirely automated and free of manual intervention, while maintaining a low computational cost. The correspondence of entangled pairs of orbitals and two-center covalent bonds can even be extended to multi-center bonds, which are bonding effects beyond the standard Lewis structures. This was achieved by measuring the genuine multipartite entanglement shared among more than two MEAOs. With more and more sophisticated but hard to interpret wavefunction ansatz becoming available, the MEAO framework offers an intuitive representation of the molecular ground states, thus opening the door to extracting properties and chemical insights such as aromaticity and agostic bonds from highly accurate numerical solutions.

Another highlight of the thesis is the development of the novel quantum information-assisted complete active space optimization (QICAS) algorithm. With QICAS, we successfully tackled the long-standing problem of active space selection and optimization. We started by noticing that the accuracy of an active space in an orbital basis $\mathcal{B}$ is intuitively linked to the correlation effects that are discarded in the non-active orbital subspace. In the form of a theorem (see Theorem 1 in Chapter 4 Section 4.2), we established for the first time a connection between orbital entanglement, measured by the sum of non-active orbital entropy (denoted as $F_{\mathrm{QI}}(\mathcal{B})$), and the energy discrepancy $\Delta E(\mathcal{B})$ between the active space approximation and the exact ground state energy. Specifically, the inequality $\Delta E(\mathcal{B}) \leq k(\hat{H}) F_{\mathrm{QI}}(\mathcal{B})$ holds where $k(\hat{H})$ is a $\mathcal{B}$-independent constant. Using the entropy of the non-active orbitals as a cost function, we were able to minimize the correlation in the ground state that the active space ansatz as a powerful but limited ansatz would fail to recover. Based on an MPS solution with low bond dimension, we managed to get an estimate of the correlation beyond the active space, and optimize for the energetically optimal active orbitals. As a result, QICAS produces for small systems energetically optimal active spaces, without the need for solving the full configuration interaction (FCI) problem within the active space many times as in the standard complete active space self-consistent field (CASSCF) approach. For larger systems, QICAS prepares a warm starting orbital basis, and drastically reduces the required number of micro- and macro-iterations in a subsequent CASSCF calculation, for achieving the desired accuracy of the active space. Conceptually, QICAS offers a fresh perspective into the electronic ground state problem. Using orbital entanglement as a guide, we can choose a suitable representation of the ground state wavefunction such that the given ansatz approximation achieves maximal accuracy.

All these results demonstrated the tremendous potential of quantum information theoretical concepts and tools for the many-electron ground state problem. In particular, orbital entanglement and correlation analyses allow for (i) quantitative assessment of electron correlation, (ii) highly interpretable representations of wavefunctions, and (iii) the improvement or even invention of wavefunction methods for describing correlated electrons. The versatility and broad relevance of orbital entanglement is certainly not limited

to the ground state problem. In some other problems such as state-average calculations and time evolution simulations, one faces an even steeper challenge posed by the entanglement. In state-average calculations, the requirement for a good orbital basis is even more stringent, as the same set of orbitals are used for both ground and excited states, which are not expected to display a similar entanglement structure. During time evolution, the wavefunction moves through different regions of the Hilbert space. To keep up with the time-evolved state with the limited coverage by an ansatz and describe the shifting entanglement structure, the reference orbitals would also need to evolve in time. These major problems exemplify the broad relevance of orbital entanglement and correlation analysis. We therefore firmly believe that the insights and methods developed in this thesis can be potentially transferred to a wide range of areas in quantum physics and chemistry.

Appendix A

Correlation Sum Rule

In this section we will show that the quantum and classical correlation of ρ sum up to the total correlation of ρ, if its closest product state $\pi_\rho = \rho_A \otimes \rho_B$ and its closest classical state χ_ρ are simultaneously diagonalized. For the definitions of the closest product/classical state, we refer the reader to Section 1.1.

From here on, we assume that π_ρ and χ_ρ can be simultaneously diagonalized. First, we observe that the descrepancy Δ between the total correlation I and the sum of quantum and classical correlation, Q and C, respectively, can be written as

$$\begin{aligned}\Delta &= I(\rho) - Q(\rho) - C(\rho) \\ &= (S(\rho_A) + S(\rho_B) - S(\rho)) - (S(\chi_\rho) - S(\rho)) - (S(\chi_A) + S(\chi_B) - S(\chi_\rho)) \\ &= S(\rho_A) + S(\rho_B) - S(\chi_A) - S(\chi_B),\end{aligned} \tag{A.1}$$

where $\chi_{A,B}$ are the reduced states of χ_ρ on subsystem A and B, respectively. We can then show that the descrepancy Δ vanishes, by showing that the spectrum of ρ_A and that of χ_A coincide (and the same applies for subsystem B). Let us denote the eigenstate of χ_ρ as $\{|i\rangle \otimes |j\rangle\}$. From this it follows that the eigenvalues of ρ_A are precisely its diagonal entries in this basis

$$\lambda_i = (\rho_A)_{ii} = \langle i|\rho_A|i\rangle = \sum_j \langle i| \otimes \langle j|\rho|i\rangle \otimes |j\rangle. \tag{A.2}$$

Moreover, the eigenvalues of χ_A are given by[8]

$$\begin{aligned}\mu_i &= \langle i|\mathrm{Tr}_B[\chi_\rho]|i\rangle \\ &= \langle i|\mathrm{Tr}_B\left[\sum_{kj} |k\rangle\langle k| \otimes |j\rangle\langle j|\rho|k\rangle\langle k| \otimes |j\rangle\langle j|\right]|i\rangle \\ &= \sum_j \langle i| \otimes \langle j|\rho|i\rangle \otimes |j\rangle = \lambda_i.\end{aligned} \tag{A.3}$$

Using similar considerations, the spectrum of ρ_B and χ_B also coincide. As a result, the descrepancy Δ (A.1) must vanish, leading to the sum rule

$$I(\rho) = Q(\rho) + C(\rho). \tag{A.4}$$

This allows us to dissect the total correlation exactly into quantum and classical correlation contributions. When $\rho_{A/B}$ is not simultaneously diagonalized as $\chi_{A/B}$, its diagonal entries still coincide with those of $\chi_{A/B}$, namely the elements of $\vec{\mu}$. From this, it follows that the spectrum of $\rho_{A/B}$ given by $\vec{\lambda}$ majorizes $\vec{\mu}$, leading to the inequality $S(\rho_{A/B}) > S(\chi_{A/B})$ by the Schur concavity of the von Neumann entropy. Hence, a general relation between the total, quantum, and classical correlation reads as

$$I(\rho) \geq Q(\rho) + C(\rho). \tag{A.5}$$

Appendix B

Atomic-like Orbitals in Benzene

The pre-normalized canonical Hartree-Fock orbitals $\tilde{\phi}_i$'s within the π-subspace of the one-particle Hilbert space of the benzene ring are related to the p_z orbitals α_i's by

$$\tilde{\phi}_i = \mathbf{U}_{ij}\alpha_j, \tag{B.1}$$

where

$$\mathbf{U} = \begin{pmatrix} \frac{1}{\sqrt{6}} & \frac{1}{\sqrt{6}} & \frac{1}{\sqrt{6}} & \frac{1}{\sqrt{6}} & \frac{1}{\sqrt{6}} & \frac{1}{\sqrt{6}} \\ -\frac{1}{\sqrt{12}} & -\frac{1}{\sqrt{3}} & -\frac{1}{\sqrt{12}} & \frac{1}{\sqrt{12}} & \frac{1}{\sqrt{3}} & \frac{1}{\sqrt{12}} \\ \frac{1}{2} & 0 & -\frac{1}{2} & -\frac{1}{2} & 0 & \frac{1}{2} \\ -\frac{1}{2} & 0 & \frac{1}{2} & -\frac{1}{2} & 0 & \frac{1}{2} \\ -\frac{1}{\sqrt{12}} & \frac{1}{\sqrt{3}} & -\frac{1}{\sqrt{12}} & -\frac{1}{\sqrt{12}} & \frac{1}{\sqrt{3}} & -\frac{1}{\sqrt{12}} \\ \frac{1}{\sqrt{6}} & -\frac{1}{\sqrt{6}} & \frac{1}{\sqrt{6}} & -\frac{1}{\sqrt{6}} & \frac{1}{\sqrt{6}} & -\frac{1}{\sqrt{6}} \end{pmatrix}, \tag{B.2}$$

is a unitary matrix. The atomic-like orbitals $\tilde{\alpha}_i$ proposed by us is obtained by applying the inverse $\mathbf{U}^{-1}$ to the *normalized* canonical Hartree-Fock orbitals $\phi_i = \tilde{\phi}_i/\|\tilde{\phi}_i\|$

$$\tilde{\alpha}_i = \mathbf{U}^{-1}_{ij}\phi_j. \tag{B.3}$$

The above transformation can be achieved by a sequence of two-orbital rotations.

- **Step 1**

$$\begin{aligned} \phi_1 &\leftarrow -\tfrac{1}{\sqrt{2}}\phi_1 + \tfrac{1}{\sqrt{2}}\phi_6, \quad & \phi_1 &\leftarrow \tfrac{1}{\sqrt{2}}\phi_1 + \tfrac{1}{\sqrt{2}}\phi_6 \\ \phi_2 &\leftarrow -\tfrac{1}{\sqrt{2}}\phi_2 + \tfrac{1}{\sqrt{2}}\phi_5, \quad & \phi_5 &\leftarrow \tfrac{1}{\sqrt{2}}\phi_2 + \tfrac{1}{\sqrt{2}}\phi_5 \\ \phi_3 &\leftarrow -\tfrac{1}{\sqrt{2}}\phi_3 + \tfrac{1}{\sqrt{2}}\phi_4, \quad & \phi_4 &\leftarrow \tfrac{1}{\sqrt{2}}\phi_3 + \tfrac{1}{\sqrt{2}}\phi_4 \end{aligned}$$

- **Step 2**

$$\tilde{\alpha}_1 \leftarrow -\tfrac{1}{\sqrt{3}}\phi_1 + \sqrt{\tfrac{2}{3}}\phi_2, \quad \phi_2 \leftarrow \sqrt{\tfrac{2}{3}}\phi_1 + \tfrac{1}{\sqrt{3}}\phi_2$$
$$\phi_5 \leftarrow -\tfrac{1}{\sqrt{3}}\phi_5 + \sqrt{\tfrac{2}{3}}\phi_6, \quad \tilde{\alpha}_6 \leftarrow \sqrt{\tfrac{2}{3}}\phi_5 + \tfrac{1}{\sqrt{3}}\phi_6$$

- **Step 3**

$$\tilde{\alpha}_2 \leftarrow -\tfrac{1}{\sqrt{2}}\phi_2 - \tfrac{1}{\sqrt{2}}\phi_4, \quad \tilde{\alpha}_4 \leftarrow -\tfrac{1}{\sqrt{2}}\phi_2 + \tfrac{1}{\sqrt{2}}\phi_4$$
$$\tilde{\alpha}_3 \leftarrow -\tfrac{1}{\sqrt{2}}\phi_3 + \tfrac{1}{\sqrt{2}}\phi_5, \quad \tilde{\alpha}_5 \leftarrow \tfrac{1}{\sqrt{2}}\phi_3 + \tfrac{1}{\sqrt{2}}\phi_5$$

We then arrive at the atomic-like orbitals $\tilde{\alpha}_i$'s.

Appendix C

Gradient-Based Orbital Optimization

In this section, we describe the general framework for gradient-based orbital optimization used in Chapter 3 and 4. The goal is to solve the following optimization problem given a cost function $F(\mathcal{B})$ depending on the orbital basis $\mathcal{B}$

$$\mathcal{B}^* = \arg\min_{\mathcal{B}} F(\mathcal{B}). \tag{C.1}$$

The first task is to parametrize the set of all possible orbital bases of size D, which is in fact a manifold. Every two bases $\mathcal{B}_1 = \{\phi_i\}_{i=1}^D$ and $\mathcal{B}_2 = \{\varphi_i\}_{i=1}^D$ are connected by a unitary transformation $\mathbf{U}$ via

$$\varphi_i = \sum_{j=1}^{D} U_{ij}\phi_j. \tag{C.2}$$

In this thesis we only deal with real orbital bases. Therefore the unitary transformation $\mathbf{U}$ is actually orthogonal. If we choose a fixed orbital basis as a reference, then the parametrization of the manifold of all orbital bases can be achieved by the following parametrization the group of $D \times D$ orthogonal matrices

$$\mathbf{U} = \exp(\mathbf{X}), \quad \theta_{ij} = -X_{ji}, \tag{C.3}$$

where $\mathbf{X}$ is an anti-symmetric matrix. Then the $(D-1)D/2$ independent degrees of freedom in $\mathbf{X}$ becomes our parameter space, and the cost function $F(\mathcal{B})$ can be written as $F(\mathbf{X})$. The set of all anti-symmetrice matrices is a vector space, with basis elements being the generators $\mathbf{A}^{(ij)}$ of Jacobi rotations

$$(\mathbf{A}^{(ij)})_{kl} = \begin{cases} 1 & i = k,\ j = l \\ -1 & i = l,\ j = k \\ 0 & \text{otherwise} \end{cases}. \tag{C.4}$$

The Jacobi rotation involving the i-th and j-th orbitals is then

$$\mathbf{J}^{(ij)}(\theta) = \begin{pmatrix} 1 & & & & & & 0 \\ & \ddots & & & & & \\ & & \cos(\theta) & \cdots & \sin(\theta) & & \\ & & \vdots & & \vdots & & \\ & & -\sin(\theta) & \cdots & \cos(\theta) & & \\ & & & & & \ddots & \\ 0 & & & & & & 1 \end{pmatrix}. \tag{C.5}$$

With the basis $\mathbf{A}^{(ij)}$, any anti-symmetric matrix $\mathbf{X}$ can be expanded as

$$\mathbf{X} = \sum_{i<j} \theta_{ij} \mathbf{A}^{(ij)}. \tag{C.6}$$

We optimize the cost function $F(\mathbf{X}(\boldsymbol{\theta}))$ by using the Newton-Raphson method. For this we need the anti-symmetrized gradient $\mathbf{G}$

$$G_{ij} = -G_{ji} = \frac{\partial F(\mathbf{X}(\boldsymbol{\theta}))}{\partial \theta_{ij}} = \lim_{\delta \to 0} \frac{F(\mathbf{X}(\boldsymbol{\theta}) + \delta \mathbf{A}^{(ij)}) - F(\mathbf{X}(\boldsymbol{\theta}))}{\delta}, \tag{C.7}$$

and the approximated Hessian $\mathbf{H}$

$$H_{ij} = H_{ji} = \frac{\partial^2 F(\mathbf{X}(\boldsymbol{\theta}))}{\partial \theta_{ij}^2} = \lim_{\delta \to 0} \frac{F(\mathbf{X}(\boldsymbol{\theta}) + \delta \mathbf{A}^{(ij)}) + F(\mathbf{X}(\boldsymbol{\theta}) - \delta \mathbf{A}^{(ij)}) - 2F(\mathbf{X}(\boldsymbol{\theta}))}{\delta^2}. \tag{C.8}$$

Note that we only calculate the diagonal part of the Hessian, namely the second derivatives with respect to the same parameter. In the following sections we will explain how are the first and second derivatives we use are analytically derived. Once the gradients and the diagonal part of the Hessian is obtained, the $\mathbf{X}$ matrix is updated at each numerical iteration by the following equation

$$\mathbf{X} \leftarrow \mathbf{X} - \alpha[\mathbf{H} - (\min(\mathbf{H}) - \beta)]^{-1}\mathbf{G}, \tag{C.9}$$

where α (typically between 0.1 and 0.3) is the step size and β is a level shift hyper-parameter (typically between 10^{-4} to 10^{-1}). When the objective is the maximize a function, then α takes negative values. After every step, we reset the orbital basis of reference to be the current basis, i.e., $\mathbf{X} = \mathbf{0}$. Therefore we only need the analytic expressions for the first and relevant second derivatives evaluated at $\mathbf{X} = \mathbf{0}$.

C.1 MEAO

The two-particle RDM Γ is defined as

$$\Gamma(\mathcal{B})^{ij}_{kl} = \langle f^\dagger_{i\uparrow} f^\dagger_{j\downarrow} f_{l\downarrow} f_{k\uparrow} \rangle. \tag{C.10}$$

The objective function for maximizing the entanglement between connected orbitals is

$$F_{\mathrm{MEAO}}(\mathcal{B}) = \sum_{(i,j)} |\Gamma(\mathcal{B})^{i\bar{i}}_{j\bar{j}}|^2 + |\Gamma(\mathcal{B})^{i\bar{j}}_{j\bar{i}}|^2. \tag{C.11}$$

Here (i,j) denotes a pair of orbitals from two different atomic centers, and i ($\bar{i}$) denotes the i-th spin-up (-down) orbital.

A Jakobi rotation on the pair (k,l) by an angle θ transforms $\Gamma(\mathcal{B})$ to a new basis $\mathcal{B}'$ as

$$\Gamma(\mathcal{B})^{ij}_{kl} = \sum_{abcd} \mathbf{J}^{(kl)}(\theta)_{ia}\mathbf{J}^{(kl)}(\theta)_{jb}\mathbf{J}^{(kl)}(\theta)_{kc}\mathbf{J}^{(kl)}(\theta)_{ld}\Gamma(\mathcal{B})^{ab}_{cd}. \tag{C.12}$$

Then it is straightforward to calculate the first derivative of F with respect to θ_{kl} evaluated at the current basis $\mathcal{B}$ (which we omit for simplicity)

$$\begin{aligned}
\left.\frac{\partial F_{\mathrm{MEAO}}}{\partial\theta_{kl}}\right|_{\theta_{kl}=0} &= 2\sum_{(i,j)}(\Gamma^{ii}_{jj})\left.\frac{\partial\Gamma^{i\bar{i}}_{j\bar{j}}}{\partial\theta_{kl}}\right|_{\theta_{kl}=0} + (\Gamma^{i\bar{j}}_{i\bar{j}})\left.\frac{\partial\Gamma^{ij}_{ij}}{\partial\theta_{kl}}\right|_{\theta_{kl}=0}, \\
\left.\frac{\partial\Gamma^{i\bar{i}}_{j\bar{j}}}{\partial\theta_{kl}}\right|_{\theta_{kl}=0} &= \delta_{ik}(\Gamma^{l\bar{i}}_{j\bar{j}}+\Gamma^{i\bar{l}}_{j\bar{j}}) - \delta_{il}(\Gamma^{k\bar{i}}_{j\bar{j}}+\Gamma^{i\bar{k}}_{j\bar{j}}) + \delta_{jk}(\Gamma^{i\bar{i}}_{l\bar{j}}+\Gamma^{i\bar{i}}_{j\bar{l}}) - \delta_{jl}(\Gamma^{i\bar{i}}_{k\bar{j}}+\Gamma^{i\bar{i}}_{j\bar{k}}), \\
\left.\frac{\partial\Gamma^{i\bar{j}}_{j\bar{i}}}{\partial\theta_{kl}}\right|_{\theta_{kl}=0} &= \delta_{ik}(\Gamma^{l\bar{j}}_{j\bar{i}}+\Gamma^{i\bar{j}}_{j\bar{l}}) - \delta_{il}(\Gamma^{k\bar{j}}_{j\bar{i}}+\Gamma^{i\bar{j}}_{j\bar{k}}) + \delta_{jk}(\Gamma^{i\bar{l}}_{j\bar{i}}+\Gamma^{i\bar{j}}_{l\bar{i}}) - \delta_{jl}(\Gamma^{i\bar{k}}_{j\bar{i}}+\Gamma^{i\bar{j}}_{k\bar{i}}).
\end{aligned} \tag{C.13}$$

And likewise the diagonal elements of the Hessian are obtained via

$$\begin{aligned}
\left.\frac{\partial^2 F_{\mathrm{MEAO}}}{\partial\theta^2_{kl}}\right|_{\theta_{kl}=0} &= \sum_{(i,j)} 2\left(\left.\frac{\partial\Gamma^{i\bar{i}}_{j\bar{j}}}{\partial\theta_{kl}}\right)^2\right|_{\theta_{kl}=0} + 2\Gamma^{i\bar{i}}_{j\bar{j}}\left.\frac{\partial^2\Gamma^{i\bar{i}}_{j\bar{j}}}{\partial\theta^2_{kl}}\right|_{\theta_{kl}=0} \\
&\quad + 2\left(\left.\frac{\partial\Gamma^{i\bar{j}}_{i\bar{j}}}{\partial\theta_{kl}}\right)^2\right|_{\theta_{kl}=0} + 2\Gamma^{i\bar{j}}_{i\bar{j}}\left.\frac{\partial^2\Gamma^{i\bar{j}}_{i\bar{j}}}{\partial\theta^2_{kl}}\right|_{\theta_{kl}=0}, \\
\left.\frac{\partial^2\Gamma^{i\bar{i}}_{j\bar{j}}}{\partial\theta^2_{kl}}\right|_{\theta_{kl}=0} &= -2(\delta_{ik}+\delta_{il}+\delta_{jk}+\delta_{jl})\Gamma^{i\bar{i}}_{j\bar{j}} + 2(\delta_{ik}\Gamma^{ll}_{j\bar{j}}+\delta_{il}\Gamma^{k\bar{k}}_{j\bar{j}}+\delta_{jk}\Gamma^{i\bar{i}}_{l\bar{l}}+\delta_{jl}\Gamma^{i\bar{i}}_{k\bar{k}}) \\
&\quad - 2(\delta_{ik}\delta_{jl}+\delta_{jl}\delta_{ik})(\Gamma^{i\bar{j}}_{i\bar{j}}+\Gamma^{i\bar{j}}_{j\bar{i}}+\Gamma^{j\bar{i}}_{i\bar{j}}+\Gamma^{j\bar{i}}_{j\bar{i}}), \\
\left.\frac{\partial^2\Gamma^{i\bar{j}}_{j\bar{i}}}{\partial\theta^2_{kl}}\right|_{\theta_{kl}=0} &= -2(\delta_{ik}+\delta_{il}+\delta_{jk}+\delta_{jl})\Gamma^{i\bar{j}}_{j\bar{i}} + 2(\delta_{ik}\Gamma^{l\bar{j}}_{j\bar{l}}+\delta_{il}\Gamma^{k\bar{j}}_{j\bar{k}}+\delta_{jk}\Gamma^{i\bar{l}}_{l\bar{i}}+\delta_{jl}\Gamma^{i\bar{k}}_{k\bar{i}}) \\
&\quad - 2(\delta_{ik}\delta_{jl}+\delta_{jl}\delta_{ik})(\Gamma^{i\bar{i}}_{j\bar{j}}+\Gamma^{j\bar{j}}_{i\bar{i}}+\Gamma^{i\bar{j}}_{i\bar{j}}+\Gamma^{j\bar{i}}_{j\bar{i}}).
\end{aligned} \tag{C.14}$$

When the 2RDM is calculated from a mean-field trial wavefunction, we can express the relevant part of the 2RDM with 1RDM γ

$$\Gamma^{i\bar{j}}_{k\bar{l}} = \langle f^\dagger_{i\uparrow}f^\dagger_{j\downarrow}f_{l\downarrow}f_{k\uparrow}\rangle = \langle f^\dagger_{i\downarrow}f_{k\downarrow}\rangle\langle f^\dagger_{j\downarrow}f_{l\downarrow}\rangle = \gamma^i_k\gamma^{\bar{j}}_{\bar{l}}, \tag{C.15}$$

which can be substituted into the expressions of the gradient and second derivatives above.

C.2 QICAS

To obtain the QICAS orbitals, we minimize the following cost function

$$F_{\mathrm{QI}}(\mathcal{B}) = \sum_{i\in\mathcal{A}} S(\rho_i), \tag{C.16}$$

where $\mathcal{A}$ collects all active orbitals. The derivatives of F_{QI} can be broken down using the chain rule

$$\frac{\partial F_{\mathrm{QI}}}{\partial\theta_{ij}}(\mathbf{0}) = -\sum_{i\in\mathcal{A}}\sum_{k=0}^{3}\log(\lambda_k^{(i)}(\mathbf{0}))\frac{\partial\lambda_k^{(i)}}{\partial\theta_{ij}}(\mathbf{0}), \tag{C.17}$$

where

$$\begin{aligned}
\lambda_0^{(i)}(\mathbf{X}) &= 1-\gamma(\mathbf{X})_i^i-\gamma(\mathbf{X})_{\bar{i}}^{\bar{i}}+\Gamma(\mathbf{X})_{i\bar{i}}^{i\bar{i}},\\
\lambda_1^{(i)}(\mathbf{X}) &= \gamma(\mathbf{X})_i^i-\Gamma(\mathbf{X})_{i\bar{i}}^{i\bar{i}},\\
\lambda_2^{(i)}(\mathbf{X}) &= \gamma(\mathbf{X})_{\bar{i}}^{\bar{i}}-\Gamma(\mathbf{X})_{i\bar{i}}^{i\bar{i}},\\
\lambda_3^{(i)}(\mathbf{X}) &= \Gamma(\mathbf{X})_{i\bar{i}}^{i\bar{i}}.
\end{aligned} \tag{C.18}$$

Here, $\gamma(\mathbf{X})$ and $\Gamma(\mathbf{X})$ are the 1- and 2-RDMs in the rotated basis given by

$$\begin{aligned}
\gamma(\mathbf{X})_i^i &= \sum_{ab}(e^{\mathbf{X}})_{ia}(e^{\mathbf{X}})_{ib}\gamma(\mathbf{0})_b^a,\\
\Gamma(\mathbf{X})_{i\bar{i}}^{i\bar{i}} &= \sum_{abcd}(e^{\mathbf{X}})_{ia}(e^{\mathbf{X}})_{ib}(e^{\mathbf{X}})_{ic}(e^{\mathbf{X}})_{id}\Gamma(\mathbf{0})_{c\bar{d}}^{a\bar{b}},
\end{aligned} \tag{C.19}$$

The derivatives of the RDMs at $\mathbf{X}=\mathbf{0}$ are gievn by

$$\begin{aligned}
\frac{\partial\gamma(\mathbf{0})_i^i}{\partial\theta_{ij}} &= \gamma(\mathbf{0})_i^j+\gamma(\mathbf{0})_j^i,\\
\frac{\partial\gamma(\mathbf{0})_j^j}{\partial\theta_{ij}} &= -\gamma(\mathbf{0})_i^j-\gamma(\mathbf{0})_j^i,\\
\frac{\partial\Gamma(\mathbf{0})_{i\bar{i}}^{i\bar{i}}}{\partial\theta_{ij}} &= \Gamma(\mathbf{0})_{i\bar{i}}^{j\bar{i}}+\Gamma(\mathbf{0})_{i\bar{i}}^{i\bar{j}}+\Gamma(\mathbf{0})_{j\bar{i}}^{i\bar{i}}+\Gamma(\mathbf{0})_{i\bar{j}}^{i\bar{i}}.\\
\frac{\partial\Gamma(\mathbf{0})_{j\bar{j}}^{j\bar{j}}}{\partial\theta_{ij}} &= -\Gamma(\mathbf{0})_{j\bar{j}}^{i\bar{j}}-\Gamma(\mathbf{0})_{j\bar{j}}^{j\bar{i}}-\Gamma(\mathbf{0})_{i\bar{j}}^{j\bar{j}}-\Gamma(\mathbf{0})_{i\bar{j}}^{j\bar{j}}.
\end{aligned} \tag{C.20}$$

The diagonal elements of the Hessian are calculated as

$$\frac{\partial^2 F_{\mathbf{QI}}(0)}{\partial\theta_{ij}^2} = -\sum_{i\in\mathcal{A}}\sum_{k=0}^{3}\left[\frac{1}{\lambda_k^{(i)}(\mathbf{0})}\left(\frac{\partial\lambda_k^{(i)}(\mathbf{0})}{\partial\theta_{ij}}\right)^2+\log(\lambda_k^{(i)}(\mathbf{0}))\frac{\partial^2\lambda_k^{(i)}(\mathbf{0})}{\partial\theta_{ij}^2}\right], \tag{C.21}$$

which involves the second derivatives of the RDMs

$$\begin{aligned}
\frac{\partial^2 \gamma(\mathbf{0})^i_i}{\partial \theta^2_{ij}} &= -2\gamma(\mathbf{0})^i_i + 2\gamma(\mathbf{0})^j_j, \\
\frac{\partial^2 \gamma(\mathbf{0})^j_j}{\partial \theta^2_{ij}} &= 2\gamma(\mathbf{0})^i_i - 2\gamma(\mathbf{0})^j_j, \\
\frac{\partial^2 \Gamma(\mathbf{0})^{i\bar{i}}_{i\bar{i}}}{\partial \theta^2_{ij}} &= -4\Gamma(\mathbf{0})^{i\bar{i}}_{i\bar{i}} + 2 \sum_{(a,b,c,d)\in\mathcal{P}(i,i,j,j)} \Gamma(\mathbf{0})^{b\bar{d}}_{a\bar{c}}, \\
\frac{\partial^2 \Gamma(\mathbf{0})^{j\bar{j}}_{j\bar{j}}}{\partial \theta^2_{ij}} &= -4\Gamma(\mathbf{0})^{j\bar{j}}_{j\bar{j}} + 2 \sum_{(a,b,c,d)\in\mathcal{P}(i,i,j,j)} \Gamma(\mathbf{0})^{b\bar{d}}_{a\bar{c}},
\end{aligned} \tag{C.22}$$

where $\mathcal{P}(i,i,j,j)$ collects all permutations of the tuple (i,i,j,j).

Appendix D

Tabulated Data

This section collects the data for producing some of the figures in this thesis. The P-SSR entanglement values for H_{16} in Table D.1 were used in Figure 2.5, and the N-SSR entanglement values in Table D.2 are listed here for completeness. The C_2 CASCI/CASSCF energies with HF, MP2, and QICAS active orbitals, along the dissociation curve are summarized in Table D.3 and D.4, which were used in Figure 4.8. The energies at each macro iteration during a CASSCF calculation for Cr_2 with different starting orbital bases are tabulated in Table D.5 and D.6, which were used to produce Figure 4.9 and Table 4.1 in the main text.

N	$R = 1$	$R = 2$	$R = 3$	$R = 5$
2	(1, 0.00079)	(1, 0.00004)	(1, 0.00001)	(3, 0.00015)
	(2, 0.00155)	(2, 0.00027)	(2, 0.00013)	(4, 0.00101)
	(3, 0.00289)	(3, 0.00111)	(3, 0.00071)	(5, 0.00401)
	(4, 0.00481)	(4, 0.00308)	(4, 0.00244)	(6, 0.01019)
	(5, 0.00708)	(5, 0.00642)	(5, 0.00589)	(7, 0.01751)
	(7, 0.01090)	(7, 0.01409)	(7, 0.01505)	
	(8, 0.01149)	(8, 0.01549)	(8, 0.01685)	
4	(1, 0.00317)	(1, 0.00020)	(6, 0.00192)	(6, 0.00132)
	(2, 0.00104)	(2, 0.00007)	(7, 0.02821)	(7, 0.03748)
	(3, 0.00002)		(8, 0.04705)	(8, 0.06498)
8	(1, 0.02806)	(1, 0.01858)	(6, 0.01120)	(1, 0.00065)
	(2, 0.00036)	(2, 0.00217)	(7, 0.00561)	(2, 0.00554)
				(8, 0.00091)
12	(1, 0.06344)	(1, 0.05666)	(1, 0.04819)	(1, 0.03391)
16	(1, 0.09116)	(1, 0.10340)	(1, 0.10637)	(1, 0.08142)
20	(1, 0.06569)	(1, 0.06303)	(1, 0.05458)	(1, 0.03310)
24	(1, 0.03235)	(1, 0.02917)	(1, 0.02084)	(1, 0.00418)
	(2, 0.00024)	(2, 0.00030)	(2, 0.00200)	(2, 0.01301)
28	(1, 0.00709)	(1, 0.00380)	(1, 0.00078)	(6, 0.00169)
	(2, 0.00142)	(2, 0.00113)	(2, 0.00030)	(7, 0.03275)
	(3, 0.00005)		(3, 0.00002)	(8, 0.05492)
	(4, 0.00002)			
30	(1, 0.00306)	(1, 0.00082)	(1, 0.00018)	(3, 0.00046)
	(2, 0.00381)	(2, 0.00170)	(2, 0.00071)	(4, 0.00193)
	(3, 0.00468)	(3, 0.00314)	(3, 0.00199)	(5, 0.00535)
	(4, 0.00559)	(4, 0.00506)	(4, 0.00417)	(6, 0.01064)
	(5, 0.00642)	(5, 0.00719)	(5, 0.00708)	(7, 0.01584)
	(6, 0.00710)	(6, 0.00914)	(6, 0.01011)	(8, 0.01805)
	(7, 0.00753)	(7, 0.01052)	(7, 0.01242)	
	(8, 0.00768)	(8, 0.01102)	(8, 0.01328)	

Table D.1: Tuples (d, E_{P}) of orbital separation distance d and P-SSR entanglement E_{P} between orthonormal atomic orbitals for different numbers of electrons N in the ground state of H_{16} in STO-3G basis.

N	$R=1$	$R=2$	$R=3$	$R=5$
2	(1, 0.00079)	(1, 0.00004)	(1, 0.00001)	(3, 0.00015)
	(2, 0.00155)	(2, 0.00027)	(2, 0.00013)	(4, 0.00101)
	(3, 0.00289)	(3, 0.00111)	(3, 0.00071)	(5, 0.00401)
	(4, 0.00481)	(4, 0.00308)	(4, 0.00244)	(6, 0.01019)
	(5, 0.00708)	(5, 0.00642)	(5, 0.00589)	(7, 0.01751)
	(6, 0.00929)	(6, 0.01056)	(6, 0.01067)	(8, 0.02091)
	(7, 0.01090)	(7, 0.01409)	(7, 0.01505)	
	(8, 0.01149)	(8, 0.01549)	(8, 0.01685)	
4	(1, 0.00315)	(1, 0.00020)	(6, 0.00192)	(6, 0.00132)
	(2, 0.00102)	(2, 0.00007)	(7, 0.02821)	(7, 0.03748)
			(8, 0.04705)	(8, 0.06498)
8	(1, 0.02361)	(1, 0.01714)	(6, 0.01097)	(1, 0.00065)
	(2, 0.00016)	(2, 0.00213)	(7, 0.00560)	(2, 0.00554)
				(8, 0.00091)
12	(1, 0.03441)	(1, 0.03542)	(1, 0.03722)	(1, 0.03344)
16	(1, 0.04525)	(1, 0.05546)	(1, 0.06732)	(1, 0.07892)
20	(1, 0.03529)	(1, 0.03805)	(1, 0.04065)	(1, 0.03261)
24	(1, 0.02639)	(1, 0.02565)	(1, 0.01995)	(1, 0.00418)
		(2, 0.00015)	(2, 0.00196)	(2, 0.01301)
28	(1, 0.00696)	(1, 0.00378)	(1, 0.00078)	(6, 0.00169)
	(2, 0.00132)	(2, 0.00112)	(2, 0.00030)	(7, 0.03275)
			(3, 0.00002)	(8, 0.05492)
30	(1, 0.00305)	(1, 0.00082)	(1, 0.00018)	(3, 0.00046)
	(2, 0.00381)	(2, 0.00170)	(2, 0.00071)	(4, 0.00193)
	(3, 0.00468)	(3, 0.00314)	(3, 0.00199)	(5, 0.00535)
	(4, 0.00559)	(4, 0.00506)	(4, 0.00417)	(6, 0.01064)
	(5, 0.00642)	(5, 0.00719)	(5, 0.00708)	(7, 0.01584)
	(6, 0.00709)	(6, 0.00914)	(6, 0.01011)	(8, 0.01805)
	(7, 0.00753)	(7, 0.01052)	(7, 0.01242)	
	(8, 0.00768)	(8, 0.01102)	(8, 0.01328)	

Table D.2: Tuples (d, E_{N}) of orbital separation distance d and N-SSR entanglement E_{N} between orthonormal atomic orbitals for different numbers of electrons N in the ground state of H_{16} in STO-3G basis.

R	HF-CASCI	HF-CASSCF	HF-QICAS-CASCI	Error	HF-MP2-CASCI	Error
0.90	-75.12946759	-75.20144209	-75.19934023	0.0021	-75.18463955	0.0168
0.95	-75.27135392	-75.34401603	-75.34240062	0.0016	-75.32828484	0.0157
1.00	-75.37418035	-75.44713825	-75.44586770	0.0013	-75.43240495	0.0147
1.05	-75.44681960	-75.51972363	-75.51869917	0.0010	-75.50581173	0.0139
1.10	-75.49619999	-75.56875202	-75.56805195	0.0007	-75.55544219	0.0133
1.15	-75.52774827	-75.59969614	-75.59886872	0.0008	-75.58676044	0.0129
1.20	-75.54573301	-75.61685395	-75.61600405	0.0008	-75.60407385	0.0128
1.25	-75.55352667	-75.62360515	-75.62280752	0.0008	-75.61078031	0.0128
1.30	-75.55380393	-75.62260941	-75.62185183	0.0008	-75.60956170	0.0130
1.35	-75.54868975	-75.61595998	-75.61522372	0.0007	-75.60253499	0.0134
1.40	-75.53986690	-75.60530313	-75.60453251	0.0008	-75.59137073	0.0139
1.45	-75.52865167	-75.59193145	-75.59115951	0.0008	-75.57738559	0.0145
1.50	-75.51604788	-75.57685721	-75.57614399	0.0007	-75.56161491	0.0152
1.55	-75.50279544	-75.56087022	-75.56011649	0.0008	-75.54486974	0.0160
1.60	-75.48942913	-75.54458384	-75.54390621	0.0007	-75.52778131	0.0168
1.65	-75.47498850	-75.52847206	-75.52755548	0.0009	-75.52024140	0.0082
1.70	-75.46761485	-75.51603912	-75.51439989	0.0016	-75.51093774	0.0051
1.75	-75.45996259	-75.50679056	-75.50449374	0.0023	-75.50138186	0.0054
1.80	-75.45221991	-75.49754368	-75.49602688	0.0015	-75.49179947	0.0057
1.85	-75.44449233	-75.48847010	-75.48691210	0.0016	-75.48235903	0.0061
1.90	-75.43691689	-75.47969780	-75.47818189	0.0015	-75.47318460	0.0065

Table D.3: HF-CASCI$(8,8)$, HF-CASSCF$(8,8)$, HF-QICAS-CASCI$(8,8)$ energy (a.u.) and HF-MP2-CASCI$(8,8)$ (a.u.) for C_2 with cc-pVDZ basis set as functions of the internuclear distance R (Å). The columns directly after HF-QICAS-CASCI and HF-MP2-CASCI show the error between the corresponding CASCI energy and the HF-CASSCF energy. For QICAS the bond dimension is set at $m = 100$ with 50 DMRG sweeps. For the HF-MP2-QICAS, the natural orbitals of the MP2 solution is used for the subsequent CASCI calculation. The HF-CASSCF energy at R = 1.65Å is computed with the Molpro[135]–[137] package, and all other HF-(MP2)-CASCI/CASSCF energies with PySCF[219].

R	HF-CASCI	HF-CASSCF	HF-QICAS-CASCI	Error	HF-MP2-CASCI	Error
1.95	-75.42960501	-75.47132136	-75.46992772	0.0014	-75.46436648	0.0070
2.00	-75.42262399	-75.46341031	-75.46210159	0.0013	-75.45596985	0.0074
2.05	-75.41605627	-75.45601527	-75.45499966	0.0010	-75.44804145	0.0080
2.10	-75.40992543	-75.44917221	-75.44834985	0.0008	-75.44061440	0.0086
2.15	-75.40428211	-75.44290490	-75.44184310	0.0011	-75.43371138	0.0092
2.20	-75.39914843	-75.43722600	-75.43621747	0.0010	-75.42734653	0.0099
2.25	-75.39451911	-75.43213719	-75.43156663	0.0006	-75.42152625	0.0106
2.30	-75.39039472	-75.42762900	-75.42695443	0.0007	-75.41624947	0.0114
2.35	-75.38676296	-75.42368088	-75.42330421	0.0004	-75.41150757	0.0122
2.40	-75.38360577	-75.42026186	-75.41983790	0.0004	-75.40728441	0.0130
2.45	-75.38087573	-75.41733213	-75.41692488	0.0004	-75.40355674	0.0138
2.50	-75.37852375	-75.41484545	-75.41454286	0.0003	-75.40029491	0.0146
2.55	-75.37653318	-75.41275185	-75.41246927	0.0003	-75.39746416	0.0153
2.60	-75.37484268	-75.41100054	-75.41083042	0.0002	-75.39502619	0.0160
2.65	-75.37341422	-75.40954236	-75.40939055	0.0002	-75.39294095	0.0166
2.70	-75.37220493	-75.40833169	-75.40829325	0.0000	-75.39116835	0.0172
2.75	-75.37110250	-75.40761748	-75.40678190	0.0008	-75.38966973	0.0177
2.80	-75.37023221	-75.40677594	-75.40649893	0.0003	-75.38840902	0.0181
2.85	-75.36949194	-75.40607585	-75.40587908	0.0002	-75.38735350	0.0184
2.90	-75.36886008	-75.40549195	-75.40531755	0.0002	-75.38647408	0.0188
2.95	-75.36831894	-75.40500335	-75.40479502	0.0002	-75.38574544	0.0190
3.00	-75.36785398	-75.40459304	-75.40432654	0.0003	-75.38514585	0.0192

Table D.4: HF-CASCI$(8,8)$, HF-CASSCF$(8,8)$, HF-QICAS-CASCI$(8,8)$ energy (a.u.) and HF-MP2-CASCI$(8,8)$ (a.u.) for C_2 with cc-pVDZ basis set as functions of the internuclear distance R (Å). The columns directly after HF-QICAS-CASCI and HF-MP2-CASCI show the error between the corresponding CASCI energy and the HF-CASSCF energy. For QICAS the bond dimension is set at $m = 100$ with 50 DMRG sweeps. For the HF-MP2-QICAS, the natural orbitals of the MP2 solution is used for the subsequent CASCI calculation. All HF-(MP2)-CASCI/CASSCF energies are calculated with PySCF[219].

Method(N_{CAS}, D_{CAS})	# Micro	Energy (a.u.)	$\langle S^2 \rangle$
HF-CASSCF(12, 12)	0	-2098.56762004	0.0000
	8	-2098.65815254	0.0000
	16	-2098.78440779	0.0000
	24	-2098.90386814	0.0000
	32	-2098.97374464	0.0000
	40	-2099.07661965	0.0000
	48	-2099.15989834	0.0000
	56	-2099.22523508	0.0000
	66	-2099.26654074	0.0000
	76	-2099.26725524	0.0000
	80	-2099.26725943	0.0000
	82	-2099.26725956	0.0000
	83	-2099.26725956	0.0000
HF-QICAS-CASSCF(12, 12)	0	-2099.21963835	0.0000
	10	-2099.26689887	0.0000
	16	-2099.26725514	0.0000
	19	-2099.26725944	0.0000
	21	-2099.26725956	0.0000
	22	-2099.26725956	0.0000
HF-CASSCF(12, 14)	0	-2098.56831064	0.0000
	8	-2098.27411466	0.0231
	16	-2098.79419658	0.0000
	24	-2098.92256223	0.0000
	32	-2099.03522226	0.0000
	40	-2099.09255949	0.0000
	48	-2099.18377830	0.0000
	56	-2099.26174338	0.0000
	64	-2099.28119366	0.0000
	72	-2099.28981686	0.0000
	82	-2099.29106266	0.0000
	92	-2099.29109795	0.0000
	94	-2099.29109837	0.0000
	95	-2099.29109845	0.0000
HF-QICAS-CASSCF(12, 14)	0	-2099.24319492	0.0000
	10	-2099.29090519	0.0000
	18	-2099.29109765	0.0000
	21	-2099.29109853	0.0000
	22	-2099.29109856	0.0000

Table D.5: Energy as a function of the number of micro iterations in CASSCF(12,12) and CASSCF(12,14) for Cr_2 in the cc-pV5Z-DK basis set at $R = 1.679\,\text{Å}$, starting from HF-orbitals and from QICAS optimized orbitals.

Method(N_{CAS}, D_{CAS})	# Micro	Energy (a.u.)	$\langle S^2 \rangle$
HF-CASSCF(12, 12)	0	-2098.55947438	0.0000
	8	-2098.62309906	0.0000
	16	-2098.76339556	0.0000
	24	-2098.85949993	0.0000
	32	-2098.95413261	0.0000
	40	-2099.14159937	0.0000
	48	-2099.24342692	0.0000
	56	-2099.26371403	0.0000
	66	-2099.26724865	0.0000
	72	-2099.26745342	0.0000
	76	-2099.26745730	0.0000
	77	-2099.26745741	0.0000
	78	-2099.26745743	0.0000
HF-QICAS-CASSCF(12, 12)	0	-2099.11949368	0.0000
	10	-2099.26475360	0.0000
	18	-2099.26726838	0.0000
	25	-2099.26745489	0.0000
	28	-2099.26745735	0.0000
	29	-2099.26745742	0.0000
HF-CASSCF(12, 14)	0	-2098.55949885	0.0000
	8	-2098.62956185	0.0000
	16	-2097.84547862	0.1102
	24	-2098.91240284	0.0000
	32	-2098.94968193	0.0000
	40	-2099.05590176	0.0000
	48	-2099.17568356	0.0000
	56	-2099.25780515	0.0000
	64	-2099.28634932	0.0000
	72	-2099.29085930	0.0000
	82	-2099.29122633	0.0000
	92	-2099.29130420	0.0000
	96	-2099.29130780	0.0000
	98	-2099.29130824	0.0000
	99	-2099.29130834	0.0000
HF-QICAS-CASSCF(12, 14)	0	-2099.13797545	0.0000
	10	-2099.29041858	0.0000
	18	-2099.29130378	0.0000
	21	-2099.29130838	0.0000
	22	-2099.29130846	0.0000

Table D.6: Energy as a function of the number of micro iterations in CASSCF(12,12) and CASSCF(12,14) for Cr_2 in the aug-cc-pV5Z-DK basis set at $R = 1.679\,\text{Å}$, starting from HF-orbitals and from QICAS optimized orbitals.

Bibliography

[1] A. Einstein, B. Podolsky, and N. Rosen, "Can quantum-mechanical description of physical reality be considered complete?" *Phys. Rev.*, vol. 47, pp. 777–780, 10 1935. DOI: 10.1103/PhysRev.47.777.

[2] J. S. Bell, "On the Einstein Podolsky Rosen paradox," *Phys. Phys. Fiz.*, vol. 1, no. 3, p. 195, 1964. DOI: 10.1103/PhysicsPhysiqueFizika.1.195.

[3] R. F. Werner, "Quantum states with Einstein-Podolsky-Rosen correlations admitting a hidden-variable model," *Phys. Rev. A*, vol. 40, no. 8, p. 4277, 1989. DOI: 10.1103/PhysRevA.40.4277.

[4] V. Vedral, M. B. Plenio, M. A. Rippin, and P. L. Knight, "Quantifying entanglement," *Phys. Rev. Lett.*, vol. 78, pp. 2275–2279, 12 1997. DOI: 10.1103/PhysRevLett.78.2275.

[5] W. K. Wootters, "Entanglement of formation of an arbitrary state of two qubits," *Phys. Rev. Lett.*, vol. 80, pp. 2245–2248, 10 1998. DOI: 10.1103/PhysRevLett.80.2245.

[6] E. M. Rains, "Bound on distillable entanglement," *Phys. Rev. A*, vol. 60, pp. 179–184, 1 1999. DOI: 10.1103/PhysRevA.60.179.

[7] B. C. Hiesmayr, M. Huber, and P. Krammer, "Two computable sets of multipartite entanglement measures," *Phys. Rev. A*, vol. 79, p. 062 308, 6 2009. DOI: 10.1103/PhysRevA.79.062308.

[8] K. Modi, T. Paterek, W. Son, V. Vedral, and M. Williamson, "Unified view of quantum and classical correlations," *Phys. Rev. Lett.*, vol. 104, p. 080 501, 8 2010. DOI: 10.1103/PhysRevLett.104.080501.

[9] M. Horodecki, "Entanglement measures.," *Quantum Inf. Comput.*, vol. 1, no. 1, pp. 3–26, 2001. DOI: 10.26421/QIC1.1-2.

[10] R. Horodecki, P. Horodecki, M. Horodecki, and K. Horodecki, "Quantum entanglement," *Rev. Mod. Phys.*, vol. 81, pp. 865–942, 2 2009. DOI: 10.1103/RevModPhys.81.865.

[11] W. Dür, H.-J. Briegel, J. I. Cirac, and P. Zoller, "Quantum repeaters based on entanglement purification," *Phys. Rev. A*, vol. 59, pp. 169–181, 1 1999. DOI: 10.1103/PhysRevA.59.169.

[12] W. K. Wootters, "Quantum entanglement as a quantifiable resource," *Philos. Trans. R. Soc. London, Ser. A*, vol. 356, no. 1743, p. 1717, 1998. DOI: 10.1098/rsta.1998.0244.

[13] E. Chitambar and G. Gour, "Quantum resource theories," *Rev. Mod. Phys.*, vol. 91, p. 025 001, 2 2019. DOI: 10.1103/RevModPhys.91.025001.

[14] D. Bouwmeester, J.-W. Pan, K. Mattle, M. Eibl, H. Weinfurter, and A. Zeilinger, "Experimental quantum teleportation," *Nature*, vol. 390, no. 6660, p. 575, 1997. DOI: 10.1038/37539.

[15] C. H. Bennett and S. J. Wiesner, "Communication via one- and two-particle operators on Einstein-Podolsky-Rosen states," *Phys. Rev. Lett.*, vol. 69, pp. 2881–2884, 20 1992. DOI: 10.1103/PhysRevLett.69.2881.

[16] C. H. Bennett and G. Brassard, "Quantum cryptography: Public key distribution and coin tossing," *Theor. Comput. Sci.*, vol. 560, pp. 7–11, 2014. DOI: 10.1016/j.tcs.2014.05.025.

[17] I. R. Klebanov, D. Kutasov, and A. Murugan, "Entanglement as a probe of confinement," *Nucl. Phys. B.*, vol. 796, no. 1-2, pp. 274–293, 2008. DOI: 10.1016/j.nuclphysb.2007.12.017.

[18] A. Lewkowycz and J. Maldacena, "Exact results for the entanglement entropy and the energy radiated by a quark," *JHEP*, vol. 2014, no. 5, pp. 1–29, 2014. DOI: 10.1007/JHEP05(2014)025.

[19] Y. Afik and J. R. M. de Nova, "Entanglement and quantum tomography with top quarks at the LHC," *Eur. Phys. J. Plus*, vol. 136, no. 9, p. 907, 2021. DOI: 10.1140/epjp/s13360-021-01902-1.

[20] S. Hawking, J. Maldacena, and A. Strominger, "Desitter entropy, quantum entanglement and AdS/CFT," *JHEP*, vol. 2001, no. 05, p. 001, 2001. DOI: 10.1088/1126-6708/2001/05/001.

[21] I. Bloch, "Quantum coherence and entanglement with ultracold atoms in optical lattices," *Nature*, vol. 453, no. 7198, pp. 1016–1022, 2008. DOI: 10.1038/nature07126.

[22] M. Cramer, A. Bernard, N. Fabbri, L. Fallani, C. Fort, S. Rosi, F. Caruso, M. Inguscio, and M. B. Plenio, "Spatial entanglement of bosons in optical lattices," *Nat. Commun.*, vol. 4, no. 1, p. 2161, 2013. DOI: 10.1038/ncomms3161.

[23] A. Osterloh, L. Amico, G. Falci, and R. Fazio, "Scaling of entanglement close to a quantum phase transition," *Nature*, vol. 416, no. 6881, pp. 608–610, 2002. DOI: 10.1038/416608a.

[24] T. J. Osborne and M. A. Nielsen, "Entanglement in a simple quantum phase transition," *Phys. Rev. A*, vol. 66, p. 032 110, 3 2002. DOI: 10.1103/PhysRevA.66.032110.

[25] A. Kitaev and J. Preskill, "Topological entanglement entropy," *Phys. Rev. Lett.*, vol. 96, no. 11, p. 110 404, 2006. DOI: 10.1103/PhysRevLett.96.110404.

[26] M. Levin and X.-G. Wen, "Detecting topological order in a ground state wave function," *Phys. Rev. Lett.*, vol. 96, p. 110 405, 11 2006. DOI: 10.1103/PhysRevLett.96.110405.

[27] J. H. Bardarson, F. Pollmann, and J. E. Moore, "Unbounded growth of entanglement in models of many-body localization," *Phys. Rev. Lett.*, vol. 109, p. 017 202, 1 2012. DOI: 10.1103/PhysRevLett.109.017202.

[28] D. A. Abanin, E. Altman, I. Bloch, and M. Serbyn, "Colloquium: Many-body localization, thermalization, and entanglement," *Rev. Mod. Phys.*, vol. 91, p. 021 001, 2 2019. DOI: 10.1103/RevModPhys.91.021001.

[29] N. Schuch, M. M. Wolf, F. Verstraete, and J. I. Cirac, "Entropy scaling and simulability by matrix product states," *Phys. Rev. Lett.*, vol. 100, p. 030 504, 3 2008. DOI: 10.1103/PhysRevLett.100.030504.

[30] J. Eisert, M. Cramer, and M. B. Plenio, "Colloquium: Area laws for the entanglement entropy," *Rev. Mod. Phys.*, vol. 82, no. 1, pp. 277–306, 2010. DOI: 10.1103/RevModPhys.82.277.

[31] A. Hamma, S. Santra, and P. Zanardi, "Quantum entanglement in random physical states," *Phys. Rev. Lett.*, vol. 109, p. 040 502, 4 2012. DOI: 10.1103/PhysRevLett.109.040502.

[32] E. Bianchi, L. Hackl, M. Kieburg, M. Rigol, and L. Vidmar, "Volume-law entanglement entropy of typical pure quantum states," *PRX Quantum*, vol. 3, p. 030 201, 3 2022. DOI: 10.1103/PRXQuantum.3.030201.

[33] U. Schollwöck, "The density-matrix renormalization group in the age of matrix product states," *Ann. Phys.*, vol. 326, no. 1, pp. 96–192, 2011. DOI: 10.1016/j.aop.2010.09.012.

[34] F. Verstraete, M. M. Wolf, D. Perez-Garcia, and J. I. Cirac, "Criticality, the area law, and the computational power of projected entangled pair states," *Phys. Rev. Lett.*, vol. 96, p. 220 601, 22 2006. DOI: 10.1103/PhysRevLett.96.220601.

[35] G. Vidal, "Class of quantum many-body states that can be efficiently simulated," *Phys. Rev. Lett.*, vol. 101, p. 110 501, 11 2008. DOI: 10.1103/PhysRevLett.101.110501.

[36] P. Pulay and T. P. Hamilton, "UHF natural orbitals for defining and starting MC-SCF calculations," *J. Chem. Phys.*, vol. 88, no. 8, pp. 4926–4933, 1988. DOI: 10.1063/1.454704.

[37] R. S. Grev and H. F. Schaefer, "Natural orbitals from single and double excitation configuration interaction wave functions: Their use in second-order configuration interaction and wave functions incorporating limited triple and quadruple excitations," *J. Chem. Phys.*, vol. 96, no. 9, pp. 6850–6856, 1992. DOI: 10.1063/1.462574.

[38] M. L. Abrams and C. D. Sherrill, "Natural orbitals as substitutes for optimized orbitals in complete active space wavefunctions," *Chem. Phys. Lett.*, vol. 395, no. 4-6, pp. 227–232, 2004. DOI: 10.1016/j.cplett.2004.07.081.

[39] G. Barcza, Ö. Legeza, K. H. Marti, and M. Reiher, "Quantum-information analysis of electronic states of different molecular structures," *Phys. Rev. A*, vol. 83, p. 012 508, 1 2011. DOI: 10.1103/PhysRevA.83.012508.

[40] R. C. Clay and M. A. Morales, "Influence of single particle orbital sets and configuration selection on multideterminant wavefunctions in quantum monte carlo," *J. Chem. Phys.*, vol. 142, no. 23, 2015. DOI: 10.1063/1.4921984.

[41] C. Krumnow, L. Veis, Ö. Legeza, and J. Eisert, "Fermionic orbital optimization in tensor network states," *Phys. Rev. Lett.*, vol. 117, p. 210 402, 21 2016. DOI: 10.1103/PhysRevLett.117.210402.

[42] J. Hubbard, "Electron correlations in narrow energy bands," *Proceedings of the Royal Society of London. Series A. Mathematical and Physical Sciences*, vol. 276, no. 1365, pp. 238–257, 1963. DOI: 10.1098/rspa.1963.0204.

[43] J. Simons, "Why is quantum chemistry so complicated?" *J. Am. Chem. Soc.*, vol. 145, no. 8, pp. 4343–4354, 2023. DOI: 10.1021/jacs.2c13042.

[44] P.-O. Löwdin, "Quantum theory of many-particle systems. III. extension of the hartree-fock scheme to include degenerate systems and correlation effects," *Phys. Rev.*, vol. 97, pp. 1509–1520, 6 1955. DOI: 10.1103/PhysRev.97.1509.

[45] T. Kato, "On the eigenfunctions of many-particle systems in quantum mechanics," *Commun. Pure Appl. Math.*, vol. 10, no. 2, pp. 151–177, 1957, ISSN: 10970312. DOI: 10.1002/cpa.3160100201.

[46] C. Møller and M. S. Plesset, "Note on an approximation treatment for many-electron systems," *Phys. Rev.*, vol. 46, pp. 618–622, 7 1934. DOI: 10.1103/PhysRev.46.618.

[47] J. Paldus and X. Li, "A critical assessment of coupled cluster method in quantum chemistry," *Adv. Chem. Phys.*, vol. 110, pp. 1–175, 1999. DOI: 10.1002/9780470141694.ch1.

[48] R. J. Bartlett and M. Musiał, "Coupled-cluster theory in quantum chemistry," *Rev. Mod. Phys.*, vol. 79, pp. 291–352, 1 2007. DOI: 10.1103/RevModPhys.79.291.

[49] K. Andersson, P.-Å. Malmqvist, and B. O. Roos, "Second-order perturbation theory with a complete active space self-consistent field reference function," *J. Chem. Phys.*, vol. 96, no. 2, pp. 1218–1226, 1992, ISSN: 0021-9606, 1089-7690. DOI: 10.1063/1.462209.

[50] T. Kinoshita, O. Hino, and R. J. Bartlett, "Coupled-cluster method tailored by configuration interaction," *J. Chem. Phys.*, vol. 123, no. 7, p. 074 106, 2005, ISSN: 0021-9606, 1089-7690. DOI: 10.1063/1.2000251.

[51] L. Gagliardi, D. G. Truhlar, G. Li Manni, R. K. Carlson, C. E. Hoyer, and J. L. Bao, "Multiconfiguration Pair-Density Functional Theory: A New Way To Treat Strongly Correlated Systems," *Acc. Chem. Res.*, vol. 50, no. 1, pp. 66–73, 2017, ISSN: 0001-4842. DOI: 10.1021/acs.accounts.6b00471.

[52] S. Wouters and D. Van Neck, "The density matrix renormalization group for ab initio quantum chemistry," *EPJ D*, vol. 68, pp. 1–20, 2014. DOI: 10.1140/epjd/e2014-50500-1.

[53] M.-C. Bañuls, J. I. Cirac, and M. M. Wolf, "Entanglement in fermionic systems," *Phys. Rev. A*, vol. 76, no. 2, p. 022 311, 2007. DOI: 10.1103/PhysRevA.76.022311.

[54] M. Altunbulak and A. Klyachko, "The Pauli principle revisited," *Commun. Math. Phys.*, vol. 282, pp. 287–322, 2008. DOI: 10.1007/s00220-008-0552-z.

[55] D. A. Mazziotti, "Structure of fermionic density matrices: Complete N-representability conditions," *Phys. Rev. Lett.*, vol. 108, p. 263 002, 26 2012. DOI: 10.1103/PhysRevLett.108.263002.

[56] D. A. Mazziotti, "Two-electron reduced density matrix as the basic variable in many-electron quantum chemistry and physics," *Chem. Rev.*, vol. 112, no. 1, pp. 244–262, 2012. DOI: 10.1021/cr2000493.

[57] A. A. Klyachko, "The Pauli principle and magnetism," *arXiv:1311.5999*, 2013. DOI: 10.48550/arXiv.1311.5999.

[58] C. L. Benavides-Riveros, J. M. Gracia-Bondía, and M. Springborg, "Quasipinning and entanglement in the lithium isoelectronic series," *Phys. Rev. A*, vol. 88, p. 022 508, 2 2013. DOI: 10.1103/PhysRevA.88.022508.

[59] C. Schilling, D. Gross, and M. Christandl, "Pinning of fermionic occupation numbers," *Phys. Rev. Lett.*, vol. 110, p. 040 404, 4 2013. DOI: 10.1103/PhysRevLett.110.040404.

[60] N. Gigena and R. Rossignoli, "Entanglement in fermion systems," *Phys. Rev. A*, vol. 92, p. 042 326, 4 2015. DOI: 10.1103/PhysRevA.92.042326.

[61] C. Schilling, "Quasipinning and its relevance for N-fermion quantum states," *Phys. Rev. A*, vol. 91, p. 022 105, 2 2015. DOI: 10.1103/PhysRevA.91.022105.

[62] K. Boguslawski and P. Tecmer, "Orbital entanglement in quantum chemistry," *Int. J. Quantum Chem.*, vol. 115, no. 19, pp. 1289–1295, 2015. DOI: 10.1002/qua.24832.

[63] C. L. Benavides-Riveros and C. Schilling, "Natural extension of Hartree–Fock through extremal 1-fermion information: Overview and application to the lithium atom," *Z. Phys. Chem*, vol. 230, no. 5-7, pp. 703–717, 2016. DOI: 10.1515/zpch-2015-0732.

[64] N. Friis, "Reasonable fermionic quantum information theories require relativity," *New J. Phys.*, vol. 18, no. 3, p. 033 014, 2016. DOI: 10.1088/1367-2630/18/3/033014.

[65] C. J. Turner, K. Meichanetzidis, Z. Papić, and J. K. Pachos, "Optimal free descriptions of many-body theories," *Nat. Commun.*, vol. 8, no. 1, pp. 1–7, 2017. DOI: 10.1038/ncomms14926.

[66] C. Schilling, C. L. Benavides-Riveros, and P. Vrana, "Reconstructing quantum states from single-party information," *Phys. Rev. A*, vol. 96, p. 052 312, 5 2017. DOI: 10.1103/PhysRevA.96.052312.

[67] T. Maciazek and V. Tsanov, "Quantum marginals from pure doubly excited states," *J. Phys. A*, vol. 50, no. 46, p. 465 304, 2017. DOI: 10.1088/1751-8121/aa8c5f.

[68] C. Schilling, M. Altunbulak, S. Knecht, A. Lopes, J. D. Whitfield, M. Christandl, D. Gross, and M. Reiher, "Generalized Pauli constraints in small atoms," *Phys. Rev. A*, vol. 97, p. 052 503, 5 2018. DOI: 10.1103/PhysRevA.97.052503.

[69] R. L. Franco and G. Compagno, "Indistinguishability of elementary systems as a resource for quantum information processing," *Phys. Rev. Lett.*, vol. 120, no. 24, p. 240 403, 2018. DOI: PhysRevLett.120.240403.

[70] B. Morris, B. Yadin, M. Fadel, T. Zibold, P. Treutlein, and G. Adesso, "Entanglement between identical particles is a useful and consistent resource," *Phys. Rev. X*, vol. 10, no. 4, p. 041 012, 2020. DOI: 10.1103/PhysRevX.10.041012.

[71] F. Benatti, R. Floreanini, F. Franchini, and U. Marzolino, "Entanglement in indistinguishable particle systems," *Phys. Rep.*, vol. 878, pp. 1–27, 2020. DOI: 10.1016/j.physrep.2020.07.003.

[72] Y. A. Aoto and M. F. da Silva, "Calculating the distance from an electronic wave function to the manifold of slater determinants through the geometry of Grassmannians," *Phys. Rev. A*, vol. 102, p. 052 803, 5 2020. DOI: 10.1103/PhysRevA.102.052803.

[73] E. Olofsson, P. Samuelsson, N. Brunner, and P. P. Potts, "Quantum teleportation of single-electron states," *Phys. Rev. B*, vol. 101, no. 19, p. 195 403, 2020. DOI: 10.1103/PhysRevB.101.195403.

[74] O. Pusuluk, M. H. Yesiller, G. Torun, Ö. E. Müstecaplıoğlu, E. Yurtsever, and V. Vedral, "Classical and quantum orbital correlations in the molecular electronic states," *arXiv:2107.13992*, 2021. [Online]. Available: https://arxiv.org/abs/2107.13992.

[75] A. Galler and P. Thunström, "Orbital and electronic entanglement in quantum teleportation schemes," *Phys. Rev. Res.*, vol. 3, no. 3, p. 033 120, 2021. DOI: 10.1103/PhysRevResearch.3.033120.

[76] J. Faba, V. Martín, and L. Robledo, "Two-orbital quantum discord in fermion systems," *Phys. Rev. A*, vol. 103, no. 3, p. 032 426, 2021. DOI: 10.1103/PhysRevA.103.032426.

[77] J. Sperling and E. Agudelo, "Entanglement of particles versus entanglement of fields: Independent quantum resources," *Phys. Rev. A*, vol. 107, p. 042 420, 4 2023. DOI: 10.1103/PhysRevA.107.042420.

[78] H. Kummer, "N-representability problem for reduced density matrices," *J. Math. Phys.*, vol. 8, no. 10, pp. 2063–2081, 1967. DOI: 10.1063/1.1705122.

[79] D. A. Mazziotti, "Contracted Schrödinger equation: Determining quantum energies and two-particle density matrices without wave functions," *Phys. Rev. A*, vol. 57, pp. 4219–4234, 6 1998. DOI: 10.1103/PhysRevA.57.4219.

[80] L. Henderson and V. Vedral, "Classical, quantum and total correlations," *J. Phys. A: Math. Gen.*, vol. 34, no. 35, p. 6899, 2001, ISSN: 0305-4470. DOI: 10.1088/0305-4470/34/35/315.

[81] J. Oppenheim, M. Horodecki, P. Horodecki, and R. Horodecki, "Thermodynamical approach to quantifying quantum correlations," *Phys. Rev. Lett.*, vol. 89, p. 180 402, 18 2002. DOI: 10.1103/PhysRevLett.89.180402.

[82] S. Luo, "Using measurement-induced disturbance to characterize correlations as classical or quantum," *Phys. Rev. A*, vol. 77, p. 022 301, 2 2008. DOI: 10.1103/PhysRevA.77.022301.

[83] A. C. Doherty, P. A. Parrilo, and F. M. Spedalieri, "Detecting multipartite entanglement," *Phys. Rev. A*, vol. 71, p. 032 333, 3 2005. DOI: 10.1103/PhysRevA.71.032333.

[84] M. Huber, F. Mintert, A. Gabriel, and B. C. Hiesmayr, "Detection of high-dimensional genuine multipartite entanglement of mixed states," *Phys. Rev. Lett.*, vol. 104, p. 210 501, 21 2010. DOI: 10.1103/PhysRevLett.104.210501.

[85] Z.-H. Ma, Z.-H. Chen, J.-L. Chen, C. Spengler, A. Gabriel, and M. Huber, "Measure of genuine multipartite entanglement with computable lower bounds," *Phys. Rev. A*, vol. 83, no. 6, p. 062 325, 2011. DOI: 10.1103/PhysRevA.83.062325.

[86] M. Walter, D. Gross, and J. Eisert, "Multipartite entanglement," *Quantum Information: From Foundations to Quantum Technology Applications*, pp. 293–330, 2016. DOI: 10.1002/9783527805785.ch14.

[87] K. Boguslawski, Ö. Tecmer Pawełand Legeza, and M. Reiher, "Entanglement measures for single- and multireference correlation effects," *J. Phys. Chem. Lett.*, vol. 3, no. 21, pp. 3129–3135, 2012. DOI: 10.1021/jz301319v.

[88] J. P. Dowling and G. J. Milburn, "Quantum technology: The second quantum revolution," *Philos. Trans. R. Soc. A*, vol. 361, no. 1809, pp. 1655–1674, 2003. DOI: 10.1098/rsta.2003.1227.

[89] M. Atzori and R. Sessoli, "The second quantum revolution: Role and challenges of molecular chemistry," *J. Am. Chem. Soc*, vol. 141, no. 29, pp. 11 339–11 352, 2019. DOI: 10.1021/jacs.9b00984.

[90] I. H. Deutsch, "Harnessing the power of the second quantum revolution," *PRX Quantum*, vol. 1, p. 020 101, 2 2020. DOI: 10.1103/PRXQuantum.1.020101.

[91] S. D. Bartlett and H. M. Wiseman, "Entanglement constrained by superselection rules," *Phys. Rev. Lett.*, vol. 91, no. 9, p. 097 903, 2003. DOI: 10.1103/PhysRevLett.91.097903.

[92] H. M. Wiseman, S. D. Bartlett, and J. A. Vaccaro, "Ferreting out the fluffy bunnies: Entanglement constrained by generalized superselection rules," in *Laser Spect.* World Scientific, 2004, pp. 307–314. DOI: 10.1142/9789812703002_0047.

[93] W. Li, J. Ren, H. Yang, and Z. Shuai, "On the fly swapping algorithm for ordering of degrees of freedom in density matrix renormalization group," *J. Phys.: Condens. Matter*, vol. 34, no. 25, p. 254 003, 2022. DOI: 10.1088/1361-648X/ac640e.

[94] G. Friesecke, M. A. Werner, K. Kapás, A. Menczer, and Ö. Legeza, "Global fermionic mode optimization via swap gates," *arXiv:2406.03449*, 2024. DOI: 10.48550/arXiv.2406.03449.

[95] B. O. Roos, P. R. Taylor, and P. E. Sigbahn, "A complete active space SCF method (CASSCF) using a density matrix formulated super-CI approach," *Chem. Phys.*, vol. 48, no. 2, pp. 157–173, 1980. DOI: 10.1016/0301-0104(80)80045-0.

[96] H.-J. Werner and P. J. Knowles, "A second order multiconfiguration scf procedure with optimum convergence," *J. Chem. Phys.*, vol. 82, no. 11, pp. 5053–5063, 1985. DOI: 10.1063/1.448627.

[97] P. E. M. Siegbahn, J. Almlöf, A. Heiberg, and B. O. Roos, "The complete active space SCF (CASSCF) method in a newton–raphson formulation with application to the HNO molecule," *J. Chem. Phys.*, vol. 74, no. 4, pp. 2384–2396, 1981. DOI: 10.1063/1.441359.

[98] P.-Å. Malmqvist and B. O. Roos, "The casscf state interaction method," *Chem. Phys. Lett.*, vol. 155, no. 2, pp. 189–194, 1989. DOI: 10.1016/0009-2614(89)85347-3.

[99] P. Zanardi, "Virtual quantum subsystems," *Phys. Rev. Lett.*, vol. 87, p. 077 901, 7 2001. DOI: 10.1103/PhysRevLett.87.077901.

[100] G. Lindblad, "Expectations and entropy inequalities for finite quantum systems," *Commun. Math. Phys.*, vol. 39, no. 2, pp. 111–119, 1974. DOI: 10.1007/BF01608390.

[101] V. Vedral, "The role of relative entropy in quantum information theory," *Rev. Mod. Phys.*, vol. 74, no. 1, p. 197, 2002. DOI: 10.1103/RevModPhys.74.197.

[102] F. Hiai and D. Petz, "The proper formula for relative entropy and its asymptotics in quantum probability," *Commun. Math. Phys.*, vol. 143, no. 1, p. 99, 1991. DOI: 10.1007/BF02100287.

[103] M. A. Nielsen and I. Chuang, *Quantum computation and quantum information*, https://aapt.scitation.org/doi/abs/10.1119/1.1463744?journalCode=ajp, 2002.

[104] M. M. Wolf, F. Verstraete, M. B. Hastings, and J. I. Cirac, "Area laws in quantum systems: Mutual information and correlations," *Phys. Rev. Lett.*, vol. 100, no. 7, p. 070 502, 2008. DOI: 10.1103/PhysRevLett.100.070502.

[105] J. Watrous, *Lecture notes on the "theory of quantum information"*, 2011. [Online]. Available: https://cs.uwaterloo.ca/~watrous/TQI-notes/.

[106] C. Schilling, "Orbital Entanglement and Correlation," in *Simulating Correlations with Computers*, E. Pavarini and E. Koch, Eds. Forschungszentrum Jülich GmbH Zentralbibliothek, Verlag, 2021, ch. 9, p. 261, ISBN: 978-3-95806-529-1. [Online]. Available: https://juser.fz-juelich.de/record/896709.

[107] L. Ding, Z. Zimboras, and C. Schilling, "Quantifying electron entanglement faithfully," *arXiv:2207.03377*, 2022. DOI: 10.48550/arXiv.2207.03377.

[108] A. Peres, "Separability criterion for density matrices," *Phys. Rev. Lett*, vol. 77, no. 8, p. 1413, 1996. DOI: 10.1103/PhysRevLett.77.1413.

[109] M. Horodecki, P. Horodecki, and R. Horodecki, "Separability of mixed states: Necessary and sufficient conditions," *Phys. Lett. A*, vol. 223, no. 1-2, pp. 1–8, 1996. DOI: 10.1016/S0375-9601(96)00706-2.

[110] A. Ekert and P. L. Knight, "Entangled quantum systems and the Schmidt decomposition," *Am. J. Phys.*, vol. 63, no. 5, pp. 415–423, 1995. DOI: 10.1119/1.17904.

[111] N. Laflorencie, "Quantum entanglement in condensed matter systems," *Phys. Rep.*, vol. 646, pp. 1–59, 2016. DOI: 10.1016/j.physrep.2016.06.008.

[112] R. Ursin, F. Tiefenbacher, T. Schmitt-Manderbach, H. Weier, T. Scheidl, M. Lindenthal, B. Blauensteiner, T. Jennewein, J. Perdigues, P. Trojek, B. Ömer, M. Fürst, M. Meyenburg, J. Rarity, Z. Sodnik, C. Barbieri, H. Weinfurter, and A. Zeilinger, "Entanglement-based quantum communication over 144 km," *Nat. Phys.*, vol. 3, no. 7, pp. 481–486, 2007. DOI: 10.1038/nphys629.

[113] T. Jennewein, C. Simon, G. Weihs, H. Weinfurter, and A. Zeilinger, "Quantum cryptography with entangled photons," *Phys. Rev. Lett.*, vol. 84, no. 20, p. 4729, 2000. DOI: 10.1103/PhysRevLett.84.4729.

[114] I. Peschel and V. Eisler, "Reduced density matrices and entanglement entropy in free lattice models," *J. Phys. A: Math. Theor.*, vol. 42, no. 50, p. 504 003, 2009. DOI: 10.1088/1751-8113/42/50/504003.

[115] A. D. Gottlieb and N. J. Mauser, "New measure of electron correlation," *Phys. Rev. Lett.*, vol. 95, p. 123 003, 12 2005. DOI: 10.1103/PhysRevLett.95.123003.

[116] A. D. Gottlieb and N. J. Mauser, "Correlation in fermion or boson systems as the minimum of entropy relative to all free states," *arXiv:1403.7640*, 2014. DOI: 10.48550/arXiv.1403.7640.

[117] G. G. Amosov and S. N. Filippov, "Spectral properties of reduced fermionic density operators and parity superselection rule," *Quantum Inf. Process.*, vol. 16, no. 1, pp. 1–16, 2017. DOI: 10.1007/s11128-016-1467-9.

[118] M. Johansson, "Comment on "reasonable fermionic quantum information theories require relativity"," *arXiv:1610.00539*, 2016. DOI: 10.48550/arXiv.1610.00539.

[119] L. Ding, S. Mardazad, S. Das, S. Szalay, U. Schollwöck, Z. Zimborás, and C. Schilling, "Concept of orbital entanglement and correlation in quantum chemistry," *J. Chem. Theory Comput.*, vol. 17, no. 1, pp. 79–95, 2020. DOI: 10.1021/acs.jctc.0c00559.

[120] G.-C. Wick, A. S. Wightman, and E. P. Wigner, "Superselection rule for charge," *Phys. Rev. D*, vol. 1, no. 12, p. 3267, 1970. DOI: 10.1103/PhysRevD.1.3267.

[121] G.-C. Wick, A. S. Wightman, and E. P. Wigner, "The intrinsic parity of elementary particles," *Phys. Rev.*, vol. 88, p. 101, 1 1952. DOI: 10.1103/PhysRev.88.101.

[122] F. Verstraete and J. I. Cirac, "Quantum nonlocality in the presence of superselection rules and data hiding protocols," *Phys. Rev. Lett.*, vol. 91, no. 1, p. 010 404, 2003. DOI: 10.1103/PhysRevLett.91.010404.

[123] A. I. Krylov, "From orbitals to observables and back," *J. Chem. Phys.*, vol. 153, no. 8, 2020. DOI: 10.1063/5.0018597.

[124] A. W. Marshall, I. Olkin, and B. C. Arnold, *Inequalities: theory of majorization and its applications*. Springer, 1979. DOI: 10.1016/c2009-0-22048-4.

[125] K. G. H. Vollbrecht and R. F. Werner, "Entanglement measures under symmetry," *Phys. Rev. A*, vol. 64, no. 6, p. 062 307, 2001. DOI: 10.1103/PhysRevA.64.062307.

[126] P. Calabrese, M. Mintchev, and E. Vicari, "Entanglement entropies in free-fermion gases for arbitrary dimension," *EPL*, vol. 97, no. 2, p. 20 009, 2012. DOI: 10.1209/0295-5075/97/20009.

[127] F. Ares, S. Murciano, and P. Calabrese, "Symmetry-resolved entanglement in a long-range free-fermion chain," *J. Stat. Mech.: Theory Exp.*, vol. 2022, no. 6, p. 063 104, 2022. DOI: 10.1088/1742-5468/ac7644.

[128] I. Peschel, "Calculation of reduced density matrices from correlation functions," *J. Phys. A: Math. Gen.*, vol. 36, no. 14, p. L205, 2003. DOI: 10.1088/0305-4470/36/14/101.

[129] T. Yu and J. H. Eberly, "Sudden death of entanglement," *Science*, vol. 323, no. 5914, pp. 598–601, 2009. DOI: 10.1126/science.1167343. eprint: https://www.science.org/doi/pdf/10.1126/science.1167343.

[130] S. Kucharski, A. Balková, P. Szalay, and R. J. Bartlett, "Hilbert space multireference coupled-cluster methods. II. A model study on H_8," *J. Chem. Phys.*, vol. 97, no. 6, pp. 4289–4300, 1992. DOI: 10.1063/1.467143.

[131] L. Stella, C. Attaccalite, S. Sorella, and A. Rubio, "Strong electronic correlation in the hydrogen chain: A variational monte carlo study," *Phys. Rev. B*, vol. 84, p. 245 117, 24 2011. DOI: 10.1103/PhysRevB.84.245117.

[132] M. Motta, D. M. Ceperley, G. K.-L. Chan, J. A. Gomez, E. Gull, S. Guo, C. A. Jiménez-Hoyos, T. N. Lan, J. Li, F. Ma, A. J. Millis, N. V. Prokof'ev, U. Ray, G. E. Scuseria, S. Sorella, E. M. Stoudenmire, Q. Sun, I. S. Tupitsyn, S. R. White, D. Zgid, and S. Zhang, "Towards the solution of the many-electron problem in real materials: Equation of state of the hydrogen chain with state-of-the-art many-body methods," *Phys. Rev. X*, vol. 7, p. 031 059, 3 2017. DOI: 10.1103/PhysRevX.7.031059.

[133] D. A. Mazziotti, "Quantum many-body theory from a solution of the N-representability problem," *Phys. Rev. Lett.*, vol. 130, p. 153 001, 15 2023. DOI: 10.1103/PhysRevLett.130.153001.

[134] P.-O. Löwdin, "On the nonorthogonality problem," in ser. Adv. Quantum Chem. P.-O. Löwdin, Ed., vol. 5, Academic Press, 1970, pp. 185–199. DOI: 10.1016/S0065-3276(08)60339-1.

[135] H.-J. Werner, P. J. Knowles, G. Knizia, F. R. Manby, and M. Schütz, *WIREs Comput. Mol. Sci.*, vol. 2, pp. 242–253, 2012. DOI: 10.1002/wcms.82.

[136] H.-J. Werner, P. J. Knowles, F. R. Manby, J. A. Black, K. Doll, A. Heßelmann, D. Kats, A. Köhn, T. Korona, D. A. Kreplin, Q. Ma, T. F. M. III, A. Mitrushchenkov, K. A. Peterson, I. Polyak, G. Rauhut, and M. Sibaev, *J. Chem. Phys.*, vol. 152, p. 144 107, 2020. DOI: 10.1063/5.0005081.

[137] https://www.molpro.net, MOLPRO, version 2019, a package of ab initio programs, H.-J. Werner, P. J. Knowles, G. Knizia, F. R. Manby, M. Schütz, and others.

[138] P. J. Knowles and N. C. Handy, "A determinant based full configuration interaction program," *Comp. Phys. Commun.*, vol. 54, pp. 75–83, 1989. DOI: 10.1016/0010-4655(89)90033-7.

[139] C. Hubig, F. Lachenmaier, N.-O. Linden, T. Reinhard, L. Stenzel, A. Swoboda, M. Grundner, and S. M. .-. add other contributors here –, *The* SyTen *toolkit*. [Online]. Available: https://syten.eu.

[140] C. Hubig, "Symmetry-protected tensor networks," Ph.D. dissertation, LMU München, 2017. [Online]. Available: https://edoc.ub.uni-muenchen.de/21348/.

[141] G. N. Lewis, "The atom and the molecule.," *J. Am. Chem. Soc.*, vol. 38, no. 4, pp. 762–785, 1916. DOI: 10.1021/ja02261a002.

[142] C. A. Coulson, "The electronic structure of some polyenes and aromatic molecules. VII. bonds of fractional order by the molecular orbital method," *Proc. Roy. Soc. A*, vol. 169, no. 938, pp. 413–428, 1939. DOI: 10.1098/rspa.1939.0006.

[143] I. Mayer, "Charge, bond order and valence in the ab initio SCF theory," *Chem. Phys. Lett.*, vol. 97, no. 3, pp. 270–274, 1983. DOI: 10.1016/0009-2614(83)80005-0.

[144] X. Fradera, M. A. Austen, and R. F. Bader, "The Lewis model and beyond," *J. Phys. Chem. A*, vol. 103, no. 2, pp. 304–314, 1999. DOI: 10.1021/jp983362q.

[145] K. B. Wiberg, "Application of the pople-santry-segal CNDO method to the cyclopropylcarbinyl and cyclobutyl cation and to bicyclobutane," *Tetrahedron*, vol. 24, no. 3, pp. 1083–1096, 1968. DOI: 10.1016/0040-4020(68)88057-3.

[146] M. Giambiagi, M. S. de Giambiagi, and K. C. Mundim, "Definition of a multicenter bond index," *Struct. Chem.*, vol. 1, pp. 423–427, 1990. DOI: 10.1007/bf00671228.

[147] A. Sannigrahi and T. Kar, "Three-center bond index," *Chem. Phys. Lett.*, vol. 173, no. 5-6, pp. 569–572, 1990. DOI: 10.1016/0009-2614(90)87254-0.

[148] R. Ponec and I. Mayer, "Investigation of some properties of multicenter bond indices," *J. Phys. Chem. A*, vol. 101, no. 9, pp. 1738–1741, 1997. DOI: 10.1021/jp962510e.

[149] M. Giambiagi, M. S. de Giambiagi, C. D. dos Santos Silva, and A. P. de Figueiredo, "Multicenter bond indices as a measure of aromaticity," *Phys. Chem. Chem. Phys.*, vol. 2, no. 15, pp. 3381–3392, 2000. DOI: 10.1039/B002009P.

[150] P. Bultinck, R. Ponec, and S. Van Damme, "Multicenter bond indices as a new measure of aromaticity in polycyclic aromatic hydrocarbons," *J. Phys. Org. Chem.*, vol. 18, no. 8, pp. 706–718, 2005. DOI: 10.1002/poc.922.

[151] F. Feixas, M. Sola, J. M. Barroso, J. M. Ugalde, and E. Matito, "New approximation to the third-order density. application to the calculation of correlated multicenter indices," *J. Chem. Theory Comput.*, vol. 10, no. 8, pp. 3055–3065, 2014. DOI: 10.1021/ct5002736.

[152] K. Binder and P. C. Hohenberg, "Phase transitions and static spin correlations in Ising models with free surfaces," *Phys. Rev. B*, vol. 6, pp. 3461–3487, 9 1972. DOI: 10.1103/PhysRevB.6.3461.

[153] P. Sengupta, A. W. Sandvik, and D. K. Campbell, "Bond-order-wave phase and quantum phase transitions in the one-dimensional extended hubbard model," *Phys. Rev. B*, vol. 65, p. 155 113, 15 2002. DOI: 10.1103/PhysRevB.65.155113.

[154] S. Szalay, G. Barcza, T. Szilvási, L. Veis, and Ö. Legeza, "The correlation theory of the chemical bond," *Sci. Rep*, vol. 7, no. 1, pp. 1–10, 2017. DOI: 10.1038/s41598-017-02447-z.

[155] J. Brandejs, L. Veis, S. Szalay, G. Barcza, J. Pittner, and Ö. Legeza, "Quantum information-based analysis of electron-deficient bonds," *J. Chem. Phys*, vol. 150, no. 20, p. 204 117, 2019. DOI: 10.1063/1.5093497.

[156] P. M. Hayden, M. Horodecki, and B. M. Terhal, "The asymptotic entanglement cost of preparing a quantum state," *J. Phys. A*, vol. 34, no. 35, p. 6891, 2001. DOI: 10.1088/0305-4470/34/35/314.

[157] R. F. Bader, "Atoms in molecules," *Acc. Chem. Res.*, vol. 18, no. 1, pp. 9–15, 1985. DOI: 10.1021/ar00109a003.

[158] I. Mayer and P. Salvador, "Overlap populations, bond orders and valences for 'fuzzy' atoms," *Chem. Phys. Lett.*, vol. 383, no. 3-4, pp. 368–375, 2004. DOI: 10.1016/j.cplett.2003.11.048.

[159] E. Matito, "An electronic aromaticity index for large rings," *Phys. Chem. Chem. Phys.*, vol. 18, no. 17, pp. 11 839–11 846, 2016. DOI: 10.1039/C6CP00636A.

[160] A. E. Reed and F. Weinhold, "Natural localized molecular orbitals," *J. Chem. Phys.*, vol. 83, no. 4, pp. 1736–1740, 1985. DOI: 10.1063/1.449360.

[161] J. Pipek and P. G. Mezey, "A fast intrinsic localization procedure applicable for ab initio and semiempirical linear combination of atomic orbital wave functions," *J. Chem. Phys.*, vol. 90, p. 4916, 1989. DOI: 10.1063/1.456588.

[162] E. Koridon, S. Yalouz, B. Senjean, F. Buda, T. E. O'Brien, and L. Visscher, "Orbital transformations to reduce the 1-norm of the electronic structure hamiltonian for quantum computing applications," *Phys. Rev. Res.*, vol. 3, p. 033 127, 2021. DOI: 10.1103/physrevresearch.3.033127.

[163] G. Knizia, "Intrinsic atomic orbitals: An unbiased bridge between quantum theory and chemical concepts," *J. Chem. Theory Comput.*, vol. 9, no. 11, pp. 4834–4843, 2013. DOI: 10.1021/ct400687b.

[164] B. O. Roos, A. C. Borin, and L. Gagliardi, "Reaching the maximum multiplicity of the covalent chemical bond," *Angew. Chem., Int. Ed. Engl.*, vol. 46, no. 9, p. 1469, 2007. DOI: 10.1002/anie.200603600.

[165] P. W. Atkins and R. S. Friedman, *Molecular quantum mechanics*. Oxford University Press, USA, 2011. DOI: 10.1093/hesc/9780199541423.001.0001.

[166] K. Boguslawski, P. Tecmer, G. Barcza, Ö. Legeza, and M. Reiher, "Orbital entanglement in bond-formation processes," *J. Chem. Theory Comput*, vol. 9, no. 7, pp. 2959–2973, 2013. DOI: 10.1021/ct400247p.

[167] M. Mottet, P. Tecmer, K. Boguslawski, Ö. Legeza, and M. Reiher, "Quantum entanglement in carbon–carbon, carbon-phosphorus and silicon-silicon bonds," *Phys. Chem. Chem. Phys.*, vol. 16, pp. 8872–8880, 2014. DOI: 10.1039/C4CP00277F.

[168] L. Freitag, S. Knecht, S. F. Keller, M. G. Delcey, F. Aquilante, T. Bondo Pedersen, R. Lindh, M. Reiher, and L. González, "Orbital entanglement and casscf analysis of the Ru-NO bond in a ruthenium nitrosyl complex," *Phys. Chem. Chem. Phys.*, vol. 17, pp. 14 383–14 392, 2015. DOI: 10.1039/C4CP05278A.

[169] C. Duperrouzel, P. Tecmer, K. Boguslawski, G. Barcza, Ö. Legeza, and P. W. Ayers, "A quantum informational approach for dissecting chemical reactions," *Chem. Phys. Lett.*, vol. 621, pp. 160–164, 2015. DOI: 10.1016/j.cplett.2015.01.005.

[170] Y. Zhao, K. Boguslawski, P. Tecmer, C. Duperrouzel, G. Barcza, Ö. Legeza, and P. W. Ayers, "Dissecting the bond-formation process of d^{10}-metal-ethene complexes with multireference approaches," *Theor. Chem. Acc.*, vol. 134, no. 10, p. 120, 2015. DOI: 10.1007/s00214-015-1726-3.

[171] C. J. Stein and M. Reiher, "Measuring multi-configurational character by orbital entanglement," *Mol. Phys.*, vol. 115, no. 17-18, pp. 2110–2119, 2017. DOI: 10.1080/00268976.2017.1288934.

[172] C. Stemmle, B. Paulus, and Ö. Legeza, "Analysis of electron-correlation effects in strongly correlated systems (N_2 and N_2^+) by applying the density-matrix renormalization-group method and quantum information theory," *Phys. Rev. A*, vol. 97, p. 022 505, 2 2018. DOI: 10.1103/PhysRevA.97.022505.

[173] S. Keller, M. Dolfi, M. Troyer, and M. Reiher, "An efficient matrix product operator representation of the quantum-chemical hamiltonian," *J. Chem. Phys.*, vol. 143, p. 244 118, 2015. DOI: 10.1063/1.4939000.

[174] S. Keller and M. Reiher, "Spin-adapted matrix product states and operators," *J. Chem. Phys.*, vol. 144, p. 134 101, 2016. DOI: 10.1063/1.4944921.

[175] S. Knecht, E. D. Hedegaard, S. Keller, A. Kovyrshin, Y. Ma, A. Muolo, C. J. Stein, and M. Reiher, "New approaches for ab initio calculations of molecules with strong electron correlation," *Chimia*, vol. 70, pp. 244–251, 2016. DOI: 10.2533/chimia.2016.244.

[176] T. H. Dunning Jr., "Gaussian basis sets for use in correlated molecular calculations. I. the atoms boron through neon and hydrogen," *J. Chem. Phys.*, vol. 90, p. 1007, 1989. DOI: 10.1063/1.456153.

[177] E. Hückel, "Quantentheoretische Beiträge zum Benzolproblem. I. Die Elektronenkonfiguration des Benzols und verwandter Verbindungen," *Z. Phys.*, vol. 70, pp. 204–286, 1931. DOI: 10.1007/BF01339530.

[178] E. R. Sayfutyarova, Q. Sun, G. K.-L. Chan, and G. Knizia, "Automated construction of molecular active spaces from atomic valence orbitals," *J. Chem. Theory Comput.*, vol. 13, no. 9, pp. 4063–4078, 2017. DOI: 10.1021/acs.jctc.7b00128.

[179] L. Ding, "Fermionic entanglement and correlation," *arXiv:2207.03848*, 2022. DOI: 10.48550/arXiv.2207.03848.

[180] Ö. Legeza and J. Sólyom, "Optimizing the density-matrix renormalization group method using quantum information entropy," *Phys. Rev. B*, vol. 68, p. 195 116, 19 2003. DOI: 10.1103/PhysRevB.68.195116.

[181] J. Rissler, R. M. Noack, and S. R. White, "Measuring orbital interaction using quantum information theory," *Chem. Phys.*, vol. 323, no. 2-3, pp. 519–531, 2006. DOI: 10.1016/j.chemphys.2005.10.018.

[182] C. Adami and N. J. Cerf, "Von Neumann capacity of noisy quantum channels," *Phys. Rev. A*, vol. 56, pp. 3470–3483, 5 1997. DOI: 10.1103/PhysRevA.56.3470.

[183] B. Groisman, S. Popescu, and A. Winter, "Quantum, classical, and total amount of correlations in a quantum state," *Phys. Rev. A*, vol. 72, p. 032 317, 3 2005. DOI: 10.1103/PhysRevA.72.032317.

[184] M. Grant and S. Boyd, *CVX: Matlab software for disciplined convex programming, version 2.1*, https://cvxr.com/cvx, 2014.

[185] M. Grant and S. Boyd, "Graph implementations for nonsmooth convex programs," in *Recent Advances in Learning and Control*, ser. Lecture Notes in Control and Information Sciences, V. Blondel, S. Boyd, and H. Kimura, Eds., Springer-Verlag Limited, 2008, pp. 95–110. DOI: 10.1007/978-1-84800-155-8_7.

[186] K. Wang, X. Wang, and M. M. Wilde, "Quantifying the unextendibility of entanglement," *New J. Phys.*, vol. 26, no. 3, p. 033 013, 2024. DOI: 10.1088/1367-2630/ad264e.

[187] D. M. Greenberger, M. A. Horne, and A. Zeilinger, "Going beyond Bell's theorem," in *Bell's theorem, quantum theory and conceptions of the universe*, Springer, 1989, pp. 69–72. DOI: 10.1007/978-94-017-0849-4_10.

[188] N. D. Mermin, "Quantum mysteries revisited," *Am. J. Phys*, vol. 58, no. 8, pp. 731–734, 1990. DOI: 10.1119/1.16503.

[189] W. Dür, G. Vidal, and J. I. Cirac, "Three qubits can be entangled in two inequivalent ways," *Phys. Rev. A*, vol. 62, p. 062 314, 6 2000. DOI: 10.1103/PhysRevA.62.062314.

[190] D. T. Pope and G. J. Milburn, "Multipartite entanglement and quantum state exchange," *Phys. Rev. A*, vol. 67, p. 052 107, 5 2003. DOI: 10.1103/PhysRevA.67.052107.

[191] H. Zhai, H. R. Larsson, S. Lee, Z.-H. Cui, T. Zhu, C. Sun, L. Peng, R. Peng, K. Liao, J. Tölle, J. Yang, S. Li, and G. K.-L. Chan, "Block2 : A comprehensive open source framework to develop and apply state-of-the-art DMRG algorithms in electronic structure and beyond," *J. Chem. Phys.*, vol. 159, no. 23, p. 234 801, 2023, ISSN: 0021-9606, 1089-7690. DOI: 10.1063/5.0180424.

[192] T. M. Krygowski and M. K. Cyrański, "Structural aspects of aromaticity," *Chem. Rev.*, vol. 101, no. 5, pp. 1385–1420, 2001. DOI: 10.1021/cr990326u.

[193] F. Feixas, E. Matito, J. Poater, and M. Solà, "On the performance of some aromaticity indices: A critical assessment using a test set," *J. Comput. Chem.*, vol. 29, no. 10, pp. 1543–1554, 2008. DOI: 10.1002/jcc.20914.

[194] T. Helgaker, P. Jorgensen, and J. Olsen, *Molecular electronic-structure theory*. John Wiley & Sons, 2013. DOI: 10.1002/9781119019572.

[195] C. J. Stein and M. Reiher, "Automated selection of active orbital spaces," *J. Chem. Theory Comput.*, vol. 12, no. 4, pp. 1760–1771, 2016. DOI: 10.1021/acs.jctc.6b00156.

[196] K. D. Vogiatzis, D. Ma, J. Olsen, L. Gagliardi, and W. A. De Jong, "Pushing configuration-interaction to the limit: Towards massively parallel MCSCF calculations," *J. Chem. Phys.*, vol. 147, no. 18, p. 184 111, 2017. DOI: 10.1063/1.4989858.

[197] D. A. Kreplin, P. J. Knowles, and H.-J. Werner, "Second-order mcscf optimization revisited. i. improved algorithms for fast and robust second-order casscf convergence," *J. Chem. Phys.*, vol. 150, no. 19, p. 194 106, 2019. DOI: 10.1063/1.5094644.

[198] D. A. Kreplin, P. J. Knowles, and H.-J. Werner, "Mcscf optimization revisited. ii. combined first-and second-order orbital optimization for large molecules," *J. Chem. Phys.*, vol. 152, no. 7, p. 074 102, 2020. DOI: 10.1063/1.5142241.

[199] B. G. Levine, A. S. Durden, M. P. Esch, F. Liang, and Y. Shu, "CAS without SCF—Why to use CASCI and where to get the orbitals," *J. Chem. Phys.*, vol. 154, no. 9, 2021, ISSN: 0021-9606. DOI: 10.1063/5.0042147.

[200] B. O. Roos, "The complete active space self-consistent field method and its applications in electronic structure calculations," *Adv. Chem. Phys.*, vol. 69, pp. 399–445, 1987. DOI: 10.1002/9780470142943.ch7.

[201] K. Pierloot, "The CASPT2 method in inorganic electronic spectroscopy: From ionic transition metal to covalent actinide complexes∗," *Mol. Phys.*, vol. 101, no. 13, pp. 2083–2094, 2003. DOI: 10.1080/0026897031000109356.

[202] V. Veryazov, P.-Å. Malmqvist, and B. O. Roos, "How to select active space for multiconfigurational quantum chemistry?" *Int. J. Quantum Chem.*, vol. 111, no. 13, pp. 3329–3338, 2011. DOI: 10.1002/qua.23068.

[203] H. J. A. Jensen, P. Jørgensen, H. Ågren, and J. Olsen, "Second-order Møller–Plesset perturbation theory as a configuration and orbital generator in multiconfiguration self-consistent field calculations," *J. Chem. Phys.*, vol. 88, no. 6, pp. 3834–3839, 1988. DOI: 10.1063/1.453884.

[204] J. M. Bofill and P. Pulay, "The unrestricted natural orbital–complete active space (UNO–CAS) method: An inexpensive alternative to the complete active space–self-consistent-field (CAS–SCF) method," *J. Chem. Phys.*, vol. 90, no. 7, pp. 3637–3646, 1989, ISSN: 0021-9606. DOI: 10.1063/1.455822.

[205] S. Keller, K. Boguslawski, T. Janowski, M. Reiher, and P. Pulay, "Selection of active spaces for multiconfigurational wavefunctions," *J. Chem. Phys.*, vol. 142, no. 24, 2015, ISSN: 0021-9606. DOI: 10.1063/1.4922352.

[206] J. Zou, K. Niu, H. Ma, S. Li, and W. Fang, "Automatic selection of active orbitals from generalized valence bond orbitals," *J. Phys. Chem. A*, vol. 124, no. 40, pp. 8321–8329, 2020. DOI: 10.1021/acs.jpca.0c05216.

[207] L. Ding and C. Schilling, "Correlation paradox of the dissociation limit: A quantum information perspective," *J. Chem. Theory Comput.*, vol. 16, no. 7, pp. 4159–4175, 2020. DOI: 10.1021/acs.jctc.0c00054.

[208] M. Bensberg and M. Reiher, "Corresponding active orbital spaces along chemical reaction paths," *J. Phys. Chem. Lett.*, vol. 14, no. 8, pp. 2112–2118, 2023. DOI: 10.1021/acs.jpclett.2c03905.

[209] Perez-Garcia, D and Verstraete, Frank and Wolf, MM and Cirac, JI, "Matrix product state representations," *Quantum Inf. Comput.*, vol. 7, no. 5-6, pp. 401–430, 2007, ISSN: 1533-7146. DOI: 10.26421/qic7.5-6-1.

[210] S. R. White, "Density matrix formulation for quantum renormalization groups," *Phys. Rev. Lett.*, vol. 69, no. 19, pp. 2863–2866, 1992. DOI: 10.1103/PhysRevLett.69.2863.

[211] U. Schollwöck, "The density-matrix renormalization group," *Rev. Mod. Phys.*, vol. 77, no. 1, pp. 259–315, 2005. DOI: 10.1103/RevModPhys.77.259.

[212] S. R. White and R. L. Martin, "Ab initio quantum chemistry using the density matrix renormalization group," *J. chem. Phys.*, vol. 110, no. 9, pp. 4127–4130, 1999. DOI: 10.1063/1.478295.

[213] K. H. Marti and M. Reiher, "The density matrix renormalization group algorithm in quantum chemistry," *Z Phys. Chem.*, vol. 224, no. 3-4, pp. 583–599, 2010. DOI: 10.1524/zpch.2010.6125.

[214] G. K.-L. Chan and S. Sharma, "The density matrix renormalization group in quantum chemistry," *Annu. Rev. Phys. Chem.*, vol. 62, pp. 465–481, 2011. DOI: 10.1146/annurev-physchem-032210-103338.

[215] A. Baiardi and M. Reiher, "The density matrix renormalization group in chemistry and molecular physics: Recent developments and new challenges," *J. Chem. Phys.*, vol. 152, p. 040 903, 2020. DOI: 10.1063/1.5129672.

[216] G. Moritz and M. Reiher, "Decomposition of density matrix renormalization group states into a Slater determinant basis," *J. Chem. Phys.*, vol. 126, no. 24, 2007. DOI: 10.1063/1.2741527.

[217] *QIO: Quantum information-assisted orbital optimization package. Accessed on March 21st, 2024*. Christian Schilling Group, 2024. [Online]. Available: https://github.com/schilling-group/QIO.

[218] G. K.-L. Chan and M. Head-Gordon, "Highly correlated calculations with a polynomial cost algorithm: A study of the density matrix renormalization group," *J. Chem. Phys.*, vol. 116, no. 11, pp. 4462–4476, 2002. DOI: 10.1063/1.1449459.

[219] Q. Sun, T. C. Berkelbach, N. S. Blunt, G. H. Booth, S. Guo, Z. Li, J. Liu, J. D. McClain, E. R. Sayfutyarova, S. Sharma, S. Wouters, and G. K.-L. Chan, "Pyscf: The python-based simulations of chemistry framework," *Wiley Interdiscip. Rev. Comput. Mol. Sci*, vol. 8, no. 1, e1340, 2018. DOI: 10.1002/wcms.1340.

[220] V. Bondybey and J. English, "Electronic structure and vibrational frequency of Cr_2," *Chem. Phys. Lett.*, vol. 94, no. 5, pp. 443–447, 1983. DOI: 10.1016/0009-2614(83)85029-5.

[221] N. B. Balabanov and K. A. Peterson, "Systematically convergent basis sets for transition metals. I. All-electron correlation consistent basis sets for the 3d elements Sc–Zn," *J. Chem. Phys.*, vol. 123, no. 6, p. 064 107, 2005. DOI: 10.1063/1.1998907.

[222] W. Kutzelnigg and W. Liu, "Quasirelativistic theory equivalent to fully relativistic theory," *J. Chem. Phys.*, vol. 123, no. 24, p. 241 102, 2005. DOI: 10.1063/1.2137315.

[223] D. Peng and M. Reiher, "Exact decoupling of the relativistic Fock operator," *Theor. Chem. Acc.*, vol. 131, pp. 1–20, 2012. DOI: 10.1007/s00214-011-1081-y.

[224] W. Mizukami, K. Mitarai, Y. O. Nakagawa, T. Yamamoto, T. Yan, and Y.-y. Ohnishi, "Orbital optimized unitary coupled cluster theory for quantum computer," *Phys. Rev. Res.*, vol. 2, p. 033 421, 3 2020. DOI: 10.1103/PhysRevResearch.2.033421.

[225] S. Yalouz, B. Senjean, J. Günther, F. Buda, T. E. O'Brien, and L. Visscher, "A state-averaged orbital-optimized hybrid quantum–classical algorithm for a democratic description of ground and excited states," *Quantum Sci. Technol.*, vol. 6, no. 2, p. 024 004, 2021. DOI: 10.1088/2058-9565/abd334.

[226] A. Fitzpatrick, A. Nykänen, N. W. Talarico, A. Lunghi, S. Maniscalco, G. García-Pérez, and S. Knecht, "A self-consistent field approach for the variational quantum eigensolver: Orbital optimization goes adaptive," *arXiv:2212.11405*, 2022. DOI: 10.48550/arXiv.2212.11405.

[227] W. Dobrautz, I. O. Sokolov, K. Liao, P. L. Ríos, M. Rahm, A. Alavi, and I. Tavernelli, "Toward real chemical accuracy on current quantum hardware through the transcorrelated method," *J. Chem. Theory Comput.*, 2024. DOI: 10.1021/acs.jctc.4c00070.

[228] G. Knizia and G. K.-L. Chan, "Density matrix embedding: A simple alternative to dynamical mean-field theory," *Phys. Rev. Lett.*, vol. 109, p. 186 404, 18 2012. DOI: 10.1103/PhysRevLett.109.186404.

[229] S. Wouters, C. A. Jiménez-Hoyos, Q. Sun, and G. K.-L. Chan, "A practical guide to density matrix embedding theory in quantum chemistry," *J. Chem. Theory Comput.*, vol. 12, no. 6, pp. 2706–2719, 2016. DOI: 10.1021/acs.jctc.6b00316.

[230] S. Yalouz, S. Sekaran, E. Fromager, and M. Saubanère, "Quantum embedding of multi-orbital fragments using the block-Householder transformation," *J. Chem. Phys.*, vol. 157, no. 21, p. 214 112, 2022. DOI: 10.1063/5.0125683.

Acknowledgement

This has been a truly wonderful journey. Granted, starting the PhD in the middle of the pandemic was not easy. And no, it has not always been a smooth sailing. And yes, there are times when I wanted to pull my hairs out. And no, my neck and back are not in a good shape anymore. Where was I going with all this... Ah right, a truly wonderful journey. And I could not have arrived here without the supports from many people in my life.

First I would like to thank my supervisor Christian for his continuous guidance and support. You always gave me the freedom and encouraged me to develop my own ideas, to learn new things, and to join interesting projects even if they would not be a part of my thesis. I truly learned a great deal from you (unfortunately not in terms of latte arts).

Also many thanks to all my colleagues in the Schilling group (who also helped proofread parts of this thesis): Julia, Damiano, Cheng-Lin, and Ke. Working and hanging out with you has been a real blast, and we will always share that jail cell of a coffee room together.

To my collaborator Stefan Knecht, thank you for helping me transition from someone who knows nothing about quantum chemistry, to someone who knows *almost* nothing about quantum chemistry.

To everyone in the Schollwöck chair, Mattia, Matjaz, Lukas, Héloïse, Tim, Henning, Giovanni, Sebastian..., I enjoyed those lovely banters and occasional beers that brightened my days.

I thank my parents for keeping their composure when I told them I was going for a PhD and not a "proper job". Thank you for only wanting me to be happy.

Finally, to my partner Gian, thank you for tolerating my "zombie mode" every time I was stuck on a problem and telling me the answer was four, for being my rock, and for letting me be yours.